HARVARD UNIVERSITY
Graduate School of Arts and Sciences

DISSERTATION ACCEPTANCE CERTIFICATE

The undersigned, appointed by the

Department of Physics

have examined a dissertation entitled

The Physics of High-Temperature Superconducting Cuprates in van der Waals Heterostructures

presented by Shu Yang Frank Zhao

candidate for the degree of Doctor of Philosophy and hereby certify that it is worthy of acceptance.

Signature _____

Typed name: Professor Philip Kim, Chair

Signature _____

Typed name: Professor Jenny Hoffman

Signature _____

Typed name: Professor Subir Sachdev

Date: July 21, 2021

The Physics of High-Temperature Superconducting Cuprates in van der Waals Heterostructures

A DISSERTATION PRESENTED
BY
SHU YANG FRANK ZHAO
TO
THE DEPARTMENT OF PHYSICS
IN THE
GRADUATE SCHOOL OF ARTS AND SCIENCE

IN PARTIAL FULFILLMENT OF THE REQUIREMENTS
FOR THE DEGREE OF
DOCTOR OF PHILOSOPHY
IN THE SUBJECT OF
PHYSICS

HARVARD UNIVERSITY
CAMBRIDGE, MASSACHUSETTS
UNITED STATES OF AMERICA
JULY 2021

Dissertation Advisor: Professor Philip Kim Shu Yang Frank Zhao

The Physics of High-Temperature Superconducting Cuprates in van der Waals Heterostructures

Abstract

Advances in crystal handling techniques specialized to van der Waals (vdW) materials – crystals with only weak vdW bonds between strongly bonded crystal planes – have brought about a new generation of devices with emergent properties in atomically thin layers and interfaces, which do not appear in their bulk counterpart. Many vdW materials, such as the cuprate high temperature superconductor $Bi_2Sr_2CaCu_2O_{8+x}$ (BSCCO), spontaneously react with air and thermally decompose even at room temperature, rendering the powerful arsenal of vdW crystal handling techniques inapplicable. In this Dissertation, we develop a versatile suite of novel vdW fabrication techniques so that we can handle chemically sensitive vdW crystals like any other. We first demonstrate that the vdW heterointerface between graphene and hexagonal boron nitride can be electrochemically intercalated with lithium in a controlled way, like the interface between graphene crystals. Next, we use a scanning nano X-ray diffraction probe to visualize the crystal structure of an exfoliated BSCCO crystal 2 unit cells thick with 100 nm spatial resolution. We find that while the exfoliated and bulk crystals have the same incommensurate lattice modulations (ILM), the ILM spatial distribution is different in the exfoliated crystal, where it is correlated with the local strain. Next, we create BSCCO Hall bar devices down to 2 unit cells, where we observe Hall sign reversal both above and below the superconducting transition temperature. As the samples become thinner, the region over which the Hall resistance reverses sign enlarges due to enhanced superconducting fluctuations in the atomically thin samples as well as a decrease of carrier mobility. We obtain quantitative agreement between theory and experiment, which establishes excess charges at the core of superconducting vortices as the origin of Hall sign reversal below T_C. Finally, we engineer twist Josephson junctions between BSCCO crystals, with quality approaching that of intrinsic Josephson junctions in single crystals. Our angle-dependent critical current clearly reflects the expected d-wave symmetry of the order parameter. At 45° twist angle, we observe fractional Shapiro steps which indicate the presence of a second harmonic in the Josephson junction current-phase relation, originating from co-tunneling of Cooper pairs at the twist junction. Such a process is expected to support an emergent interfacial topological superconducting phase, persisting to the superconducting transition temperature of the cuprate crystal.

Contents

Contributing Authors

S.Y.F.Z. is grateful for the contributions by the following colleagues and friends, without whom none of this would have been possible.

The following authors contributed to Chapter 4:

Nicola Poccia, Margaret G. Panetta, Cyndia Yu, Jedediah W. Johnson, Christa Harper, Hyobin Yoo, and Philip Kim.

Chapter 5 is adapted from the following publication:

S.Y. Frank Zhao, Giselle A. Elbaz, D. Kwabena Bediako, Cyndia Yu, Dmitri K. Efetov, Yinsheng Guo, Jayakanth Ravichandran, Kyung-Ah Min, Suklyun Hong, Takashi Taniguchi, Kenji Watanabe, Louis E. Brus, Xavier Roy, and Philip Kim. *Controlled Electrochemical Intercalation of Graphene/h-BN van der Waals Heterostructures*, Nano Letters **18**, 460-466 (2018)

Chapter 6 is adapted from the following publication:

Nicola Poccia, **S.Y. Frank Zhao**, Hyobin Yoo, Xiaojing Huang, Hanfei Yan, Yong S. Chu, Ruidan Zhong, Genda Gu, Claudio Mazzoli, Kenji Watanabe, Takashi Taniguchi, Gaetano Campi, Valerii M. Vinokur, and Philip Kim. *Spatially correlated incommensurate lattice modulations in an atomically thin high-temperature* $Bi_{2.1}Sr_{1.9}CaCu_{2.0}O_{8+y}$ *superconductor*. Phys. Rev. Materials, **4**, 114007 (2020).

Chapter 7 is adapted from the following publication:

S. Y. Frank Zhao, Nicola Poccia, Margaret G. Panetta, Cyndia Yu, Jedediah W. Johnson, Hyobin Yoo, Ruidan Zhong, G.D. Gu, Kenji Watanabe, Takashi Taniguchi, Svetlana V. Postolova, Valerii M. Vinokur, and Philip Kim. *Sign-Reversing Hall Effect in Atomically Thin High-Temperature* $Bi_{2.1}Sr_{1.9}CaCu_{2.0}O_{8+\delta}$ *Superconductors*. Phys. Rev. Lett. **122**, 247001 (2019).

The following authors contributed to Chapter 8:

Nicola Poccia, Xiaomeng Cui, Pavel A. Volkov, Hyobin Yoo, Rebecca Engelke, Yuval Ronen, Ruidan Zhong, Genda Gu, Stephan Plugge, Tarun Tummuru, Marcel Franz, Jedediah H. Pixley, and Philip Kim.

To Miranda, and all the children of the world,

Who will one day become giants,

Upon whose shoulders future generations may stand.

Acknowledgments

It has been a tremendous privilege to observe, as an insider, the growth of our scientific knowledge. Around my first year of high school, graphene had been isolated for the first time. In my last, the topological insulator was discovered. In the first weeks of my freshman undergraduate year, the Large Hadron Collider was turned on. Shortly after I graduated, the Higgs boson had been announced. From there, the discoveries came in ever more quickly. I remember asking, when I visited Columbia during open house week, what is left to do now that most of the basic properties of graphene is already known? Boy, that was naive!

It is also a great privilege to have the chance to personally contribute, though in an insignificant way, to the scientific enterprise. It is said that the advances of a single Ph.D. project represents a tiny slice of human knowledge, too small to see in the grand picture. But speaking personally, it took all of the admittedly little strength and intelligence that I could muster, along with the enormous encouragement, help and guidance of those friends, family, colleagues and teachers who have helped me navigate my life.

There is absolutely no doubt that progress would not have been possible without the foresight, guidance, and encouragement of Philip Kim. He always encouraged me to do something a little differently. When things inevitably didn't work, he has the confidence to believe in me when I didn't believe in myself. And when I thought I had made a great discovery, he would insist, correctly, that I check and check again. At which point the "great discovery" often turns out to be some mistake. Yet even then, or perhaps especially then, Philip never lost confidence in me or my results. He allowed me the freedom to explore the field as if I was already an accomplished scientist, yet pointed the way to the real problems when I was lost. He taught me that it is not enough to simply do the experiments that others could do - one must strive to do the things that

might never be doable. For this, and more, I am eternally grateful.

I have also had the wonderful opportunity to be mentored by Ken Burch in my undergraduate years. He was the one who steered me to experimental condensed matter physics, and transport in mesoscopic devices in particular. His infinite ideas, boundless energy and many useful tricks continues to inspire my work today.

In addition, my work today is really the product of many teachers throughout my education. In particular, Zhao, Zhiheng introduced me to astronomy and taught me at a very young age about the Hertzsprung-Russell diagram (among many other things), with which the chaos of seemingly random celestial points of light is brought to order. He kindled that fire of curiosity, which was again fed by George Dimou and John Ambrosio. Henri van Bemmel taught me the value of hard work, and was the first to show me how to run a good experiment. To them, and so many other exceptional teachers who have shaped me into the person that I am today, I am indebted.

I have also learned how to be a scientist from the very talented and thoughtful group members that I had the privilege to work with. Nicola Poccia brought light and excitement to the gravest of moments, and showed me that a great scientist is not only those who are the most imaginative or knowledgeable, but are also those who knows the most imaginative and knowledgeable scientists. It was also an exceptional opportunity to work with the chemist and physicist Kwabena Bediako, who showed me that physics and chemistry are simply a continuation of the other, and a condensed matter physicist ought to be fluent in both. His example inspired me to study single-crystal synthesis for my post-doctoral research in Prof. Joe Checkelsky's group at MIT. Hyobin Yoo showed me the value of visualizing atomic lattices, and whose atomic resolution TEM pictures continues to guide my thinking. I hope to emulate the example of Yuval Ronen, Gil-Ho Lee and Ke Wang, who showed me how much could be accomplished in a few short years, and whose leadership continues to inspire. Wei Tsen and Jayakanth Ravichandran encouraged me to look for new frontiers by studying new materials using new techniques, which was the main line of thinking that led to this dissertation. I also thank Mehdi Rezaee not only for his deep friendship but also the crazy idea to connect the glovebox to liquid nitrogen cooling, a trick which is at the root of many successes. I'm grateful to Dmitri Efetov who showed me the ropes. And Alex

Cui, in whose capable hands this project now rests. I am also thankful to Giselle Elbaz, Hiroshi Idzuchi, Luis Jauregui, Laurel Anderson, Rebecca Engelke, Onder Gul, Zeyu Hao, Joon Young Park, Artem Talanov, Jonah Waissman, Thomas Werkmeister, Zhongying Yan, Andrew Zimmerman, Si Young Lee, Tamar Mentzel, J.-D. Pillet, Young Jae Shin, and all the members of the Philip Kim group for their friendship, support, and the wonderful and stimulating environment that they have created.

I have also had the distinct privilege of mentoring four extremely talented, hardworking and intelligent undergraduates, Cyndia Yu, Margaret Panetta, Jedediah Johnson, and Christa Harper. Each of them have brought their great enthusiasm into their work, and each reminded me of my own reasons for entering physics. I am also very happy that Cyndia and Margaret had chosen to continue their careers in physics in graduate school at Stanford and Chicago respectively. I have no doubt that we will hear of great achievements from them.

Progress in research often comes only after many setbacks, and it is impossible without the support of my friends, many of whom I made along the way. To my friends from Columbia, among them Sky Cheung, Drew Edelberg, Felix Clark, Amy Jahnke, Laura Havener, Matt Anthony, Russell Smith, Marisa Baglaneas, Zach Greene, Rex Brown, Xiaoxiao Zhang, Ryne Carbone, Zizhou Gong and Yun Tian, and with apologies to those who I didn't have the chance to name, thank you for your warm welcome, and thank you for a wonderful and memorable two years in New York.

Then, as our group moved over to Cambridge with Xiaomeng Liu and Austin Cheng, we have had the good luck of setting up the lab together and sharing in some very interesting experiences. I will always remember the many bike rides with Austin, all the way to Providence (but thankfully not all the way back), and who could forget the toast he gave at our wedding! And I will always be inspired by Xiaomeng and his love of creating *things*. At the same time, we have met many friends in our new group. I will always remember the many trips that we went on with Katie Huang, Jing Shi, Gil-Ho Lee, Hyobin Yoo, Andy Joe and many others. Sometimes it was to see the sunrise over the Atlantic. At other times it was to help with Austin and Katie's engagement ceremony amid New York's splendor. Or the trip to Japan with Jesse Crossno when he shared his vision for a more energy efficient future while we fed the wandering deer of Nara. Or it was

the long drive (and back) with Andy to Cornell to attend Clair Han and Shu Wang's wedding.

By chance, I also found some old high school friends - Clair Han and Tarjinder Singh - right in Cambridge. Tarjinder could always be relied on for his bright outlook, whose rays of optimism penetrated the thickest fog of despair. Clair and Shu are always a lot of fun to be around, and their advice and insight is a beacon of wisdom. And then there is Alex Piggott, whose exploits inspires me to always do better. And I couldn't have done it without friends from far away - Tim Adams, Alvin Yang, Sorin Mitrea, Kunal Tiwari, Dina Mistry, Dalini Maharaj, Ryan McGinn, John Hartley, and the rest of the U of T gang, who I know are all pulling for me.

Scientific progress is not merely the work of scientists. Behind every discovery are loving family members whose contributions are no less important than that of the researcher, yet whose essential work are all too often forgotten. I will always treasure the memory of my father, Zhao, Qi, who among so many other things brought me to his lab so that I can see cells with my own eyes. I still remember the time when he talked about the electron microscope, of both the scanning and transmission variety, though regrettably I still have not learned how to use the latter. And then there is my mother, Ding, Yaoyu, who had the foresight to send me to astronomy class when I was four years old. And then, when we immigrated to Canada, she showed me what it meant to work long and hard, but she also taught me the importance of occasionally doing nothing. At the moment when everything appeared to fall apart, her strength and resolve to succeed kept us going. I hope to be able to emulate her strength, and I could not have done anything without her support and example.

Finally, I am grateful to my wife Yang Song, whose approving smile brightens my life. I am grateful for the many good moments that we had together, but I am even more thankful for the moments when she stuck by my side when things weren't going our way. Like the time when we canoed 14 km together in a thunderstorm in the middle of New Hampshire, dripping water as we went. Or all the times I came home late to work on experiments. Each of my success has really been Yang's, for it is her encouragement, patience and inspiration that kept me going. We have built so much together, and I hope we will have the time together to build so much more, with our daughter Miranda. The future stretches before us like an empty canvas, for us to paint with the hues of our lives. Let us advance, and find the most vibrant colors.

More is different.

Philip W. Anderson

1

Van der Waals Heterostructures as a Platform for Novel Physics

It is sometimes thought that systems of enormous complexity may be reduced to the behavior of its individual constituent members. By understanding everything about the electron, we may predict the electronic properties of any material. While philosophically this view may yet prove to be correct, today it is of limited practical utility. Three objects moving under the force of their mutual gravity challenged the mathematical abilities of the best human minds, just as the calculation of an exact quantum description of even tens of mutually interacting particles challenge the best supercomputers today [1].

On the other hand, systems composed of large numbers of strongly interacting individual par-

ticles often behave in surprising ways. For instance, electrons moving in a periodic crystalline potential created by a large lattice of ions can be magnetically deflected in the opposite direction as its negative electrical charge would normally suggest. Upon cooling, the same electrons may suddenly flow without dissipation[2]. As Philip Anderson once pointed out, the behavior of the whole is often different than that of the parts.

Indeed, materials present an interesting playground to explore such emergent behavior. With typical separation between atoms on order of Angstroms (10^{-10} m)[2], a crystal one atomic layer thick cut to 10×10 μm^2 – about half the diameter of the thinnest human hair – already contains about 10^9 atoms. With 94 naturally occurring elements each with unique chemical characteristics, a nearly inexhaustible list of materials may be synthesized, limited only by our imagination and ingenuity.

1.1 Van der Waals Materials

Van der Waals (vdW), or two-dimensional (2D) materials are crystals whose constituent atoms are strongly bonded in a 2D plane, but with planes attached to one another only through weak van der Waals forces[3,4]. The strong anisotropy between the in-plane and out-of-plane bond strength allows remarkably large, but atomically thin, crystals to be mechanically cleaved from a bulk single crystal[5,6]. The resulting surfaces are free of dangling chemical bonds, eliminating sites for impurities and charge traps[7]. These two remarkable properties give vdW materials enormous versatility.

Surprising physical properties emerge on two different levels in vdW systems: within one vdW material itself, and in its interactions with others. First, the library of vdW crystals spans the spectrum of material classes[3,4,8,9]. First and most important is semimetallic graphene, composed of a single layer of carbon atoms arranged in a honeycomb lattice[5,10,11]. When the carbon atoms are replaced with boron and nitrogen atoms at the two honeycomb sublattice sites

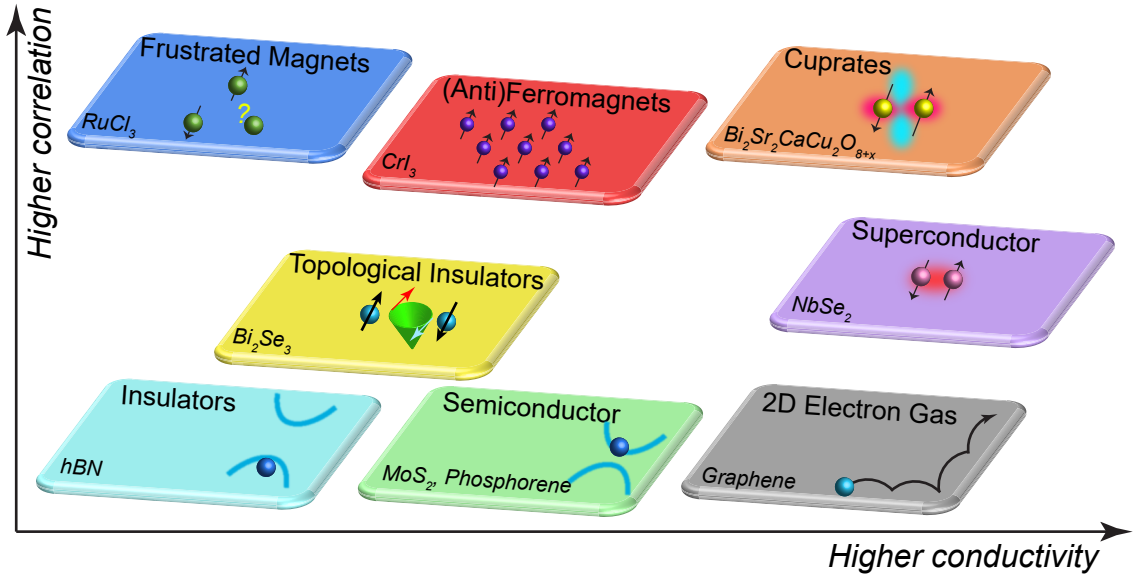

Figure 1.1: Van der Waals crystals spans almost every electronic category: from insulators to superconductors, where the physics can be well understood in single-electron band theory, as well as in materials where electron-electron interactions dominate.

respectively, the resulting hexagonal boron nitride (*h*-BN) crystal forms a wide-bandgap insulator whose surface can be made atomically clean [12]. MoS_2 is a vdW semiconductor whose bandgap becomes direct exactly when it is a single layer in thickness [13], and $NbSe_2$ is a superconductor even at the monolayer limit [14,15,16]. The 2D ferromagnets such as CrI_3 retains ferromagnetism even when thinned down to a single unit cell [17,18,19,8]. More exotic still are the proximate quantum spin liquid $RuCl_3$ [20,21] and topological insulator Bi_2Se_3 [22,23] and its magnetic analog $MnBi_2Te_4$ [24]. Finally, even the high temperature superconductors are represented, in both the cuprate ($Bi_2Sr_2CaCu_2O_{8+x}$) (BSCCO) [25,26,27] and iron pnictide (FeSe) families [28,29].

1.2 Van der Waals Heterostructures

Compared to their bulk counterparts, atomically thin vdW crystals are extraordinarily sensitive to the local electromagnetic and chemical environment [5,25,30,31]. For example, the carrier density of vdW monolayers can be electrostatically tuned [5] by about 10^{13} cm^{-2}. Further, these charge

carriers also interact with the charges carriers and lattices of neighboring vdW crystals placed nearby[12,32]. This opens a second route to emergent properties, where stacks of vdW materials may be engineered to spectacular effect[33,34,35,36]. For example, simply by stacking two graphene crystals on top of each other at small twist angles, both lattices distort themselves into triangular structural domains[35], and at just the right angle, superconductivity emerges near a correlated insulator state[36].

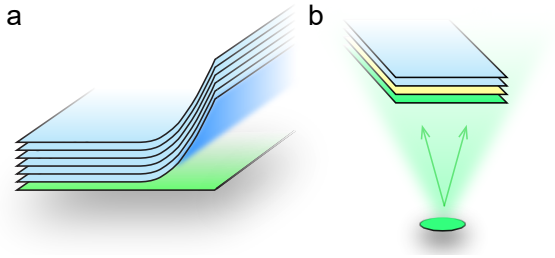

Figure 1.2: Van der Waals heterostructures are made from the top down by cleaving a bulk crystal into an atomically thin layer, and then **a.** using a pick-up method to re-assemble it into a heterostructure. **b.** Epitaxial film growth techniques such as MBE grows crystal layers directly onto a substrate. Layer composition is controlled by restricting the chemical species available at each step.

A formidable arsenal of tools has been developed to manipulate vdW crystals. An array of nanolithography techniques borrowed from semiconductor device manufacturing allows for almost arbitrary control over the in-plane geometry of devices[37]. Control over vertical stacking relies on the dry pick-up technique, which allows vdW crystals to be selectively stacked into *heterostructures* composed of vdW planes of almost any type[38,39], arranged in almost any order[40], placed on almost any substrate[41], and twisted to any relative lattice orientation[36]. Remarkably, when stacked with the utmost care, the resulting interfaces are atomically clean without intruding impurities, even at the atomic level[32]. Well constructed vdW heterostructures may thus be regarded as artificial materials, whose layer structures can be tuned with atomic precision, and whose physical properties are determined by the interactions among the constituents of the entire structure, rather than individual vdW layers.

High quality heterostructures with atomically engineered layers can also be made in many

other ways, each with its own advantages. First, single crystals naturally grow in well-ordered atomic lattices, and in crystals such as BSCCO[42], SmOFeAs[43,44] and $Ba_6Nb_{11}S_{28}$[45], the crystal is arranged into two-dimensional layers, each taking on different electronic roles as in a heterostructure. For example, in BSCCO, the electronically conductive CuO_2 layers host the mobile superconducting charge carriers, while BiO, SrO and Ca layers structurally stabilizes the crystal, and hosts interstitial oxygen dopants which provides the pool of free carriers (holes) needed for superconductivity. However, the structure of such materials are fixed by the chemistry of the constituent elements, and while these structures may be tuned, especially through doping and elemental substitution[46], it is difficult to arbitrarily change the stacking structure beyond the crystal structures that naturally grow from a set of starting precursors.

Atomic layer-by-layer epitaxial film growth techniques, such as pulse laser deposition (PLD) or molecular-beam epitaxy (MBE)[47], is a powerful platform for chemically synthesizing artificial heterostructures of many material classes, with excellent crystallinity and perfect interfaces between layers[48] over macroscopic ($\gg$ millimeter) scales[49,50]. By introducing chemical precursors for individual layers, complex heterostructures may be controllably made. For example, two-dimensional electron gases are realized in MBE grown, modulation doped GaAs heterostructures, whose electronic mobility surpasses that of the best vdW graphene heterostructures[48]. Interfacial superconductivity in MBE-grown monolayer FeSe on a strontium titanate substrate reaches a superconducting transition temperature ten times higher than bulk FeSe[51,52,53]. Superlattices of $(LuFeO_3)_m$ and $(LuFe_2O_4)_1$ is a room-temperature multiferroic[54], whereas none of the layers individually has such a high transition temperature.

In order to realize pristine interfaces between crystals with control over the arrangement of precise atomic layers, atomic layer-by-layer MBE heterostructures are chemically grown on an atomically clean substrate heated to precisely controlled temperatures in ultrahigh vacuum, with the chemical elements in each layer evaporated one layer at a time[47]. In contrast, van der Waals heterostructures are built from the top down, where high-quality bulk single crystals are mechan-

ically exfoliated into small nanocrystals between 0.5 and 500 μm in lateral size. Suitable small crystals are then identified, and stacked[55] using special polymers with temperature tunable adhesion[56,57]. By taking advantage of strong van der Waals forces between vdW crystals, it is possible to directly adhere vdW crystals to each other without using polymers or adhesives in between[56]. Strong interlayer vdW force also aids in creating an atomically clean interface, as trapped impurities are pushed into bubbles[58].

Compared with MBE heterostructures, vdW heterostructures stacked from pre-exfoliated crystals are less sensitive to lattice and elemental mismatches between layers, and offers great freedom in the choice of materials. The top-down control also allows flexibility in the choice of substrates[41] and tight control over interlayer twist angles[36]. However, sample fabrication tends to be laborious and requires skill and care, which increase nonlinearly with heterostructure complexity. The resulting stacks are small (0.5 - 30 μm), usually restricted by imperfections such as bubbles. This makes it difficult to apply bulk sample characterization techniques requiring large sample volumes, such as neutron beam scattering, nuclear magnetic resonance, and magnetic susceptibility measurements. The difficulty of preparing large-area samples also limit industrial applications[7].

1.3 Air-Sensitive van der Waals Heterostructures

While the first experiments involving vdW materials have focused on inert compounds such as graphene and *h*-BN, some of the most interesting vdW materials are chemically reactive and degrade in different ways. For example, semiconducting transition metal dichalcogenides such as $MoTe_2$ very slowly degrade in air over a time-scale of days[59]. Superconducting $NbSe_2$ and magnetic CrI_3 rapidly react with oxygen, but can be protected with a *h*BN cover[16,17]. Finally, monolayer BSCCO rapidly reacts with water, and will lose oxygen dopants in tens of minutes even at room temperature[25]. These problems are made particularly worse in atomically thin vdW crys-

tals, as the entire crystal consists of a surface layer with no protected bulk.

The extreme surface sensitivity of BSCCO in particular requires new techniques, which must all be performed inside an inert gas or high vacuum environment below room temperature. These requirements rule out all types of standard nanofabrication processes available in the cleanroom, as well as standard vdW pickup techniques, which rely on polymer heating far above room temperature to control adhesion[56,57,51]. In this dissertation, we will present several such techniques developed specifically for BSCCO, which enable us to do almost all of the fabrication steps available to ordinary vdW materials, but are generally applicable to any air- or heat-sensitive vdW material. Along the way, these techniques allow us to explore such varied problems as electrochemistry at vdW interfaces between different crystals[60,61], the origin of the Hall anomaly in BSCCO single crystals[26], and the engineering of a high-temperature topological superconductor[62].

Festkörperphysik ist eine Schmutzphysik
[Solid-state physics is the physics of dirt]

Wolfgang E. Pauli

2

A Theoretical Overview of Superconductivity

Superconductivity is a state of matter where macroscopic collections of electronic charge carriers condense into a state described by a single quantum mechanical wavefunction. The particles in the condensate must never strongly interact with its environment, which might suddenly "collapse" the wavefunction, erase its quantum mechanical nature, and contribute to dissipation. Indeed, such protection from interactions is the microscopic origin of the zero electrical resistance characteristic of a superconductor.

Until the discovery of superconductivity in certain copper oxides in 1986[63], superconductivity was believed to be a low-temperature effect manifesting only below 30 K[42]. However, by

1993, the record for the highest superconducting transition temperature had risen to 133 K at ambient pressure in a HgBaCaCuO system[64], a material of enormous structural and electronic complexity[65]. If solid state physics is the study of dirt, it is sometimes in such fertile soil that complex phenomena are found. The cuprates represent one of the central areas of focus for condensed matter physics, and despite over 30 years of intensive study, theoretical questions remain outstanding.

In this chapter, we shall outline the basic phenomenology of superconductivity, and sketch a theoretical foundation necessary to approach the topics in later chapters.

2.1 Superconductivity

When certain materials are cooled below a transition temperature T_C, the material undergoes a thermodynamic phase transition where the electrical resistance vanishes. Simultaneously, any magnetic fields are expelled from the bulk of the material, either to the exterior or into nonsuperconducting domains. These two phenomena, along with macroscopic phase coherence, are the defining features of superconductivity[66,67].

At the microscopic scale, these empirical observations may be explained if the charge carriers are bosonic, which naturally condense into a quantum mechanical ground state. Low-energy scattering is prohibited by the nonzero minimum energy, proportional to the number density of the condensate, needed to scatter a single boson from the condensate. It is then natural to expect the condensate to behave as a quantum mechanical object described by a complex wavefunction, even at nonzero temperature in disordered materials. Moreover, such a quantum object naturally transport charges without energy dissipation. Magnetic flux exclusion also arises naturally, as screening supercurrents may spontaneously appear without energy cost to suppress penetrating magnetic fields, which otherwise increases the free energy. However, there is a crucial piece missing: the electron is naturally a fermion with spin 1/2, and pairs of free electrons in

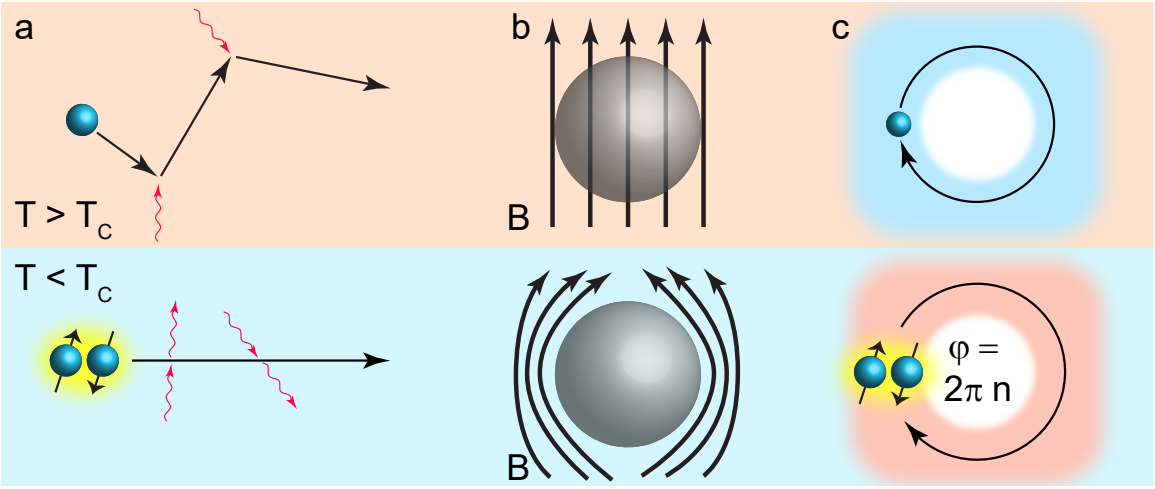

Figure 2.1: Phenomenology of Superconductivity. A superconductor is schematically shown above and below T_C. **a.** shows fermionic charge carriers scattered by small excitations above T_C, while below T_C scattering of Cooper pairs is prohibited below the gap energy. **b.** A normal metal allows a small magnetic field to pass through. Below T_C, the superconductor expels a small magnetic field to the exterior of the sample. **c.** An electron going around a hole in a nonsuperconducting sample is in general not phase coherent, because it will be scattered multiple times before circling the hole (unless the hole is sufficiently small). In a superconductor, scattering is prohibited, so the condensate wavefunction must pick up a phase $\varphi = 2\pi n$, where n is an integer.

three dimensions do not form bosonic bound states until an attractive interaction exceeds a finite threshold strength[66], much like the finite square well problem in *three* dimensions, which does not admit bound solutions until the well is sufficiently strong.

2.2 BCS Theory and the Superconducting Gap

Bardeen, Cooper and Shrieffer (BCS) proposed a solution[68,69]. Cooper[68] considers two free electrons at Fermi energy E_F above a background of others, whose sole purpose is to lift E_F above zero by occupying all states of lower energy. The density of states, which is the phase space volume of all allowed states at a specified energy, is consequently lifted from zero. Cooper's insight is that the additional density of states available at nonzero E_F renders the problem analogous to the finite square well in *one* dimension (with constant density of states), and admits bound solutions to Schrodinger's equation with an attractive potential of any strength, even one arbitrarily weak.

At low temperature, our electron pair must then settle into the bound state, as it is of lower energy, and others must also do the same. The bosonic Cooper pairs then immediately condense into the degenerate ground state.

In most known superconductors, superconductivity originates from interactions between electrons and lattice vibrations (*phonons*). Such interactions are typically weak, and most phonon-mediated BCS superconductors have T_C below 30 K, except in a few families of compounds where conditions are optimal[70,71]. Such materials often refered to as *conventional BCS superconductors*.

In a conventional BCS superconductor, fermionic charge carriers pair up and condense, until the condensate is at equilibrium with normal charge carriers, termed *quasiparticles*. Such a many-body state may be described in the language of second quantization. We define the particle creation operator $c^\dagger_{k\uparrow}$ which creates a quasiparticle[72,67] with wavevector k and spin $\uparrow$ from vacuum, with its annihilation operator hermitian conjugate $c_{k\uparrow}$. These particles are simple plane waves, which are eigenstates of Schrodinger's equation in free space. These operators obey the anticommutation relation for fermions[66,67]:

$$\{c_{k,\sigma}, c^\dagger_{k',\sigma'}\} = \delta_{k,k'}\delta_{\sigma,\sigma'} \tag{2.1}$$

$$\{c^\dagger_{k,\sigma}, c^\dagger_{k',\sigma'}\} = \{c_{k,\sigma}, c_{k',\sigma'}\} = 0 \tag{2.2}$$

and we may define the usual number operator

$$n_{k,\sigma} = c^\dagger_{k,\sigma} c_{k,\sigma} \tag{2.3}$$

In macroscopic samples, the number of charge carriers in the system is not fixed: the system establishes equilibrium with its environment by freely exchanging particles. In such a grand canonical

ensemble, BCS writes a simple approximate wavefunction[69]

$$|\psi\rangle = \prod_k (u_k + v_k c^\dagger_{k,\uparrow} c^\dagger_{-k,\downarrow}) |\varphi_0\rangle \tag{2.4}$$

where $|\varphi_0\rangle$ is the vacuum state with no particles.

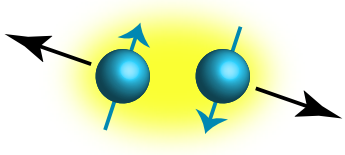

Figure 2.2: A Cooper pair is a boson composed of two charge carriers. In the case of singlet superconductors where the total spin is 0, the Cooper pair is composed of carriers of the opposite spins and wavevector.

The form of the BCS wavefunction is suggestive: at each wavevector $\vec{k}$, there is a complex amplitude v_k for the particle to pair with a partner with the opposite wavevector $-\vec{k}$ and the opposite spin. This Cooper pair then condenses into the ground state. On the other hand, there is also a complex amplitude u_k for the particle to *not* pair, in which case no particles are added to the condensate. We must then expect that $|u_k|^2 + |v_k|^2 = 1$, and in the simplest case if the relative phase difference φ between u and v is a constant (vs. k), then φ is the complex phase of the condensate wavefunction.

We have written down a simple trial wavefunction for the BCS ground state. Now it remains to find the values of u and v given a simple pairing potential. In the simplest case, the Hamiltonian must contain the kinetic energy of each Cooper pair, plus an attractive interaction energy between them. We write the minimal form of the potential which will yield superconductivity[67]:

$$H = \sum_{k,\sigma} \varepsilon_k n_{k,\sigma} + \sum_{k,m} V_{k,m} c^\dagger_{k,\uparrow} c^\dagger_{-k,\downarrow} c_{-m,\downarrow} c_{m,\uparrow} \tag{2.5}$$

The BCS ground state must minimize the free energy in the grand canonical ensemble at zero

temperature:

$$\delta \langle \psi | H - \mu N | \psi \rangle = 0 \tag{2.6}$$

where μ is the chemical potential, equivalent to the Fermi energy at zero temperature, and N is the number operator for the condensate. We know the expectation value $\langle \psi | N | \psi \rangle = 2 \sum_k |v_k|^2$, by the construction of our trial wavefunction[66]. The interaction term scatters Cooper pairs from wavevector m to k, which requires a filled state at m and an empty one at k, and must then involve those probability amplitudes[66]. We may then evaluate the expectation value in (2.6), and for now assuming real u and v:

$$\langle \psi | H - \mu N | \psi \rangle = 2 \sum_k \xi_k v_k^2 + \sum_{k,m} V_{k,m} u_k v_k^* u_m^* v_m \tag{2.7}$$

where $\xi_k = \varepsilon_k - \mu$ is the quasiparticle energy measured relative to the chemical potential μ.

With the constraint that $|u_k|^2 + |v_k|^2 = 1$ with real u and v, we are ready to minimize the free energy. Writing $u_k = \sin \theta_k$ and $v_k = \cos \theta_k$, the derivative $\partial < H - \mu N > / \partial \theta_k$ must vanish when the free energy is minimal. Thus,

$$\frac{\partial < H - \mu N >}{\partial \theta_k} = 0 = -2\xi_k \sin 2\theta_k + \sum_m V_{k,m} \cos 2\theta_k \sin 2\theta_m \tag{2.8}$$

with the solution

$$2\xi_k \tan 2\theta_k = -\sum_m V_{k,m} \sin 2\theta_m \tag{2.9}$$

We define the quantities

$$\Delta_k = -\sum_m V_{k,m} u_m v_m = -\frac{1}{2} \sum_m V_{k,m} \sin 2\theta_m \tag{2.10}$$

and

$$E_k = (\Delta_k^2 + \xi_k^2)^{1/2} \tag{2.11}$$

These simplify the solutions for θ in 2.9:

$$\tan 2\theta_k = -\frac{\Delta_k}{\xi_k} \tag{2.12}$$

which implies that

$$2u_k v_k = \sin 2\theta_k = \frac{\Delta_k}{E_k}; \qquad v_k^2 - u_k^2 = \cos 2\theta_k = -\frac{\xi_k}{E_k} \tag{2.13}$$

We may now finish the derivation by substituting (2.13) into (2.10):

$$\Delta_k = -\frac{1}{2}\sum_m \frac{\Delta_m}{(\Delta_m^2 + \xi_m^2)^{1/2}} V_{k,m} \tag{2.14}$$

which for the simplest possible attractive potential $V_{k,m} = -V$ whenever $|\xi_k|$ and $|\xi_m| \leq \hbar\omega_D$, and 0 elsewhere. Anticipating an electron-phonon mediated pairing mechanism, we set ω_D as the Debye frequency – the characteristic frequency of phonons, above which the phonons will be too slow-moving to respond[67]. Then, if we set $\Delta_k = \Delta$ to be independent of k whenever $\xi_k \leq \hbar\omega_D$, we will reduce (2.14) to find

$$2 = V\sum_k \frac{1}{(\Delta_k^2 + \xi_k^2)^{1/2}} \tag{2.15}$$

which can be analytically solved by turning the sum into an integral over energy with the help of the density of states at Fermi energy $N(0)$, with the solution

$$\Delta = \frac{\hbar\omega_D}{\sinh(\frac{1}{N(0)V})} \approx 2\hbar\omega_D e^{-1/N(0)V} \tag{2.16}$$

and with BCS ground state coefficients

$$v_k^2 = \frac{1}{2}\left[1 - \frac{\xi_k}{(\Delta^2 + \xi_k^2)^{1/2}}\right] \tag{2.17}$$

and up to phase, $u_k^2 = 1 - v_k^2$.

We may now derive the energy change when one single quasiparticle with wavevector $|l, \uparrow\rangle$ is added to the BCS ground state, without its Cooper pair partner[67]. Working from (2.7), we must first remove the Cooper pair with wavevector l, which changes both the kinetic and interaction energy terms:

$$E_- = \langle \psi' | H - \mu N | \psi' \rangle - \langle \psi_{BCS} | H - \mu N | \psi_{BCS} \rangle = -2\xi_l v_l^2 - 2\sum_m V_{l,m} u_l v_l^* u_m^* v_m \tag{2.18}$$

We have assumed that u, v are all real, so we recognize that the second term contains the definition for Δ in (2.10). We also add in the energy ξ_l of the lone excited quasiparticle. After the energy subtraction and addition:

$$E_{-+} = \xi_l(1 - 2v_l^2) + 2u_l v_l \Delta \tag{2.19}$$

where we use (2.13) twice: once to simplify the second term, and again through the relation $u_k^2 = \frac{1}{2}(1 + \xi_k/E_k)$ derived from (2.13):

$$E_{-+} = (\xi_l^2 + \Delta^2)/E_l = E_l \tag{2.20}$$

where $E_l = (\Delta_l^2 + \xi_l^2)^{1/2}$.

Thus, Δ takes on the physical meaning of the minimum energy needed to excite the condensate by adding a quasiparticle into the system at the Fermi energy. The superconducting condensate is gapped from excitations with an energy gap Δ, and is thus protected from excitations unless the perturbation is strong enough to overcome the gap.

In our simple pairing potential, which is independent of k at low energy, Δ is constant. This is often referred to as s-wave superconductivity, in analogy with the isotropic s-orbital. In materials with strongly anisotropic lattices, the $\Delta(k)$ may reflect the same symmetry as the crystal lattice. This is sometimes referred to as *anisotropic s-wave pairing* (see section 9.9.1 in [66]). In such cases, while the strength of the gap changes with lattice directions, the gap never vanishes and the phase of the condensate does not depend on k[73].

In the next section, we shall see that this is not always the case. For example, strong evidence has emerged for a $d_{x^2-y^2}$-wave superconductivity in the cuprate superconductors[73], where the gap changes sign as a function of k. We note that this is still an active area of debate, and a small s-wave component may well coexist with the dominant d-wave order parameter, especially near material edges where additional crystal symmetries are broken.

2.3 Pairing Symmetry and the Cuprates

As we have seen in (2.10) and in the BCS gap equation (2.14), $\Delta(k)$ reflects the symmetry of the pairing potential responsible for superconductivity[74,73]. When $\Delta(k)$ breaks symmetries of the underlying crystal lattice, it is said to be unconventional[66]. Measurement of the symmetry of $\Delta(k)$ therefore places constraints on theories of pairing mechanism specific to a material[75]. Materials with unconventional pairing symmetry may also be useful for engineering unusual quantum states in such materials[76,77,62], with possible applications including quantum computing.

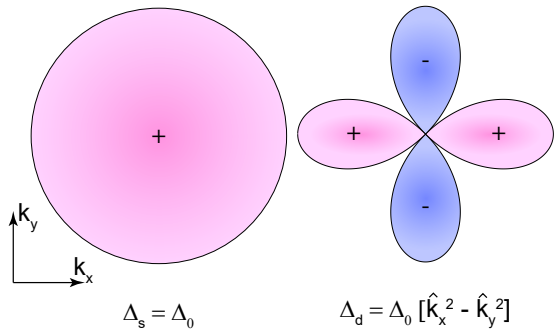

Figure 2.3: *s* **and** *d* **wave gap structures.**

In the case of copper-oxide high temperature superconductors, there is strong evidence that the gap has *d*-wave order parameter, which changes sign under rotation by 90° (see figure 2.3)[74,73]. $\Delta(k)$ is highest in magnitude along the *antinodal* directions along the copper-oxygen-copper bonds, while it vanishes at the diagonal *nodal* directions[78]. The quasiparticle density of states is thus expected to be nonzero all the way to the Fermi energy, in contrast to *s*-wave superconductors[78,73].

Evidence for *d*-wave order parameter (OP) in the cuprates shows up in many experiments. First, measurements of thermal excitations, such as specific heat, are sensitive to energy gaps in the quasiparticle spectrum. The absence of a gap appears as a T^2 scaling of low-temperature specific heat, instead of an exponential suppression as thermal excitations are frozen out below the gap energy[79]. Such low-energy states are also seen in tunneling experiments, where the dI/dV smoothly approaches zero below the gap[80]. The quasiparticle excitation spectrum may also be measured with momentum space resolution in ARPES experiments, where it is seen to explicitly vanish in certain k-space directions[78].

While these experiments are able to probe the quasiparticle density of states, it is difficult to rule out the effect of disorder, which may add states below the gap[73]. The strongest evidence for *d*-wave OP come from quantum interference experiments near in-plane grain boundaries in superconducting films where the crystal lattices change direction[73], or at the boundary between cuprate superconductors and elemental metallic superconductors, which host conventional superconductivity[74]. Such quantum interference experiments are cleverly engineered to measure the condensate's phase difference along different crystallographic directions.

2.4 Josephson Junctions

The crystal grain boundary junctions from the previous section are examples of Josephson junctions (JJ), which form whenever two superconductors are joined together through a sufficiently

short weak link so that a current flows without resistance[66]. The weak link may take on a variety of forms, including non-superconducting metals, insulating tunnel barriers, and even ferromagnets. Fundamentally, the physics of JJs are rich, and they may be used to probe basic properties of superconductors, such as the pairing symmetry of the cuprates discussed in the previous section. Technologically, they form the core of such devices as the Superconducting Quantum Interference Device (SQUID), the Josephson voltage standard, and various implementations of the superconducting quantum bit (qubit).

The superconductivity inside a Josephson junction is weak, and the superconducting phase is consequently allowed to sharply change across the junction as an external current is applied. For most junctions, this *current-phase relation* holds that[81]:

$$I = I_C \sin\gamma \tag{2.21}$$

where I_C is the critical current, I is the current through the junction, and γ is the gauge-invariant phase difference across the junction, which has contributions due to the superconducting OP phase change across the junction γ_0, plus a term from the magnetic vector potential $\vec{A}$:

$$\gamma = \gamma_0 - (2\pi/\Phi_0)\int \vec{A}\cdot d\vec{s} \tag{2.22}$$

where the path integral is taken through the junction.

As the current across the junction is increased, the Josephson phase γ increases accordingly until the supercurrent is too high to be supported in the junction at I_C. At this point, the voltage V across the junction jumps to a nonzero value, along with the resistance.

If we bias the JJ at a constant voltage V, γ will increase, according to the second Josephson relation:

$$\frac{d\gamma}{dt} = \frac{2eV}{\hbar} \tag{2.23}$$

where e is the elementary charge. The current through the junction will also oscillate.

The current-phase relation depends on the detail of the Josephson junction, and sometimes deviates from (2.21). For example, Josephson junctions between d-wave superconductors with a 90° relative twist angle will naturally have a ground state $\gamma = \pi$, or equivalently a negative I_C, due to the sign change in the OP[62]. Similar effects are achieved in ferromagnet JJs[82]. Such JJs are referred to as *π Josephson junctions*. In addition, harmonics of higher order may also be seen in special cases. We shall encounter such a case in Chapter 8, when Josephson junctions are formed between BSCCO crystals twisted to 45°.

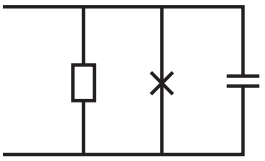

Figure 2.4: RCSJ Model. A Josephson junction may be modeled as an ideal JJ in parallel with a resistor and capacitor.

As a circuit element, physical Josephson junctions are modeled as an ideal Josephson junction described by (2.21) and (2.23), in parallel with a capacitor and resistor, in the *Resistively and Capacitatively Shunted Junction* (RCSJ) Model[66,83]. Here, the resistor models the dissipative transport at finite voltages, and the capacitive term captures the capacitive coupling between the two superconductors at the junction. Using Kirchoff's circuit laws, we see that:

$$I = I_C \sin\gamma + V/R + CdV/dt \tag{2.24}$$

We then use the second Josephson relation (2.23) to eliminate V. The resulting differential equation contains a characteristic frequency of the JJ, the *plasma frequency* ω_p:

$$\omega_p = \left(\frac{2eI_C}{\hbar C}\right)^2 \tag{2.25}$$

and the dimensionless quality factor Q, which describes the amount of damping (due to dissipation) in the system.

$$Q = \omega_p RC = R\left(\frac{2eI_C C}{\hbar}\right)^{1/2} \tag{2.26}$$

which simplifies (2.24) to

$$\frac{d^2\gamma}{d\tau^2} + \frac{1}{Q}\frac{d\gamma}{d\tau} + \sin\gamma = \frac{I}{I_C} \tag{2.27}$$

where $\tau = 1/\omega_p$.

Mathematically, (2.27) is equivalent to the equation of motion of a point particle moving about the coordinate γ, under a friction damping term and a potential $U(\gamma)$:

$$U(\gamma) = -E_J\cos\gamma - (\hbar I/2e)\gamma \tag{2.28}$$

where the Josephson coupling energy $E_J = \hbar I_C/2e$.

The first term in $U(\gamma)$ comes from the current-phase relation (2.21), and it implies that the current-phase relation is related to the junction's free energy via a derivative. Thus, we may interpret the condition that $\gamma = 0$ with no external currents to be consequence that $\gamma = 0$ in the ground state of the junction [83].

The second term tilts the potential as current bias is increased (see figure 2.5). When the tilt is small, the phase particle stays at rest at one of the local minima on the potential. As I reaches I_C, the tilt becomes so great that it removes the periodic minima in the first term (in other words, $dU/d\gamma$ is nonzero everywhere). At this point, the phase particle rolls down the slope, $d\gamma/d\tau$ becomes nonzero, and the system jumps out of the supercurrent state.

When the current bias $|I|$ is then lowered back below I_C, the behavior of the phase particle depends on the damping $1/Q$. When damping is large so that Q « 1, dissipation (which shows up as friction in our mechanical analog) strongly affects the system, and the phase particle is *retrapped* into a potential energy minimum as soon as they appear at $I_R = I_C$. However, if the

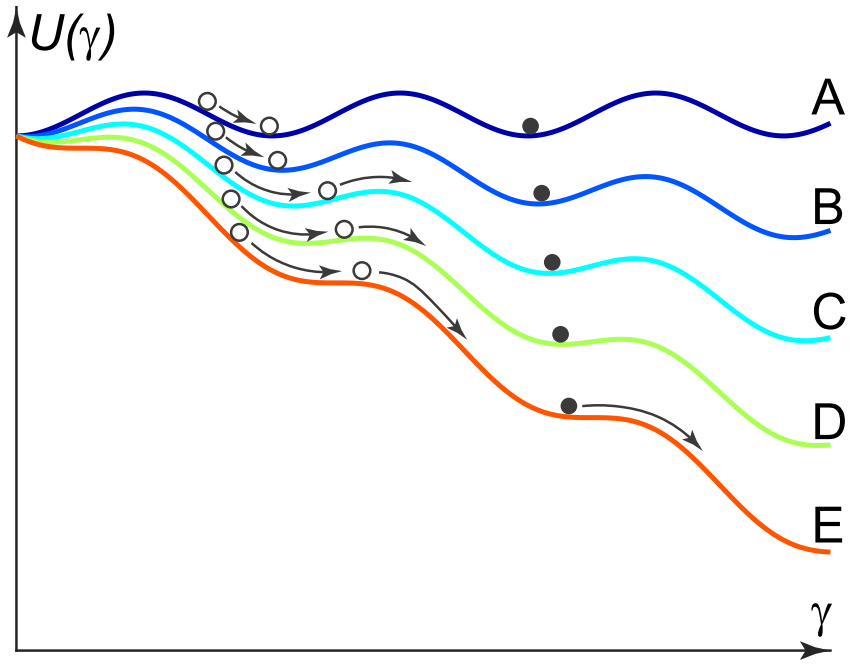

Figure 2.5: RCSJ Washboard Potential from (2.28). The behavior of a JJ is modeled by a fictitious particle in the washboard potential $U(\gamma)$. For an underdamped junction initially at zero current (solid circle), the test particle remains in a local minimum until the current bias is great enough to eliminate the local minima at the critical current in E. The particle rolls down the slope and junction V becomes nonzero. For a JJ already in the voltage state (hollow circle), the minima must be deep enough to overcome the inertia of the ball, so that the retrap current (B) is smaller than the critical current.

damping is small so that $Q > 1$, then the inertia of the phase particle is dominant, and retrapping only occurs at $I_R < I_C$. The amount of hysteresis that appears in I-V sweeps then measures the damping[66]:

$$Q = \frac{4I_C}{\pi I_r} \tag{2.29}$$

Next, we apply an AC voltage bias at radio frequency in addition to the usual DC bias. We can model this simply by adding an oscillatory term to the voltage $V(t) = V + v\cos\omega t$. We substitute

this expression into the Josephson relation (2.23), and integrate to obtain γ:

$$\gamma(t) = \frac{2e}{\hbar}\left(Vt + \frac{v\sin\omega t}{\omega} + \gamma_0\right) \tag{2.30}$$

where γ_0 is a constant of integration. Now we may substitute this expression into the current-phase relation (2.21). As we shall discuss later, if the current-phase relation takes a different form, the JJ response may change.

$$I = I_C \sin\left(\omega_0 t + \gamma_0 + \frac{\omega_0 v}{\omega V}\sin\omega t\right) \tag{2.31}$$

where we define $\omega_0 = 2eV/\hbar$. To treat the $\sin(\sin(\cdot))$ term, we use the angle addition to product identity to separate the $\sin\omega t$ term from the others, so that we may then apply the identities[83]

$$\cos(a\sin\omega t) = J_0(a) + 2\sum_{\eta=1}^{\infty}(-1)^{\eta}J_{2\eta}(a)\cos(2\eta\omega t) \tag{2.32}$$

$$\sin(a\sin\omega t) = 2\sum_{\eta=0}^{\infty}(-1)^{\eta}J_{2\eta+1}(a)\cos((2\eta+1)\omega t) \tag{2.33}$$

where J_η is the Bessel function of the first kind, of integer order. Then, setting $a = \omega_0 v/(\omega V_0)$, our current relation becomes

$$I(t) = I_C\left\{J_0(a)\sin(\omega_0 t + \gamma_0) + \sum_{\eta=1}^{\infty}J_\eta(a)\left(\sin[(\eta\omega + \omega_0)t + \gamma_0] - (-1)^{\eta}\sin[(\eta\omega - \omega_0)t + \gamma_0]\right)\right\} \tag{2.34}$$

If we measure the DC junction voltages with standard voltmeters, which average over millisecond time scales, the terms which oscillate rapidly in time will average out to zero. So then the

contribution of the sum is nonzero only when $\eta\omega = \omega_0$, or:

$$V = \eta\frac{\hbar\omega}{2e}; \quad \forall\eta \in \mathbb{Z} \tag{2.35}$$

At each of these quantized voltages, the current may[66] take on any value within

$$\frac{V_k}{R} \pm I_C J_k\left(\frac{2ev}{\hbar\omega}\right) \tag{2.36}$$

Experimentally, the JJ is usually current-biased at DC with the RF radiation coupled in via an antenna, so it is close to the current-biased regime. In this case, the I-V curve usually looks like a staircase, with plateaus of constant voltage at each of the quantized voltages above. Each step of constant voltage is called a *Shapiro step*.

For underdamped Josephson junctions, it is important that the RF frequency ω is far above the JJ plasma frequency[84]. Otherwise, the Josephson junction may enter a chaotic regime, where the I-V behavior is difficult to predict[85]. In BSCCO intrinsic Josephson junctions between CuO_2 planes, this is a particular challenge, as the Josephson coupling energy is very strong. Shapiro steps were observed by using terahertz radiation far above the plasma frequency[84], shunting the JJ with a metal[86], or by using the weakly superconducting surface JJs[87], which had been chemically weakened by environmental exposure during fabrication.

In rare cases, the current phase relation in (2.21) takes a different form[88]. For example, at a transition from a conventional Josephson junction to a π junction, the sign of I_C in the current-phase relation must change. If there are any small higher-order contributions to the current-phase relation, these must dominate as the first order term vanishes at the transition. Since the current-phase relationship is 2π periodic in phase γ[88], the current-phase relationship can always be written as a Fourier series, and higher-order contributions must appear as higher harmonics in γ. The presence of these terms in the current-phase relation leads to the appearance of fractional

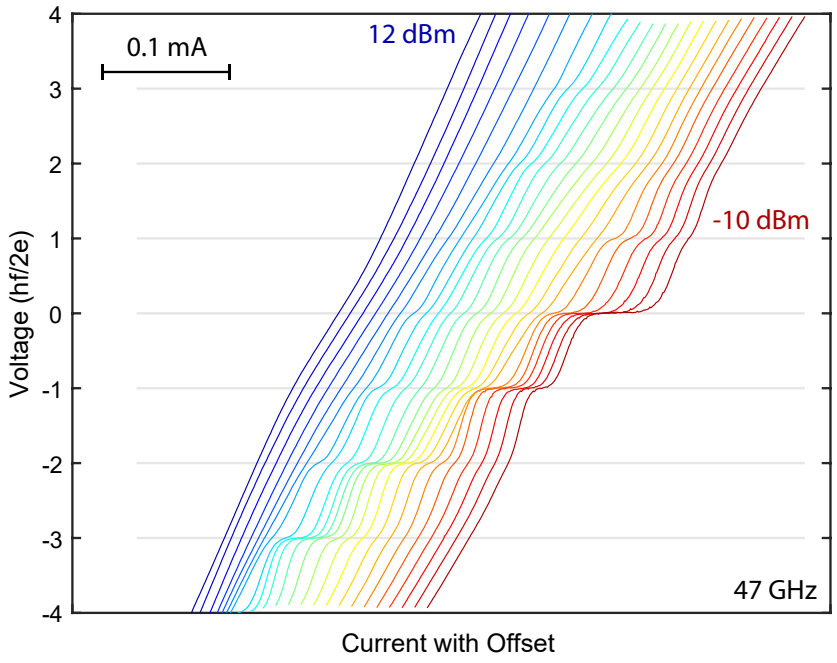

Figure 2.6: Shapiro steps in a Josephson junction between two near-optimally-doped $Bi_2Sr_2CaCu_2O_{8+x}$ crystals, twisted to a relative angle 43.7°. Data taken at 70 K.

Shapiro steps. That is, k in (2.35) takes on fractional values. Experimentally, half fractional steps were previously seen in SFS Josephson junctions near the $0 - \pi$ transition[89].

2.5 Ginzburg-Landau Equations

While the BCS theory provides a microscopic view of superconductivity and its underlying mechanism, the Ginzburg-Landau theory captures the phenomenon of superconductivity. It excels at calculating the behavior of superconductors in experimental conditions, where factors such as sample geometry, boundaries and inhomogeneity enter. It is based on the Landau theory of phase transitions, and was formulated in 1950 before the BCS theory, and yet, it was shown later[90] that the G-L theory may be derived from BCS theory itself, in the limit near T_C and for sufficiently gradual variation in ψ and vector potential A.

In the Landau theory of phase transitions, we first identify an order parameter which becomes nonzero in the low temperature regime below the critical temperature T_C. GL identified the appropriate choice as a complex wave-function ψ defined over all points in space, where $|\psi|^2$ equals the local density of superconducting electrons.

Next, we write down the free energy density f at each point in space:

$$f = f_0 + \alpha|\psi|^2 + \frac{\beta}{2}|\psi|^4 + \frac{1}{2m^*}\left|\left(\frac{\hbar}{i}\nabla - \frac{e^*}{c}A\right)\psi\right|^2 + \frac{h^2}{8\pi} \tag{2.37}$$

where f_0 is the free energy of the normal state, α and β are material dependent parameters, m^* is the effective mass, and h is the local magnetic induction.

The form of (2.37) can be understood in the following way. First, deep inside a uniform superconductor and away from electromagnetic fields, the second and third terms dominate. They are the lowest order terms in the Taylor expansions in $\psi^*\psi$, which are guaranteed to be real. $\alpha(T)$ is tuned so the material has the appropriate transition temperature: $\alpha = a(T - T_C)$. Next, the gradient term is simply the kinetic energy of the superfluid, as the object in round brackets is simply the momentum operator in real space. Finally, we include the energy associated with magnetic fields in free space. The final term is responsible for the Meissner effect, as screening supercurrents spontaneously appear at zero energy cost to suppress the free energy contribution from external magnetic fields.

$F = \int_{\mathbb{R}^3} f(r)dr$ may be minimized with respect to ψ^* and A respectively, yielding the two Ginzburg-Landau equations:

$$-\frac{\hbar^2}{2m^*}\left[\vec{\nabla} - \frac{ie^*}{\hbar c}\vec{A}(r)\right]^2\psi + \alpha\psi + \beta|\psi|^2\psi = 0 \tag{2.38}$$

$$\vec{j}(r) = -\frac{ie^*\hbar}{2m^*}\left[\psi^*\nabla\psi - \psi\nabla\psi^*\right] - \frac{e^{*2}}{m^*c}|\psi|^2\vec{A}(r) \tag{2.39}$$

The Ginzburg-Landau equations reveal that there are two different length scales associated with superconductivity. First, at sample edges, superconductivity is continuously suppressed over a *coherence length* ξ. Next, magnetic fields are pushed out of the bulk of a superconductor with screening supercurrents, over the *London penetration depth* λ_L.

First, we derive ξ by allowing a superconductor to occupy the region $x \geq 0$ away from magnetic fields. Without loss of generality, we may set ψ real. Then, (2.38) becomes:

$$-\frac{\hbar^2}{2m^*\alpha}\frac{d^2\psi}{dx^2} + \psi + \frac{\beta}{\alpha}\psi^3 = 0 \tag{2.40}$$

where we note that $\alpha < 0$ for a superconducting state to be energetically favorable. We re-scale ψ by setting $f^2 = \beta\psi^2/|\alpha|$, and

$$\xi^2 = \frac{\hbar^2}{2m^*|\alpha|} \tag{2.41}$$

Then, the G-L equation becomes $-\xi^2 f'' - f + f^3 = 0$ with solution

$$f = \tanh\left(\frac{x}{\sqrt{2}\xi}\right) \tag{2.42}$$

so ξ is the characteristic length over which superconductivity is suppressed. Physically, it is related to the size of the Cooper pair in BCS theory. Since α changes sign at T_C in order to tune the G-L model in and out of the superconducting state, ξ diverges at T_C.

A second length scale emerges in the suppression of magnetic fields. Let us place a superconductor in the region $z \geq 0$, and apply a magnetic field parallel to the surface: $\vec{B} = B(z)\hat{x}$. Using (2.39), but neglecting the gradients in ψ (associated with currents), and using Maxwell's equations to substitute j,

$$\nabla \times j = \frac{c}{4\pi}\nabla \times (\nabla \times h) = -\frac{e^{*2}}{m^* c}|\psi|^2 \nabla \times A \tag{2.43}$$

which we may simplify to

$$\frac{d^2H}{dz^2} = \frac{4\pi e^{*2}}{m^* c^2}|\psi|^2 H \tag{2.44}$$

from which we may read out the characteristic length scale

$$\lambda_L = \left(\frac{m^* c^2}{4\pi e^{*2}|\psi|^2}\right) \tag{2.45}$$

which deep into the superconductor (compared with ξ), $|\psi| = \sqrt{\alpha/\beta}$

2.6 Type I and II Superconductors and Vortices

When a superconductor is placed into a strong magnetic field (but not yet strong enough to destroy superconductivity completely), flux lines are pushed into non-superconducting domains. This decreases the free energy as the rest of the material becomes superconducting, but possibly at an energy cost near the interface.

Crossing the domain boundary into the superconducting region, the magnetic field drops over a distance λ_L while the superfluid density $|\psi|^2$ increases over ξ. This is energetically favorable when ξ is small, and the competition over these two length scales govern the behavior of the superconductor in magnetic field.

Quantitatively, we define the Ginzburg-Landau parameter $\kappa = \frac{\lambda_L}{\xi}$. Using the G-L equations, we may numerically calculate the free energy difference between the system with one such domain boundary, and a fully superconducting system[66]

$$\delta = 1.89\xi \qquad \kappa \ll 1; \tag{2.46}$$

$$\delta = -1.10\lambda_L \qquad \kappa \gg 1; \tag{2.47}$$

When $\kappa < 1/\sqrt{2}$, the domain boundary wall has positive energy, and domain walls are made as

large as possible. This is the "intermediate state" in Type I superconductors discussed in section 2.3 of[66]. On the other hand, when $\kappa > 1/\sqrt{2}$, the domain wall has negative energy, and the system creates as many magnetic domains as possible.

What is the minimum flux enclosed in each magnetic domain? The condition that the OP's phase must advance by integer multiples of 2π around any closed loop imposes a limit. First, we observe that the supercurrent velocity is related to $\psi = |\psi|e^{i\varphi}$ by

$$m^* v = -2eA/c + \hbar\nabla\varphi \tag{2.48}$$

where we implicitly invoked the BCS Cooper pair with charge $2e$. Integrating both sides on a contour integral around an area S, which encloses a magnetic flux, we observe that

$$\oint_{\partial S} m^* v ds + \frac{e}{c}\oint_{\partial S} A ds = \hbar \oint_{\partial S} \nabla\varphi ds \tag{2.49}$$

Now we recognize that for ψ to be single-valued, $\oint_{\partial S} \nabla\varphi ds = 2\pi n$ for some integer n, and we use Stoke's theorem on the second term, so that:

$$\oint_{\partial S} m^* v ds + \frac{e}{c}\int_S \nabla \times A dn = \hbar 2\pi n \tag{2.50}$$

and by Maxwell's equations, $\nabla \times A = H$. Now we can take S to be infinitely large region, far away from the flux, and the superfluid velocity should go to zero. Then, the first term vanishes, and

$$\Phi = n\frac{hc}{2e}; \quad n \in \mathbb{Z} \tag{2.51}$$

So that the minimum flux enclosed in a magnetic domain is $\Phi_0 = 2.0678 \times 10^{-15}$ T m^2.

A Type II superconductor placed in a weak magnetic field will initially push all flux lines to its exterior. When the magnetic field approaches the lower critical field at H_{C1}, vortices start to

enter the superconductor. As magnetic field continues to increase, the vortices start to interact among themselves, and order themselves into a lattice. Finally, superconductivity is destroyed at the upper critical field H_{C2}.

In a vortex, the magnetic field is focused to its normal core by a circulating screening supercurrent. At a distance on order of ξ, the superconductivity is restored to the bulk value. Magnetic field is also suppressed to zero on the length scale of λ_L. Quantitatively, we can calculate[66] the superfluid density by setting $\psi = \psi_\infty f(r) e^{i\theta}$. This forces the gauge to $A = A(r)\hat{\theta}$. Using the G-L equation,[66] shows that

$$f(r) \approx \tanh \frac{\nu r}{\xi} \tag{2.52}$$

where ν is a constant of order 1. This is shown in figure 2.7

Next, in the extreme Type II limit where $\lambda_L \gg \xi$, the magnetic field drops off as

$$h(r) \to \frac{\Phi_0}{2\pi\lambda^2} \left(\frac{\pi\lambda}{2r}\right)^{1/2} e^{-r/\lambda}; \quad r \to \infty \tag{2.53}$$

and

$$h(r) \approx \frac{\Phi_0}{2\pi\lambda^2} \left(\ln \frac{\lambda}{r} + 0.12\right); \quad \xi \ll r \ll \lambda \tag{2.54}$$

The motion of vortices under an applied current dominates the transport properties of a superconductor in a magnetic field. As an applied current flows past a single vortex, a Lorentz force $F = J \times B/c$ is applied by the current onto the magnetic flux, where J is the current density. The vortex thus moves perpendicular to the transport current at velocity v, which is determined by a friction-like term. The moving magnetic flux then induces an electric field $E = B \times v/c$ parallel to J, which dissipates the energy of the applied current, and results in a nonzero resistance.

When vortices are positioned close to one another, the flux from one vortex will drift away from the other, due to the Lorentz force from the circulating screening current. Such repulsive forces between vortices pushes them into a lattice.

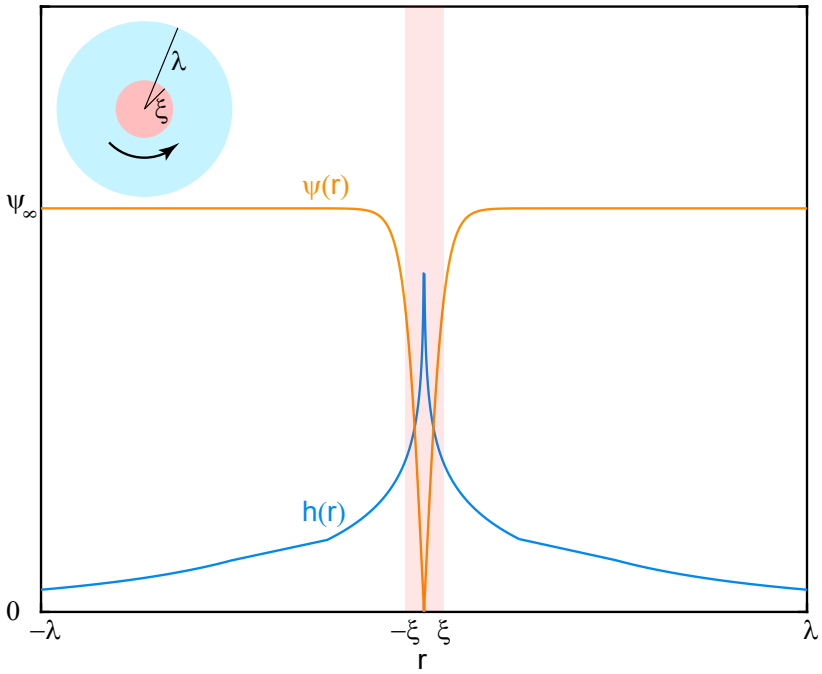

Figure 2.7: Structure of a Vortex. Inset shows schematic of a superconducting vortex. Red and blue circles show the coherence length ξ and penetration depth λ_L respectively. A circulating supercurrent (arrow) shows the supercurrent screening the magnetic field. **Main plot** shows the approximate magnetic field strength $h(r)$ and superfluid density $f(r)$.

One way to minimize the dissipation in a superconductor with vortices is by pinning vortices to crystal defects where superconductivity is weakest. In a vortex lattice, the trapped vortices pin the entire vortex lattice into place, significantly decreasing sample resistance. In the high temperature superconductors, with extremely high Tc and H_{C2}, the vortex lattice can melt into a "liquid" state significantly below H_{C2}. The signature of such a transition is a sudden jump in resistance, when the unpinned vortices suddenly become mobile in the absence of the vortex lattice[91].

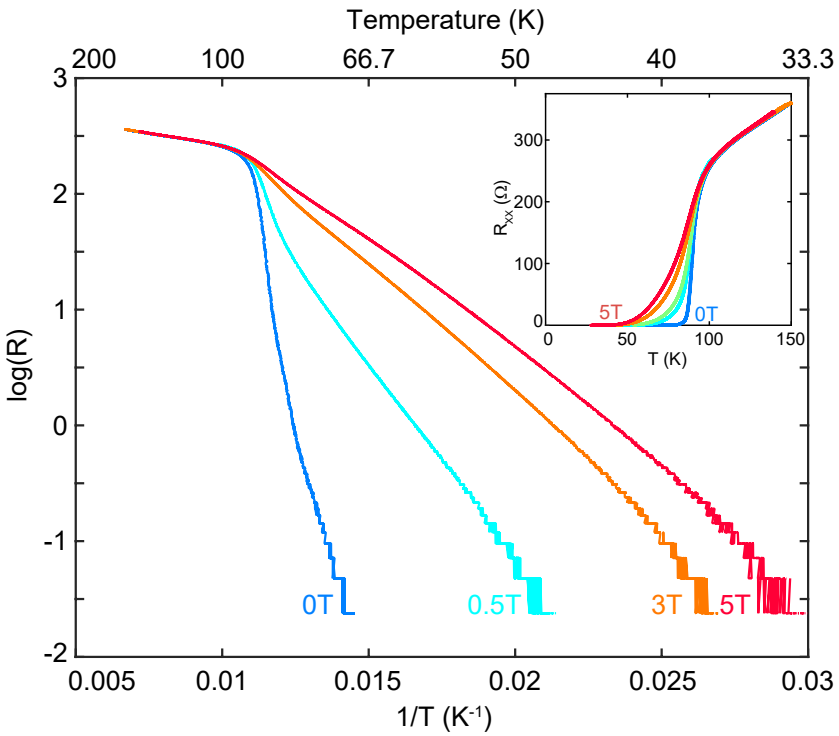

Figure 2.8: Thermally activated magnetoresistance below T_C. In a magnetic field, the resistance of a superconductor is dominated by the vortex lattice, which are pinned at defect sites. Data is from a 3 unit cell $Bi_2Sr_2CaCu_2O_{8+x}$ device.

Do an ordinary thing, in an extraordinary way.

Henri M. van Bemmel

3

High Transition Temperature Copper-Oxide Superconductors

At their discovery[63], the copper-oxide superconductors captured the imagination of the condensed matter physics community. At the time, the highest temperature at which superconductivity was believed to survive was 30 K[42]. Most superconductors at the time had been elemental metals or intermetallic compounds – good metals – with high charge carrier density and low resistance. The cuprates were comparatively resistive, and with relatively low charge carrier density controlled by doping. Moreover, their parent compounds at zero doping were strong antiferromagnets, it was thought that magnetic ordering suppressed superconductivity. Even the nature of superconductivity in the cuprates was strange - spectroscopic and thermodynamic

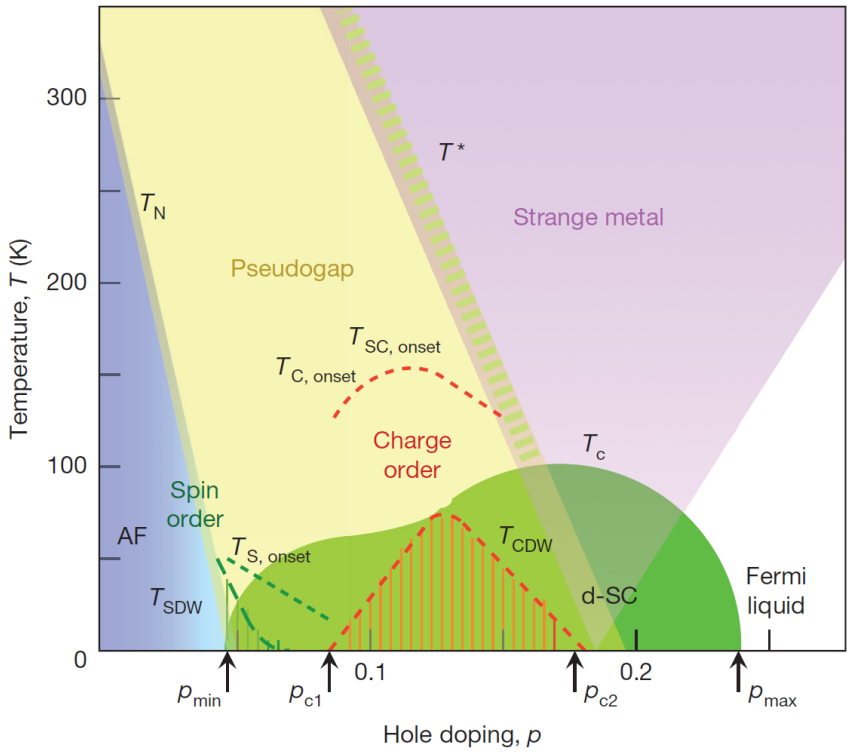

Figure 3.1: Phase diagram for a cuprate superconductor. Reproduced with permission from [42]

measurements revealed quasiparticle states all the way down to the Fermi energy [73].

Indeed, superconductivity and antiferromagnetism are not the only electronic phases accessible in the cuprates. By tuning their chemical structure (and misfit strain between atomic layers [92]), doping and temperature, the cuprates enters into electronic phases as varied as charge density waves, spin density waves, the pseudogap, and strange metal phases [42]. For many of these phases, complete and consensual theoretical description remains an outstanding challenge. To make the matter more pressing, some of the same phases, such as the strange metal, appear in other *strongly correlated* materials such as the iron-based superconductors [93,94].

Such rich phenomenology in the cuprates point to extraordinary complexity [95], where the physics of spin [96] and charge [97,98] conspire with self-organized inhomogeneity of the dopants [99,100]

and lattice [101,102]. The oxygen dopants, which occupy interstitial sites in the buffer layers, strongly influence local electronic properties at the atomic scale [100]. Their nanoscale organization appear as features in X-ray diffraction [99,103,65], which in turn are spatially organized into micro-scale puddles, each with its own local electronic property. A macro-scale transport current must navigate through such a nanoscale phase-separated landscape [103], which is ever changing above 200 K [99] and under X-ray illumination [104]. The result is a system rich with electronic phases which coexist and compete [42], whose complete theoretical understanding has yet to emerge [42], and whose mastery [104,25,99] might open new technological possibilities [62,105].

In this chapter, we will explore the structure of the cuprate family of superconductors. We will survey the cuprate phase diagram. Finally, we will discuss the difficulties posed by the intricate patterns of organization which are destroyed above room temperature [99], which must not be disturbed during the device fabrication process.

3.1 Basic Structure of Cuprate Superconductors

The cuprate family of superconductors contains many members, yet their structural and electronic properties share many similarities. Structurally, they are all composed of CuO_2 planes separated by other buffer layers, which stabilizes the structure and acts as reservoirs for oxygen and other dopants. By convention, we assign the $\hat{a}$ and $\hat{b}$ crystallographic directions to be in the CuO_2 plane, with $\hat{c}$ perpendicular. The CuO_2 planes form either a square lattice or very nearly so, depending on the compound [106].

The electronic properties of cuprates are strongly affected by carrier density via doping. In most of the cuprates, the oxygen stoichiometry directly controls the carrier density, which are hole-like in almost all of the cuprates, with a few exceptions [107]. Oxygen dopants are highly mobile above 200 K, and they naturally order themselves in the crystal lattices [99], which may be controlled using thermal annealing in vacuum or oxygen [25], or X-rays [104]. Depending on the crystal, oxygen

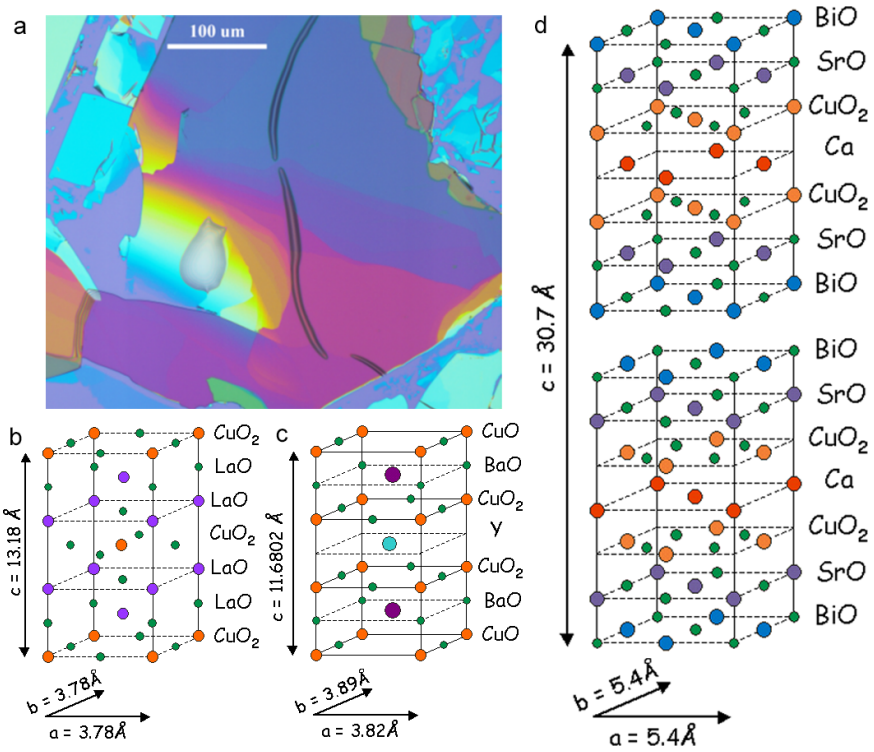

Figure 3.2: Cuprate crystal structure. **a.** Large crystals of BSCCO may be mechanically exfoliated onto a substrate. Colors indicate crystal thickness. **b.** LSCO structure. **c.** YBCO structure. Note the difference between CuO_2 planes and CuO chains. **c.** BSCCO structure. The two half unit cells are offset from each other by a in-plane translation at the BiO layer, which is weakly bonded via vdW forces only. Lattice structure diagrams reproduced from J.E. Hoffman

dopants may take the form of extra, non-stoichiometric atoms occupying interstitial sites (such as in $Bi_2Sr_2CaCu_2O_{8+x}$), or they might be in the form of missing oxygen at a fraction of lattice sites (such as in $YBa_2Cu_3O_{7-x}$). Crystals with the latter type of oxygen dopants tend to have higher charge carrier mobility. Finally, certain cuprates such as $La_{2-x}Sr_xCuO_4$ also contain substitution dopants. These tend to be non-mobile at room temperature, and their spatial organization are quenched from the high-temperature crystal growth process [106].

Broadly, they may be separated into three families [106]. Here, we list their most prominent members respectively: $La_{2-x}Sr_xCuO_4$, $YBa_2Cu_3O_{7-x}$, and $Bi_2Sr_2CaCu_2O_{8+x}$.

The $La_{2-x}Sr_xCuO_4$ (LSCO) family was the first to be discovered, in the form of $La_{5-x}Ba_xCu_5O_{5(3-y)}$[63]. The simplest members of this family contains only 3 elemental species. Single-crystals of LSCO are large enough to reach centimeter scales[108], and high quality epitaxial LSCO MBE films[49] are also available in this family, grown with an atomic layer-by-layer MBE method[109]. In the case of LSCO in particular, the *Sr* dopants are not mobile near room temperature, and even a dopant gradient across a single epitaxial film is possible[110]. T_C in this family tends to be lower than the others, at 45 K in La_2CuO_{4+y}[106]. Notably, while almost all the other cuprates are hole-doped, a member of this family – $R_{2-x}M_xCuO_4$, where R = Pr, Nd, Sm or Eu, and M = Ce, Th, [Ce+Sr] – is electron doped with a nonzero T_C with qualitatively similar phase diagram as the other cuprates[107].

Next, the $YBa_2Cu_3O_{7-x}$ (YBCO) family of compounds reach a maximum T_C of 93 K under ambient conditions, and are the favorite of the transport community. These crystals achieve some of the highest carrier mobility in the cuprates, which enabled the mapping of their Fermi surface via quantum oscillation measurements at high magnetic field[111,112]. In YBCO in particular, electrically conductive copper oxide chains exist in addition to the usual copper oxide planes, which contribute to transport measurements[106], but do not participate in superconductivity.

Finally, the $Bi_2Sr_2CaCu_2O_{8+x}$ (BSCCO) family are the most complex among the cuprates, but also holds the record for the highest T_C at 135 K in $HgBa_2Ca_2Cu_3O_{8+\delta}$. The CuO_2 planes appear in groups of n closely spaced layers. For example, each half unit cell of $Bi_2Sr_2CaCu_2O_{8+x}$ (Bi-2212) contains two CuO_2 planes with a Ca spacer layer in between. These groups of CuO_2 planes are sandwiched by other buffer layers (ex. BiO and SrO in Bi-2212). In a unit cell, two such units are placed with a relative translation. As a function of n, T_C is always highest in the $n = 3$ compound. The decrease in T_C for $n > 3$ is thought to originate from the low doping level in interior copper oxide layers, as the oxygen dopants are in the outermost layers of each half unit cell[106].

Structurally, there are strong structural supermodulations in the $\hat{b}$ direction on top of the unit

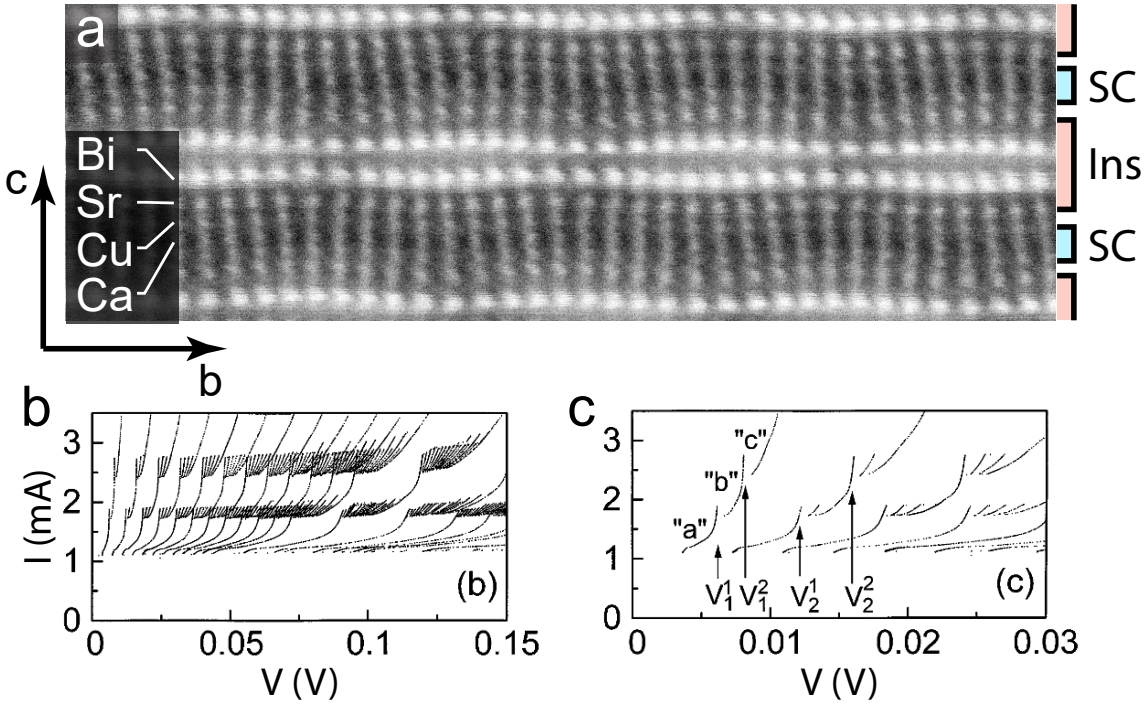

Figure 3.3: Intrinsic Josephson junctions a. Cross-sectional scanning TEM micrograph of BSCCO crystal. Bright dots are columns of atoms. The supermodulation along $\hat{b}$ is clearly visible. The superconducting CuO_2 layers buried between insulating BiO and SrO layers naturally create a stack of Josephson junctions intrinsic to the crystal. They appear as a periodic series of jumps in c-axis transport measurement, as shown in **b**. **c** shows the same data as (b) but is zoomed in along V. Periodic structures are visible in the I-V. (b) and (c) are adapted with permission from [114]

cell structure [102], which are not typically drawn in the idealized structural models. Such supermodulations become readily visible in STM [100], diffraction and in high resolution transmission electron microscopy imaging, and are thought to originate from misfit strain between different atomic layers [92]. We shall discuss the direct imaging of such supermodulations in real space via a focused scanning nano X-ray beam diffraction technique, in Chapter 6.

The neighboring BiO layers in BSCCO family are bonded only via weak van der Waals forces. This property makes BSCCO the favorite material for surface sensitive techniques such as ARPES and STM, as a pristine surface can be easily prepared under ultra high vacuum and even at cryo-

genic temperatures[113]. This property allows it to be mechanically exfoliated into atomically thin single crystals up to hundreds of μm in size. While on the surface this advance opened the possibility of bringing the arsenal of vdW crystal manipulation techniques to bear, as we shall discuss below, BSCCO's chemical reactivity to air[113] and its oxygen dopant's mobility[99] makes such experiments technically demanding. Superconducting monolayers of BSCCO which is electrically isolated from other passivating layers have only recently been reported[25].

Another consequence of the weak interlayer bonding in BSCCO (and $Tl_2Ba_2Ca_2Cu_3O_{10+x}$) is the discovery of intrinsic Josephson effects in the c-axis transport properties of single crystals[115]. The superconducting CuO_2 layers are separated from the others through BiO and SrO tunnel barriers, which form SIS Josephson junctions with critical current of around 1 kA / cm^2. In chapter 8, we will exploit this fact, as well as our new cryogenic vdW pickup technique, to fabricate twist Josephson junctions between BSCCO crystals with quality comparable to the single-crystal intrinsic junctions. By twisting the two crystals with respect to one another, we discover that a half-integer Shapiro step emerges within about $45° \pm 1°$ twist angle, which points to the co-tunneling of Cooper pairs[62] that is theoretically expected to support high temperature topological superconductivity[62,260].

3.2 Cuprate Electronic Phase Diagram

Despite the great diversity among the copper oxide superconductors, they share qualitatively similar electronic properties from their shared copper oxide planes. This can be greatly modified by changing the dopant density p, whose effect is summarized in the phase diagram. In addition to high temperature superconductivity, a great wealth of different phenomena appears in the cuprates, and their interplay and competition is a hotly studied topic[42].

The cuprate parent compounds with no substitution doping and stoichiometric oxygen content are antiferromagnetic insulators, with $p = 0$. With no doping, each Cu^{2+} site has one charge

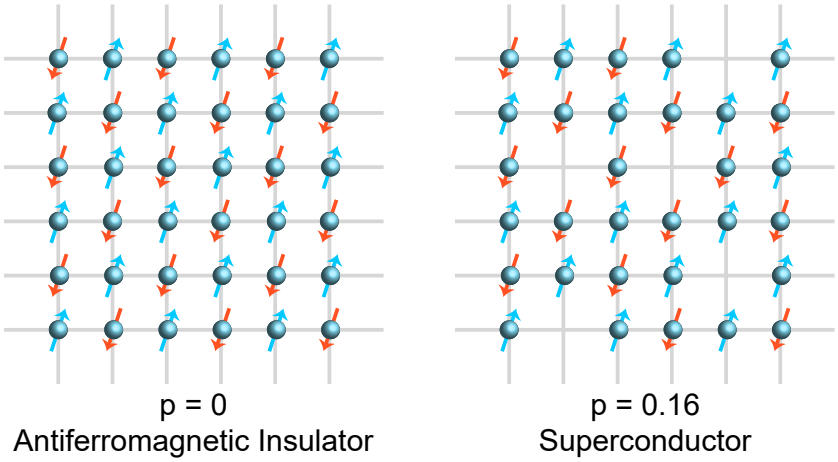

Figure 3.4: Doping a Mott insulator In undoped cuprates at $p = 0$, each copper site has 1 electron whose spin is anti-aligned with its neighbors. Strong Coulomb repulsion between sites prohibit double-occupancy, and freezes the electrons in place. Dopants take away electrons from the copper sites, freeing up sites and restoring mobility to the charge carriers.

carrier in its $3d$ orbital, which overlaps a nearby oxygen $2p$ orbital [106]. In theory, the resulting electronic structure forms a single half filled band at the Fermi energy, but conduction is suppressed due to strong on-site Coulomb repulsion, which penalizes double-occupancy with a high energy cost. The charges are then localized on each site, as in a traffic jam. Virtual hopping of electrons between copper sites leads to an antiferromagnetic ground state spin configuration below the Neel temperature, due to the Pauli exclusion principle.

By adding dopants near the copper oxide plane, charges are removed in the hole-doped cuprates (figure 3.4). These open holes unblock the traffic jam, and restores charge flow to the system. As dopants are added, the Neel temperature drops, and the material becomes increasingly metallic. Beyond a minimum doping level p_{min}, superconductivity emerges at low temperature.

There are a number of similarities between superconductivity in the cuprates and that in conventional phonon-mediated BCS superconductors such as Pb. The electrical resistance is zero below T_C, and there is a Meissner state at low magnetic field. The magnetic penetration depth λ_L

is long and coherence length ξ very short, as expected for a superconductor with low superfluid density. In a larger magnetic field beyond H_{C1}, vortices form, as expected for Type II superconductors, with the expected flux quantum. These experimental facts point to the existence of Cooper pairs with a charge of $2e$, as in a conventional BCS superconductor[66].

There are also important differences. First, there is some agreement that the pairing symmetry in cuprates is dominated by a d wave gap[116]. This is supported by numerous thermodynamic, spectroscopic and tunneling experiments which show the existence of low-energy excitations below the gap energy[78,73], and phase sensitive experiments which directly show a sign change in the order parameter as a function of crystallographic direction[74], as well as vortices with fractional flux quantum appearing at grain boundaries with mismatched lattice directions[73]. However, the debate is not completely settled, as some experiments points to either a weak s-wave order parameter coexisting with the d-wave OP[117], or to a complete s wave order parameter[118]. We will discuss this matter in more detail in Chapter 8.

As doping p increases, T_C approaches a maximum at optimal doping p_{opt}. Crystals with $p < p_{opt}$ are underdoped, and those with $p > p_{opt}$ are overdoped. For the oxygen doped crystals, doping level may be modified after crystal growth by annealing the crystal at extended temperatures either in vacuum or oxygen environment[25]. For BSCCO, $p_{opt} = 0.16$ per Cu site, equivalent to about 2×10^{14} cm^{-2} per half-unit-cell (with 2 CuO_2 planes). We note that this is beyond the charge carrier density achievable using standard electrostatic gating techniques on SiO_2 substrates, but within the reach of electrolytic gating techniques[119,27,120].

In the underdoped regime and at temperature slightly above T_C, the resistance of the sample suddenly grows from zero as the sample exits the superconducting state. In most conventional superconductors, this coincides with a closing of the superconducting gap Δ, but in the cuprates, an energy gap remains visible in spectroscopic, thermodynamic and transport probes in a wide temperature range up to T^* far above T_C[121]. Indeed, direct measurements of the Fermi surface reveals that this gap has the same d-wave symmetry as the superconducting gap, but with higher

energy scale and the (single-particle) density of states inside the gap never reaches zero[78]. This is the *pseudogap* regime of cuprate superconductors.

There are two conflicting and controversial views of the pseudogap. One suggestion is that the pseudogap is directly related to superconductivity, where charge carriers are paired into localized Cooper pairs inside the pseudogap, but they are not spatially connected together because there is insufficient phase stiffness. Experiments in support of this view include shot noise experiments across LSCO tunnel junctions[122], which observe carriers with charge greater than e above the superconducting temperature, increased thermal conductance above T_C attributed to vortices in the pseudogap regime[123], as well as observation of the superconductor-insulator transition via electrolytic doping, revealing a critical sheet resistance corresponding to the quantum of resistance for pairs[119]. A conflicting view of the pseudogap is that it originates from causes distinct from superconductivity, which opens a gap phenomenologically similar to the superconducting gap, but is distinct from it with a significantly different energy scale[78]. Complicating the picture, thermal fluctuations are known to lead to Cooper pair formation (with finite lifetime) above T_C in thin films of even conventional superconductors[124].

Inside the pseudogap, charge and spin density waves appear[125,42], and sometimes together as in the 'stripe phase' at $p = 1/8$ in the LSCO family[108]. These phases are believed to compete with superconductivity, as the appearance of the stripe phase causes a depression in T_C at the same p[42].

In the slightly overdoped regime, the pseudogap closes even though the superconducting gap stays open at low temperature. Recent ARPES measurements appear to suggest that the pseudogap disappears suddenly with doping alongside the strange metal phase around $p = 0.19$ in BSCCO[126], while in YBCO the Hall density at extreme magnetic fields (to suppress the influence of superconductivity and vortex contributions to Hall resistance) suddenly increase around the same doping[125].

In the optimally doped crystals above T_C and T^*, the resistance of the sample increases linearly with temperature. Indeed, measurements indicate that this trend persists well above room tem-

perature[127]. This is surprising, as in most materials, the resistance increases as a higher power of T, and in Fermi liquids is expected that $R \approx T^2$, which is observed in the deeply overdoped regime. Similar behavior is also observed in iron pnictide superconductors above optimal doping[93].

In comparison, the physics of overdoped regime is thought to be more conventional. In strongly doped cuprates, there is a Lifshitz transition at high doping where the carrier type goes from hole to electron-like. In LSCO and YBCO, this occurs at $p = 0.20$ and 0.29 respectively. Above the superconducting transition, the gap is fully closed, and the resistance scales like T^2[42].

3.3 Superconductivity in Copper-Oxide Monolayers

In order to elucidate the details of the different phases outlined above, and exploit the unique electronic features of the cuprates in new generations of devices[62], experimentalists have attempted to mechanically exfoliate BSCCO into small crystals on a substrate, which then might open the possibility of deploying the full array of tools developed for the other vdW crystals such as graphene. The effort has proven to be difficult, as BSCCO has proven not only reactive to the water and carbon dioxide in air, but also, oxygen dopants readily escape from the surface BiO layers, changing the crystal doping in the process. In particular, this frustrates all standard vdW pick-up techniques, which relies on high temperature to control adhesion to the polymeric transfer medium.

One such experiment[25] illustrates these difficulties. In the first experiment to successfully isolate a single half-unit-cell of $Bi_2Sr_2CaCu_2O_{8+x}$ and retain a fully superconducting state with almost the same T_C as the bulk material, Yu et al. tuned the carrier density with the sample in the cryostat by heating the sample up between 300 - 380 K. The doping of the superconductor changed accordingly, and the resulting single device accessed the entire phase diagram. To fabricate the sample, the authors quickly performed the entire fabrication procedure on a cold stage at -40 °C, and completed the whole fabrication procedure quickly within about 2 hours. For contacts, the authors pressed indium electrodes coated with gold onto the BSCCO crystal sur-

face, instead of the usual micron-scale evaporated contacts defined via electron beam (or photo-) lithography. Even under such extreme conditions, T_C of the resulting devices decreased when the total fabrication time was longer than 1 hour.

In the next chapter, we shall outline the unique techniques that we have developed specifically to solve this problem. These technical developments allow us to bring nearly the full capability of a university fabrication cleanroom into an inert argon environment without the use of solvents or resists, all the while keeping our sample at or below room temperature. As we will discuss in Chapter 8, these techniques allow us to stack BSCCO crystals atop one another to create transparent Josephson junctions with electrical characteristics comparable to intrinsic junctions of single crystals, yet with precise control over the relative twist angle between them.

Simplicity is the ultimate sophistication.

Leonardo da Vinci

4

Air-Free and Cryogenic Fabrication Techniques

The remarkable simplicity with which van der Waals materials can be combined in seemingly arbitrary configurations, along with the vast library of vdW materials available, have brought about new ways of controlling and probing electronic matter. One of the most interesting vdW material available is $Bi_2Sr_2CaCu_2O_{8+x}$, as a prototypical example of cuprate high-temperature superconductor, which is also one of the first materials to be mechanically exfoliated into an atomically thin form[6]. However, its chemical reactivity[113,128] alongside its oxygen dopants' propensity to lose their spatial self-organization at room temperature[99] have until very recently[129,26,27] made it impossible[20] to synthesize atomically thin crystals, while preserving its pristine and complex

nature[25].

In this chapter, we describe a new set of techniques designed specifically to solve these fabrication problems, yet flexible enough to be used on any van der Waals material or heterostructure, powerful enough to reproduce almost the full capability of a university cleanroom, and simple enough to yield multiple functional complex devices in a single day.

4.1 Nanofabrication on van der Waals Heterostructures

Van der Waals device fabrication consists of five basic steps (figure 4.1), which together defines the geometry of vdW devices of almost arbitrary complexity. First, vdW materials are mechanically exfoliated and identified, which are assembled into a stack using various transfer techniques[130,57,131,132]. While simple vdW heterostructures are easy to create, it takes great skill and patience to realize a heterostructure of high quality and complexity[34]. Next, lithography selects an area of interest on the device, and this region may be etched away, or a material (such as a metal contact) may be deposited with high resolution. These steps are repeated until the device reaches the required functionality. Occasionally, additional vdW heterostructures may also be placed on top of pre-fabricated electrodes[133]. Finally, the finished device must be packaged and mounted on the cryostat, with all necessary electrical connections.

Each of these steps poses challenges in air sensitive devices. Typical vdW stacking methods relies on high heat to control polymer adhesion[57,131], and the polymer must be subsequently washed away in solvents. Lithography relies on polymeric resists, which must be written in complex and bulky electron beam- or photo-lithography writers. Plasma etchers expose the sample to harsh chemical environments. Physical vapor deposition systems often heat up the sample. Finally, the wire bonder used to connect the finished device to the chip carrier is difficult to operate, and usually found in air.

We have developed a set of device fabrication techniques tailored to BSCCO. Together, these

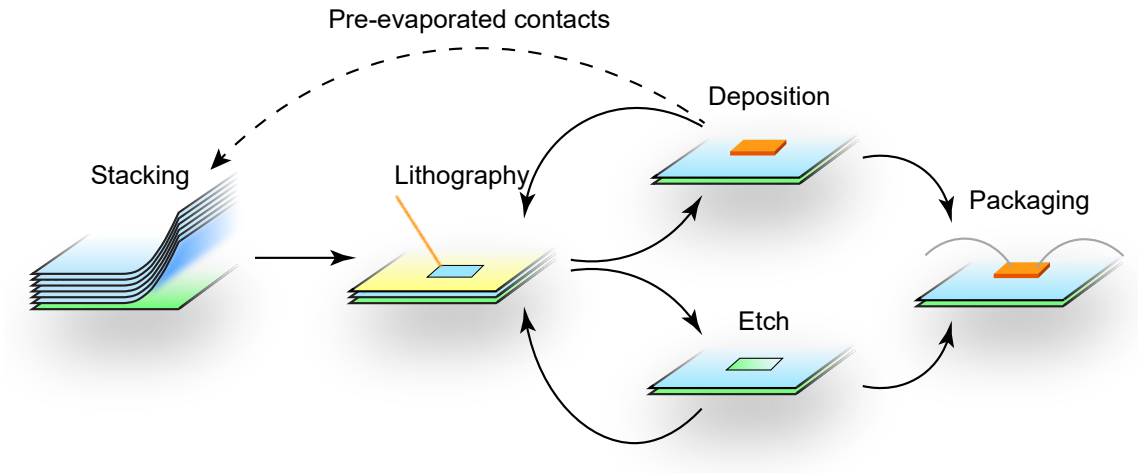

Figure 4.1: General vdW Device Fabrication Procedure. vdW device nanofabrication generally consists of five steps: stacking, lithography, deposition, etch, and packaging. Multiple lithography/deposition and etch steps may be required to yield a working device. Pre-deposited contacts may also be used as bottom contacts, for vdW stacks to place on top.

techniques allow us to stack arbitrary van der Waals materials, evaporate metallic contacts, and etch the devices into arbitrary shapes – all the essential steps required for making standard van der Waals heterostructures – all within an inert gas environment and without any heating. The essential idea is two-fold. First, we move lithographic steps onto an optically transparent, yet mechanically robust, silicon nitride membrane. This allows the use of standard lithographic techniques to etch holes into the membrane, and then transferring the pattern onto the BSCCO substrate. Second, we discovered that polydimethylsiloxane (PDMS) – a soft, rubber-like polymer – becomes extraordinarily sticky close to its glass transition temperature near $-100°C$[134], as its rigidity near and below T_g significantly increases surface adhesion[135]. This allows us to control the transfer stamp adhesion with temperature, just like the standard pickup polymers such as polycarbonate (PC) and poly(propylene carbonate) (PPC)[56], but at low working temperatures and without the need to clean the melted polymer using solvents. Together, these techniques allow us to fabricate a large variety of vdW heterostructures with any sensitive vdW material down to monolayer thickness.

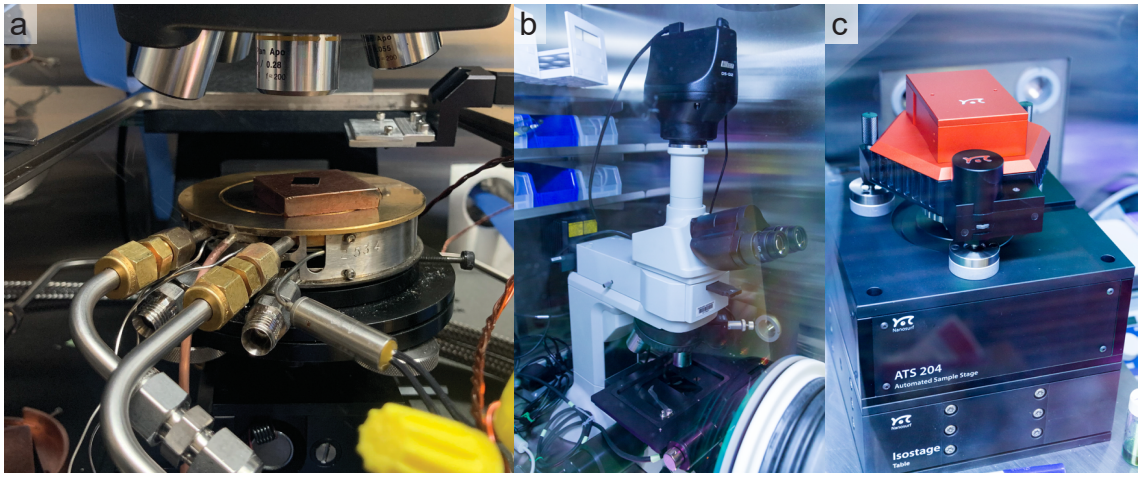

Figure 4.2: a. Transfer station liquid nitrogen cooled stage, with microscope above and manipulator arm in background. b. High resolution optical microscope. c. Atomic force microscope.

4.2 High Gas Purity in a Glovebox

In order to assemble our devices in an inert environment, we miniaturized our laboratory's essential fabrication tools to fit inside an argon glovebox. First, the glovebox (MBraun MB-200B) filters out solvents, water and oxygen from the argon medium, establishing an oxygen and water concentration below 100 parts per billion (ppb). In order to fabricate van der Waals heterostructures, we outfitted the glovebox (fig. 4.2) with a probe station (modified Signatone S-1160 with motorized and liquid nitrogen cooled sample stage), atomic force microscope (NanoSurf FlexAFM), microscope (Nikon Eclipse LV100), $-40°C$ sample freezer, and attached vacuum annealer, oxygen plasma etcher, evaporator and argon ion mill (AJA).

An argon glovebox works by creating a hermetic environment filled with pure argon gas. Compared to ultra-high-vacuum chambers, they allow direct handling of materials and equipment by hand through a thick butyl glove, at the cost of higher contamination levels. The best commercial gloveboxes are usually rated to about 100 parts per billion (ppb) level contamination, which correspond to a partial pressure of about 10^{-5} mBar. We strive to minimize the contamination

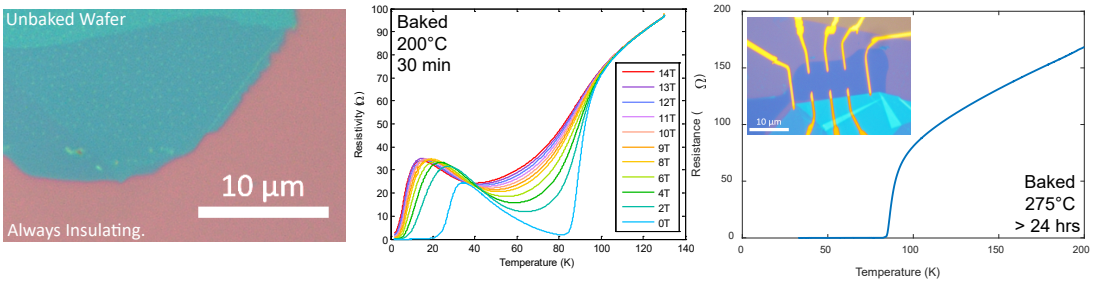

Figure 4.3: Baking the substrate is crucial in eliminating water contamination. BSCCO exfoliated on unbaked wafers are covered in spots, and are electrically insulating at low temperature. With mildly baked substrates, a superconducting transition is visible, but there is a pronounced reentrant feature below T_C, and resistance only truly vanishes at low temperature. Samples prepared on thoroughly dried substrates do not suffer from this problem.

level far below this value.

Objects are brought into the box through an airlock, where the gas is evacuated to about 50 mBar using an oil-free scroll pump and back-filled with argon four times. To minimize outgassing, porous and hydrophillic materials such as paper, glass and foams are eliminated. Plastics are also minimized. We pressurize the box to 3-10 mBar over atmospheric pressure so that small holes leak outwards. A gas circulation system continuously blows the glovebox gas into purifiers, which continuously removes water and oxygen, as well as other polar molecules and solvents.

Our sample substrate is the first major source of contamination, and substrate preparation was crucial. We used highly doped silicon wafers with 285 nm oxide layer. After sonicating the substrates in acetone and isopropyl alcohol, we bake the substrates on a hotplate (in argon) at 275°C for more than one day in order to completely dry off any adsorbed water[136]. Shorter baking times resulted in reproducible artifacts in the resistance-temperature data below T_c, while unbaked substrates yielded insulating BSCCO with spots clearly visible under the microscope (see figure 4.3).

To further reduce contamination, it is necessary to obtain the highest purity argon environment possible. Our glovebox continuously blows argon gas through purifiers, which consist of columns of 13X zeolite molecular sieves (solvent purifier), followed by molecular sieves mixed

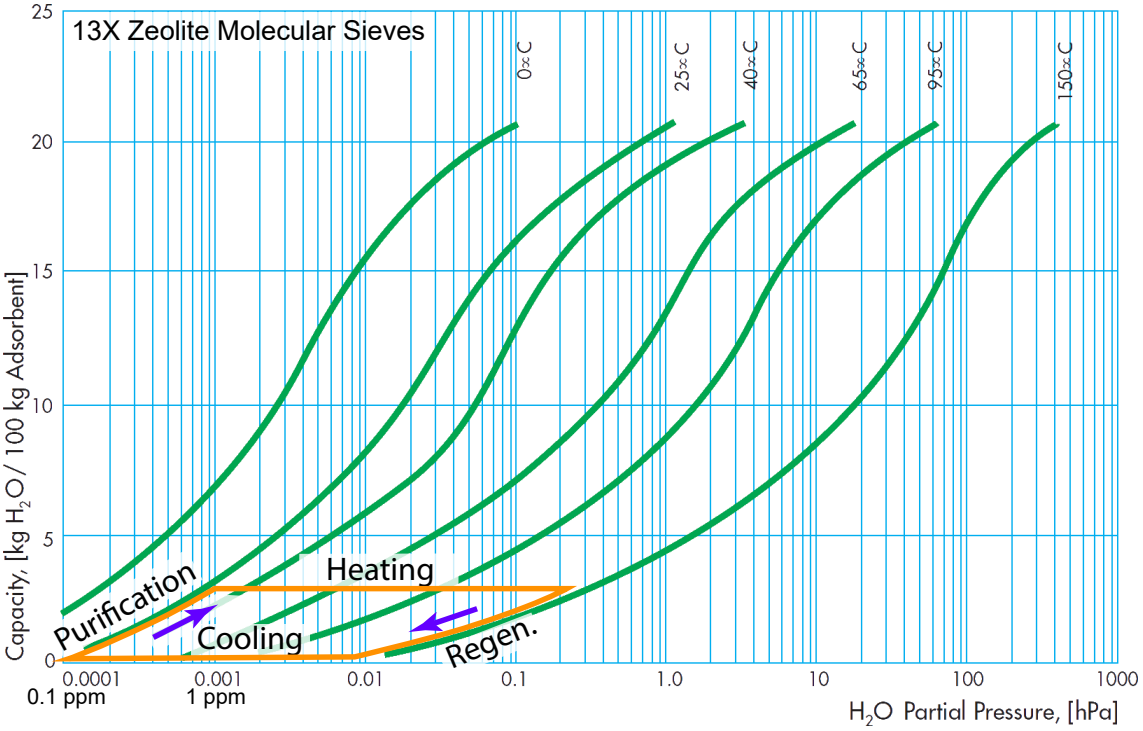

Figure 4.4: Molecular sieve isotherm. Equilibrium isotherms for Grace Davison Sylobead 13X zeolite molecular sieves [137]. In standard operation, the purifier molecular sieves adsorb water following the orange line in the direction shown. The equilibrium gas purity decreases accordingly. When the purity is intolerably low, the purifier is heated up to a higher temperature, under flowing argon, where water is released to the regeneration gas. Finally it is cooled down to room temperature to cool. The orange lines are somewhat exaggerated vertically, as our typical glovebox purity is under 0.1 ppm.

with copper catalysts (water and oxygen purifier). The copper catalysts are readily oxidized by O_2, chemically trapping the contaminant. A saturated catalyst may be regenerated by baking it near 300 °C under flowing 5% hydrogen gas, which reduces the copper oxide and releases water vapor.

The zeolite molecular sieves adsorbs polar molecules like H_2O and CO_2, and behaves like a cryopump but operating at room temperature. Figure 4.4 shows their equilibrium isotherms as a function of molecular sieve water load and the equilibrium water vapor partial pressure in the gas stream. While purifying, potentially contaminated argon gas flows through molecular sieve

column, and water is adsorbed. The water vapor partial pressure at the purifier outlet arrives at a point on the isotherm near room temperature, which steadily increases as the molecular sieves are increasingly loaded with water. Once the purity is unacceptably low, the purifier is regenerated by heating the purifier column to high temperature, where water is released to a dry argon gas stream, and molecular sieve capacity is decreased. The purifier is subsequently cooled down, and returns to purifying operations.

Figure 4.4 shows that, like a cryopump, molecular sieves' adhesion to water strongly increases when it is cooled. We have thus modified our purifier with an external cooling, heating and thermal insulation. We coiled 1/4" copper tubing around each purifier, and fixed them in place with a thermal transfer compound with maximum operating temperature of 400 °C (Chemax Corp. Tracit-300, McMaster 3568K1). When extremely pure argon is required, we flow liquid nitrogen through this copper line to cool the purifier to about -40 °C as argon flows through. Next, we wrap heater tape around the purifier, with which we boost the regeneration peak temperature from about 150 °C to 275 °C to further dry out the molecular sieves. Finally, we surround the purifiers with a fiberglass blanket for thermal insulation.

BSCCO is especially reactive to water, and we customized our glovebox to monitor and minimize water contamination. We have taken special care to minimize leaks into the glovebox. By filling the glovebox with helium tracer gas and using a sniffing helium leak detector, we detected the largest leaks around the glove/window interface, followed by diffusion through the gloves, and finally at the window/glovebox seal. We can reduce leaking at the glove cuffs by gluing butyl gloves to the plastic glove attachment with Celvaseal (Myers Vacuum), a transparent adhesive developed for repairing small leaks in vacuum chambers, and then taping the glove/attachment seam with electrical tape.

Molecular diffusion through the butyl glove is more difficult to eliminate. To minimize this effect, we made glove covers by welding (using a soldering iron) a 0.004" thick low density polyethylene sheet (McMaster 8593K71) into a cylinder open at one end, and fitted it around the glove

using a large O-ring. A plastic tube passes through the opening, through an improvised putty feedthrough. When the glovebox is put on standby mode, the bag is initially evacuated, and then filled with dry nitrogen gas. This eliminates water diffusion through the gloves whenever they are idle.

The argon gas supply cylinder and its gas delivery lines can also be a source of contamination. Briesacher, Nakamura and Ohmi[138] demonstrated that a short length of plastic 1/4" tubing increased contamination from the ppt to ppm level. We have replaced all gas supply lines with stainless steel tubing and Swagelok VCR or Swagelok compression fittings, including lengths of rubber and plastic tubing inside the purifier. We use Research grade argon cylinders, with < 0.3 ppm water as our argon source, except during purifier regeneration, where we use ultra high purity argon with < 1 ppm of water impurities.

Our glovebox uses gas-actuated valves to control argon flow in the purifier loop. By default, the pressurized gas used to actuate these valves comes from the main argon supply cylinder. In order to eliminate long lengths of plastic tubing used to link such valves together, as well as to eliminate a measurable leak at each valve's actuation mechanism, we broke this gas line from the main, clean argon supply to a separate high purity argon cylinder (< 3 ppm water). This gas only serves to actuate pneumatic valves, and does not mix with the glovebox working gas.

In order to connect our instruments to electronics outside the glovebox, we use high-vacuum compatible ceramic feedthroughs whenever possible. We find that epoxy potted cables are acceptable when feedthroughs are not available. For cables inside the glovebox, we use fluorinated ethylene propylene (FEP) jacketed ribbon cables for motors and low-frequency signal cables, and Kapton coated wires for power cables. We use polypropylene wire nuts to connect power cables together inside the glovebox. We are unable to replace the standard cables used in high-performance data cables such as USB-3 with low-outgassing alternatives.

In order to measure water concentration below the 100 ppb detection sensitivity of the glovebox electronic sensor, we simply cool a pre-baked, solvent cleaned silicon substrate under an op-

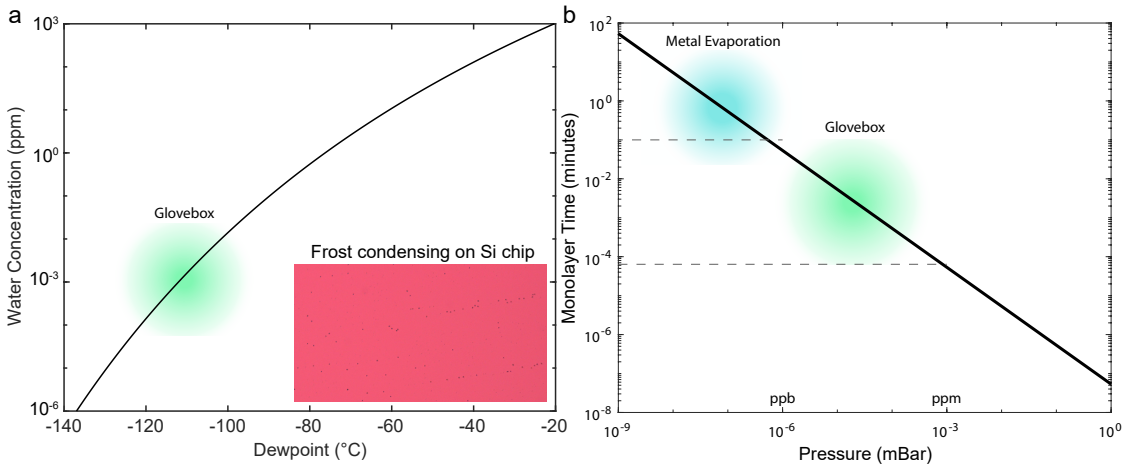

Figure 4.5: Glovebox impurity measurement a. Water impurity level as a function of frost point. Our glovebox usually performs within the green region. **b.** Time for monolayer of molecules to build up, assuming perfect adhesion to substrate at each interaction. Typical performance is highlighted with our glovebox and with a UHV system.

tical microscope. By measuring the precise temperature at which water first condenses onto the cold substrate, we extract the argon frost point which sensitively depends on the water concentration [139]. This is similar to the operation of frost-point hygrometers [140]. Together, we readily achieve a frost point between -120 to -100 $^{\circ}C$, correspoding to water concentration below 10 ppb.

4.3 Glovebox Instruments

Central to our workflow is the motorized probe station (fig 4.2d). Here, the sample can be positioned beneath a mechanical manipulator holding either a PDMS transfer stamp or stencil mask, and aligned under the guidance of a long working-distance optical microscope (Mitutoyo FS-70). We perform all vdW stacking, as well as stencil mask alignments, on this apparatus. We took special care to ensure that the sample stage coolant lines would not leak to the argon environment. A set of two flexible stainless steel coolant lines (Swagelok) brings liquid nitrogen coolant to the sample stage and back out to the lab, without cracking at cryogenic temperatures. Swagelok con-

nectors are used throughout to eliminate leaks to the argon environment. Heaters and a T-type thermocouple completes the temperature control mechanism. To combat mechanical vibrations, the probe station floats on top of a spring-based vibration dampener (Minus-k). A flexible stainless steel vacuum line with ultimate pressure of about 20 mBar holds the sample down on the stage.

Connected to our glovebox is an integrated evaporator system, capable of electron beam and thermal evaporation, sputtering, and argon ion milling in the same vacuum chamber. We typically achieve a background pressure $< 5 \times 10^{-8}$ mBar, after coating the chamber with a thin layer of Cr. A separate chamber is configured for rapid thermal annealing and oxygen plasma etching. We decouple mechanical vibrations between glovebox and evaporator using a large diameter rubber tube.

We modified our evaporator specifically to minimize heating in cuprate samples. First, we chose one of the smallest possible thermal evaporation sources (RD Mathis model ME17-.030W-AO) to minimize sample heating and to minimize stencil mask shadowing, which worsens resolution. Second, we re-positioned our thermal source, so that it sits perpendicular to the plane of the tilting sample holder. This is necessary because the stencil mask is typically 50 μm from the sample, and if the line of sight between source and sample is not perpendicular to the sample (as is the microscope optics), then the evaporated pattern will be offset from the expected position in the microscope. Next, in order to isolate vibrations from evaporator cryopumps from the sensitive instruments in the glovebox, the loadlock is connected to the main glovebox through a rubber connector.

To control sample heating, we fitted our evaporator stage with 6 thermoelectric Peltier coolers (TE Technology VT-31-1.0-1.3). As designed by the company, the sample stage is cooled to 5°C with chilled water, and is not compatible with liquid nitrogen. We re-designed our sample holder by adding the Peltier coolers to a cavity milled into a copper piece underneath the sample (figure 4.6). In order to maximize the temperature difference between sample and the cooling water, the

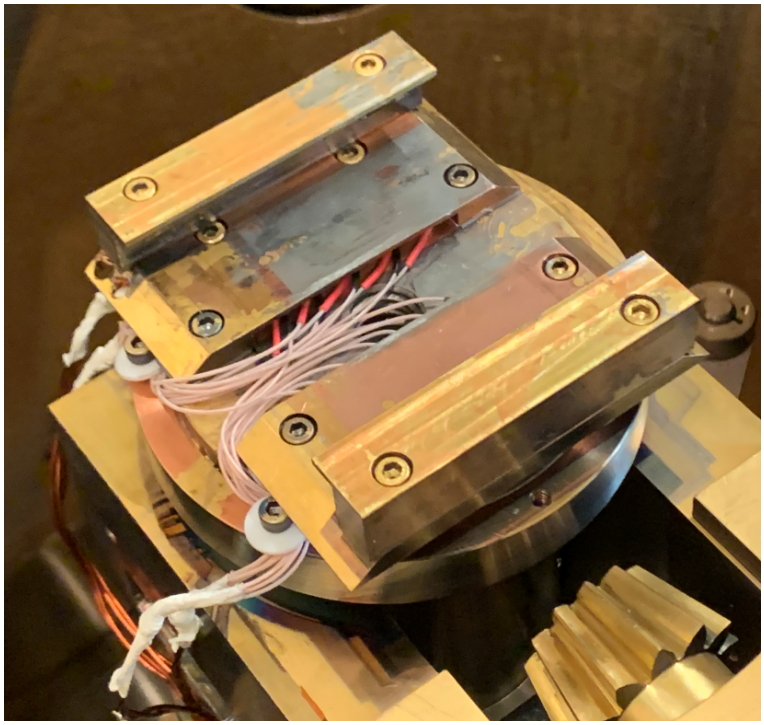

Figure 4.6: Peltier cooled evaporator stage. We have modified the integrated evaporator with a Peltier cooled stage capable of reaching at least -30° C.

Peltier coolers are glued to two separate pieces of copper at both the cold and hot sides using a ultra-high-vacuum compatible, low-outgassing silver thermal compound (Aremco 641-EV-HT). Several sheets of PTFE plastic between the hot and cold copper pieces, as well as PTFE washers underneath the screw heads holding the assembly together, minimizes heat transfer between the two copper pieces. We achieve a sample temperature below -30°C.

4.4 PDMS Cryogenic Pickup

The ability to manipulate vdW materials and create arbitrary stacks of high quality [56] is the foundation of van der Waals device fabrication. In order to create cuprate devices of high complexity, a low temperature transfer method must be devised. At the core of every dry-transfer method

(see [130] for a review) is a polymer which deforms under pressure above a glass or melting transition temperature T_g. Far above T_g, the polymer is flexible and conform to the shape of objects it is in contact with, at a microscopic level. We take advantage of this fact by first deforming a polymer slightly above T_g to conform to the shape of the target vdW crystal. Then, cooling the transfer stamp below T_g, adhesion is enhanced as polymer rigidity is restored, allowing the target crystal to be picked up [135]. Then, taking advantage of strong van der Waals forces between vdW crystals (often of different types with different lattice orientations), subsequent vdW layers can be picked up underneath the first crystal. Finally, the entire stack is released onto a substrate far above T_g. The canonical transfer polymers are poly(propylene carbonate) (PPC) [56] and polycarbonate (PC) [57].

For the cuprates, this procedure has two important problems. First, the typical release temperature is just above the polymer melting transition at 80°C and 200°C for PPC and PC respectively. Second, after release, the substrate is covered in a thick layer of polymer which must be removed in solvent or by high temperature annealing in vacuum.

We discovered that polydimethylsiloxane (PDMS) adheres to 2D materials extremely well at around -100°C. Better yet, above -50°C, adhesion is low enough that stacks can be easily released, but without the polymer melting. This simple discovery is at the core of our cryogenic pick-up technique. In retrospect, this is not surprising – T_g for PDMS is around -123°C [134].

PDMS is well known as a medium for "transfer printing" [141] and specifically for dropping off vdW materials pre-exfoliated to PDMS directly from tape [132]. At and above room temperature, adhesion to PDMS is too low to overcome a vdW crystal's adhesion to the substrate. By lowering the temperature towards T_g, the adhesion of PDMS is greatly enhanced, and we can arbitrarily pick up exfoliated vdW crystals.

We prepare our PDMS using Dow Corning Sylgard 184 with a 10:1 mix ratio between precursor and crosslinker. The preparation is mixed and degassed, poured onto a flat mold, and cured at 60°C overnight. The 1 mm thick blocks are cut out and placed onto a hot glass slide pre-heated

to 300°C for 10-20 minutes to promote adhesion, so that it does not fall onto the substrate during transfer. Finally, the stamps are placed into the glovebox and baked at 200°C overnight, to remove adsorbed water.

To manipulate vdW crystals, we simply adhere the corner of our PDMS onto our crystal using our manipulator at -80°C, and cool the substrate to -100°C. While cold, we lift the transfer stamp. It is important that only a small area is in contact with the substrate, otherwise the silicon wafer may detach from the stage due to the high substrate adhesion to the stamp. We can then either pick up additional vdW crystal layers, or release the stack onto the substrate above -50°C. It is important that these procedures be done inside a water-free environment, or else the sample would be coated with frost.

4.5 Stencil Mask

To avoid solvents and resists in the fabrication process, we have developed a simple, yet high-resolution stencil mask technique, shifting the lithography process onto a silicon nitride (SiN) membrane. SiN coated silicon wafers were purchased from Nova Electronic Materials, with 500 nm LPCVD grown low-stress SiN layers on both sides of a 300 μm silicon core. The process for exposing a suspended membrane is illustrated in figure 4.7. Using photolithography (Shipley 1805 photoresist), we etch away SiN inside a square window 624 or 924 μm in size with edges aligned to the flats of the silicon wafer, for suspended SiN square windows about 200 and 500 μm in size respectively. The exposed silicon core was then removed using a potassium hydroxide solution at about 75°C, suspending the SiN membrane on the opposite side of the wafer. Finally, the device contact pattern was written onto the exposed SiN membrane via photolithography and etched via reactive ion etch. This technique yields a resolution of ~1 μm. We may also write the contact pattern directly on the exposed SiN membrane using a gallium focused ion beam, achieving a resolution of ~200 nm in the evaporated contacts.

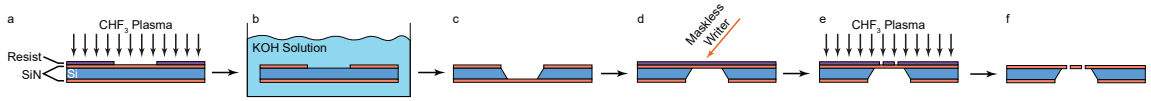

Figure 4.7: a. A photoresist layer was patterned. CHF_3 plasma removes the exposed SiN on one side. b. Silicon underneath is removed, exposing a suspended SiN membrane on the opposing side (c). d. Photoresist again coats the suspended membrane, and is patterned via photolithography. e. CHF_3 removes the exposed SiN and creates stencil mask holes (f).

Figure 4.8a illustrates the stencil mask alignment procedure. After exfoliation, the crystal of the correct shape and thickness is identified, and aligned to the pre-fabricated SiN mask under the guidance of the microscope. Once the mask is in contact with the substrate, the vacuum grease (Apiezon H or N) glues the two together, and the vacuum suction cups are released. We readily achieve an alignment accuracy of ~ 1 μm (fig. 4.8b). We then evaporate gold through the stencil mask. To enable easy handling without touching the mask, the substrate is first glued to a copper or silicon plate. A conical centrifuge tube is then used to protect the sample awaiting evaporation. We easily achieve a resolution of 200 nm by using stencil masks written directly using a gallium focused ion beam (fig. 4.8c-d).

4.6 Stencil Mask for Etching

The ability to shape samples by etching is another critical capability in vdW device fabrication. One way to do this is to use argon ion milling [142], where accelerated argon atoms abrade the sample surface. The rigid stencil mask that we use forces our mask and sample to be about 50 μm apart. This gap allows sputtered material from the sample to re-deposit randomly below the mask. In order to fix this problem, we developed a new transfer technique for SiN, inspired by Li et al [143]. We found that it is possible to detach the SiN from its substrate and adhere it directly on top of the substrate, where it conforms to the shape of the sample, eliminating the sample-mask distance.

In order to do so, we cut out a square on a dust-free suspended SiN membrane, supported only by a narrow bridge at each corner. The etch pattern is simultaneously written in the middle

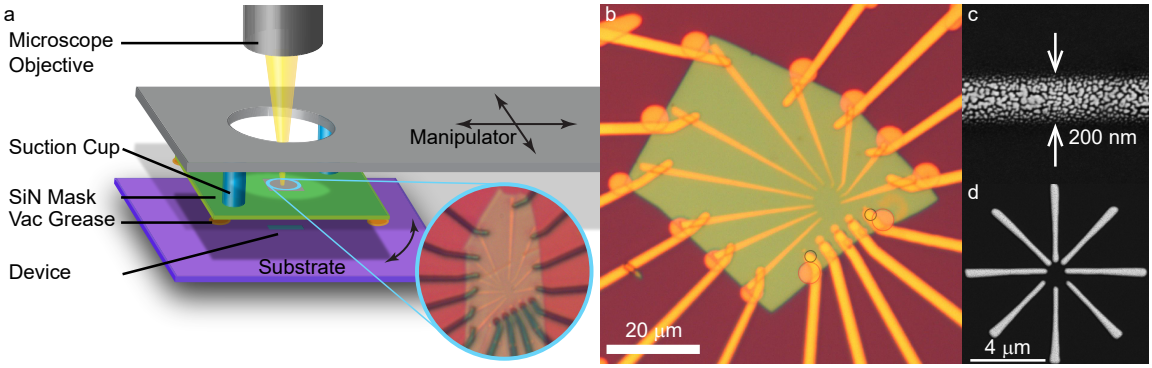

Figure 4.8: Stencil Mask Evaporation a. Stencil mask alignment. The substrate is placed on a motorized stage, underneath a transparent silicon nitride (SiN) mask. The mask is held in place using vacuum suction cups on another motorized manipulator. A microscope guides the mask onto the BSCCO crystal, and the vacuum grease glues it to the substrate. The vacuum suction cups are then released, and the sample/mask assembly is ready for metal evaporation. **Inset.** image of mask aligned to a BSCCO/BN/graphene stack, with pre-fabricated contacts and vias on the BN layer. Dark lines are holes in SiN. **b**. Same type of sample after evaporation. **c - d.** SEM images of gold evaprated with high resolution FIB masks. Lines in (c) are grains in the thin evaporated gold.

of the square. Next, using a shaped PDMS stamp with four contact points just inside the four SiN bridges, we pick up the square at low temperature, breaking the bridges. Next, we align the etch pattern to the device, and release the membrane on the sample substrate. The trick is to minimize the contact area between PDMS and the sample, such that the minimal adhesion with the substrate overcomes the PDMS adhesion, which itself must be stronger than the strength of the SiN bridges connecting the suspended patch to the rest of the wafer.

To etch the samples, we have outfitted our evaporator with an argon ion mill. We etch with argon ions accelerated to 300 eV and at the lowest possible power which ignites the plasma. We subsequently remove the mask using a flat PDMS transfer stamp.

A prototypical device is shown in figure 4.9, where multiple leads are placed around a circular device area shaped by this method. The resulting devices preserves high-temperature superconductivity.

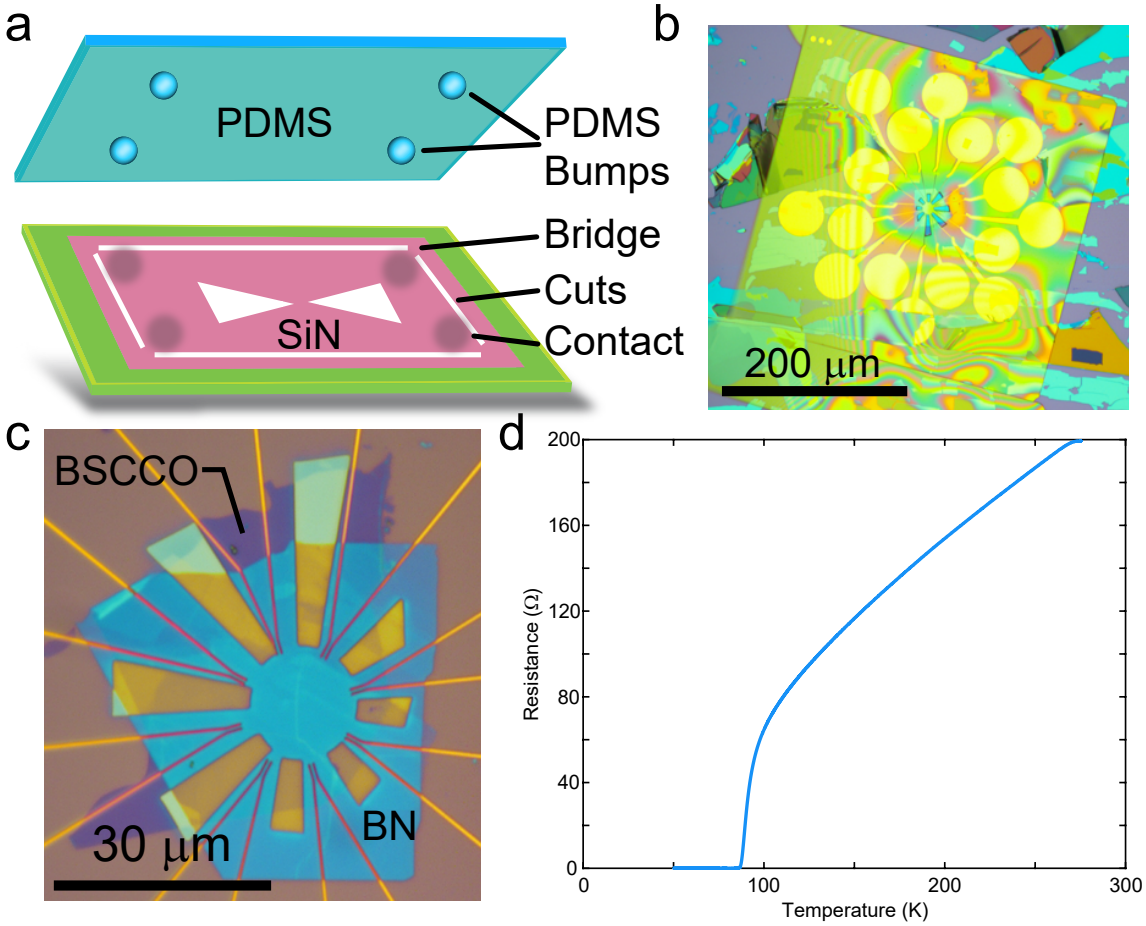

Figure 4.9: Stencil Mask for Etch a. Stencil mask pickup. The SiN membrane on its carrier silicon chip with pre-cut etch pattern and trenches is placed underneath a patterned PDMS block, where four bumps are aligned with the SiN bridges at each corner. The mask is picked up at -100°C, breaking the bridges, and then aligned and placed on the target device above -50°C. Van der Waals forces holds it in place. A device is pictured in **b.** where the yellow square is the SiN mask, with the etch pattern near the middle. **c.** shows the finished device after etching and SiN removal (via PDMS). **d.** shows resistance vs temperature of the etched device, showing a superconducting transition reaching zero resistance at 85 K.

4.7 Device Packaging

In order to place a finished sample into a cryostat with electrical connections, we have placed a wirebonder inside our glovebox (West-Bond 7476E), shown in figure 4.10. The bonder's pneu-

matically activated wire clamp is connected to the argon supply line. We have constructed a custom sample holder consisting of a large aluminum block, thermally isolated from the bonder stage via a PTFE base. We cool the aluminum block to about -100°C on the transfer stage. The aluminum block's large thermal inertia then keeps our device cold while wirebonding. The ceramic chipholder is placed on a copper grounding clip, whose copper base is mechanically clipped to the sample holder, and reaches up to touch the bottom of the ceramic chip holder. After wirebonding, we seal the device package using a pre-baked glass cover slip and Apiezon N vacuum grease.

4.8 Monolayer BSCCO in van der Waals Heterostructures

The electronic properties of monolayer van der Waals materials can often be experimentally controlled via interactions with its environment. In the case of monolayer BSCCO[25], oxygen doping can be changed simply by annealing the crystal near room temperature in the vacuum of a cryostat, making nearly the entire electronic phase diagram accessible in a single device. At the same time, our twist Josephson junctions in Chapter 8 demonstrates how the inherent freedom in constructing vdW heterostructures may be exploited to engineer emergent electronic phases at atomically sharp vdW interfaces.

One experiment that exploits the reduced crystal dimensionality is the measurement of electronic compressibility[144,145,146,147]. As fermionic charge carriers are added into a non-interacting electron gas at zero temperature, the chemical potential μ increases as eigenstates of the Hamiltonian are filled up. The relation between these two quantities is the electronic compressibility $\kappa = 1/n^2 \cdot \partial n/\partial \mu$, where n is the number of charge carriers[145]. For non-interacting fermionic gases, the compressibility is simply the density of states, but when interactions are turned on, many-body interactions may modify κ[144,146] or even change its sign[148,149,145].

The electronic compressibility may be measured via ARPES[147], quantum capacitance[146], or,

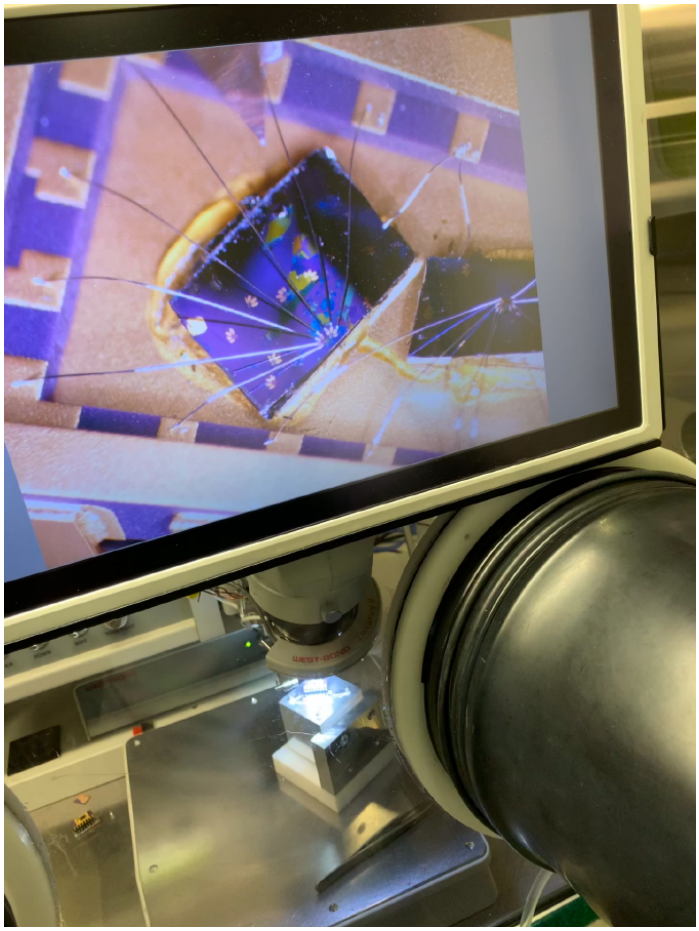

Figure 4.10: In-Glovebox Wirebonder. Image shows wirebonder inside glovebox. Sample is sitting on pre-cooled sample holder under the microscope (bottom). The image through the microscope is displayed on a thin display mounted just above the glovebox window. Sample package and device is visible in the microscope image. Wirebonder tip is near the top of the image.

in our case, penetrating electric field [148,144]. BSCCO monolayers are just thin enough to be comparable to its Thomas-Fermi screening length, so that a weak electric field would penetrate the screening charge carriers in the monolayer. In order to measure this penetrating electric field, we place pre-patterned graphene nanoribbons on top of monolayer BSCCO, which is itself on top of a silicon gate. All three electronic layers are separated from one another with insulating *h*BN and SiO_2 dielectrics (figure 4.11 c inset).

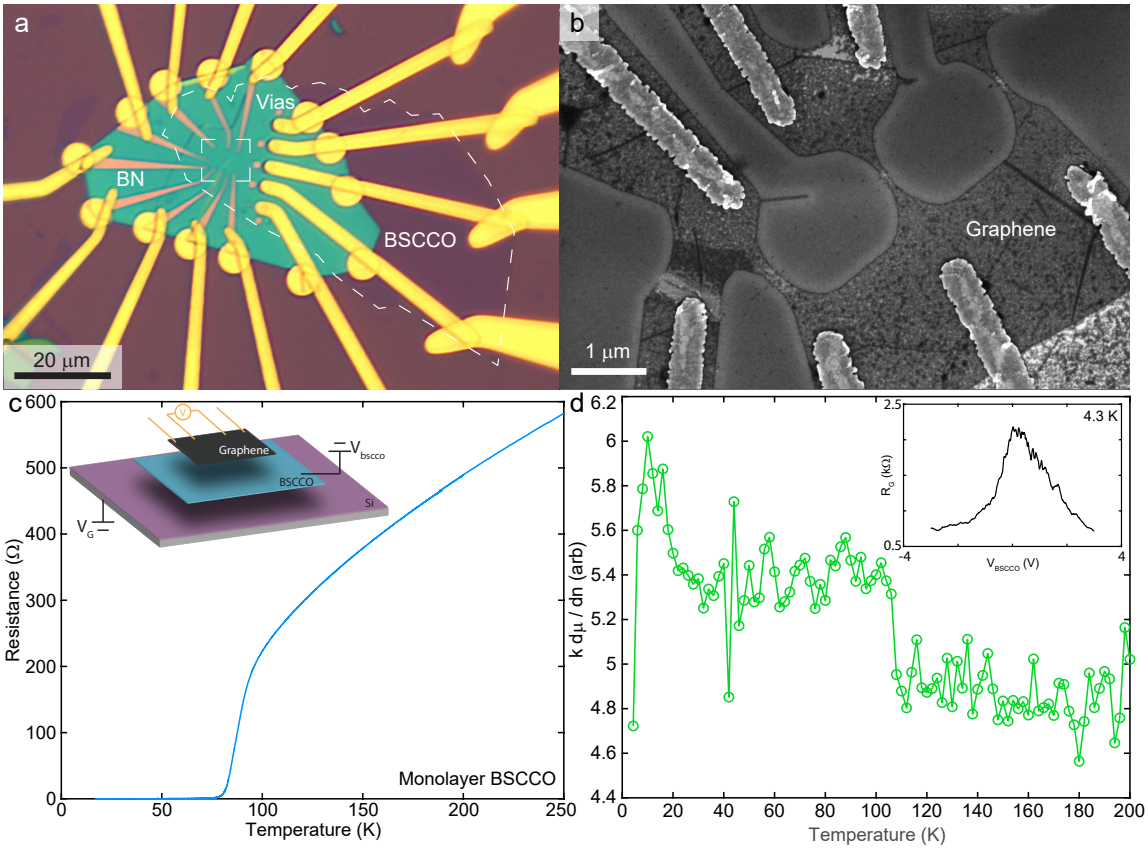

Figure 4.11: Electronic Compressibility of Monolayer BSCCO a. vdW heterostructure with monolayer BSCCO below *h*BN dielectric layer and pre-patterned graphene nanoribbons. White dashed line marks the monolayer BSCCO crystal outline. Gold contacts are evaporated through five circular vias in the *h*BN layer to make electrical contact to BSCCO crystal beneath. **b.** Scanning electron microscope image of the pre-patterned graphene nanoribbons in the white square in (a). Graphene nanoribbons are very sensitive to electric fields, and is used here to measure the electric field penetrating the monolayer BSCCO crystal. **c.** Resistance vs temperature for monolayer BSCCO in vdW heterostructure. **Inset** shows device schematic. *h*BN and SiO_2 dielectric layers are hidden for clarity. **d. Inset** shows graphene response to an applied gate voltage on the BSCCO layer. This sets up an unscreened electric field at the graphene layer. **e.** Preliminary measurement of the electronic compressibility in such a heterostructure.

Our fabrication methods have made it possible to achieve high-temperature superconducting monolayer BSCCO devices in a van der Waals heterostructure (fig. 4.11c). By mechanically exfoliating directly onto a substrate cooled to -35 ° C, and immediately cooling down the substrate during sample preparation, the superconductivity may be preserved. Simultaneously, complex

pre-fabricated vdW heterostructures may be stacked and lithographically patterned (fig. 4.11 b) on other substrates using conventional methods, then picked up using the cryogenic transfer technique and placed over the BSCCO monolayer. The result is shown in figure 4.11a.

In order to measure electronic compressibility[144], we first measure the graphene electronic resistance R_G response to an unscreened electric field, applied via a voltage on the BSCCO layer (fig 4.11d inset). In order to minimize noise, the graphene excitation current is applied using a lock-in amplifier. Next, we fix the voltage V_{BSCCO} where the slope $|dR_G/dV_{BSCCO}|$ is highest. This reflects the point where the graphene nanoribbon sensor is most sensitive. Finally, we apply a low-frequency AC voltage to the silicon back-gate and measure the resistance modulation in the graphene layer using a double-lock-in method, where the voltage output of the lock-in amplifier measuring the graphene resistance is fed into a second lock-in amplifier set to the back-gate modulation frequency. Finally, by comparing the response of the graphene resistance to each gate, we can extract a number proportional to the inverse electronic compressibility $d\mu/dn$ (fig. 4.11d).

In the next chapter, we shall illustrate a powerful technique for *in-situ* modification of the doping of a conducting vdW layer in a heterostructure. By drop-casting an air sensitive electrolyte on top of a vdW device immediately after wire-bonding, we controllably insert an intercalating chemical species between vdW layers, with consequences in electrical and optical properties.

Let's be experimentalists.

Ken S. Burch

5

Controlled Electrochemical Intercalation of Graphene/*h*-BN van der Waals Heterostructures

Electrochemical intercalation is a powerful method for tuning the electronic properties of layered solids. In this chapter, we report an electrochemical strategy to controllably intercalate lithium ions into a series of van der Waals (vdW) heterostructures built by sandwiching graphene between hexagonal boron nitride (*h*-BN). We demonstrate that encapsulating graphene with *h*-BN eliminates parasitic surface side reactions while simultaneously creating a new heterointerface that permits intercalation between the atomically thin layers. To monitor the electrochemical process, we employ the Hall effect to precisely monitor the intercalation reaction. We also simulta-

neously probe the spectroscopic and electrical transport properties of the resulting intercalation compounds at different stages of intercalation. We achieve the highest carrier density $> 5 \times 10^{13}$ cm^{-2} with mobility $> 10^3$ $cm^2/(V\,s)$ in the most heavily intercalated samples, where Shubnikov-de Haas quantum oscillations are observed at low temperatures. These results set the stage for further studies that employ intercalation in modifying properties of vdW heterostructures.

5.1 Introduction

Graphite intercalation compounds (GICs) exhibit a variety of interesting properties that differ significantly from semimetal graphite [150]. For example, CaC_6 and YbC_6 display superconductivity [151], while $Li_{0.25}Eu_{1.95}C_6$ and EuC_6 exhibit ferro- and antiferromagnetic ordering, respectively [152]. Intercalation compounds also represent technologically significant materials. LiC_6 is the prototypical anode material in Li ion batteries. By analogy to these bulk graphite intercalation compounds, the intercalation of few-layer graphene has also been realized [153,154,155]. Upon intercalation of Li, the optical properties of few-layer graphene crystals (with thicknesses down to 1 nm) change significantly [153], Ca-intercalated few-layer-graphene is superconducting [154], and $FeCl_3$ intercalated bilayer graphene showed a hint of ferromagnetism [155]. In addition, there have been theoretical predictions that heavy doping and proximity induced spin-orbit coupling from certain intercalants may induce exotic electronic properties in the graphene channel [156].

Recently, it was demonstrated that one can stack different van der Waals (vdW) atomic layers to form vdW heterostructures, creating a new generation of few-atomic layer functional heterostructures with emergent properties [12,33]. In particular, graphene encapsulated by *h*-BN, a layered insulator, forms a vdW heterostructure where the two dimensional (2D) graphene channel is well isolated from the environment [12]. As in intercalation compounds of bulk vdW materials, the intercalation of vdW heterostructures may create a new generation of functional heterostructures with emergent properties. Furthermore, the use of *h*-BN protecting layers may enable the

formation of stable intercalation compounds that differ significantly from the bulk intercalation compound due to the presence of two dissimilar surfaces at the heterointerface[157].

Compared to traditional intercalation methods for van der Waals materials, these synthetic *h*-BN/graphene vdW heterostructures present several challenges for intercalation. For example, bulk alkali metal intercalated vdW crystals are chemically highly unstable, prohibiting subsequent exfoliation into few-atomic-layer intercalated nanocrystals. Conversely, conventional chemical intercalation methods involve highly reactive reagents and high temperatures[150], often incompatible with microfabrication procedures for electronic device characterization. Another challenge associated with electrochemical intercalation of atomically thin vdW heterostructures stems from the difficulties in measuring the sub-picoampere electrochemical currents produced from atomically thin van der Waals structures having micron-size lateral dimensions. Such a small current can easily be dominated by current contributions from parasitic reactions occurring in the electrolyte, precluding the use of standard electrochemistry techniques such as cyclic voltammetry.

Our strategy to overcome these hurdles was to employ an electrochemical technique on a prefabricated mesoscopic electrical device, thus replacing conventional molten metal reagents with a relatively inert electrolyte, and using the applied bias to deliver a controllable driving force. We demonstrate (i) that *h*-BN is an effective passivation layer for 2D devices with respect to electrochemical degradation; (ii) the formation of a prototype heterostructure intercalation compound and show for the first time the insertion of Li ions into the interface between single-layer graphene and *h*-BN crystals; and (iii) the use of the Hall effect to monitor the progress of intercalation as a function of applied bias, rather than standard voltammetry methods[158]. Our approach is not restricted only to graphene/*h*-BN heterostructures, or only to the intercalation of Li; it can be generalized to a wide range of heterostructures, opening the field to a new system of intercalation compounds[61].

In our experiment, we use mechanical exfoliation followed by van der Waals dry assembly tech-

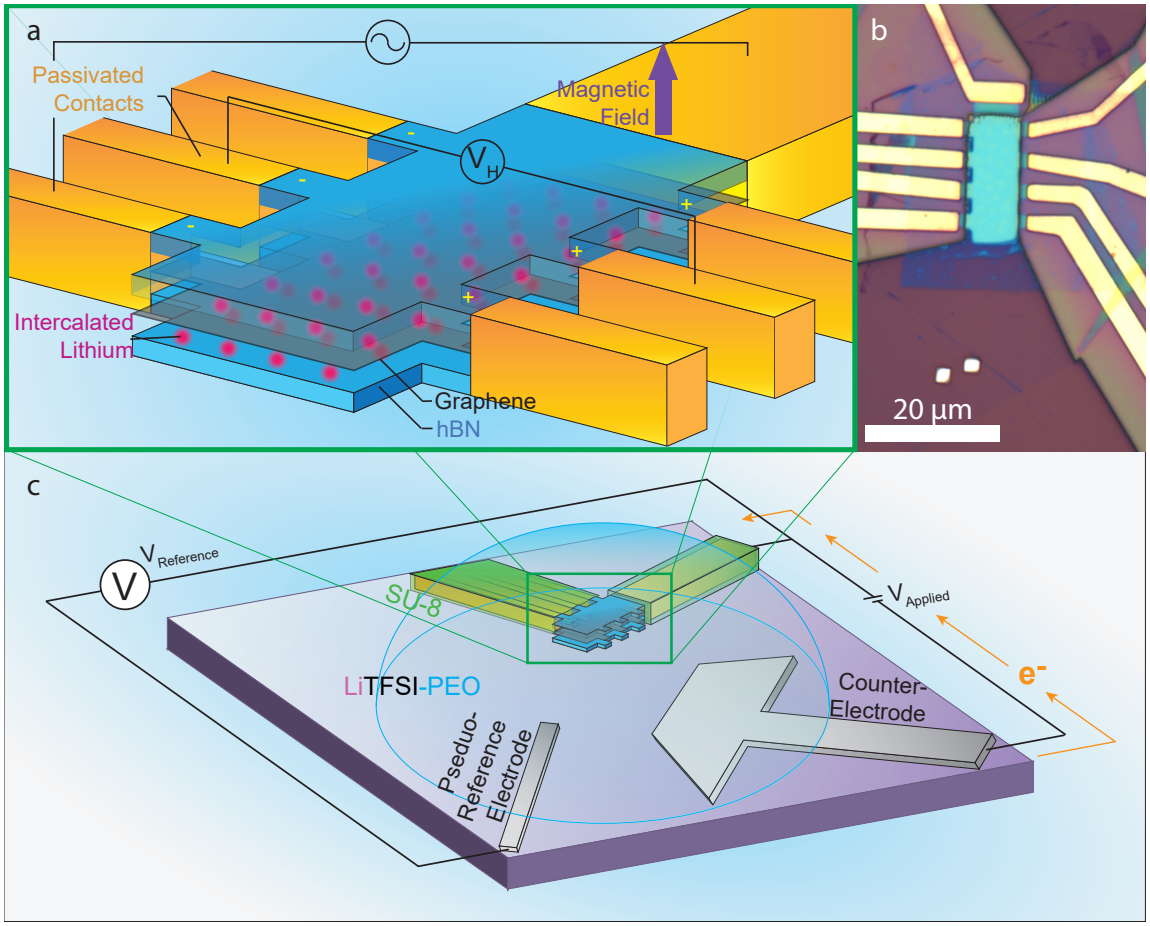

Figure 5.1: Schematic of the Hall bar device. a. A *h*-BN/graphene/*h*-BN heterostructure is patterned into a Hall bar with edge Cr/Pd/Au (2/15/60nm) contacts. A channel is left open at the entrance of the Hall bar to allow interactions with the electrolyte. An AC current is applied across the device in a 0.5 T magnetic field, inducing a transverse Hall voltage across the device. The Hall voltage is used to monitor the intercalation reaction.(b) Optical micrograph of a representative heterostructure device before electrolyte deposition. Note that all electrodes are covered with SU-8 photoresist, leaving only an edge of graphene in contact with the electrolyte. (c) The solid polymer LiTFSI-PEO electrolyte is dropcast over the Hall bar device (working electrode) shown in part a as well as a Pt pseudoreference electrode and counter electrode. To drive the electrochemical reaction, a voltage is applied between the counter electrode and working electrode, and the intercalation voltage is measured versus a Pt pseudoreference.

niques[131] to fabricate vdW heterostructures, using monolayer (1LG) or bilayer (2LG) graphene sandwiched between ~30 nm thick *h*-BN crystals. The vdW stacks are then shaped into Hall bar geometries, with only the well-defined graphene edges in the vdW stack exposed to the electrolyte.

Intercalation is thus only allowed from the edge of the sample (Figure 5.1b). Using this technique, we can unambiguously and directly observe the reversible doping of graphene as Li ions intercalate and de-intercalate the *h*-BN/graphene interface, despite any side reactions that take place at electrolyte-exposed conducting surfaces. Figure 5.1 depicts the basic design of our electrochemical cell. Here, we use the graphene channel as a working electrode. The graphene channel itself is electrically contacted by gold electrodes using the edge contact method[131]. All gold contacts and wires in our devices are covered with a passivating SU-8 layer written at 2 $\mu C/cm^{-2}$ at 30 keV that is both electrochemically inert and electrically insulating. This simultaneously protects the Au from corrosive reactions occurring at high voltage and limits the number of side reactions occurring in the cell. The device includes a Pt counter-electrode and a Pt pseudoreference electrode.

We cover the whole device with a solid electrolyte composed of lithium bis(trifluoromethane)sulfonimide (LiTFSI) vacuum dried at 180 ° C suspended in a BHT inhibitor free poly(ethylene oxide) (PEO) matrix with molecular weight 100,000 g/mol. Both powders are mixed at 1:38 ratio (PEO monomer units : LiTFSI) and dissolved in acetonitrile pre-dried in 4 Å activated molecular sieves. The solution is drop-cast by hand using a micropipette in an argon glovebox with water and oxygen contamination below 0.1 ppm. The ensuing film was dried at 320 K under vacuum overnight. To keep the electrolyte free of air contamination, the sample was either mounted to the sealed cryostat directly inside an argon glovebox (for the microscopy cryostat), or the sample package (a ceramic DIP-16 chip carrier) was sealed using a glass cover slip glued to the sealing ring using Dow Corning vacuum grease. This cover was able to protect a sensitive chemical indicator for oxygen from air (under ambient conditions) for about 72 hours.

To control the intercalation progress, we monitor intercalation in real time using Hall effect measurements (with a small applied magnetic field of 0.5 T), simultaneously probing the electrical transport properties and the charge carrier density of the crystals as Li ions are inserted [158]. Using this technique, we can unambiguously observe the reversible doping of graphene as Li ions intercalate and de-intercalate the *h*-BN/graphene interface. Figure 5.1b shows an optical microscope image of a typical device used for the experiment. To facilitate magneto-transport measurements, the graphene heterostructure is patterned into a Hall bar geometry. Note that the standard Hall bar geometry is modified slightly, with the source contact at the end of the Hall bar split into two on the far side of the device, so that the corresponding etched edge can be exposed directly to the electrolyte.

In order to drive the electrochemical reaction, we used a Keithley 2400 SourceMeter to provide the electrical potential to the Pt counter-electrode, while an Agilent 34401A digital multimeter set to $>$ 10 GΩ input impedance read back the pseudo-reference Pt electrode potential. The graphene working electrode was kept grounded. In order to perform the simultaneous resistance and Hall effect measurements, a Stanford Research Systems (SRS) SR-830 lock-in amplifier supplied 1 μA of current at 17 Hz flowing across the Hall bar device. The graphene devices were $<$ 1 kΩ in resistance, therefore the AC contribution to the graphene working electrode potential was less than 1 mV, significantly less than the electrochemical intercalation energy scale.

Figure 5.2 shows the resistivity and estimated carrier density obtained from Hall measurement for two devices built from 1LG and 2LG sandwiched between *h*-BN. In both cases, while the electrode potential is swept toward increasingly negative values at 325 K (i.e., toward more reducing potential), the graphene channel carrier density increases linearly with the applied voltage, while the resistance of the sample decreases, consistent with electrostatic gating of the graphene crystal, through the *h*-BN dielectric, close to the high-resistance Dirac point [159]. As we reach a thresh-

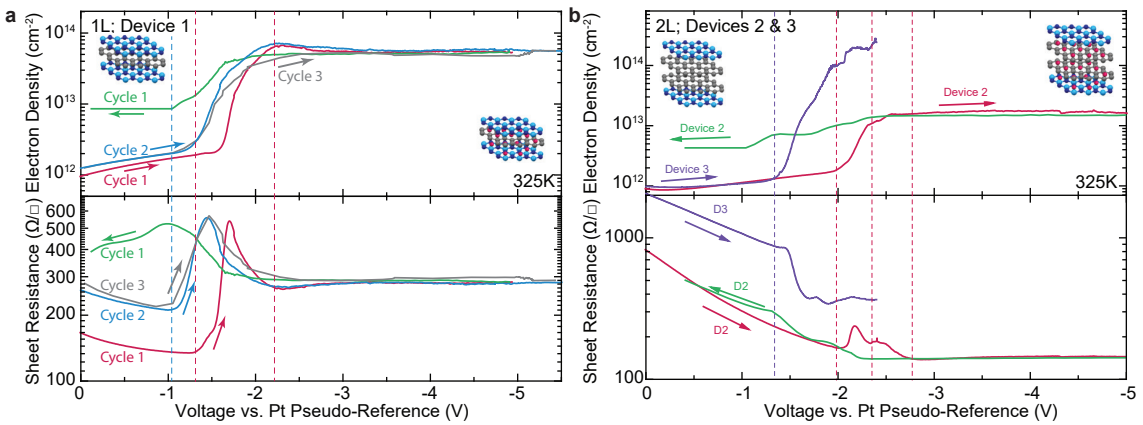

Figure 5.2: Electronic in-situ monitoring of intercalation. Measured electron density and sample resistivity in intercalating and de-intercalating graphene heterostructures fabricated with (a) single layer graphene and (b) bilayer graphene. In both cases, on the first intercalation cycle (red), electron density increases linearly at low potentials, while resistance decreases, consistent with electrostatic gating across the h-BN. Once the electrochemical potential exceeds a certain threshold, electron density suddenly increases by about an order of magnitude and then saturates, while at the same time resistance spikes. This suggests the onset of the electrochemical reaction. When the potential is swept back toward zero (green), the sample de-intercalates at a slightly lower voltage but follows the same general trend in reverse. In part a, blue and silver traces show subsequent intercalation cycles on the same device, where the same trend is observed but with a lower threshold voltage. In part b, for the 2LG case, data from a second device is shown instead (purple), showing an intercalation run to the highest achieved electron density in 2LG. This sample is intercalated in an optical cryostat sealed directly inside an argon glovebox, minimizing contamination relative to the other samples sealed in a DIP-16 package using a dried glass coverslip.

old voltage (about -1.4 V for cycle 1 in Figure 5.2a), the carrier density begins to increase at a significantly higher rate, suggesting the intercalation of Li ions into the heterostructure. At the same threshold voltage, we observe a spike in the sheet resistance of the device, consistent with a decrease in the graphene mobility as charged Li ions move into the device.

The exact threshold voltage value varies somewhat from device to device, where contact resistances between the gold contacts and graphene and between graphene and electrolyte change due to microscopic differences between devices. This results in an ohmic voltage loss between our heterostructure working electrodes and the Pt pseudoreference. With these sample-to-sample variations, the typical threshold voltage is between -1 and -3 V.

On the reverse scan, we observe a concordant steep decrease of the charge carrier density asso-

ciated with a slightly broader maximum in the resistance of the device. We note that deintercalation happens at a lower voltage than the initial intercalation threshold voltage. Immediately after de-intercalation, our measurements indicate the graphene heterostructures contain more electrons than the pristine device, suggesting that some Li ions remain between the sheets initially. After holding the device at 0 V overnight (>12 h), the device returns to its fully de-intercalated state where the residual charge density becomes 10^{12} cm^{-2}. Subsequently, a second intercalation sweep in the same geometry reveals a response very similar to the first intercalation. Overall, the reversibility of the reaction demonstrates that our measurements are not a result of a sudden delamination of the van der Waals heterostructure, which would result in a permanent increase of electrostatic gating efficiency at all potentials.

In transport measurements, we measure the homogeneity of the sample by measuring the Hall signal taken from different contact pairs along the Hall bar. In Figure 5.3, we plot the sheet resistance taken from pairs of contacts on the left and right sides of the device, and estimated Hall density taken from pairs of contacts adjacent to each other on the Hall bar, from the first two intercalation cycles shown in Figure 5.2a. This measurement reveals a uniform sheet resistance throughout both intercalation cycles, as well as simultaneous increase in charge carrier density. Above threshold voltage, the estimated density appears to deviate between the two contact pairs. This is an artifact of the small Hall voltages at high carrier density, since a sweep of the magnetic field at 250K reveals an identical slope in V_{xy} taken at the two contact pairs (Figure 5.3 inset), indicating identical carrier densities in the two regions. Thus, we conclude that the intercalating samples are kept in equilibrium throughout our experiments.

These Hall potentiometry data demonstrate that the reversible electrochemical intercalation and de-intercalation of Li ions in the interface between graphene and *h*-BN crystals is possible. For 2LG samples, the intercalated Li ions can insert either in the graphene/graphene interface or in the graphene/*h*-BN interfaces. Raman spectroscopy is a useful probe to investigate the distribution of intercalation in few-layer-graphene intercalations[160,161]. Specifically, both the G- and

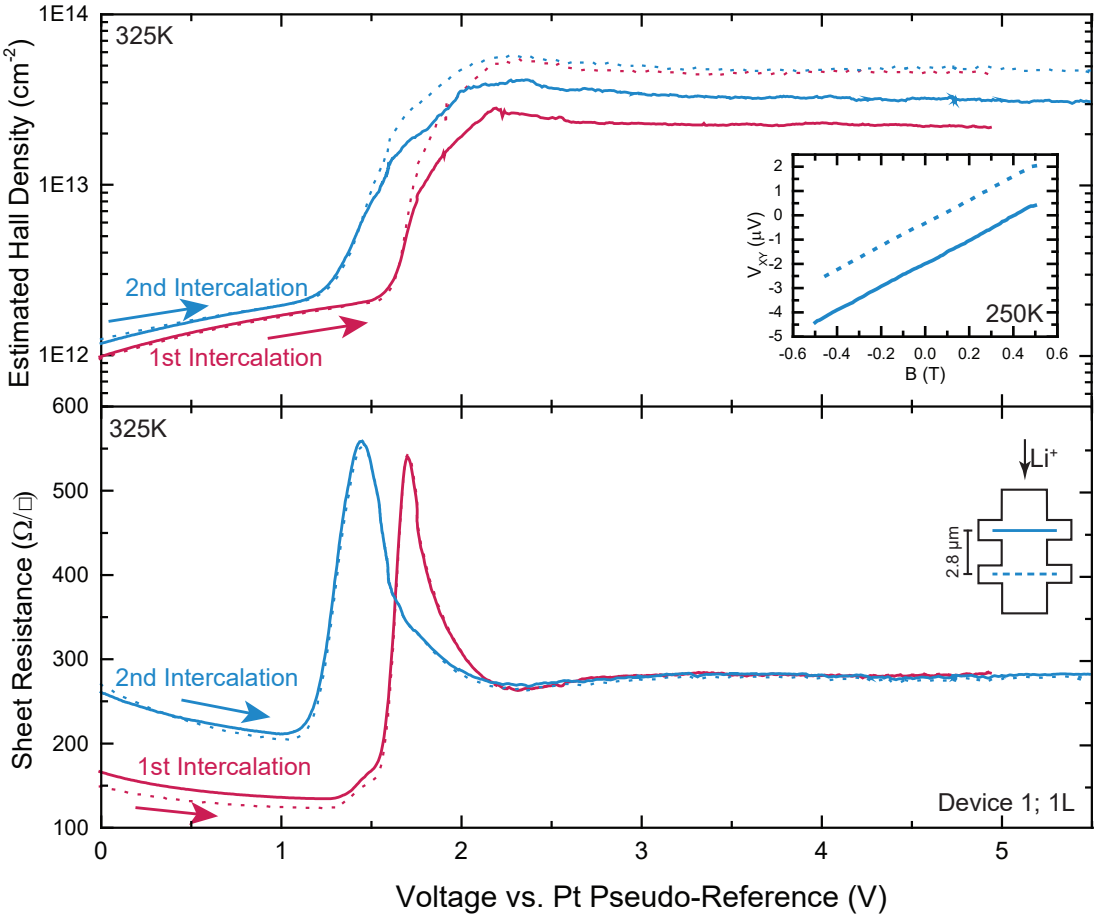

Figure 5.3: Uniformity of the intercalating sample. Estimated Hall density and sheet resistance during intercalation of Device 1 shown in Figure 5.2a. Solid curves appeared in Figure 2a, while dotted data is taken from an adjacent pair of contacts. For resistance, these pairs are located on the left and right sides of the device. For Hall data, contact pair locations are drawn in the cartoon inset, and are located 2.8 μm apart. All data matches very closely, except for the estimated Hall carrier density after intercalation. Here the difference is due to a constant offset in the Hall voltage (inset), while the slope remained the same, implying that the carrier density is identical after the intercalation.

2D peaks of graphene (near 1582 and 2700 cm^{-1}, respectively, in pristine graphene) are good indicators of the charge density in the graphene basal plane [161,162].

We performed in situ Raman spectroelectrochemistry to further confirm that Li ions can intercalate the graphene/*h*-BN interface. Figure 5.4 shows the evolution of the Raman G and 2D peaks of graphene as a function of applied cell potential for both 1LG and 2LG samples. The 1LG structure is once again very instructive. As the cell potential increases, the graphene G peak sharpens and shifts at low voltages due to increasing carrier density in graphene. A fit of the G peak position in Figure 5.4d suggests that the carrier density increases approximately linearly with the applied voltage (so that the Fermi energy increases approximately as $V_{EG}^{1/2}$), consistent with electrostatic gating through the *h*-BN layer. As the cell voltage approaches the threshold, the G peak rapidly blueshifts, and both G and 2D peaks subsequently disappear, while the corresponding *h*-BN peak[163] at 1370 cm^{-1} remains visible. This suggests that the graphene layer is sufficiently doped by the Li intercalant as to be Pauli-blocked, while the *h*-BN layer remains unaffected. Comparison with graphite literature[161] shows that Pauli-blocking and the vanishing of the graphite Raman peaks is a signature of stage 1 intercalation in bulk Li intercalated graphite LiC_6. This observation further suggests that Li is coming into direct contact with the graphene, and supports the notion of graphene/*h*-BN interface intercalation. Using the excitation laser wavelength ($\lambda = 532$ nm) as a lower bound for the Fermi energy, the graphene was doped to $E_F > 1.16$ eV, corresponding to a charge density of 9.9×10^{13} cm^{-2}, a very high carrier density normally inaccessible using electrostatic gating through a thick *h*-BN crystal alone.

In both the 1LG and 2LG heterostructures, the Raman spectra do not exhibit an appreciable D peak at 1350 cm^{-1}, which is commonly associated with chemical disorder or damage of the in-plane covalent graphene bonds[165]. The absence of Raman D peak during the intercalation/deintercalation process suggests that the Li ions are inserted into the graphene/*h*-BN interface without damaging the in-plane bonds between the carbon atoms, leaving the graphene lattice itself intact. Furthermore, Raman spectra taken on the same device through multiple cy-

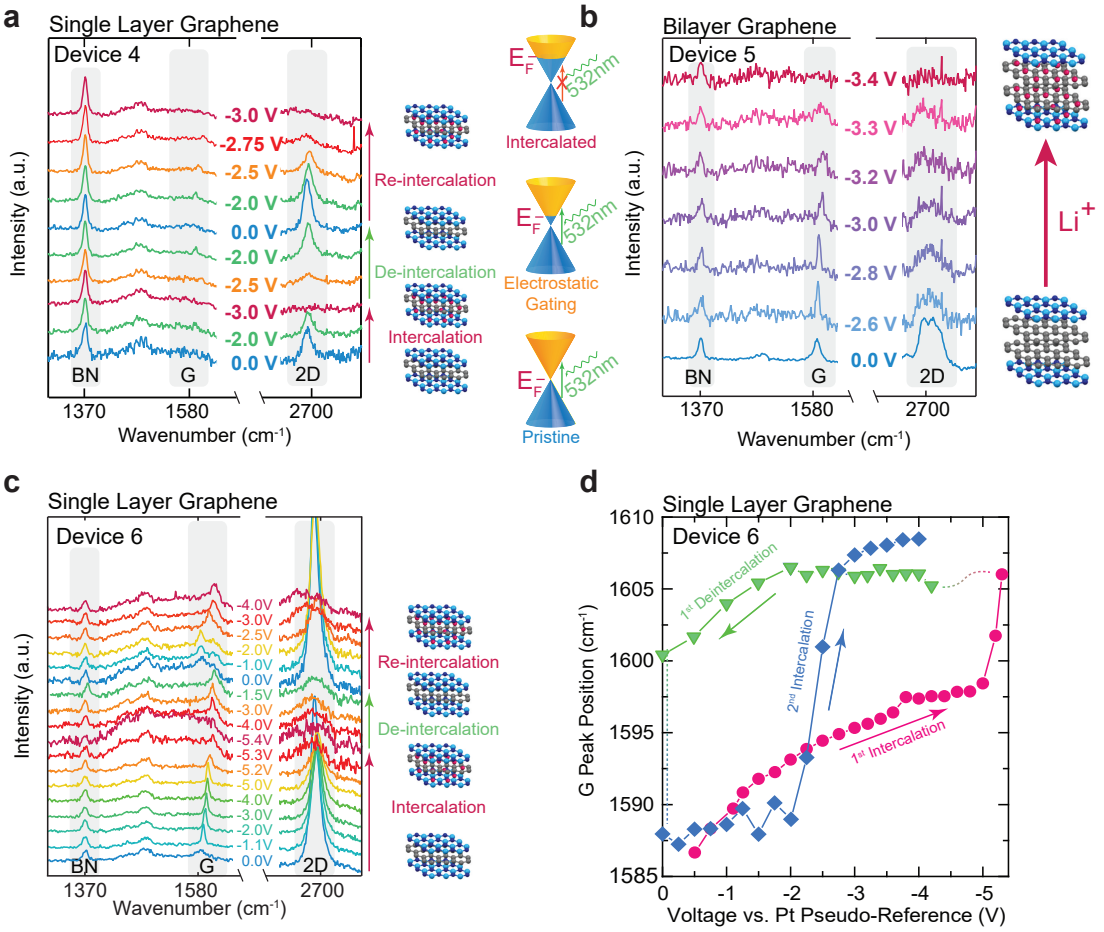

Figure 5.4: Raman in-situ monitoring of intercalation. (a-c) Representative Raman spectra demonstrating the evolution of the G and 2D peaks with applied potential while the h-BN peak remains constant for 1LG (a, c) and 2LG (b) encapsulated in h-BN. The electrolyte fluorescence background is subtracted from all Raman spectra, and the spectra are offset for clarity. Note the gradual blue-shift in the graphene G peak. Beyond the threshold intercalation voltage, all graphene spectroscopic signatures disappear. Dirac cones show, schematically, the doping of the graphene crystal and subsequent Pauli blocking. The relative intensities of the peaks differ from optical interference effects [164] arising from differences in the heterostructure thickness, due to the choice of h-BN crystals. (d) G-peak position measured from the spectra shown in part c as a function of applied voltage for 1LG encapsulated in h-BN. Note the sudden change in G peak position, showing that the graphene had suddenly intercalated after reaching the threshold voltage. The threshold voltage in parts c and d was higher than other devices because the contact resistance between gold and graphene was abnormally high in this particular device.

cles (Figure 5.4a,c) demonstrate the reversibility of the Raman behavior. The graphene Raman peaks reappear when we reach a threshold voltage during the reverse cell potential scan. A second

intercalation cycle produces similar Raman spectra as the first cycle with the G peak shifting as a function of gate potential.

The 2LG structure undergoes two forms of intercalation: at the graphene/graphene interface and at the graphene/*h*-BN interface. We observe behavior in Raman that cannot be ascribed solely to intercalation of the graphene/graphene interface (Figure 5.4b). In bulk graphite, stage 2 behavior (LiC_{12}), which denotes that only one side of each graphene layer is occupied by the intercalant, is characterized by a broadened, blue-shifted, but nevertheless present G peak[161]. In our 2LG device, the Raman G and 2D peaks both disappear at high voltage (while the *h*-BN D mode remains unchanged), indicating doping beyond the C_6LiC_6 stage ($> 3 \times 10^{14}$ cm^{-2}) for each layer of graphene.

5.4 Electrical Properties of the Lithiated Graphene/*h*-BN Heterostructure

The cycling Hall measurement described above was performed at slightly elevated temperature (325 K or 52 °C) to enable simultaneous monitoring of the carrier density during the intercalation process. We also performed low temperature transport characterization of intercalated samples. For this experiment, the intercalated device was cooled quickly (at a cooling rate of 10 K/min) while holding the applied cell potential. It is known that Li ions become immobile in the PEO matrix when cooled below the polymer glass transition temperature of $T_g \approx 200$ K. Below T_g, all electrochemical processes are completely frozen out and no de-intercalation processes occur even when the cell potential is brought back to 0 V. This allows us to create stable intercalated vdW heterostructures.

With the samples frozen at a predefined electrochemical potential, we measure the Hall voltage as a function of the applied magnetic field. We find that the electron density of the 1LG heterostructures saturates around a maximum of 7×10^{13} cm^{-2}, although the exact value varies between devices and maximum applied electrochemical potentials. On the basis of density func-

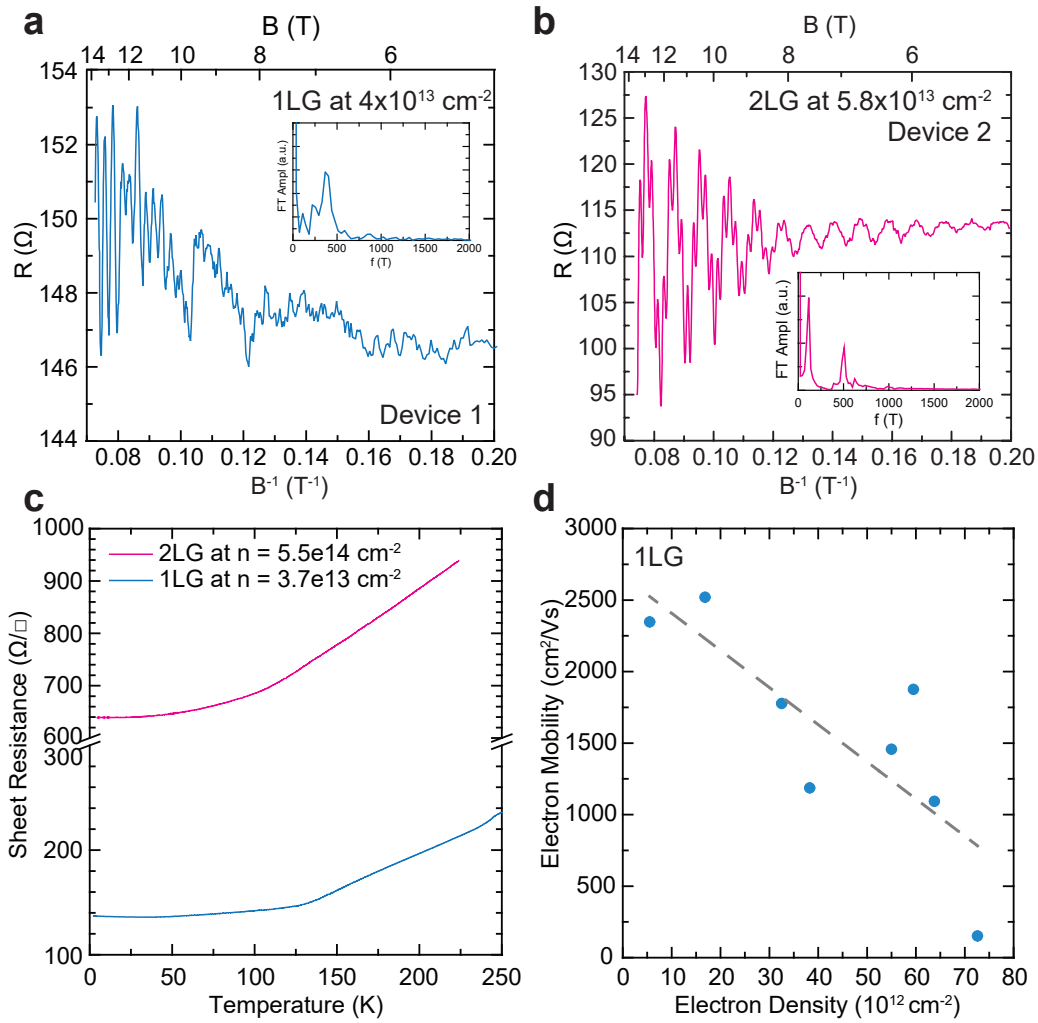

Figure 5.5: Low temperature transport properties of intercalated heterostructures. (a) Measured R_{xx} as a function of B^{-1} in a 1LG device with Hall carrier density 4.0×10^{13} cm^{-2} at 1.8 K. Periodic SdH oscillations are visible. The inset shows the Fourier transform of SdH, indicating a peak corresponding to the carrier density $(3.66 \pm 0.08) \times 10^{13}$ cm^{-2}. (b) R_{xx} as a function of B^{-1} in a 2LG device with Hall carrier density 5.8×10^{13} cm^{-2} at 1.8 K. The inset shows the Fourier transform of SdH, indicating two peaks corresponding to the carrier densities $(1.07 \pm 0.01) \times 10^{13}$ and $(4.84 \pm 0.01) \times 10^{13}$ cm^{-2}. (c) Resistivity of intercalated 1LG (blue) and 2LG (red) heterostructures at cryogenic temperatures, showing metallic behavior. (d) Electron mobility vs electron density from multiple intercalated 1LG devices, cooled to below 10 K. The line is a guide to the eye showing a general decrease of mobility after increasing intercalation.

tional theory (DFT) calculations suggesting that each intercalating Li ion donates 0.88 electron charge to the conducting graphene system [157], we calculate a Li:C stoichiometric ratio of approximately 1:60, about 1/10 of the electron density of stage 1 Li intercalated bulk graphite. This ratio is smaller, yet consistent with our DFT calculations suggesting an upper bound of Li:C stoichiometry 1:20 in *h*-BN/graphene/*h*-BN sandwich structure. Overall, this data indicates that the graphene/*h*-BN interface is far less amenable to hosting Li atoms than two neighboring graphene planes.

The intercalation process injects a large number of Li ions into the graphene/*h*-BN heterostructure. At the Li densities achieved here, the Li atoms are likely to be distributed randomly relative to the graphene lattice, creating scattering sites for the conducting electrons in graphene [158]. Correspondingly, we observe a large decrease in mobility after intercalation, from 200000 $cm^2/(V\ s)$ readily achieved in clean 1LG devices to approximately 1500 $cm^2/(V\ s)$. Despite this relatively low mobility value, we observe Shubnikov-de Haas (SdH) oscillation of magnetoresistance R_{xx} as a function of applied magnetic field B at 1.8 K (Figure 5.5a). The observed SdH oscillations in intercalated 1LG heterostructure exhibit a single period oscillation in B^{-1} (inset in Figure 5.5a). Assuming spin and valley degeneracy of 1LG, the density estimated from SdH oscillation is $4 \times 10^{13}\ cm^{-2}$, in agreement with the density measured from the Hall measurement.

Similar measurements performed on 2LG heterostructures revealed the maximum carrier density up to $5.5 \times 10^{14}\ cm^{-2}$. By assuming that the carrier density of the graphene/*h*-BN interfaces in 2LG matches that of the 1LG heterostructure ($7 \times 10^{13}\ cm^{-2}$), we can estimate an electron density in the graphene/graphene interface of $4.8 \times 10^{14}\ cm^{-2}$. This data indicates that the graphene-graphene interface can host significantly more Li ions than the *h*-BN/graphene interface in agreement with our DFT calculation.

SdH oscillations are also visible in the 2LG devices but only if the electron density is kept low ($< 6 \times 10^{13}\ cm^{-2}$) by keeping the cell potential close to the threshold before the cooldown. As shown in Figure 5.5b, the SdH oscillations show two distinct frequencies, unlike the 1LG

case, corresponding to conduction in two separate bands. Two similar SdH oscillation frequencies have been observed in electrolytically gated bilayer graphene samples[166] suggesting different populations in the lower and higher subbands of 2LG. In our experiment, the total carrier density in both bands matches with the value derived from Hall data.

Finally, we discuss the temperature dependent transport in the intercalated compound. For this measurement, we slowly warm up the samples (at 5 K/min) under magnetic field and measure R_{xx} and Hall resistance R_{xy} of the samples to obtain the density and mobility of the samples at different temperatures. Figure 5.5c shows that R_{xx} increases monotonically for 1LG and 2LG as temperature increases, indicating metallic behaviors of both samples. We note that both mobility and density typically remain approximately constant below 200 K. However, when the intercalated devices are warmed above the polymer T_g, chemical reactions resume as a function of the cell potential. We note that the electron mobility decreases significantly at higher temperatures and at higher doping. At the highest carrier density of 5.5×10^{14} cm^{-2} for 2LG, the electron mobility decreases to 18 cm^2/(V s) when $T < 100$ K. An overview of the mobilities attained in multiple 1LG devices intercalated to different densities is presented in Figure 5.5d. We observe a general trend in decreasing mobility with increasing intercalation density, consistent with increasing intervalley scattering due to increasing numbers of Li ions associated with the graphene layer.

5.5 Summary and Outlook

In summary, we have demonstrated the electrochemical intercalation of Li into graphene encapsulated between *h*-BN layers. Passsivation of the device components (graphene surface and electrodes) prevents electrochemical side reactions that lead to the modification of the sample surface. Our device platform allows for in situ characterization of the doping level and electrical transport properties as the intecalation progresses. Using our Hall potentiometry method,

we can not only very precisely monitor the intercalation through Hall effect, but we can also intercalate the galleries in the graphene/*h*-BN interface. The effect of intercalation into vdW heterostructure is most prominent in the 1LG case, where gating effects are not enough to explain the observed high doping levels in both the Raman and transport data. Our technique enables the engineering of novel vdW heterostructures with diverse functionality and applications.

A physicist is an atom's way of knowing about atoms.

George Wald

6

Spatially Correlated Incommensurate Lattice Modulations in an Atomically Thin BSCCO Superconductor

We report high spatial resolution, below 100 nm, scanning nano x-ray diffraction (SnXRD) imaging of incommensurate lattice modulations (ILM) in $Bi_{2.1}Sr_{1.9}CaCu_{2.0}O_{8+y}$ van der Waals heterostructures of thicknesses down to two unit cells. We reveal the distinct long-range and short-range ILMs in a bulk sample and at the surface. We find that the size and mutual orientation of the puddle-like domains of the ILM are determined by the dimensionality of the system. In the two-unit-cell sample, the wave vectors of the long- and short-range orders become anticorrelated, and the emergent spatial patterns have a directional gradient. These emergent patterns imply

static mesoscopic lattice modulation. Our findings open a route for local strain engineering to modulate properties of two-dimensional high-temperature superconductors.

sectionIntroduction

High-temperature superconducting cuprate perovskites are composed of CuO_2 layers intercalated between charge reservoir layers. The differences between these two structural units give rise to intriguing and unconventional crystallographic patterns up to the mesoscale which can control superconducting properties [167,168,169,170,171,172,173,174,175]. Although the *c*-axis period changes from one cuprate system to another due to different staging of dopants, incommensurate modulations along the *b* axis are common to optimally doped cuprates [176,177,178,179,180]. The incommensurate lattice modulation (ILM) gives rise to diffuse scattering beyond the Bragg peaks in diffraction patterns, as generally occurs for structural ordering in small domains deviating from the order of the periodic crystallographic structure. In $Bi_2Sr_2CaCu_2O_{8+y}$ (BSCCO), the ILM produces both weak-diffuse and sharp-intense satellite diffraction peaks up to high temperatures [179,180,181]. The ILM is correlated with the distribution of oxygen interstitials in the SrO [182,100] and BiO layers [183]. Furthermore, ILM is also correlated with the spatial variation of the superconducting gaps [173] and Fermi surface reconstruction [184]. The inhomogeneous distribution of the ILM can thus change the spatial distribution of the superconducting gap [185] and thus introduce a random field that breaks electronic nematic orders [186,187,188]. An interplay between superconducting gap fluctuations, local strain, and dopant distributions has been recently included in percolative models of high-temperature superconductivity based on which transport data have been reinterpreted [189].

Two-dimensional (2D) crystals of superconducting BSCCO is the ultimate realization of 2D superconductivity at high temperatures [190,25]. Their high electronic tunability has been demonstrated via electric-field effects [191], as well as by superconductor-to-insulator transition experiments [25,27]. Hall-effect experiments have shown the dominant role of superconducting and vortex fluctuations in the electronic transport [26]. Since the elastic properties of the atomically thin crystals can differ from those in the bulk [192], one may wonder if the properties of the ILM would also

change in this extreme 2D limit.

6.1 Imaging the Incommensurate Lattice Modulations in a Bulk Single Crystal

In this chapter we undertake this task using scanning nano x-ray diffraction (SnXRD) imaging with spatial resolution of 70-100 nm in order to study the evolution of and the interplay between *puddlelike* domains of the two types of ILMs at the bulk and atomically thin limits, in fully superconducting BSCCO crystals. Our samples are composed of a layered perovskite near optimum doping with oxygen interstitials ($p = 0.16$ holes per Cu) subject to misfit strain [193,194,195], with an orthorhombic structure and incommensurate modulation along the long b axis with the period $(\lambda/b) \approx 4.7$ [172,174,179,180,181], where λ is the modulation wavelength and $b = 0.547$ nm is the b-axis lattice parameter.

The ILMs are believed to originate from misfit strains between atomic layers in the BSCCO lattice of different compositions [167,168,169,170,171,172,173,174,175]. Such strain in the active superconducting atomic layers modifies electronic properties in parallel to the effects of doping [193] and become an important factor controlling the maximum critical temperature in the phase diagram of many families of high-temperature superconductors, ranging from cuprates [193] and diborides [194] to the iron-based superconductors [195]. This implies that in low-dimensional systems the strain fields can also control the periodic reorganization of charge on distances varying from the atomic scales [196] to mesoscales [197,35].

Figure 6.1(a) shows the real-space representation of the lattice modulations in BSCCO, constructed using the high-angle annular dark field (HAADF) scanning transmission electron microscopy (STEM) images taken along the three different crystallographic axes. The results are combined into a three-dimensional (3D) representation. The observed one-dimensional (1D) lattice modulation is running along the (010) crystal axis in real space. While these STEM images

offer a convenient visualization of the crystallographic structure of 2D materials[197], the cross-sectional STEM study on atomically thin samples requires special sample preparation techniques that may change the atomic structures and cannot provide comprehensible information regarding ILMs in the 2D plane. To avoid these problems, we have visualized the spatial distribution of the ILMs using SnXRD at the bulk and atomically thin limits. In previous x-ray diffraction (XRD) studies of BSCCO[172,174,179,180,181], the 1D ILM has been reported to have both diffuse short-range order (SRO) satellites at $q_s = (0, 0.21, 2n)$ and long-range order (LRO) satellites at $q_L = (0, 0.21, 2n + 1)$ (where q_s and q_L are the reciprocal lattice units (r.l.u.) and n is an integer number) around Bragg peaks. The LRO are 3D ILMs, while the SRO arises from the stacking-fault interfaces between the LRO domains[171,174,179].

The SnXRD measurements combined with advanced analytic tools have proven to be extremely useful for revealing the spatial correlations between the distinct lattice, charge, spin, and quenched disorder domains in cuprates[99,103,65,200], iron pnictides[201], vanadium dioxide[202], and chromium[203]. However, only a few of these experiments have properly exploited the recent technological advances in x-ray focusing, which enabled beam sizes below 100 nm[198,199]. In our experiment we reduce the beam size down to 70–100 nm in order to scan the sample in the $a - b$ plane with a scanning step of 100 nm in both directions. At each location, we obtain the XRD corresponding to the wave vector (h, k, l) in r.l.u. within the tightly focused beam spots. To study the ILMs running along the (010) crystallographic direction, we typically record the diffraction pattern in the $h = 0$ plane.

The experiment was conducted at the Hard X-ray Nanoprobe beamline (HXN)[198], of National Synchrotron Light Source II. A microscope setup using zone plate optics[199] was used to provide a sufficient working distance for the Bragg diffraction measurement. The incident 12 keV X-ray beam was focused by a zone plate with 50 nm outermost zone width and 350 μm diameter together with a central beamstop and the order-sorting aperture (OSA). The sample crystals were placed at the focal plane and aligned with the horizontal rotational axis. The Bragg

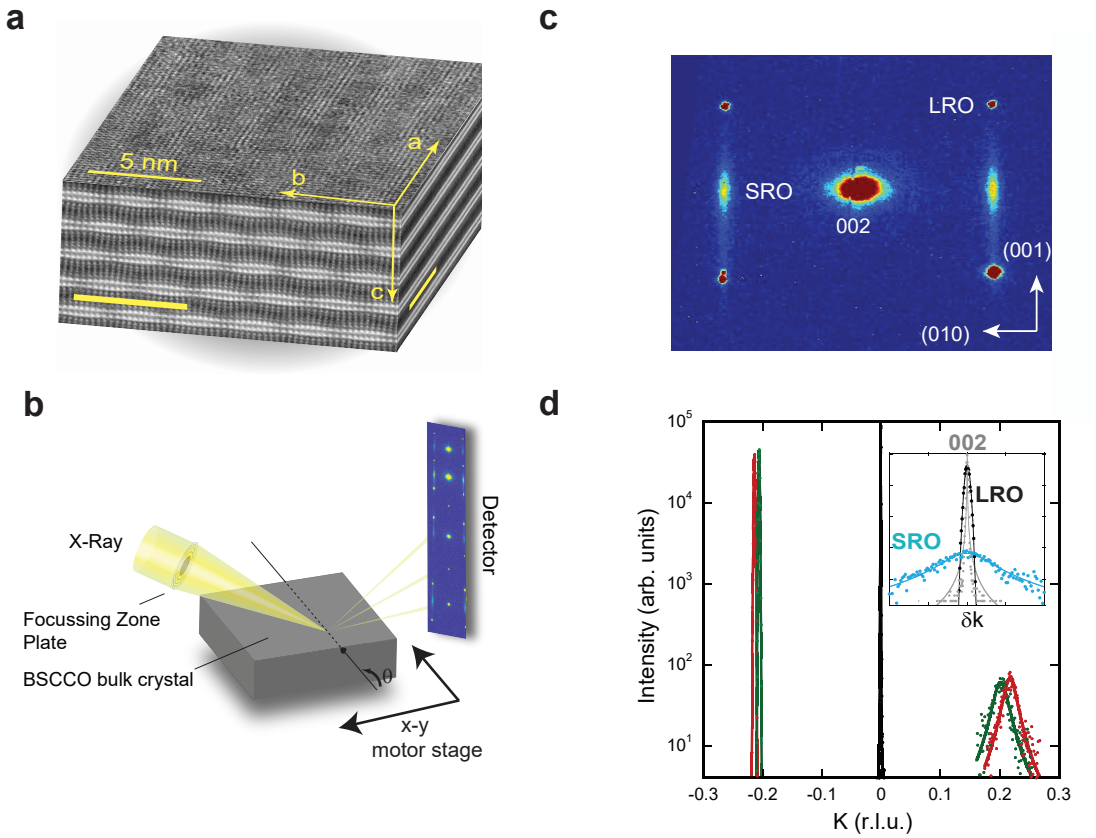

Figure 6.1: Scanning nano x-ray diffraction of a BSCCO bulk single crystal. (a) Scanning transmission electron microscopy (STEM) image of the BSCCO crystal structure where the atomic structure of the incommensurate supermodulation is visible in all combinations of the $a - b - c$ crystallographic planes. (b) Schematic diagram of the SnXRD imaging setup at the Hard X-ray Nanoprobe beamline (HXN) [198,199] at the NLSL-II. An x-ray zone plate, together with a central beamstop (not shown) and an order-sorting aperture (not shown), focuses the impinging monochromatic x-ray beam with energy 12 keV down to 70 nm. The sample (a BSCCO single crystal) can be positioned in the beam by accurate translations $x - y$, while the incidence angle to sample can be controlled by θ rotation. The diffracted beam is collected by a 2D detector whose image is integrated from a wide-range angular scan. While the experiment used the horizontal diffraction geometry, we show the rotated schematic to preserve the same sample orientation as (a). (c) Reciprocal space map around the [002] Bragg peak collected during the rocking scan. The superlattice reflections due to the LRO and SRO domains of the incommensurate modulation are visible. (d) LRO (at $k = -0.21$) and SRO ($k = 0.21$) peaks, collected at two different places with tightly focused beam in the same crystal, along the best fit using a Lorentzian line shape (continuous lines). The central Bragg peaks are also shown. The cuts are taken where indicated by the labels. The insets show the profiles of the [002], LRO and SRO peaks along $\hat{k}$ direction, centered at $k = 0$, to highlight the different width peaks.

diffraction peaks were searched by rotating the sample and monitoring the diffraction signal over a large solid angle using a CMOS flat-panel X-ray detector (Dexela 1512NDT) mounted about 0.2 m downstream of the sample. We recorded XRD patterns, summing over a series of images when rocking the crystal around the vicinity of the SRO and LRO peaks. Once the target Bragg peaks were located, a pixel array detector with smaller pixels (55 um) and higher dynamic range (Merlin from Quantum Detectors) was used to collected nano-diffraction datasets while scanning the sample with a piezo motor stage with 100 nm step size. We have mapped the samples by collecting 61×21 XRD patterns in Regions of Interest of 2×6 μm^2. The experimental setup required to keep the crystal at a fixed 2θ orientation angle. Hence, each diffraction pattern, during the scanning has been collected at a fixed 2θ orientation such as the SRO, LRO and [002] Bragg diffraction peak were visible. The profiles has been extracted by integrating XRD intensity along (010) and (001) direction in a selected $b^* - c^*$ area covering the peaks (see Fig. 6.1c and Fig. 6.4c) and subtracting the background calculated around the peaks. The XRD profiles along (010) and (001) directions have been fitted using Lorentzian line shapes and the obtained fit parameters, Full-Width Half Maximum, $FWHM_k$ and $FWHM_l$, and wavevectors, k and l. Thus, using standard crystallographic analysis, we extracted the coherence lengths along (010) and (001) direction, $\xi_b = b/FWHM_k$, $\xi_c = c/FWHM_l$ where $b = 0.547(2)$ nm and $c = 3.070(4)$ are the lattice parameters. Small incidence beam divergence is neglected in the analysis of the peaks' FWHM. The k and l have been used for building the color-maps and the scatter-plots of wavevectors. A review on the analysis method is shown in[204]. The preferential orientations of the puddles, in each ∂k map, have been investigated by calculating the gradient magnitude and direction for each ∂k map (see Fig. 6.6f and Fig. 6.2e). The gradient is calculated in angles measured counterclockwise from the positive x-axis, corresponding to the (100) direction in the maps.

Figure 6.1(b) shows the schematic for the SnXRD setup. A large-scale reciprocal space map is taken by integrating the diffraction patterns over a wide range of incidence angles, measured

in bulk BSCCO single crystals, while in Fig. 6.1(c) we zoom in on the [002] peak with the surrounding LRO and SRO superstructure peaks. We observe that the LRO and SRO peak location along (010) are modulated from spot to spot on the same sample relative to the [002] Bragg peak position. This is shown in Fig. 6.1(d), where we plot the XRD profiles along the (010) axis, integrated along (001) in order to simultaneously study the SRO, LRO, and the [002] Bragg peaks, for two different representative locations on the same single crystal. The scanning has been performed with the crystal at a fixed orientation where the LRO, SRO, and [002] peaks are detected, in the reciprocal space locations as indicated by the labels in Fig. 6.1(c). The LRO and SRO peaks change their wave vector k, while the [002] peak remains inside the experimental pixel resolution $\Delta k_{exp} = 6 \times 10^{-4}$ r.l.u. The SRO shows a broader distribution with its FWHM $\approx$ 0.025 r.l.u., which is about ten times larger than the LRO peak (FWHM $\approx$ 0.0025), as highlighted in the inset of Fig. 6.1(d). The coherence length of the ILMs can be quantitatively estimated by standard crystallographic methods using the FWHM of the satellite diffraction peaks. We have found that the LRO satellite reveals a large in-plane domain size ξ_b^{LRO} above 100 nm while we have $\xi_b^{SRO} = 11$ nm for the SRO satellite. The broader elongation of the SRO peaks occurs also along the (001) axis, indicating the 2D nature of the SRO structures. We do observe that the in-plane domain size ξ_b is larger than the out-of-plane domain size ξ_c for both LRO and SRO modulations. In particular, we find that the out-of-plane SRO domain size ($\xi_c^{SRO} = 4.1$ nm) is slightly larger than the c axis of a single unit cell ($c = 3.1$ nm), suggesting that SRO modulations are similar to stacking faults [179] arising at the interface between different LRO domains. Furthermore, SRO peaks only appear around Bragg peaks with l even, implying that these modulations are out of phase with respect to each other.

We have used SnXRD for visualizing the spatial distribution of the LRO and SRO ILMs in real space. More precisely, we calculated and mapped the LRO and SRO wavevector fluctuations, δk and δl, along the k and l directions, respectively, to visualize ILM textures on the sample. The wavevector fluctuations are defined as $\delta k = k - \bar{k}$ and $\delta l = l - \bar{l}$, where k and l are the wave

vectors of the superlattice peaks along $\hat{k}$ and $\hat{l}$ directions, respectively, measured at each position, and $\bar{k}$ and $\bar{l}$ are the average values of the wavevector measured at all positions. At the same time, we use the wavevector fluctuations δk and δl for the [002] Bragg peak to characterize and map the lattice strain. This will allow us to search for any possible links between ILM textures and the strain map in our study.

Figures 6.2(a) and 6.2(b) show maps of δk for the LRO and SRO. Figure 6.2(c) shows the probability density function (PDF) of the spatial in-plane LRO (red squares), SRO (black circles), and the [002] (dashed line) δk fluctuations. The gray rectangle represents the experimental resolution Δk_{exp} corresponding to a single pixel on the x-ray pixel-array detector. Both the LRO and SRO show similar PDFs, varying in the range of about $0.007 \sim 10\Delta k_{exp}$, larger than the experimental resolution. From the spatial dependence of the SnXRD measurements, we also found that the inhomogeneities of the LRO and SRO modulations in our bulk samples are correlated to each other. This positive spatial correlation can be seen in the scatter plot of δk fluctuations of the LRO and SRO shown in Fig. 6.2(d), where we observe that larger LRO corresponds to larger SRO modulations. This observation indicates a close connection between the distribution of the SRO domains and inhomogeneities of the ILMs. The LRO and SRO spatial patterns do not show significant directionality in texture. Figure 6.2(e) shows the directional distribution of $\nabla \delta k$ for the LRO and SRO, computed from the δk maps. Here we can see that the spatial variations of δk are isotropic for both LRO and SRO.

In the out-of-plane l direction, we find that the δl fluctuations of LRO and [002] remain quite homogeneous within the experimental resolution, $\Delta l_{exp} = 0.005$ r.l.u, while the map of the δl fluctuations of SRO shows larger fluctuations (see Fig. 6.3). Hence the positive correlation between the LRO and SRO inhomogeneities is a 2D structural feature occurring in the $\hat{a} - \hat{b}$ plane of the bulk sample. In the bulk sample both δk and δl fluctuations of the [002] Bragg peak remain below the experimental resolution.

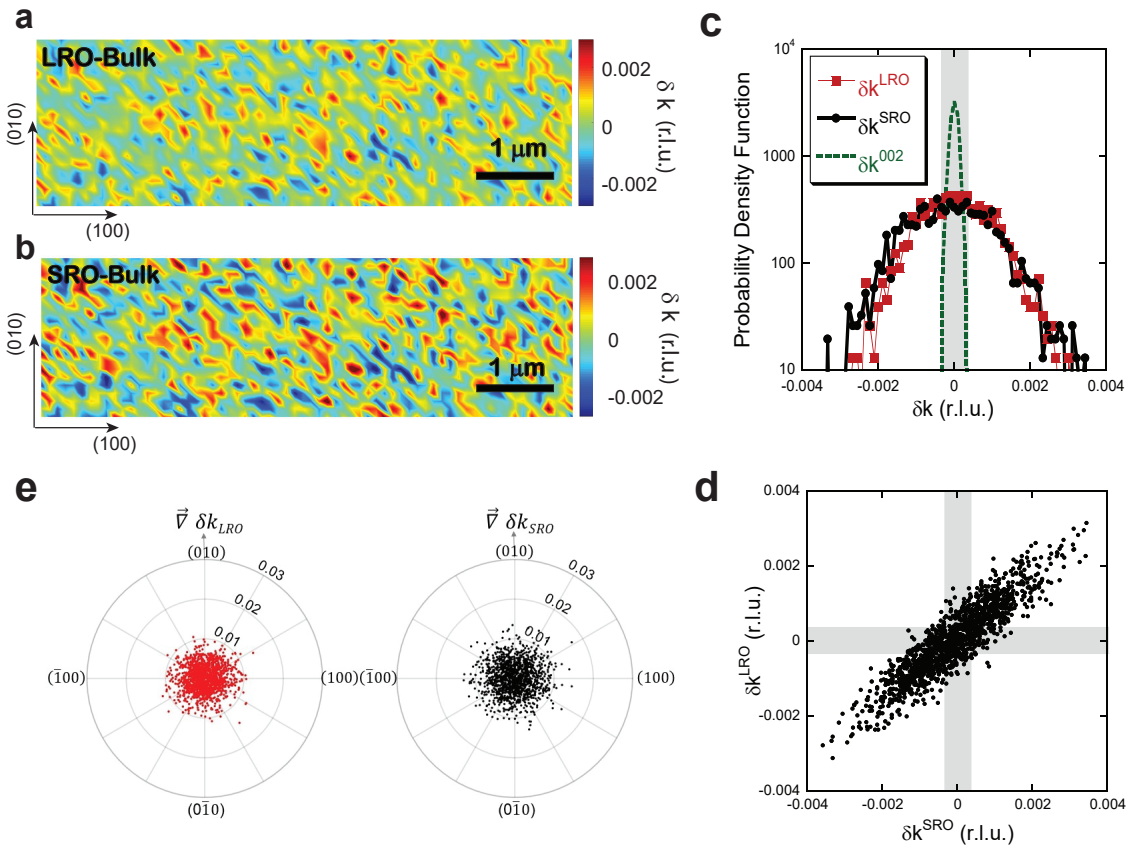

Figure 6.2: Spatial complexity of the incommensurate lattice modulations along k direction in the BSCCO bulk crystal illustrated by scanning nano x-ray diffraction maps showing the spatial variation of the propagation vector δk of (a) LRO and (b) SRO peaks. The red (blue) spots correspond to sample regions with higher (lower) wave vectors with respect to the average of 0.21 r.l.u. (c) Probability density function of δk calculated from the (red full squares) LRO and (black full circles) SRO maps. We report also the variation for the [002] Bragg peak position along the k direction, which remains inside the experimental resolution indicated by shadowed rectangle corresponding to $\Delta k_{exp} = 0.0006$ r.l.u for a single pixel. (d) Scatter plot of LRO peak propagation vector deviations vs SRO peak demonstrating the positive spatial correlation between LRO and SRO modulations. The gray rectangles correspond to the experimental resolution Δk_{exp}. (e) Polar plots of the gradient magnitude vs gradient direction of (left panel) LRO and (right panel) SRO $\nabla \delta k$ calculated from the maps in panels (a) and (b).

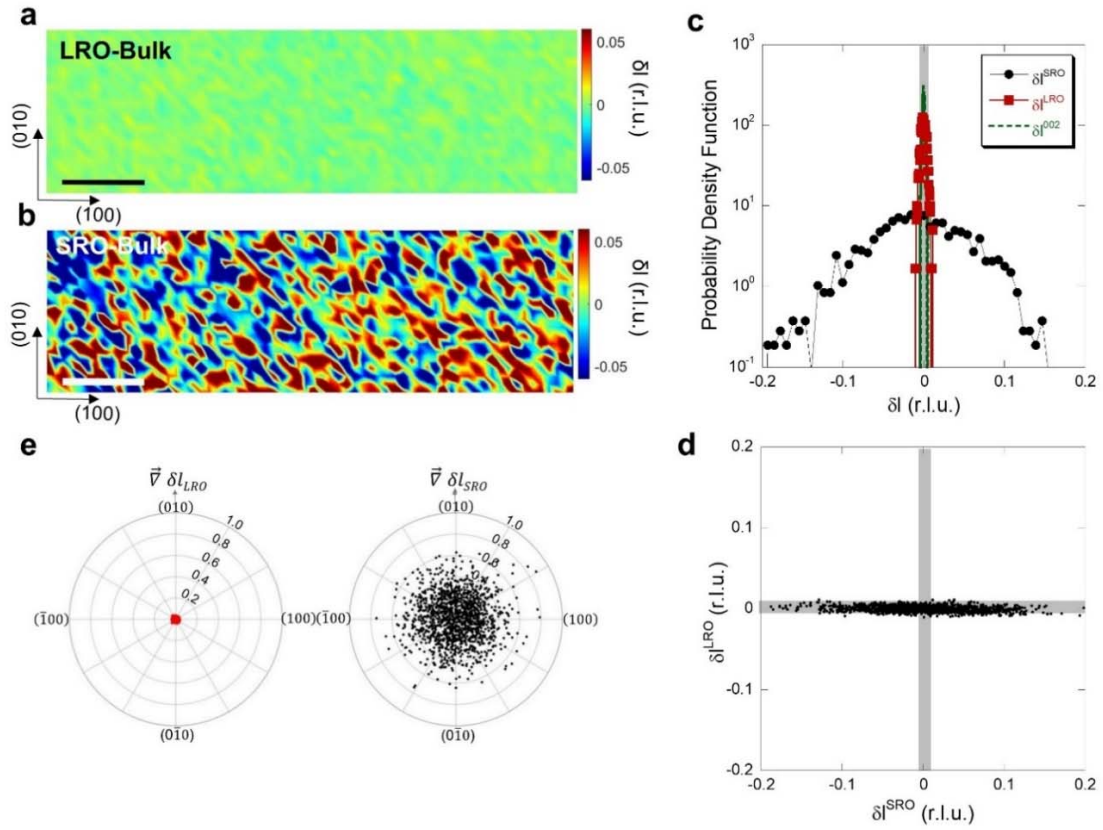

Figure 6.3: Spatial complexity of the incommensurate lattice modulations along l direction. Scanning nano X-ray diffraction maps of the wavevector variation δl of **(a)** LRO and **(b)** SRO peaks along (001) direction, in the bulk sample. The red (blue) spots correspond to sample regions with a higher (lower) wavevectors with respect to the average of 1 r.l.u. The error bar corresponds to 1 μm. c. Probability density function of δl calculated from the (red squares) LRO and (black circles) SRO maps. The variation for the [002] Bragg peak along the (001) direction remains inside the experimental resolution indicated by shadowed rectangle corresponding to $\Delta l_{exp} = 0.005$ r.l.u for a single pixel. d. Scatter plot of LRO peak propagation vector deviations versus SRO peak. The shadowed rectangles correspond to the experimental resolution Δ_{exp}. e. Polar plots of gradient magnitude versus gradient direction calculated for the maps of LRO and SRO shown in panels (a) and (b). The rotation in gradient calculations is counterclockwise and the positive x axis is along the indicated (100) direction. We do not observe any preferential orientation of δl, neither for the LRO and SRO modulations

6.2 Imaging Incommensurate Lattice Modulations in a 2 Unit Cell Crystal

Now we move to exploit the spatial imaging capability of the SnXRD to investigate the spatial distribution of lattice modulations in atomically thin BSCCO crystals. In this experiment we employ a two-unit-cell (u.c.) thick (6 nm thick in atomic force microscope measurements) BSCCO sample about 50 μm in lateral size, obtained by mechanical exfoliation. This crystal was subsequently encapsulated and protected by atomically thin hexagonal boron nitride (*h*-BN) crystals. For atomically thin BSCCO crystals, protecting the crystals with chemically inert *h*-BN is necessary to form a van der Waals (vdW) protective layer that prevents degradation of the samples. After creating the hBN/BSCCO heterostructure on the SiO_2/Si substrate, we also deposit gold markers [see Fig. 6.4(b)] necessary for alignment with the hard x-ray nanobeam's region of interest. Figure 6.4(c) shows the reciprocal space map around the [002] peak collected during the rocking scan. Despite the 2-u.c. thickness of the atomically thin crystals, both the SRO and the LRO satellites are detectable [see Fig. 6.4(c)], although their intensity results are reduced in comparison with the bulk sample. This observation is in sharp contrast to the previous XRD experiments performed on the unprotected BSCCO flakes where no SRO peaks were detected[205], suggesting that indeed the *h*-BN encapsulation is necessary for protecting the chemical integrity of the atomically thin BSCCO samples.

Figure 6.4(d) shows the line shape of the LRO and SRO profiles along the (010) direction. The XRD profiles measured at different sample spots show significant differences in width, position, and amplitude. We find that the LRO domain size, ξ^{b}_{LRO}, decreases in atomically thin crystals. At the 2D limit, ξ^{b}_{LRO} becomes equal to 15 nm, which is an order of magnitude smaller than the value of $\sim$ 100 nm obtained in the bulk sample. It is interesting to note that the domain size for the SRO decreases only slightly from 11 nm in the bulk to 7 nm in the 2-u.c. atomically thin crystals (see figure 6.5). As the thickness of the sample is only 6 nm, the *c*-axis structural coherence lengths are strongly reduced along the (001) direction: ξ_c becomes about 1 and 2.5 nm for the SRO and

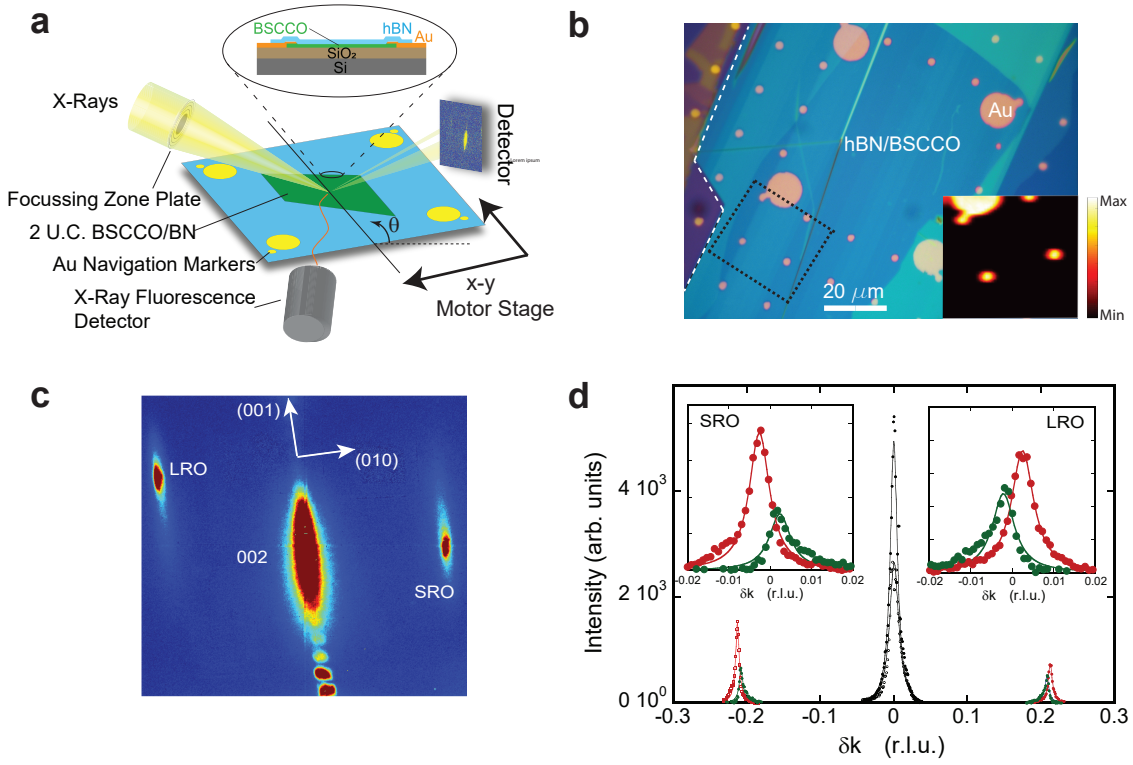

Figure 6.4: Scanning nano x-ray diffraction of a BSCCO VdW heterostructure. (a) The x-ray beam is focused on an atomically thin VdW BSCCO heterostructure. We used a similar experimental setup of Fig. 1(b), adding an x-ray fluorescence detector to locate the sample using gold markers deposited on the top of the VdW heterostructure. The x-ray detector records the diffraction pattern in the illuminated sample area from a cuprate crystal 6 nm thick (2 u.c.). (b) Optical image showing the gold marker array deposited on top of the vdW heterostructure. Inset shows a typical fluorescence map of the area in dashed box. (c) A portion of $b^* - c^*$ diffraction pattern where the [002] peak and the superlattice reflections for LRO and SRO incommensurate modulation are indicated. (d) Two typical LRO and SRO peaks along the $\hat{k}$ direction, collected at two different places on the same heterostructure. The insets highlight the δk fluctuations for both LRO and SRO modulations.

LRO modulations, respectively, as compared to 4 and 94 nm in the bulk sample.

Spatial XRD imaging of the SRO/LRO in the 2-u.c. sample reveals the effect of the reduced dimensionality to the ILMs. Figures 6.6(a) and 4(b) show spatial maps of δk for LRO and SRO wave vectors, where a different texture appears in comparison with those of the bulk sample. In order to quantify these textures, we have calculated the probability density function, the spatial

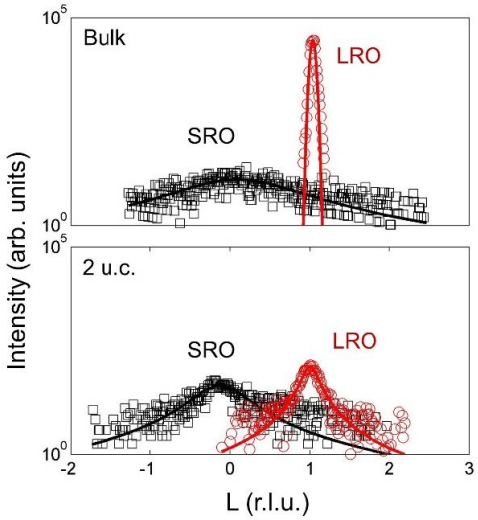

Figure 6.5: Profiles of the LRO and SRO wavevectors along (001) in the bulk crystal and in 2 u.c. thin flake. Typical LRO (red circles) and SRO (black squares) peaks along the (001) direction measured in the bulk (upper panel) and in the thin flake (lower panel).

correlations, and the gradient of the maps of ∂k and ∂l fluctuations. Although fluctuations for the LRO and SRO show a similar range to what is found in the bulk [Fig. 6.2(c)], the corresponding probability density function deviates strongly from the Gaussian-like distribution characteristic of the bulk. The spatial correlations between the LRO and SRO, shown in Fig. 6.6(d), become anticorrelated, in sharp contrast to observed correlations in the bulk crystal. We also observe directional textures of the fluctuation pattern in the 2-u.c. flake that is absent in the bulk crystal. Unlike the bulk sample [Fig. 6.2(e)], Fig. 6.6(e) shows that the angular-dependent $\nabla\partial k$ displays a preferred direction near -90°, corresponding to the (0-10) direction, where the ∂k fluctuations are larger. The negative spatial correlations between the LRO and SRO and the directional textures have also been found along the (001) direction (see Fig. 6.7). The different correlations between the SRO and LRO, from the bulk to the atomically thin crystals, are even more evident by visualizing in-plane ∂k, as a function of out-of-plane, ∂l fluctuations (see Fig. 6.8), suggesting a different correlated disorder[206] with an emerging spatial pattern appears in atomically thin

BSCCO samples.

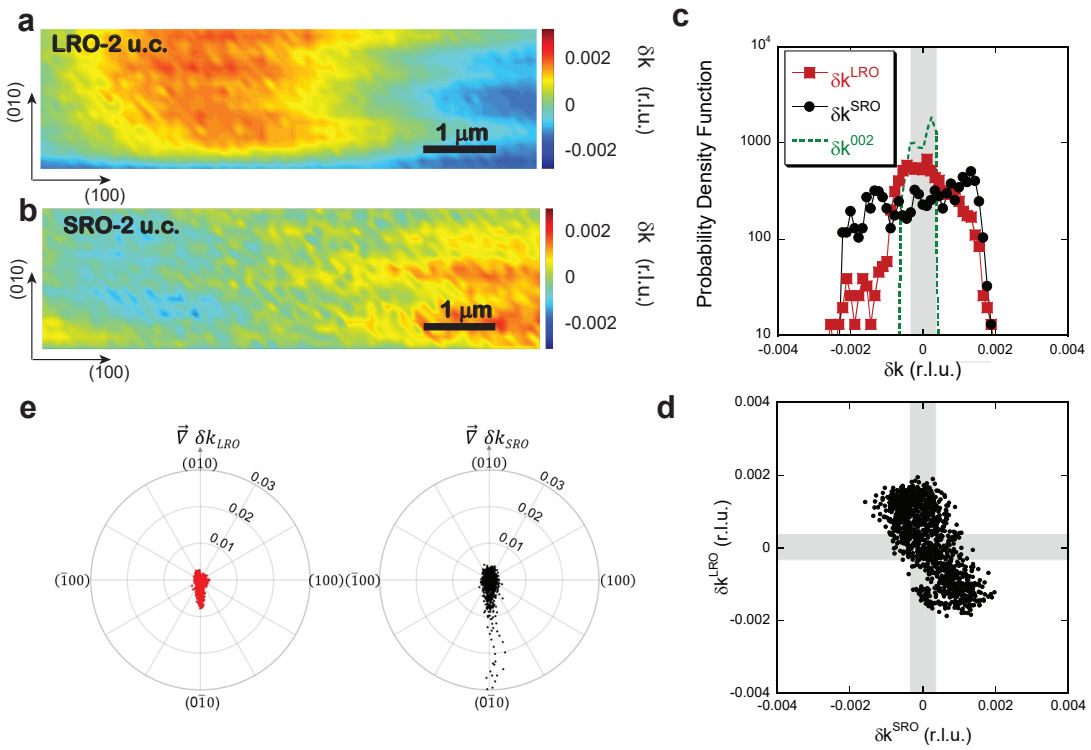

Figure 6.6: Spatial complexity of the incommensurate lattice modulations in the VdW heterostructure along *k*. Scanning nano x-ray diffraction map of a region of interest showing the spatial variation along the (010) direction, δk, of the LRO peak (panel a) and the SRO peak (panel b). The red (blue) spots correspond to sample regions with a higher (lower) propagation wave vector with respect to the average value of 0.21 (green color). (c) Probability density function of δk calculated from the LRO (red squares), the SRO (black circles), and the [002] peak (dashed green line) maps. In this case, the variation of the [002] peak exceeds the experimental resolution, Δk_{exp}, indicated by the shadowed area. (d) Scatter plot of δk for the (black circles) LRO vs SRO showing an anticorrelation between LRO and SRO. The shadowed rectangles correspond to the experimental resolution. (e) Polar plots of the gradient magnitude vs gradient direction of (left panel) LRO and (right panel) SRO calculated from the δk maps shown in panels (a) and (b). In this case we observe preferential directions of the grain arrangement in the δk maps along the (0-10) direction.

A possible explanation for the origin of these differences can be that the misfit strain between the Bi-O rock salt and the Cu-Sr-Ca perovskite layers [193,194,195] could change at a reduced dimensionality. Indeed, we find that the variation of the [002] peak is slightly larger than the experimental resolution Δk_{exp}, as shown in Fig. 6.6(c). This result indicates that the intrinsic strain of

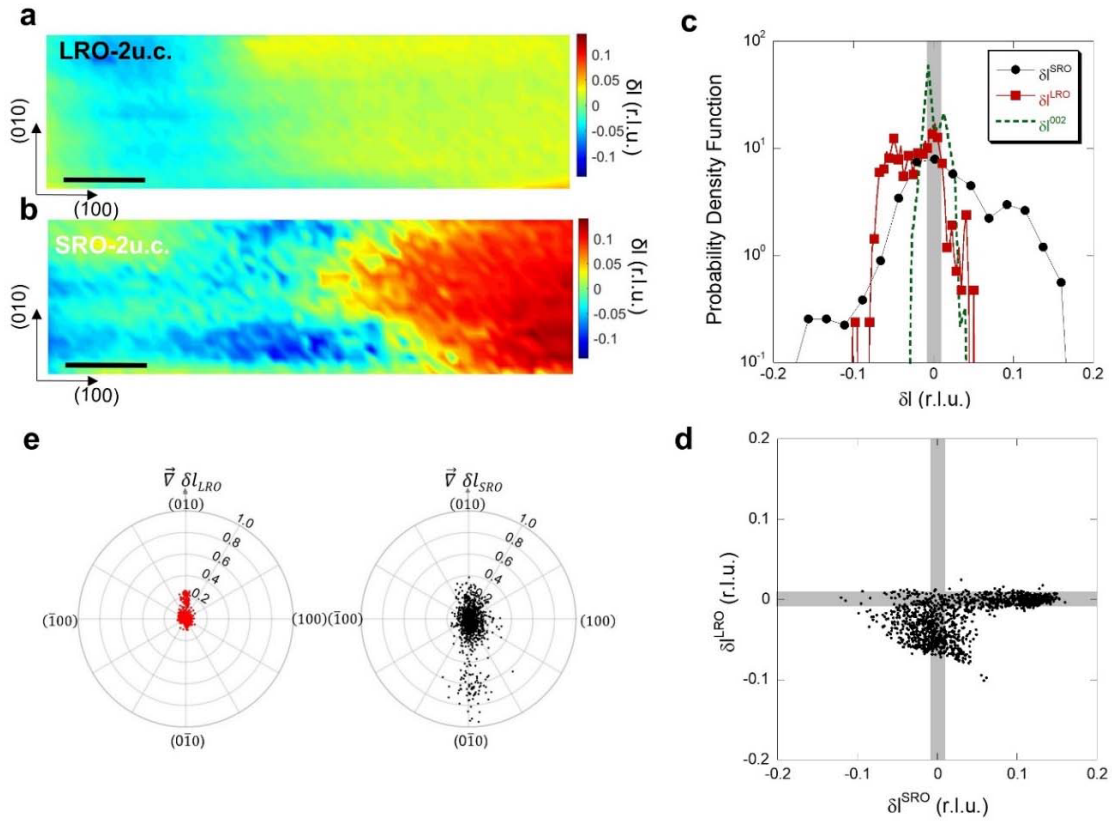

Figure 6.7: Spatial complexity of the incommensurate lattice modulations in the VdW heterostructure along l**.** Scanning nano X-ray diffraction map of a region of interest, showing the spatial variation of δl, for the LRO peak **(a)** and the SRO peak **(b)** in the vdW heterostrucutre. The red (blue) spots correspond to sample regions with a higher (lower) propagation wavevector with respect to the average value of 1 r.l.u. **c.** Probability density function of δl calculated from the LRO (red squares), the SRO (black circles) and the [002] peak (dashed green line) maps. In this case, the variation of the 002 peak exceeds the experimental resolution indicated by the shadowed area. **d.** Scatter plot of δl for the (black circles) LRO versus SRO, showing a negative correlation between LRO and SRO. The shadowed rectangles correspond to the experimental resolution $\Delta l_{exp} = 0.005$ r.l.u. **e.** Polar plots of gradient magnitude versus gradient direction of the LRO and SRO calculated from the δl maps in (a) and (b) panels. In this case we observe preferential directions of the grains arrangement in the δl maps along the (010) direction for the LRO (left panel) and along (0-10) for the SRO (right panel) direction.

an atomically thin crystal plays a role in the different spatial arrangements of the incommensurate lattice modulations. The fluctuations of the [002] peak exceed the experimental resolution Δk_{exp} just for the 2-u.c. thin sample. This behavior is accentuated along the (001) direction, where

the [002] peak is clearly larger than Δl_{exp} (see Fig. 6.7). This unusual distribution might indicate some structural instability and the related criticality[99,103,65] in the flake and calls for a further thorough investigation.

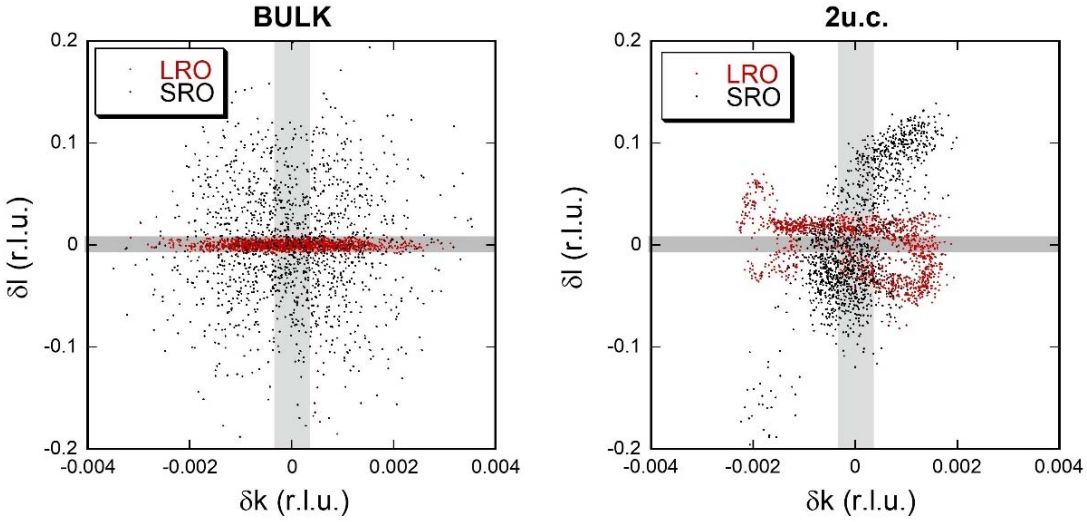

Figure 6.8: Correlated disorder arising towards the atomic scale Scatter plot of δl versus δk for (red dots) LRO and (black dots) SRO. The shadowed rectangles correspond to the experimental resolution Δl_{exp} and Δk_{exp} along the $\hat{l}$ and $\hat{k}$ directions

6.3 Conclusion and Outlook

In summary, highly resolved scanning synchrotron x-ray diffraction measurements around the [002] Bragg peak on both a bulk sample and an atomically thin BSCCO van der Waals heterostructure has enabled us to collect simultaneously (i) SRO, (ii) LRO, and (iii) [002] Bragg peaks. We have visualized the spatial distributions of the LRO and SRO wave vectors by displaying variations of δk and δl, along the $\hat{k}$ and $\hat{l}$ direction, respectively. At the same time, we have found variations of the wave vector of the [002] Bragg peak to characterize and visualize the lattice strain maps. Our results shown in Fig. 6.2(c) and Fig. 6.3 reveal that the bulk sample

does not experience a significant strain since the variation ∂k and ∂l of the (002) peak are both below the experimental resolution. In this case, the LRO and SRO textures comprise randomly arranged puddles at the nanoscale, as shown in the maps in Figs. 6.2(a) and 6.2(b), respectively, with no preferential direction. On the contrary, the appreciable lattice strain in the 2-u.c. sample is seen when both ∂k and ∂l become larger than the experimental resolution. In this case, the LRO and SRO modulations form spatial patterns. The larger strains indicate more intense electron-lattice interactions; therefore one can expect that in this case, the lattice modulations are accompanied by the corresponding charge density modulations (or charge-density waves), which arise to maintain neutrality. Then the spatial charge modulations should form the charge modulation puddles on comparable mesoscales. These are mapped in Figs. 6.6(a) and 6.6(b). The influence of the mesoscale strains on the mesoscale texture can be depicted by inspecting spatial correlations between the textures of the LRO and the (002) Bragg peak along both ∂k and ∂l directions in Fig. 6.9. In the 2-u.c. sample we observe positive correlations between ∂k of (002) and LRO peaks and somewhat larger negative correlations between ∂l of (002) and LRO modulation peaks. This is expected for multilayered structures where larger fluctuations occur in the out-of-plane direction. In our case, since the ∂k fluctuations of the LRO are anticorrelated with ∂k of the SRO [Fig. 6.2(d)], there exists a weak positive correlation between the in-plane strain and the SRO modulation, see Fig. 6.9a.

The observed modulations, which appear to be in concert with the findings of Yu et al.[25], stem from the misfit strain arising from the mismatch between the substrate and thin BSCCO flakes. These inhomogeneous ILMs may have a profound effect on the electronic properties of heterostructures. In particular, one may develop a theoretical framework to describe the interaction between transport carrier and inhomogeneous ILMs using a similar theoretical technique adopted for the inhomogeneous charge-density waves interacting with the carriers[204]. Potentially, this approach can explain the striking observation that the electronic mobility in the atomically thin films is reduced, while the Hall resistance remains intact and does not change much as

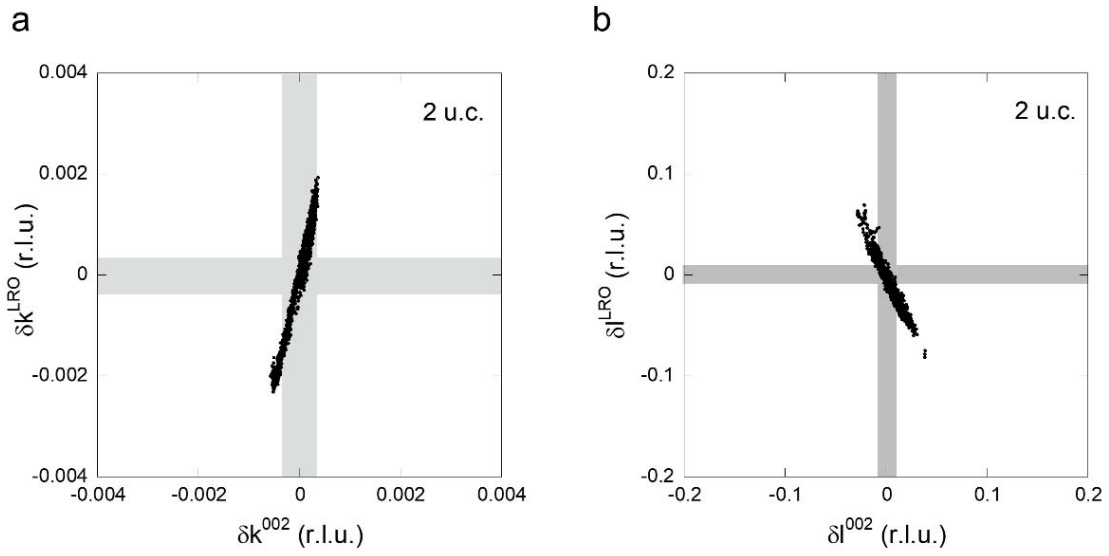

Figure 6.9: Correlations between strain and ILMs at the atomical scale length. (a.) Scatter plot of fluctuations δk of LRO versus δk of (002). (b) Scatter plot of fluctuations δl of LRO versus δl of (002). The shadowed rectangles correspond to the experimental resolution Δk_{exp} and Δl_{exp} along the $\hat{l}$ and $\hat{k}$ directions.

compared to the bulk value[26]. Finally, our findings indicate that a fine-tuning of the strain can be used to control the spatial correlations of the ILMs, providing a route for investigating and controlling correlated disorder[171] and its relation to electronic functionality in 2D high-temperature superconductors.

The Taylor expansion is how all of physics work.

Erich Poppitz

7

Sign Reversing Hall Effect in Atomically Thin High Temperature Superconductors

We developed novel techniques to fabricate atomically thin $Bi_{2.1}Sr_{1.9}CaCu_{2.0}O_{8+\delta}$ van der Waals (vdW) heterostructures down to two unit cells while maintaining a transition temperature T_C close to the bulk, and carry out magnetotransport measurements on these vdW devices. We find a double sign change of the Hall resistance R_{xy} as in the bulk system, spanning both below and above T_C. Further, we observe a drastic enlargement of the region of sign reversal in the temperature-magnetic field phase diagram with decreasing thickness of the device. We obtain quantitative agreement between experimental $R_{xy}(T, B)$ and the predictions of the vortex dynamics-based description of Hall effect in HTS both above and below T_C.

7.1 Introduction

Tunable van der Waals (vdW) structures based on atomically thin superconducting $Bi_{2.1}Sr_{1.9}CaCu_{2.0}O_{8+\delta}$ (BSCCO) crystals enables exploring unconventional electronic properties of high temperature superconductors (HTS)[36]. One of the most insightful tools to study properties of electronic systems is the Hall effect. However, the behavior of Hall resistance in HTS, in particular its sign change, remains poorly understood. As temperature, T, decreases through the fluctuation region approaching the transition temperature T_C, the Hall resistance decreases and changes its sign relative to that of the normal state. Then $R_{xy}(T)$ reverses sign again before vanishing at low temperatures [207,208].

A rich theoretical lore attributes the Hall anomalies to either vortex pinning [209], details of the vortex core electronic spectrum [210,211], hydrodynamic effects [212], superconducting fluctuations [213,214,215], Berry phase [216], and charges in the vortex core [217]. However, neither the explanation nor the consensus of the Hall behavior in the entire temperature range was achieved. A comprehensive explanation of the Hall sign reversal appeared in [218], which completely took into account both topological and normal excitation scattering effects, and especially the fact that the density of normal excitations at the vortex core differs from that far from the vortex. The results of [218] established that the sign-reversed Hall effect occurs in the temperature range where contribution from the vortex motion dominates over the effects from normal excitations and is controlled by the excess charge at the vortex core and the magnitude of the parameter $\Delta\tau/\hbar$, where $\Delta(T)$ is the superconducting gap and τ is the scattering time of normal quasiparticles.

In this chapter, we report fabrication of superconducting (SC) atomically thin BSCCO crystals with strongly enhanced fluctuation effects and their magnetotransport properties. We observe Hall sign reversal which smoothly spans the superconducting transition, and persists both deep into the superconducting state and 5K above T_C. We present quantitative description of the observed phase boundary separating the normal and sign-reversed Hall domains [218] in terms

of vortex dynamics in the entire temperature interval both below and above T_C, revealing a deep connection between vortex-like excitations above T_C [219,220] and superconducting fluctuations.

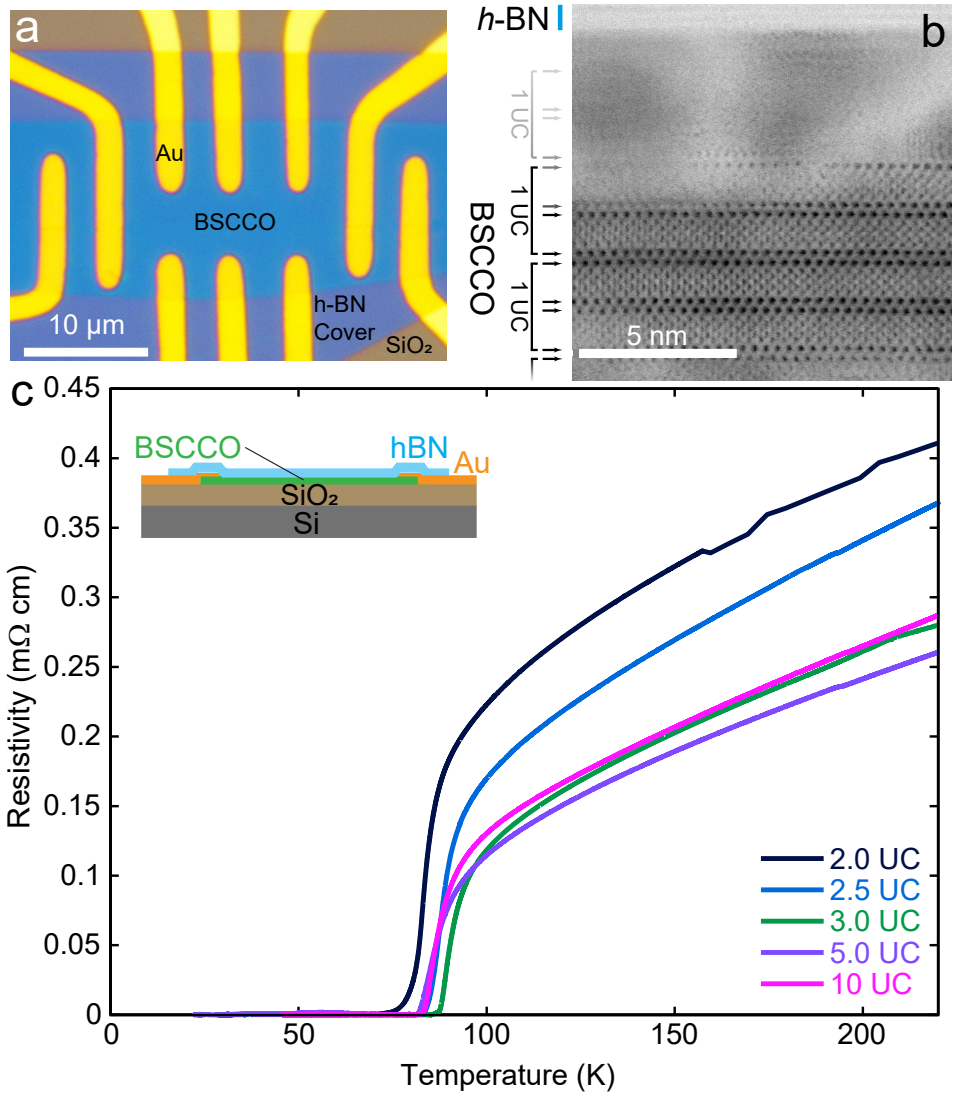

Figure 7.1: Van der Waals BSCCO device. a. Optical image of Hall bar device, showing BSCCO with contacts and hexagonal boron nitride (*h*-BN) cover, as drawn in the inset below. b. Cross-sectional view of a typical device in scanning TEM. Columns of atoms are visible as dark spots. Black arrows point to location of bismuth oxide layers (darkest spots), while gray arrows show their extrapolated positions. c. Resistivity as a function of temperature for vdW devices of different thickness.

7.2 Resistance and the Superconducting Transition Temperature

We prepare our few unit-cell (UC) thick BSCCO by mechanically exfoliating optimally doped $Bi_{2.1}Sr_{1.9}CaCu_{2.0}O_{8+\delta}$ in argon filled glovebox. After conventional nano-fabrication steps, BSCCO typically becomes insulating [128] due to chemical degradation [113] and oxygen escape [104]. We have developed a high-resolution stencil mask technique (See Chapter 4), allowing us to fabricate samples entirely in an argon environment without exposure to heat or chemicals, and subsequently sealed with a top hexagonal boron nitride (h-BN) layer. Figure 7.1a and b shows our typical Hall bar and a cross-sectional scanning TEM image of our vdW heterostructure, where dark spots are individual columns of atoms. The darkest of these are bismuth (arrows). While the outermost layers of BSCCO became amorphous, inner layers are left pristine, and retain T_C close to the bulk value. The amorphous outer layers are likely the result of water vapor traces leaking through the h-BN/SiO_2 interface, and constrains us to devices above 2 UC.

Figure 7.1(c) shows the resistivity ρ as a function of temperature T for BSCCO devices between 2 - 10 UC. We find that at a given temperature T, resistivity ρ increases as the thickness of the sample d decreases. We have normalized our resistance data with the atomic force microscopy (AFM) thickness, which is sensitive to the highly resistive amorphous surface layer. The $\rho(T)$ dependence is linear in the normal region, consistent with BSCCO near optimal doping [221] and exhibits a SC transition, at temperature slightly lower than the bulk one [222].

To describe the SC transition in $\rho(T)$ and determine the transition temperature T_C, we employ the framework of superconducting fluctuations (SF) [223,224,225], accounting for all fundamental SF contributions to conductivity: Aslamazov-Larkin, the SF change in the density of states (DOS) of normal excitations, and the dominant Maki-Thompson contribution [225,226], using both T_C and the pair-breaking parameter $\delta = h/16k_BT\tau_\varphi$ as fitting parameters. The phase-breaking time is assumed to be $\tau_\varphi \sim T^{-1}$ [227], see details in Appendix A. For all samples, the extracted T_C (given in Appendix A) is very close to the temperature of the inflection point, i.e. the temperature where

dR/dT is maximal [226,228], and lies at the foot of $\rho(T)$. As a consistency check, numerous comparative studies [229,230] of bulk HTS demonstrated that T_C extracted from magnetic susceptibility agrees with the T_C from the inflection point.

Figure 7.2(a) presents the Hall data for a 2 UC device (solid lines), and, as usual, the odd component of $R_{xy}(B)$ is shown in order to eliminate effects from device geometric imperfections. In the normal state far above T_C ($T \geq 100$ K), the Hall resistance R_{xy} is linear in applied magnetic field B. Figure 7.2(b) shows the quantity $(e\, dR_{xy}/dB)^{-1}$ measured at 100 K, which scales linearly with d, implying an excellent oxygen dopant retention in each CuO_2 plane, despite the fact that mobile oxygen dopants [104] escape from our crystals over time. The 3 UC sample, the only device fabricated and cooled down in the same day, contains a higher carrier density, which agrees with the slightly increased T_C (Fig. 7.1(c)).

7.3 Hall Sign Reversal

The Hall mobility $\mu_H = R_{xy}d/B\rho_{xx}$ is shown in Fig. 7.2c. Below 5 UC, μ_H decreases with d, due to the increasing ratio of highly resistive (yet non-insulating) surface layers compared to pristine interior layers (see Fig. 7.1b), both of which contribute to the Hall and resistivity measurements in parallel. All our samples exhibit the trend $\mu_H \sim T^{-1}$ for $T \gg T_C$, suggesting that the normal carrier momentum relaxation time is $\tau_p \sim T^{-1}$ regardless of d.

Approaching T_C, $R_{xy}(B)$ becomes nonlinear (Fig. 7.2a). The first sign reversal is observed about 5K above T_C, up to 95K for our most highly doped sample (Fig. 7.2a and figure A.2). The dip in $R_{xy}(B)$ becomes increasingly pronounced as temperature decreases and the region of negative sign extends from zero field to $B = 4.7$ T at about $T = 75$ K. Upon further cooling, $R_{xy}(B)$ flattens again and the B-interval of the negative R_{xy} shrinks, until completely vanishing at $T \approx 60$ K (see Appendix A.5). Then $R_{xy}(B)$ remains positive at all fields, until it disappears into the noise at $T \approx 40$ K.

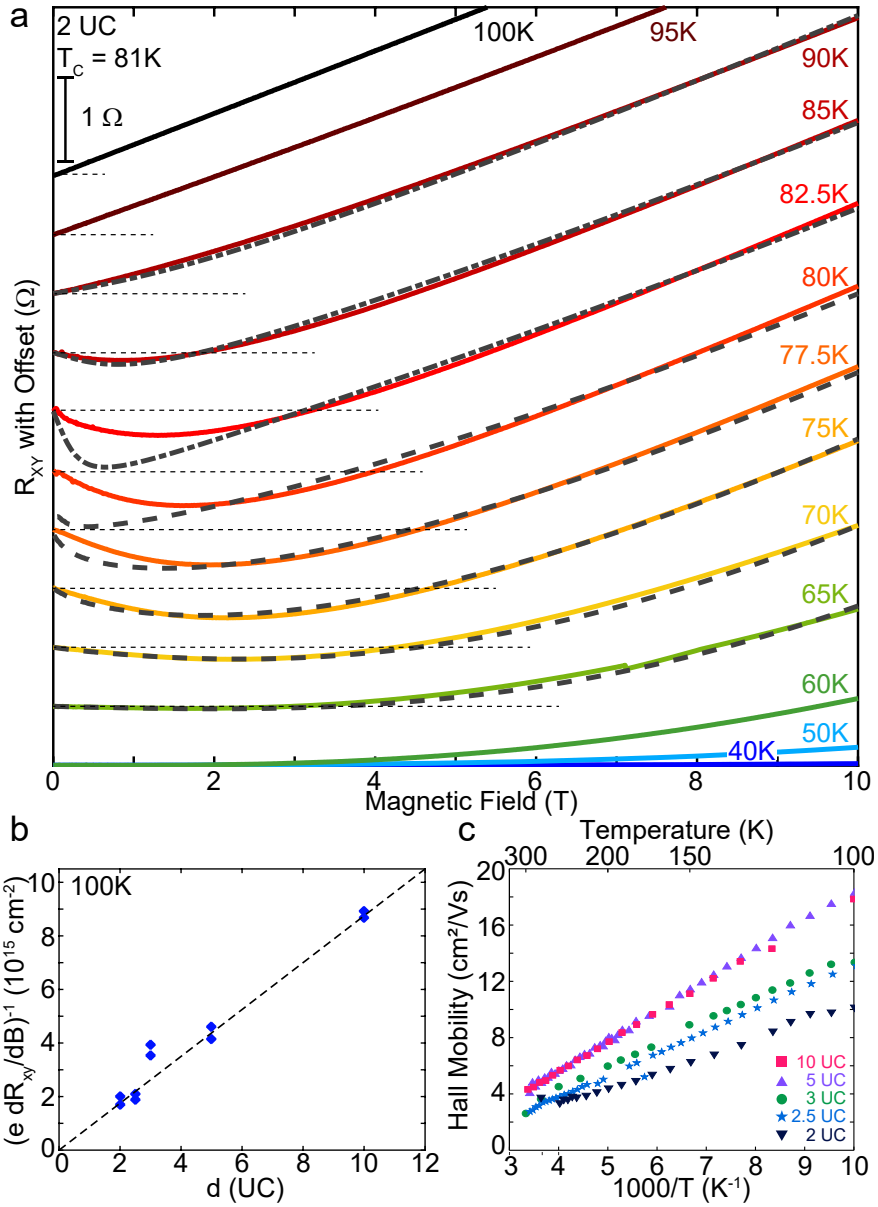

Figure 7.2: Hall effect measurements a. Hall resistance for a 2 UC sample. The curves are vertically shifted for clarity, the horizontal dashed lines mark $R_{xy} = 0$. Below 60K, the Hall effect has the same sign as in the normal state. Above 60K the sign reversal appears at magnetic fields $B < 5$ T. Dashed and dash-dot lines show fits to the data (solid lines) b. Inverse Hall resistance increases linearly with sample thickness in our devices, demonstrating good oxygen dopant retention down to 2 UCs. Data taken at 100K. c. Device mobility increases as samples become thicker, eventually saturating at 5 UC.

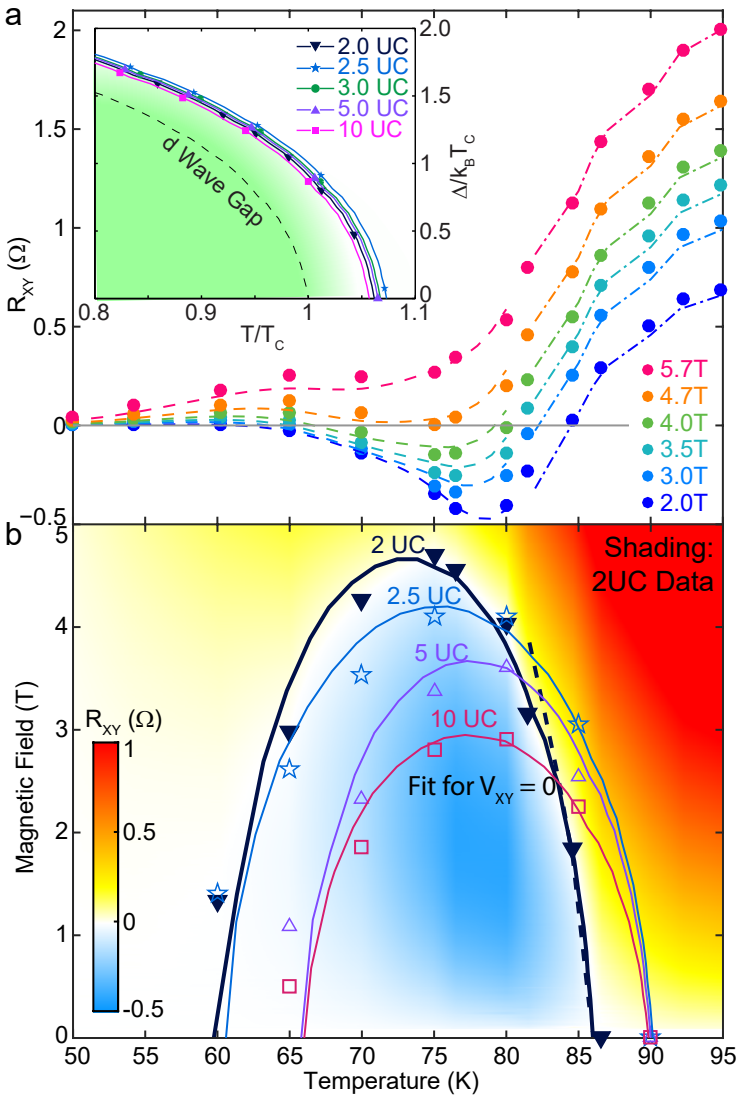

Figure 7.3: The double sign change. a. Temperature dependencies $R_{xy}(T)$ at fixed magnetic fields for the 2UC device. Fits above (dash-dot) and below (dashed lines) T_C are superimposed on experimental data (symbols). Inset: Superconducting gap extracted from fits for all samples using Eq. (7.1). T_C is the temperature extracted from analysis of $R_{xx}(T)$ in the framework of superconducting fluctuations (SF) b. The Hall sign reversal phase diagram. Shading shows Hall resistance $R_{xy}(B, T)$ for a 2UC device with T_C=81.5 K. Blue region shows the area of negative Hall resistance. Symbols show the locus $R_{xy} = 0$ for different thicknesses, and the lines are generated from fits to $R_{xy} = 0$ using Eq. (2)[218] (solid) and using Eq. (3) (dash). As thickness decreases, the Hall sign reversed region becomes larger.

The temperature evolution of $R_{xy}(T)$ at fixed B (Fig. 7.3a) highlights a double sign reversal temperature interval. Figure 7.3b summarizes regions of sign reversal for the samples with similar doping and different thickness d. The $R_{xy}(T,B) < 0$ domain grows with decreasing d, while extending across and above T_C in all our samples.

The Hall sign reversal in high-T_C is usually well pronounced in the mixed state below T_C extracted from the SF framework, the temperature where Cooper pair lifetime becomes infinite [221,231]. In conventional superconductors, Hall sign reversal usually occurs in the Gaussian fluctuations regime at $T > T_C$ [232,233]. However, there are experiments hinting at Hall sign reversal occurring slightly above T_C in 100-400 nm thick cuprate films [234,235]. In our atomically thin BSCCO flakes, the Hall sign reversal region persists well above T_C (by 5K). Importantly, in our 3 UC device with the highest T_C, sign reversal persists up to 4.1 T at the onset $T_C \approxeq 90K$ of our bulk crystal[222], and up to $T_{HSR} \approx 95$ K (Appendix A.2).

That Hall resistance $R_{xy}(T)$ does not exhibit any drastic changes when crossing T_C (Fig. 7.3) suggests the possibility of a unique universal description of the Hall effect over the entire experimental range of temperatures and magnetic fields. Such a universal description is provided by the time-dependent Ginzburg-Landau (TDGL) equation [208]. In the fluctuation regime at $T \gtrsim T_C$, where fluctuational order parameter is small, TDGL can be linearized. In this Gaussian approximation, the Hall resistance can be calculated with [215] accounting for SF effects. At $T < T_C$ the electromagnetic response of superconductors is governed by vortex dynamics. In this regime, the GL functional can be expressed in terms of collective variables representing topological vortex excitations. As observed in [207], it is the change from normal carrier- to the flux flow-dominated transport that causes the sign reversal in Hall resistance. Since the sign reversal is observed above T_C, one expects that the expansion of the TDGL with respect to vortex topological excitations will provide an adequate description of the Hall effect at temperatures from $T \gtrsim T_C$ down to

zero. This program was realized in [218], where the Hall conductivity was derived as:

$$\sigma_{xy} = \frac{\Delta^2 \cdot n_0 \cdot ec}{E_F^2 \cdot B}[(\tau\Delta/\hbar)^2 g - \mathrm{sign}(\delta n)] + \sigma_{xy}^n(1-g)\,. \tag{7.1}$$

Here n_0 and n_∞ are the normal carrier density inside and outside the vortex core respectively, and $\delta n = n_0 - n_\infty$ is the excess charge inside the vortex; τ is the relaxation time of the normal carrier in the vortex core; and parameter g expresses the SC fraction of the carriers. The second term in the rhs of Eq. (7.1) ensures a smooth transition to Hall conductivity dominated by normal carriers. We consider a two-fluid model of a d-wave symmetry superconductor[66] so that $g(T) = 1 - (T/T_C)^2$. Where the value of T_C was previously determined from the analysis of $R_{xx}(B, T)$ with SF description.

This result makes apparent that the physical origin of the Hall effect sign change is the excess charge δn of the vortex core, which is of order $n_0(\Delta/E_F)^2$ [218,235]. The sign of the vortex contribution is controlled by the relation between $\mathrm{sign}(\delta n)$ and $\tau\Delta$. In the regime $T < T_C$, this empirically fixes $\mathrm{sign}(\delta n) = 1$. Then, the first term in Eq. (7.1), the vortex core contribution σ_{xy}^{vc}, can be negative as $\Delta(T) < \hbar/\tau$. Furthermore, we note that $\sigma_{xy} \sim B^{-1}$ while $\sigma_{xy}^n \sim B$. Therefore, the total Hall sign reversal is expected at low magnetic fields, where negative vortex contribution σ_{xy}^{vc} dominates the positive normal carrier contribution σ_{xy}^n.

Using Eq. (7.1), we describe the phase boundary of the Hall sign reversed region in Fig. 7.3(b) for all the samples under study. The sign reversal locus, $R_{xy}(T, B) = 0$, follows from Eq. (7.1) and is defined by the relation:

$$B^2 = \left(\frac{\Delta}{E_F}\right)^2 \frac{n_0 c}{S_{xy}^n} \frac{[(\Delta\tau/\hbar)^2 g - 1]}{1-g}, \tag{7.2}$$

Where we estimate the normal contribution σ_{xy}^n using the empirical observation $\sigma_{xy} = S_{xy}^n(T) \cdot B$ in the normal state far enough from T_C, where $S_{xy}^n(T) \propto T^{-2}$ (see Fig. A.3), we extrapolate this

dependence to low temperatures. Then, we fit our data shown in Fig. 7.3(b) with Eq. (7.2), using as fitting parameters τ and n_0/E_F^2 (numerical values of all parameters are given in Table A.1). We obtain the relaxation rate of the normal carriers in the vortex core $\tau \approx 0.08$ ps. This agrees with the quasiparticle lifetime estimated from the scanning tunneling spectroscopy of the vortex cores in BSCCO [236] observing normal quasiparticle excitations at $E \approx 7$ meV, giving the crude estimate $\tau \cong \hbar/E \approx 0.1$ ps. The value $n_0/E_F^2 \approx (1-2)\cdot 10^{21}$ cm$^{-3}\cdot$eV^{-2} is in satisfactory agreement with the widely accepted value $n_0 \approx 10^{21}$ cm^{-3} in cuprates [237] and with the fact that E_F of cuprates is often an order of magnitude larger than the superconducting gap $\Delta(0)$ [238] which is $\Delta(0) \approx 0.02$ eV in our case. For the temperature dependence $\Delta(T)$, we take the temperature dependence of the d-wave gap (with $\Delta(0)/k_B T_{HSR} = 2.15$) [239] where T_{HSR} is the upper temperature of the onset of the Hall sign reversal (see Table in SI). The d-wave description of $\Delta(T)$ is also supported by STM measurements on BiO terraces in BSCCO [240], although tunnel spectra of exposed CuO_2 terraces suggests a nodeless SC gap [240,241]. Temperature dependencies of superconducting gap $\Delta(T)/T_C$ *vs.* T/T_C are shown in inset of Fig. 7.3a for all samples. Note that T_{HSR} determined from our fits appeared to be higher than T_C,implying nonzero $\Delta(T_C)$, which is in agreement with experimental observations in tunneling [242] and in angle-resolved photoemission spectroscopy (ARPES) [78].

Equation (7.2) for the dome-shaped sign reversal phase boundary correctly describes the sign reversal enhancement as samples become thinner (Fig.7.3). As the mobility μ_H decreases with thickness (Fig. 7.2c), σ_{xy}^n is suppressed in turn. Since μ_H is in the denominator in Eq. (7.2), the decrease of μ_H leads to enhancement of dome size. In other words, the contribution from topological excitation has more effect on the conductivity σ_{xy} when the normal component σ_{xy}^n decreases (see Eq. 7.1).

The curve $R_{xy}(B, T) = 0$ defined by Eq. (7.2) demonstrates an excellent agreement with the experimental data shown in Fig. 7.3b both for $T < T_C$ and for $T > T_C$. Using the same fitting parameters we compare the whole R_{xy} evolution with the vortex expansion of the TDGL. Figure

7.2(a) and 7.3(a) show the fits of R_{xy} at fixed T and B respectively in dashed lines, calculated according to Eq. (7.1) using $\rho_{xy} = \sigma_{xy} \cdot \rho_{xx}^2$. The vortex dynamics description agrees well with the experiment in a wide region in temperature $T < T_C$ and magnetic field. For $T > T_C$ the agreement is still fair, however, we observe some deviation of theoretical curve from experimental R_{xy} (see curve at 80 K in Fig. 7.2(a)), the deviation growing with increasing temperature. This is because the dome configuration is determined solely by the condition $\sigma_{xy} = 0$ and the behavior ρ_{xx} is irrelevant. At the same time, the behavior of ρ_{xy} accounts for the finite residual resistance ρ_{xx} at $B = 0$, which is omitted in the vortex approximation [207].

7.4 Hall Sign Reversal Above T_C

To cross-check the applicability of the vortex-based description of $R_{xy}(B)$ and $R_{xy}(T)$ at $T > T_C$, we employ the superconducting fluctuation expansion of TDGL, using the smallness of the order parameter in the fluctuation regime. Qualitatively, SF are Cooper pairs with a finite lifetime, arising above T_C. Under applied magnetic field, these pairs rotate around their center of mass and can be viewed as elemental current loops. The external current exerts Magnus force moving these loops along the circular paths. This gives rise to Hall voltage opposite to that from the normal carriers. The SF contribution to Hall conductivity manifests as a negative correction $\delta\sigma_{xy}$ to the positive normal component σ_{xy}^n [223,215]: $\sigma_{xy} = \sigma_{xy}^n + \delta\sigma_{xy}$. Expression for $\delta\sigma_{xy}$ in the Gaussian approximation [215] is:

$$\delta\sigma_{xy} = \frac{2e^2 k_B T}{hd} \zeta f(D, B, T) \tag{7.3}$$

where D is the normal carrier diffusion coefficient evaluated as $D \approx \frac{2}{3}\mu_H E_F$ (see SI section E); f is a dimensionless function (see SI for explicit form); ζ is a parameter accounting for particle-hole asymmetry in the time-dependent Ginzburg-Landau equation. The parameter ζ is expressed as the change of T_C with respect to the chemical potential μ: $\zeta = -\frac{1}{2}\partial(\ln T_C)/\partial\mu \approx 1/(\gamma E_F)$ [243,223,215]. Here γ is the dimensionless coupling constant parameterizing the attractive electron-electron in-

teraction that induces superconductivity. As temperature decreases, the SF contribution $\delta\sigma_{xy}$ increases, leading to the sign change of σ_{xy} as soon as $\delta\sigma_{xy}$ starts to dominate [233,232,244]. The Hall resistance $R_{xy}(B)$ and $R_{xy}(T)$ at $T > T_C$ is nicely described by the SF description of Eq. (7.3) (dash-dotted line in Fig. 7.2a and 7.3a), where the values of fitting parameter γE_F (see SI) correspond to $\gamma < 1$ (the weak coupling limit) and E_F previously evaluated from fits of $R_{xy}(B, T) = 0$ with Eq. (7.2). The phase boundary for $T > T_C$ is also accurately captured by the SF description in Eq. (7.3) (Fig. 7.3b, dashed line). Remarkably for $T > T_C$, the phase boundary $R_{xy}(T, B) = 0$ agrees with both vortex and SF TDGL asymptotes. The agreement between the values of E_F and fits of the phase boundary provides a crosscheck ensuring that vortex description of Eq. (7.2) works fairly well at $T > T_C$. Thus our findings support the idea that vortex-like excitations survive above T_C [245] in full concert with Nernst effect observations [219,220]. Our results apply to any bulk HTS with layered structure. Also, since disorder enters through the scattering time, our conclusions remain valid for disordered low-T_C films, see, for example, [246,247].

7.5 Summary and Outlook

In conclusion, we developed van der Waals assembly techniques specialized to the cuprates. We fabricated few-unit-cell $Bi_{2.1}Sr_{1.9}CaCu_{2.0}O_{8+\delta}$ crystals, where an appreciable enhancement of the Hall sign reversal with the system's thinning was observed. We demonstrated that the Hall resistance sign reversal occurs both below and above T_C and is well described in terms of vortex dynamics across the entire temperature interval. In the fluctuation region above T_C, the sign reversal is equally well described by superconducting fluctuations formalism which cross checks our results and connects vortex-like excitations above T_C and superconducting fluctuations.

My favorite walk is the next one.

Lorna Kingston

8

Emergent Interfacial Superconductivity between Twisted Cuprate Superconductors

Twisted interfaces between stacked van der Waals cuprate crystals enable tunable Josephson coupling, utilizing anisotropic superconducting order parameters. Employing a novel cryogenic assembly technique, we fabricate high-temperature Josephson junctions with atomically sharp twisted interface between $Bi_2Sr_2CaCu_2O_{8+x}$ crystals. The critical current density J_c sensitively depends on the twist angle. J_c nearly matches that of intrinsic junctions near 0°, and is suppressed by almost 2 orders of magnitude but remaining finite near 45°. J_c also exhibits non-monotonic behavior *vs* temperature due to competition between supercurrent contributions from nodal and anti-nodal regions of the Fermi surface. Near 45° twist angle, we observe Fraunhofer interference patterns with two periods and fractional Shapiro steps at half integer values, a signature of

co-tunneling Cooper pairs necessary for high temperature topological superconductivity.

8.1 Introduction

The nature of weak van der Waals (vdW) bonding between neighboring atomic layers offers a unique opportunity of engineering atomic interfaces with controlled twist angles[248]. For example, a moire superlattice whose spatial modulation can be adjusted by the twist stack angle can be engineered, enabling narrow electronic bands with topological structure to realize *'twistronics'*[249]. A plethora of emergent electronic states, including superconductivity[36], magnetism[250], Chern insulators[251], generalized electronic Wigner crystals[252], and correlated insulating states[253] are discovered in the twisted interface of various 2-dimensional (2D) vdW materials, including graphene[254] and transition metal dichalcogenides[255].

Atomically layered cuprate high temperature superconductors also offer a platform for twistronics by engineering the coupling between superconducting order parameters (SOP) across a twisted vdW interface. In the case of $Bi_2Sr_2CaCu_2O_{8+x}$ (BSCCO), one of the most anisotropic cuprates, insulating [SrO-BiO] buffer layers serve as tunnel barriers between superconducting CuO_2 bilayers[256], whose c-axis coherence length is shorter than the vdW layer thickness[257]. The vdW coupling between BiO double layers also allows the cleaving of crystals to expose large pristine surfaces, which have enabled multiple experiments exploiting the reduced sample thickness[26,27,25]. Recent study[25] shows that atomically thin BSCCO with a single vdW unit (containing two CuO planes) still exhibit a bulk-like superconducting transition, demonstrating the 2D nature of superconductivity.

Twisted interfacial Josephson junctions (JJ) between superconductors, in principle, can offer a probe of the pairing symmetry of Cooper pairs. For conventional superconductors with isotropic pairing mechanism, the weak coupled Cooper pairs exhibit s-wave symmetry, resulting in twist angle θ-insensitive Josephson coupling[258]. For layered superconductors with an anisotropic in-

plane SOP, however, the JJ coupling across the twisted interface is expected to be strongly θ dependent[258,259]. In particular, in a JJ between twisted d-wave superconductors, the wavefunction of tunneling Cooper pairs pick up a phase π when θ exceeds $45°$ [258,62,260]. At exactly $\theta = 45°$, direct Cooper pair tunneling is forbidden due to complete mismatch between the SOPs across the interface[258], which allows weaker higher order processes corresponding to co-tunneling of Cooper pairs to dominate[261,260,62]. Recent theoretical work[62,260,262] predict that such a second order Josephson coupling supports a topological superconducting state which spontaneously breaks time reversal symmetry, that can survive up to the critical temperature of the host superconductor at the twisted vdW cuprate interface.

8.2 Twist Josephson Junctions with Single-Crystal Intrinsic Junction Quality

Despite the vdW nature of BSCCO, the preservation of its surface superconductivity after vdW stacking remains an outstanding experimental challenge[26,27]. It is known that the surface of BSCCO crystals are sensitive to heat[25,99,104] and moisture[25,128] since self-organization[104] of oxygen dopants at the nanometer scale[100] plays a key role in the superconductivity[65]. Previous experiments involving twisted BSCCO junctions require a high temperature oxygen anneal step to restore Josephson coupling at the twist interface[263,264,265,118]. This post-annealing process often comes at the cost of interfacial structural reconstruction detectable in cross-sectional transmission electron microscopy (TEM)[266,118]. The majority of experiments observed no angular dependence in critical current[263,265,118], except one[264], where Andreev reflections through a reconstructed interfacial layer may have obscured the angle dependent SOP coupling between unreconstructed twisted JJs[259].

In this chapter, we report emergent interfacial superconductivity appearing in pristine atomically sharp twisted BSCCO Josephson junctions built via a novel cryogenic assembly technique.

We find strong angle and temperature dependent Josephson critical current associated with a *d*-wave SOP symmetry. Particularly, near 45° twist angle, where the *d*-wave SOPs are maximally mismatched, we observe emergent Shapiro steps at half integer values, which originates from a second harmonic in the JJ current-phase relation (CPR) corresponding to the co-tunneling of Cooper pairs – the necessary ingredient for the emergence of high temperature topological superconductivity[62,260].

Figure 8.1 shows our low temperature device fabrication procedure which preserves interfacial superconductivity. Here, we develop a cryogenic and solvent-free vdW transfer technique in pure argon atmosphere using a liquid nitrogen-cooled stage maintained near -90°C. Using this technique, we cleave a pre-exfoliated BSCCO crystal into two halves along the $a-b$ plane, while thermally freezing out oxygen migration and other chemical processes at the surface (Figure 8.1A). One of the two cleaved crystals is then quickly rotated to the targeted twist angle θ, and re-assembled with the remaining crystal in an overlapping region (Figure 8.1B and C). A set of electrical contacts are pre-fabricated near the original crystal before cleaving to serve as the bottom contact of the top crystal upon reassembly. An additional set of electrodes are fabricated on the top surface of the bottom crystal after reassembly, via stencil mask deposition with the sample held near -30° C. Fabrication of twist JJs without a high temperature anneal step is critical to maintain the atomic interface without significant reconstruction and oxygen dopant changes at the interface. Figure 8.1D shows the cross-sectional scanning transmission electron microscope image of a $\theta = 0°$ junction. Bright spots correspond to electron scattering on atomic columns, the brightest of which are bismuth which terminates each vdW layer. The supermodulations are found to be mutually aligned across the interface, revealing a strain between the interfacial layers[267]. Importantly, we do not observe a trilayer cuprate $Bi_2Sr_2Ca_2Cu_3O_{10+\delta}$ structure at the interface, which was previously reported in BSCCO junctions after a high temperature anneal step[266]. While the thickness of crystals is in the range of 20-50 nm depending on the device, our electrode arrangement allows us to probe superconductivity of the top and bottom layers and

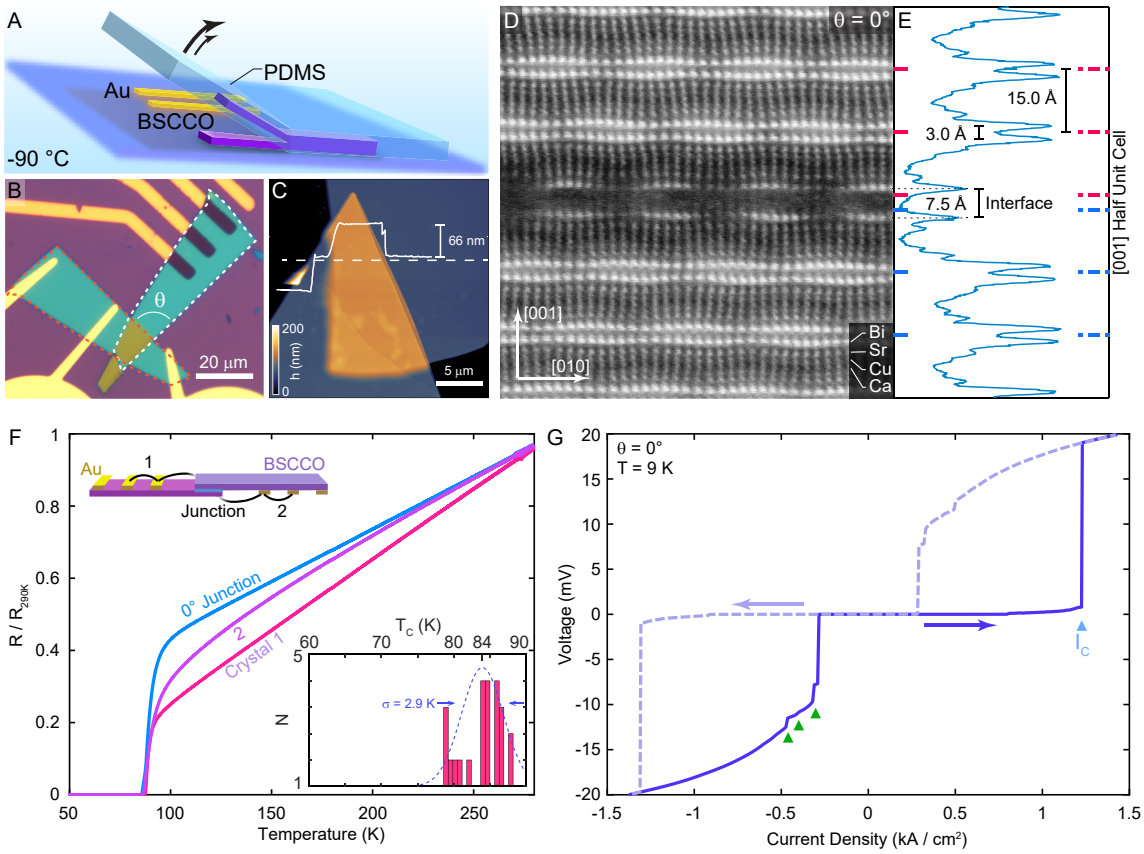

Figure 8.1: Twist Josephson junctions with intrinsic junction quality. A. Schematic diagram of the key fabrication step, where a single BSCCO crystal is cleaved using PDMS at $-90°$ C. **B.** Optical micrograph of a BSCCO twist junction. Dashes outline the identical shape of the two crystals. Corresponding schematic underneath in **Inset of F. C.** Atomic force microscope topography showing atomically flat interfaces at the junction. Line trace shows topography cut along dotted line. **D.** Cross-sectional scanning-TEM image of junction at $\theta = 0°$, showing crystalline order at the interface. **E.** Integrated intensity at each layer. **F.** Comparison of in-plane resistance in each bulk crystal *vs* the artificial junction between them, showing nearly identical junction T_C. **Inset** shows distribution T_C among all 24 JJs in the angle dependence analysis. **G.** $I-V$ curve for a $\theta = 0°$ junction in both sweep directions (arrows). As I sweeps away from zero, a voltage step occurs at the switching current $I_C = 1.2$ kA/cm^2 (blue triangle) comparable to intrinsic junctions. As I sweeps toward zero, small voltage steps (green triangles) corresponds to inelastic scattering features seen at the same voltages in intrinsic junctions (see text for detail).

the interfacial JJ between them independently (see the upper inset Fig. 8.1F). In order to study the effects of twist angle at comparable doping levels, we fabricate 24 devices with different twist angle θ ranging between 0° to 180°. The junction resistance always vanishes within a few Kelvin of the bulk transition temperature $T_C \approx 84$ K (the main panel of Figure 8.1F shows an exam-

ple), demonstrating high oxygen dopant uniformity even at the junction. We find that neither the transition temperature nor the normal-state conductivity of twist junctions are systematically correlated to θ (see B.2). The 24 devices investigated in the angle-dependence study have an average T_C similar to the bulk value with the standard deviation of 2.9 K (Fig 8.1F inset).

8.3 Evidence of d-Wave Pairing Symmetry

The four terminal device configuration across the vdW interfacial JJ allows us to measure current-voltage (*I-V*) characteristics across the twisted JJ. We first focus our discussion to the $\theta = 0°$ JJ, where the strongest Josephson coupling is expected due to SOP alignment between the top and bottom layers. Fig. 8.1G shows *I-V* curve measured at temperature $T = 9$ K. In this low temperature regime, the JJ exhibits a large hysteresis in the bias current sweep. As we sweep the bias current from a large negative value, the junction voltage V first retraps to the zero resistance state ($V = 0$) and then jumps to the resistive state at the critical current I_C, marked by the blue arrow. Upon changing the bias current polarity (dashed line), the JJ's *I-V* behavior is simply mirrored along the $I = 0$ axis. Normalizing to junction area, we obtain a critical current density $J_C \approx 1.2$ kA/cm^2 for this junction, a value comparable to J_c of intrinsic junctions[268]. We observe small voltage jumps on the retrapping side at the same voltages as inelastic tunneling features previously observed in intrinsic BSCCO JJs[256]. These observations indicate that our $\theta = 0°$ JJ forms on a vdW interface with quality comparable to intrinsic JJ in single-crystal BSCCO. In about half of our devices, only one jump is seen in the *I-V* sweep, suggesting that no additional intrinsic JJs from crystal terraces intruded the current path.

To compare the transport characteristics of twisted JJs, we normalized the bias current I by using the junction normal resistance R_N. Since I_C and R_N^{-1} are proportional to the area of the junction, the product $I_C R_N$ is independent of junction area and controls for small variations in junction quality. Figure 8.2A shows the normalized dynamic resistance $[dV/dI]/R_N$ as a func-

tion of temperature T and $I_C R_N$ for three representative angles, $\theta = 0°$, $31°$, and $44.9°$, respectively (similar data for all 24 JJs included in the angular dependence study are in figure B.3). Several features are apparent in these data sets. First, as the current sweeps from left to right, on the retrapping side ($IR_N < 0$), the constant-voltage inelastic tunneling features appear (green triangles in Fig. 8.1G). While the values of IR_N for these features increase with T, as the subgap resistance increases with T, the corresponding V remained constant. Next, on the switching side ($IR_N > 0$), the junction voltage jumps alongside dV/dI at critical current I_C, which depends on T. The detailed behavior of $I_C(T)R_N$ depends on θ, as we will detail below. Finally, we find the hysteresis of JJs reduced in the high temperature regime as $I_C(T)R_N$ decreases, as expected from the increasing damping in the JJ. For most samples, the hysteresis disappears for $T \gtrsim 60$ K.

Analyzing $I_C R_N$ for all 24 devices spreading over θ from 0° to 180°, we find a trend that the overall magnitude of $I_C R_N$ becomes smaller closer to 45° and 135° and the JJs also appear less hysteretic. The equivalence between these two angles suggests that the SOP anisotropy is small between a and b axes. To present this observation more quantitatively, we introduce a new variable $\phi = \theta \,(\mathrm{mod}\, \pi/2)$, which runs between 0 to 90°. Fig. 8.2B plots $I_C R_N$ as a function of ϕ at two representative fixed temperatures 12 K and 30 K. We observe that $I_C R_N(\varphi)$ follows $|\cos(2\phi)|$, which is expected for a direct Cooper pair tunneling between d-wave superconductors[258]. This d-wave-like angular dependence is also confirmed in the angular dependence of junction voltage just above the critical current $V(I_C)$ (see fig. B.5), which in conventional tunnelling JJs is equal to $2\Delta/e$[66].

The temperature dependence of Josephson coupling in our twisted junctions provides further insight into the pairing symmetry of the Cooper pairs in BSCCO layers. Figure 8.2C shows $I_C(T)R_N$ for several representative JJs with different ϕ. We find that for ϕ close to 0° (or equivalently 90°), $I_C(T)R_N$ exhibits a monotonic decrease as T increases, approximately following the well-known Ambegaokar-Baratoff relation (dashed line)[66]. As ϕ approaches 45°, however, a surprising non-monotonic behavior of $I_C R_N(T)$ appears. For example, for $\phi = 29°$ and 39° in

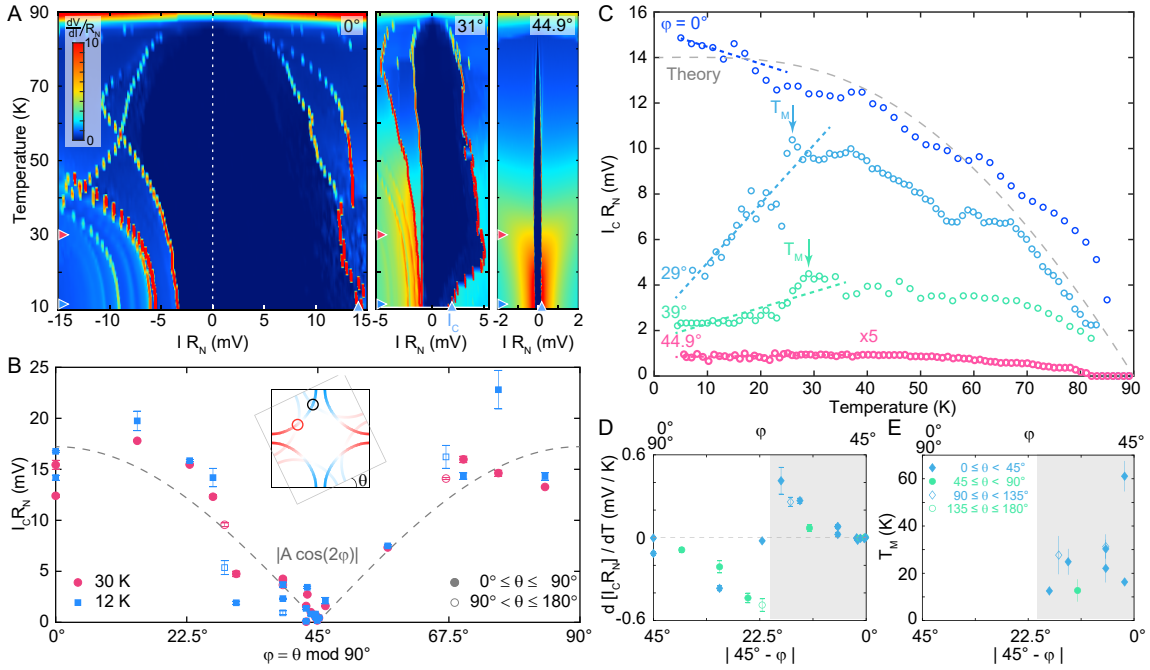

Figure 8.2: *d*-**wave SOP symmetry reflected in supercurrent tunneling. A.** Normalized differential resistance $[dV/dI]/R_N$ as a function of both characteristic voltage IR_N and temperature T. Current is swept to the right. Blue arrow points to critical current at 10 K. **B.** Angular dependence of I_CR_N for all devices at 30 and 12 K. The points follow the $|\cos(2\phi)|$ curve predicted for tunneling between *d*-wave superconductors[258]. **Inset:** schematic diagram of the Fermi surface of both crystals, with sign and magnitude of the superconducting gap $\Delta(\vec{k})$ superposed in color, which intersects at two points highlighted by circles. **C.** Temperature dependence of critical current for select devices. Dotted lines are linear fits to the low temperature data. T_M is temperature where I_C is maximal. **D.** shows the slope of the low temperature line fit, $d(I_CR_N)/dT$. **E.** T_M as a function of angle ϕ.

Fig 8.2C, $I_C(T)R_N$ increases alongside T, reaching a maximum value at $T = T_M$ and then decreases as T approaches T_C. More quantitative analysis can be found in Figure 8.2D and Figure 8.2E, where we plot the low temperature slope $d(I_CR_N)/dT$ (dotted lines in Fig 8.2C and fig. B.4) and observed T_M, respectively for various devices with different φ. These plots show a non-monotonic behavior of $I_CR_N(T)$, signaled by the positive slope of $I_CR_N(T)$ at low temperatures with finite T_M, appearing within $|\phi - \pi/4| < \pi/8$.

The strong angular dependence of non-monotonic behavior of $I_C(T)R_N$ evident in Fig 8.2D and E points to the *d*-wave symmetry of the SOP as its origin. For this purpose, let us consider a gap function $\Delta_{1,2}(\mathbf{k})$ superimposed on top of the Fermi surface $E_F^{1,2}(\mathbf{k})$[78], where $\mathbf{k}$ is the Cooper

pair wavevector in the first Brillouin zone lying in the copper-oxide plane and the index 1 or 2 denotes the top and bottom layer of BSCCO, respectively. Then in the twisted JJ, as shown in the inset in Figure 8.2B, $E_F^1(\mathbf{k})$ and $E_F^2(\mathbf{k})$ are rotated relative to each other by twisting angle θ. At $\theta \approx 0$, $E_F^1(\mathbf{k})$ and $E_F^2(\mathbf{k})$ overlaps almost completely and $\Delta_1(\mathbf{k})\Delta_2(\mathbf{k}) > 0$, since $\mathbf{k}$ is approximately conserved for tunneling Cooper pairs[258], yielding the largest Josephson critical current. As θ increases to $\sim 10°$, the Fermi surfaces overlap at two points per quadrant in $\mathbf{k}$-space, but with opposite phase difference between layers: (i) an anti-nodal contribution where $\Delta_1(\mathbf{k})\Delta_2(\mathbf{k}) > 0$ and (ii) nodal contribution $\Delta_1(\mathbf{k})\Delta_2(\mathbf{k}) < 0$. Since the supercurrent from these two components carry the opposite sign, their contributions to the total critical currents then compete. As tunneling becomes increasingly coherent at lower temperature, I_C can be suppressed at low temperature if the two contributions are similar in magnitude. The detailed calculation of J_C based on d-wave SOP considering optimally doped BSCCO indeed indicates that non-monotonic $I_C(T)R_N$ is expected for $\phi \approx \pi/8$, see section B.6 and Ref.[269].

8.4 Cooper Pair Co-Tunneling at the 0-π Transition

It is important to note that near $\phi \approx \pi/4$, the JJ coupling is strongly suppressed but remains nonzero. As Figure 8.2A shows, our $\theta = (44.9 \pm .1)°$ junction becomes fully superconducting with zero resistance at 79 K, although $I_C R_N$ is about two orders of magnitude smaller than the 0° value. Figure 8.2B (see also fig. B.3) shows several devices near 45° which also hosted supercurrents with T_C above 79 K. The origin of the finite supercurrent near 45° is encoded in the Josephson current-phase relation (CPR) $J(\gamma)$, where γ is the gauge independent phase difference across the vdW interface and J the supercurrent density[62,261,260]. We note that near 45°, the JJ coupling lacks the conventional direct Cooper pair tunneling term due to the maximally mismatched SOP across the twisted interface. The supercurrent must then tunnel through a second-order mechanism corresponding to co-tunneling of Cooper pairs, which is predicted to result in an interfacial SOP

with emergent $d_{x^2-y^2} + id_{xy}$ symmetry[62,260]. The Josephson CPR of this unusual SOP develops a strong second-order harmonic[260,62,261], which can be experimentally probed by measuring the in-plane magnetic interference ('Fraunhofer') pattern or microwave induced Shapiro steps in the I-V characteristic, reflecting the $4e$ charge of co-tunneling Cooper pairs across the junction[261,260].

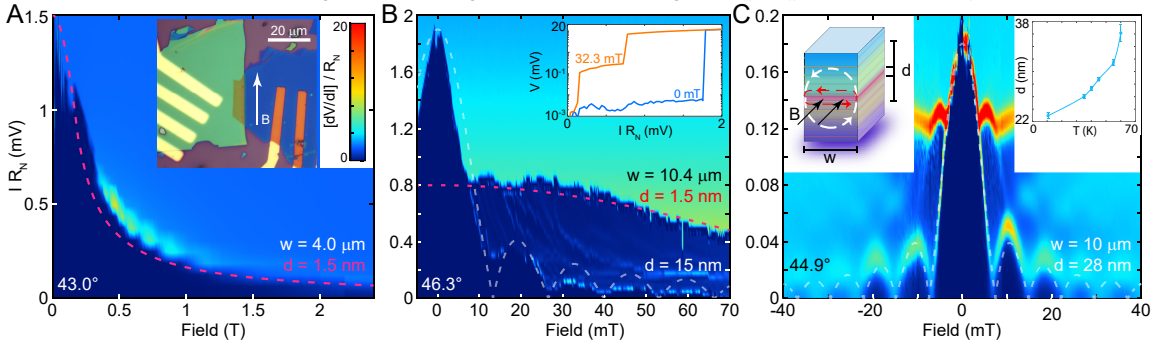

Figure 8.3: Fraunhofer pattern near 45°. dV/dI response to applied in-plane magnetic field $B_{\|}$ for twisted JJ at three angles with width w in direction perpendicular to $\vec{B}_{\|}$, measured from microscope images. **A.** Response in a 43.0° junction. Red dashed lines show the Fraunhofer pattern envelope with effective JJ thickness $d = 1.5$ nm expected in intrinsic BSCCO JJ. **Inset** shows device optical photo. **B.** Respoonse in a $\theta = 46.3°$ JJ. As θ approaches 45°, an additional Fraunhofer pattern with shorter magnetic field periodicity develops (grey dashed line), with an estimated d =15 nm shown in grey dashed line. **Inset** shows I-V characteristics at two different B field values, showing two jumps in V away from the central I_C peak. **C.** Response in a JJ at 44.9° twist. One well-developed Fraunhofer pattern corresponding to d =28 nm appears, as indicated by the white dashes line. The **left inset** shows a schematic diagram of the Josephson vortex configuration in the device with a weak interfacial JJ compared to the intrinsic JJ coupling. Orange lines show copper-oxide planes. Red and white shading highlight the magnetic flux areas, corresponding to dashed lines in main figure. The **right inset** shows experimentally evaluated d from the Fraunhofer pattern taken at different temperatures on the 44.9° JJ.

In figure 8.3, we present Fraunhofer interference patterns (FIP) obtained at three different angles by showing normalized dV/dI vs parallel magnetic field $B_{\|}$. We find that the devices further away from 45° twist exhibit less developed FIP. For 43.0° device, only 2° away from 43.0° (Fig. 8.3A), the critical current is suppressed as $B_{\|}$ increases without the clear oscillatory features. Similar FIPs have been observed in intrinsic JJs in bulk BSCCO[268,270], where the screening effect from the high critical current density of the JJs combined with inhomogeneity of the samples can lift the minima of the FIP. Following the theoretical analysis developed for the intrinsic JJ[271], we can extract the characteristic length scale from the full width of the half maxima of the central peak of

the FIP: $\Delta B_{\|} = \hbar/2ews$, where e is the elementary charge; w and s are the width and thickness of the junction. Applying this formula to the data in Fig. 8.3A (with w =4 μm), we obtain $s = 1.5$ nm, a value corresponding to the interlayer separation between CuO_2 planes, similar to the FIPs in intrinsic JJ of BSCCO.

As interfacial Josephson coupling weakens near 45°, the Josephson length increases, and the magnetic field inside the twist JJ approaches the short junction limit. At 44.9°, we observe multiple oscillations in $I_C(H)$ (figure 8.3C), with a period about 20 times shorter than that expected for intrinsic junctions. This corresponds to an effective junction thickness $d = 28$ nm as plotted in the white line in figure 8.3C. In between these two angles (figure 8.3B), both the fast and slow oscillations coexist, with d between 15 and 35 nm among all samples, while the longer period FIP is at $s = 1.5$ nm as discussed above. Such coexistence of two different oscillation periods was previously seen in coupled pairs of JJs between three niobium electrodes[272], where coupling between stacked Josephson junctions effectively changed the junction thickness. While more quantitative description can be made considering the Josephson vortex formation in the junction (shown in the inset of Fig. 8.3C), the presence of the FIP with well-defined interference minima near 45° clearly indicates the homogeneous Josephson coupling at this special angle, which can be distinctly different from the long period FIP caused by the dominant JJ coupling away from 45°.

The unconventional JJ coupling near 45° twist can further be investigated using microwave illumination. The presence of higher order harmonics in the CPR are revealed in the spacing between Shapiro steps in I-V under microwave illumination of frequency f (inset of Fig. 8.4A and D)[261,260]. In conventional JJs where the CPR is dominated by a sinusoidal term of period 2π, Shapiro steps appear as plateaus of constant voltage whenever V approaches $n \times hf/2e$, where n is an integer. As shown in our experiment in Fig. 8.4D, for the device with twist angle 43.7°, the experimentally observed Shapiro steps with integer quantized n show that the CPR in this junction is conventional. The Fourier transform of dV/dI in Fig 8.4E and F confirms this view, as the periodicity in dV/dI is completely dominated by the first harmonic of $\nu_1 = 2e/hf$ over the

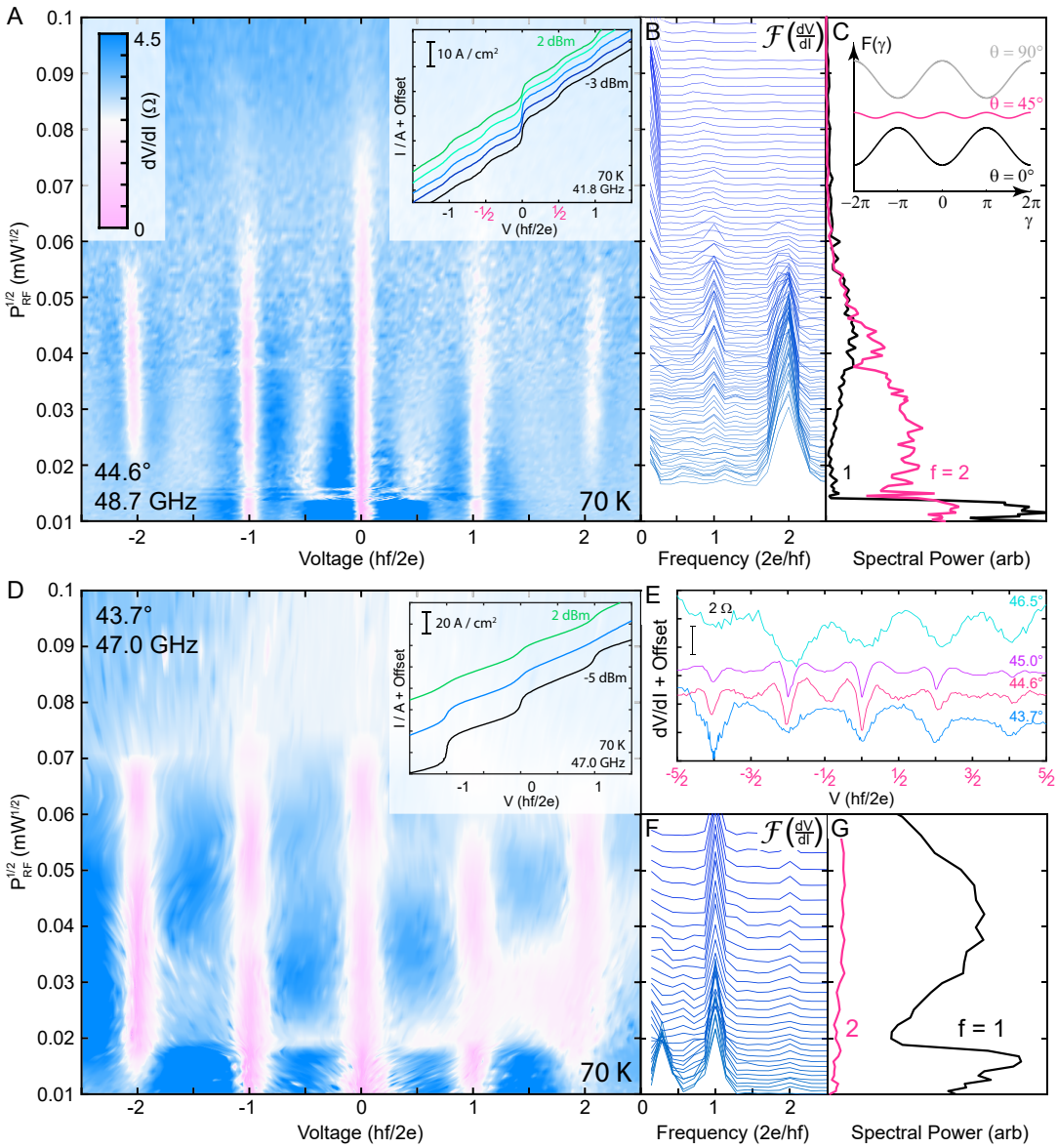

Figure 8.4: Half-integer Shapiro steps emerge close to 45°. **A.** shows dV/dI in response to microwave radiation with frequency $f = 48.7$ GHz. The inset shows I-V characteristic which develop Shapiro step features at $f = 41.8$ GHz. All measurements were carried out 70 K. **B.** and **C.** show Fourier transform of $dV/dI(V)$ and spectral power at $\nu_f = 1$ and $2 \times 2e/hf$. **Inset** shows schematic of the junction free energy F vs Josephson phase γ as twist angle changes. At 45°, the second harmonic dominates the current-phase relation. **D, F and G** shows similar data for a 43.7° device, where only integer Shapiro steps appear. **E.** shows representative dV/dI for four devices at different twist angles, where half integer steps are only observed in junctions closest to 45°

entire power range.

Remarkably, when our devices are within about 1° of 45°, additional steps at *half-integer n* appear (Fig. 8.4A and inset), which fan out linearly in V as frequency increases (see fig. B.6). These features also appear across a wide range of microwave power at constant V (see figure 8.4A), confirming their origin as Shapiro steps. At low microwave illumination power, the magnitude of the dV/dI dips at fractional and integer values of n are roughly equal, and the Fourier transform spectrum is dominated by the $\nu_2 = 2 \times 2e/hf$ peak.

The Fourier transform of $dV/dI(V)$ in Figure 8.4B displays the relative strengths of integer versus fractional Shapiro steps to estimate our junction CPR. For a junction with purely second order CPR, the $n = 1/2$ step becomes the fundamental step and should appear strong compared to the integer steps. Indeed, at low microwave power in the 44.6° device when the fractional Shapiro steps first appear, the Fourier transform is dominated by the second harmonic $\nu_2 = 4e/hf$. The corresponding dV/dI shows dips of similar strength at half integer and integer steps, indicating that the phase insensitive co-tunneling of Cooper pairs dominates over the conventional Josephson coupling close to 45°. Dominant half-integer Shapiro steps have been observed in magnetic-(SFS) JJs[89,273]. The presence of the dominant second harmonic CPR, demonstrate in 45° JJs, establishes the unconventional nature of the interfacial high-temperature superconductivity expected to support a topological superconducting phase[260] which spontaneously breaks time reversal symmetry[62].

A

Details for Sign Reversing Hall Effect in Atomically Thin High Temperature Superconductors

A.1 Superconducting fluctuations in longitudinal resistance $R_{xx}(T)$

We calculate the resistance due to superconducting fluctuations in order to determine the temperature where Cooper pair lifetime becomes infinite. We have consistently used this criteria for T_C. The correction to conductivity from superconducting fluctuations is $\Delta\sigma(T) = 1/\rho(T) - 1/\rho_n(T)$, where $\rho_n(T)$ is the normal resistivity (linear in T). According to the advance thermodynamical fluctuation theory in zero field[223,243], this correction $\Delta\sigma(T)$ consists of Aslamazov-

Larkin, DOS and the dominant Maki-Thompson contributions:

$$\Delta\sigma = \Delta\sigma_{AL} + \Delta\sigma_{DOS} + \Delta\sigma_{MT}, \tag{A.1}$$

$$\Delta\sigma_{AL} = \frac{e^2}{16\hbar s} \cdot \frac{1}{\sqrt{\varepsilon \cdot (\varepsilon + r)}}; \tag{A.2}$$

$$\Delta\sigma_{DOS} = -\frac{e^2}{2\hbar s} \cdot k_1 \cdot \ln\left(\frac{2}{\sqrt{\varepsilon} + \sqrt{\varepsilon + r}}\right); \tag{A.3}$$

$$\Delta\sigma_{MT} = \frac{e^2}{2\hbar s} \cdot \left[\frac{1}{2(\varepsilon - \gamma)} \ln\left(\frac{\sqrt{\varepsilon} + \sqrt{\varepsilon + r}}{\sqrt{\gamma} + \sqrt{\gamma + r}}\right) - k_2 \ln\left(\frac{2}{\sqrt{\varepsilon} + \sqrt{\varepsilon + r}}\right)\right];$$

Here s is the spacing of the 2D superconducting layers in the c-axis direction, $\varepsilon = \ln(T/T_C)$ is the reduced temperature,

$$r(T) = -2J^2\tau^2 a/\hbar^2 \tag{A.4}$$

is the Lawrence-Doniach anisotropy parameter, $\gamma = \tau a/\tau_\varphi = \tau a \cdot \delta \cdot 8k_B T/(\pi\hbar)$, where δ is the phase-breaking parameter. Here J as the hopping energy between neighbouring layers, τ the quasiparticle scattering time, and a given by the equation

$$a(T) = \left[\psi\left(\frac{1}{2} + \frac{\hbar}{4\pi\tau k_B T}\right) - \psi\left(\frac{1}{2}\right) - \frac{\hbar}{4\pi\tau k_B T}\psi'\left(\frac{1}{2}\right)\right]; \tag{A.5}$$

$$k_1 = \frac{-\psi'\left(\frac{1}{2} + \frac{\hbar}{4\pi\tau k_B T}\right) + \frac{\hbar}{2\pi\tau k_B T}\psi''\left(\frac{1}{2}\right)}{\pi^2 a}; \tag{A.6}$$

$$k_2 = \frac{-\psi'\left(\frac{1}{2} + \frac{\hbar}{4\pi\tau k_B T}\right) + \psi'\left(\frac{1}{2}\right) + \frac{\hbar}{2\pi\tau k_B T}\psi''\left(\frac{1}{2}\right)}{\pi^2 a}; \tag{A.7}$$

$\psi(x)$ is the digamma function.

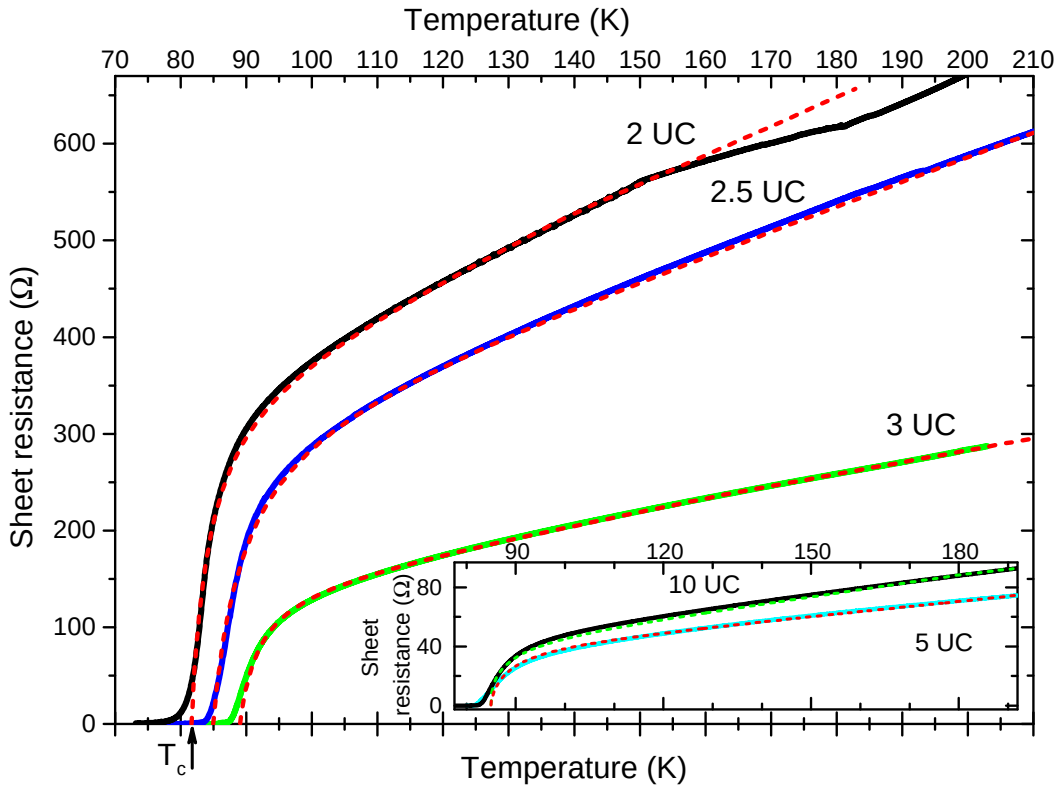

Figure A.1: Sheet resistance *vs.* temperature. Sheet resistance $R = \rho/d$ as a function of temperature for vdW devices of different thickness d. Dashed lines — fits taking into account quantum corrections to conductivity due to superconducting fluctuations. The $R(T)$ dependencies for 5 UC and 10 UC are given in inset to avoid overlapping of the curves. The arrow marks T_C for 2UC device. For all samples T_C lies at the foot of $R(T)$ curve.

This theoretical approach was applied to BSCCO films[225]

Taking interlayer distance $s = 4$ Å which is in good agreement with Cu K-edge anomalous x-ray diffraction[174] (where $s \simeq 3$ Å), interlayer hopping energy $J = 40$K[274] for 5UC sample and $J = 80$K for 10UC, pair-breaking parameter $\delta = 3 \cdot 10^{-4}$, and $\tau = 1 \cdot 10^{-14}$ sec[225] we successfully describe behaviour of $R_{xx}(T)$ at $T > T_C$ for thick samples (5 UC and 10 UC). For thinner films (3 UC and below) this fitting yields interlayer spacing $s > 10$ Å. We assume that this means that

the model of layered superconductor is not applicable anymore. Therefore, for these samples we employ the equations for quasi-two dimensional films[226].

For quasi two dimensional (quasi-2D) systems the conductance G is expressed as $G = 1/R$ (R is the sheet resistance), which is the conductivity times the film thickness d.

$$\Delta G^{AL}(T)/G_{00} = \pi^2/(8\ln t), \tag{A.8}$$

$$\Delta G^{DOS}(T)/G_{00} = \ln[\ln t/\ln(kT_c\tau/\hbar)]. \tag{A.9}$$

MT depends on τ_ϕ through

$$\delta = \pi\hbar/(8k_BT\tau_\phi), \tag{A.10}$$

$$\Delta G^{MT}(T)/G_{00} = \beta(t,\delta)\ln(\pi/(8\delta)). \tag{A.11}$$

Here, $G_{00} = \frac{e^2}{2\pi^2\hbar}$ and

$$\beta(t,\tau_\phi) = \frac{\pi^2}{4}\sum_m(-1)^m\Gamma(|m|) - \sum_{n\geq 0}\Gamma''(2n+1), \tag{A.12}$$

where m is an integer $m = 0, \pm1, \pm2, \ldots$, and

$$\Gamma(|m|)^{-1} = \ln t + \psi\left(\frac{1+|m|}{2}\right) - \psi\left(\frac{1}{2}\right) - \psi'\left(\frac{1+|m|}{2}\right)\frac{\hbar}{4\pi k_BT\tau_\phi}.$$

The function $\beta(t,\tau_\phi)$[275] reduces to Larkin's $\beta(t)$ in the limit $(t\cdot\tau_\phi)^{-1} \to 0$.

The correction to conductivity due to superconducting fluctuations $\Delta\sigma(T)$ diverges at T_C, i.e. the resistance should be zero. At temperatures $T \lesssim T_C$, however, the resistance is nonzero, which is due to the presence of free mobile vortices in the system.

A.2 Hall sign reversal phase diagram

Figure A.2 shows Hall resistance R_{xy} for our 3 UC device, which had a significantly higher T_C compared to the others. Importantly, the bulk crystal's SC transition is at 90K[222], so the sign reversal persists above T_C of bulk Bi-2212.

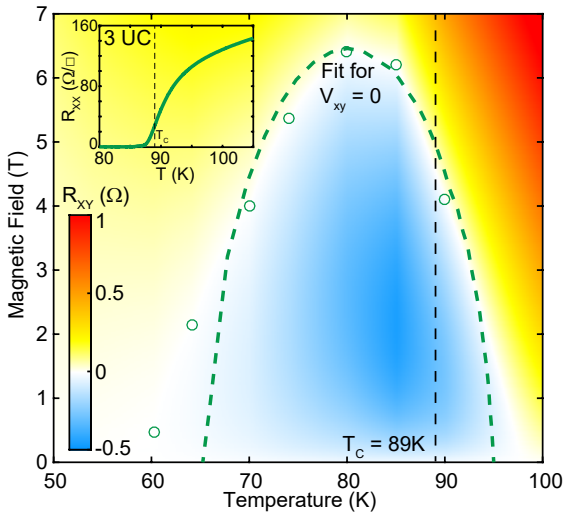

Figure A.2: The Hall sign reversal phase diagram for 3UC. Shading shows Hall resistance $R_{xy}(B, T)$ for a 3UC device. Blue region shows the area of negative Hall resistance. Symbols show the locus $R_{xy} = 0$ with the line generated from Eq. 2 in main text. Dashed vertical line shows $T_C = 89$ K from SF fit of the zero-field $R_{xx}(T)$ (inset).

A.3 Normal State Hall Conductivity

In normal state the Hall resistance is a linear function of magnetic field (Fig. A.3a). The Hall conductivity is also linear function $\sigma_{xy} = s_{xy}B$ where the slope s_{xy} increases with cooling down as $1/T^2$. In the superconducting state it is difficult to extract the contribution to Hall conductivity from normal exitations. Hence, we assume that the normal component of σ_{xy} in the superconducting state maintains the T^{-2} dependence.

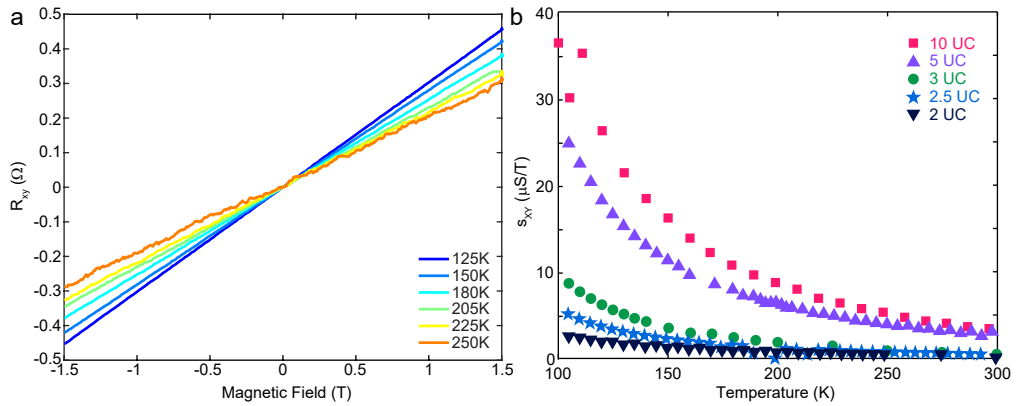

Figure A.3: Hall conductivity in the Normal State. a. R_{xy} is purely linear with the magnetic field at high temperatures. b. The slope of the Hall conductivity $s_{xy} = \sigma_{xy}/B$ in normal state *vs.* temperature.

Thick UC	T_C [K]	δ	T_{HSR} [K]	τ [ps]	n_0/E_F^2 [cm^{-3}/eV^2]	$1/\zeta = \gamma \cdot E_F$ [eV]
2	81.5	0.03	86	0.075	$1.23{\cdot}10^{21}$	0.03
2.5	84	0.003	90	0.066	$1.16{\cdot}10^{21}$	0.01
3	89	0.001	95	0.066	$3.2{\cdot}10^{21}$	0.01
5	84.5	0.001	90	0.076	$1.9{\cdot}10^{21}$	0.15
10	85	0.001	90	0.077	$1.3{\cdot}10^{21}$	0.5

Table A.1: T_C — the superconducting temperature determined from superconducting fluctuation fit of $R_{xx}(T, B = 0)$, with error ± 0.5 K, it enters the $g(T)$ Eq. (1), (2) in main text; δ — pair-braking parameter that enters quantum correction to conductivity from Maki-Thompson process; T_{HSR} — the critical temperature of the Hall sign reversal appearance that enters $\Delta(T)$, with error ± 0.5 K; τ — relaxation time of the normal carrier in the vortex core; n_0 — normal carrier density inside the vortex core; E_F — Fermi energy; γ — the coupling constant of the attractive electron-electron interaction that induces superconductivity;

A.4 Hall Effect in the Superconducting Fluctuations Regime

Contribution to Hall conductivity from superconducting fluctuations in case of quasi-two dimensional film is[215]:

$$\delta\sigma_{xy} = \frac{e^2 k_B T \zeta}{\pi\hbar}\mathrm{sign}(B)\sum_{N=0}^{\infty}\frac{(N+1)(\mathcal{E}_{\mathcal{N}+1}-\mathcal{E}_{\mathcal{N}})^3}{\mathcal{E}_{\mathcal{N}}\mathcal{E}_{\mathcal{N}+1}(\mathcal{E}_{\mathcal{N}}+\mathcal{E}_{\mathcal{N}+1})^2}|_{\omega=0} \tag{A.13}$$

The function $\mathcal{E}_{\mathcal{N}}$ describes the superconducting fluctuations in the diffusive regime:

$$\mathcal{E}_{\mathcal{N}}(\omega, B, T) = \ln\left(\frac{T}{T_{c0}}\right) + \Psi\left(\frac{1}{2} + \frac{-i\omega + \Omega_c(N+1/2)}{4\pi k_B T}\right) - \Psi\left(\frac{1}{2}\right) + \zeta\omega. \tag{A.14}$$

Here, Ψ is the digamma function, and $\Omega_c = 4|e|\mu_0 DB$ is the energy of the cyclotron motion corresponding to the collective modes, where D is the diffusion coefficient of electrons.

To compare the values of fitting parameters D, ζ with experimental measurements of Hall mobility μ_H, we use equations $eD = e \cdot \tau \cdot (v_F^2/3)$ and $\mu_H = e\tau/m$. It is found that $D = 2/3 \cdot \mu_H \cdot E_F$, where E_F is Fermi energy in eV. Substituting E_F with $1/(\gamma\zeta)$ we get $D\gamma\zeta \propto 2/3 \cdot \mu_H$.

Contribution to Hall conductivity from superconducting fluctuations in case of a layered film is[223,215]:

$$\delta\sigma_{xy} = \frac{e^2 k_B T\zeta}{\pi\hbar} \cdot \frac{d}{s} \cdot \sum_{N=0}^{\infty}(N+1) \cdot \mathcal{S}(N), \tag{A.15}$$

$$\begin{aligned}\mathcal{S}(N) = &\frac{1}{\sqrt{[\varepsilon + h(2N+1)][r+\varepsilon+h(2N+1)]}} \\ &- \frac{1}{\sqrt{[\varepsilon + h(2N+3)][r+\varepsilon+h(2N+3)]}} \\ &- \frac{h}{\sqrt{[\varepsilon + h(2N+2)]^3[r+\varepsilon+h(2N+2)]}} \\ &- \frac{h}{\sqrt{[\varepsilon + h(2N+2)][r+\varepsilon+h(2N+2)]^3}},\end{aligned} \tag{A.16}$$

where $\varepsilon = \ln\left(\frac{T}{T_C}\right)$ is the reduced temperature, $r = -2J^2\tau^2 a/\hbar^2$ is the Lawrence-Doniach anisotropy parameter (Eq. A.4), $h = B/B_{c2}(0)$ is the reduced magnetic field, where $B_{c2}(0)$ is the second critical magnetic field: both for 5UC and 10 UC best fitting is with $B_{c2}(0) =$

80 T, which corresponds to reasonable value of superconducting coherence length $\xi = 2$ nm ($B_{c2}(0) = \Phi_0/(2\pi\xi^2)$). Figure 3b (main text) compares the locus $R_{xy}(T, B) = 0$ from the experiment with fits using both the vortex limit (solid line) and the SF limit (dashes) of the time-dependent Ginzburg-Landau equation.

A.5 Magnetoresistance $R_{xx}(B)$ below T_C. Vortex confinement

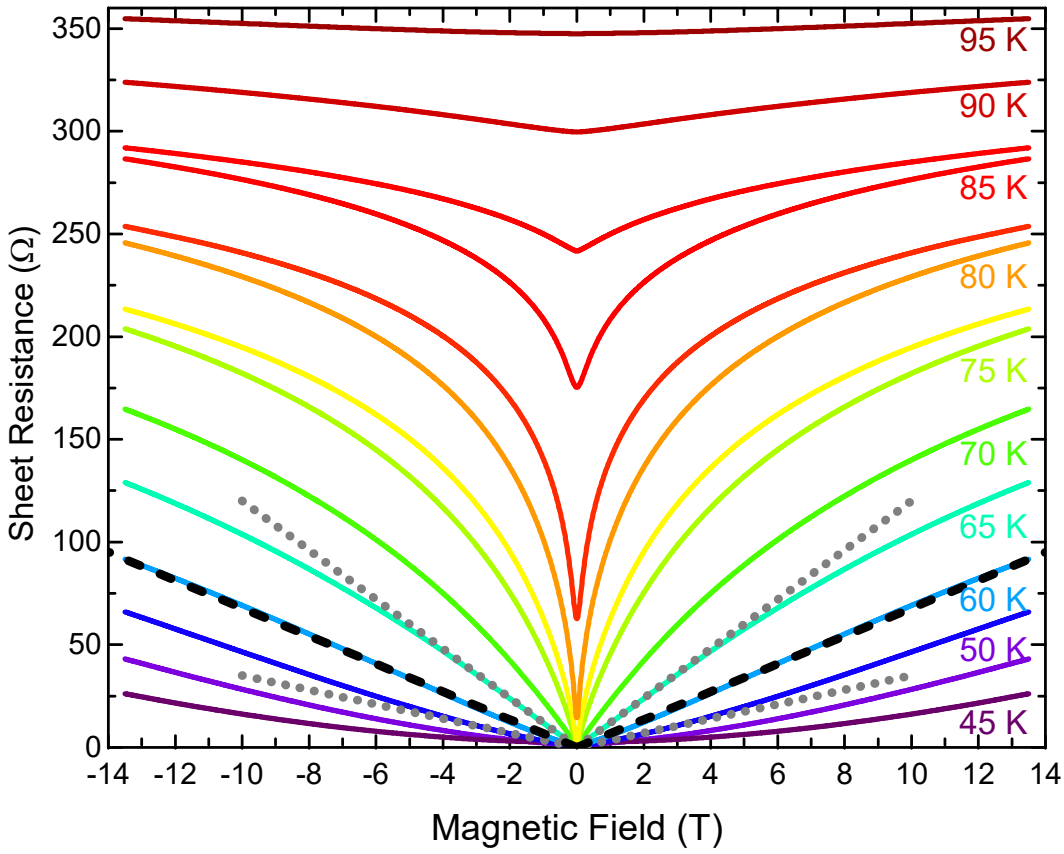

Figure A.4: Sheet resistance *vs.* magnetic field. Typical evolution of $R_{xx}(B)$ with temperatures. The 2UC device with $T_C = 81.5$ K. Dashed line emphasize the linear dependence $R(B)$ at T=60 K. The dotted lines are the tangents to isotherms lower and higher than T=60 K stressing the evolution from superlinear to sublinear behaviour.

With cooling the $R_{xx}(B)$ traces evolve from the sublinear to superlinear dependences. The

same evolution of $R(B)$ isotherms below T_C was reported in low-T superconductors[276], where it was used as a signature of the vortex-confined BKT phase[277,278]. Above T_{BKT} the vortex-antivortex pairs are unbound and all thermally induced vortices contribute to the resistance. Field-induced vortices annihilate with some fraction of antivortices, effectively reducing the number of vortices participating in the flux-flow, giving rise to a sublinear response to the applied field. The temperature T of the linear response marks $T = T_{BKT}$. Below T_{BKT} field-induced free vortices not only contribute to the resistance due to their own motion, but screen antivortices helping to dissociate vortex-antivortex pairs. This results in a superlinear response to the applied field.

B

Details for Emergent Interfacial Superconductivity between Twisted Cuprate Superconductors

B.1 Sample Fabrication Method

We have used a novel, all-dry, cryogenic pick-and-place technique to fabricate our Josephson junctions. Our technique allows us to cleave a pair of fresh surfaces of BSCCO from one pre-exfoliated single crystal, and then quickly stack the crystals together forming the twist junction. Oxygen dopants are conveniently frozen alongside any chemical degradation processes at -90 °C[99], preserving interfacial superconductivity. Since our transfer polymer does not melt at the final deposit step, the entire procedure can be cleanly performed in an argon glovebox without

solvents. Finally, since the junction is made starting from one single crystal, the twist angle can be accurately controlled to 0.5° and measured to 0.1° resolution using optical microscopy. Finally, we stress that this cryogenic pick-and-place technique should be generally applicable to any air- and heat-sensitive material.

All dry vdW pickup techniques[56,57] relies on temperature to control adhesion to a polymeric transfer stamp[135,130]. We use poly(dimethylsiloxane) (PDMS) to decrease T_g to about $-100°$ C[134], which is accessible to a liquid nitrogen cooled stage in a pure argon environment. We are careful to set the substrate temperature above the frost-point of our glovebox, where ice visibly sublimates on our substrates. This is carefully kept below $-100°C$, corresponding to roughly 10 parts per billion (ppb) of H_2O by volume[139]. Finally, PDMS freely releases vdW crystals onto the substrate at $-35°C$ without melting[132].

We prepare our PDMS using Dow Corning Sylgard 184, mixed to 10:1 base:curing agent ratio. The mixture is poured onto a clean glass slide with 1mm thickness, vacuum degassed, and baked overnight at 90 °C. The cured PDMS is then cut into 2 × 2 mm square, and placed onto a glass slide, and baked to 300 °C for 15 minutes for adhesion.

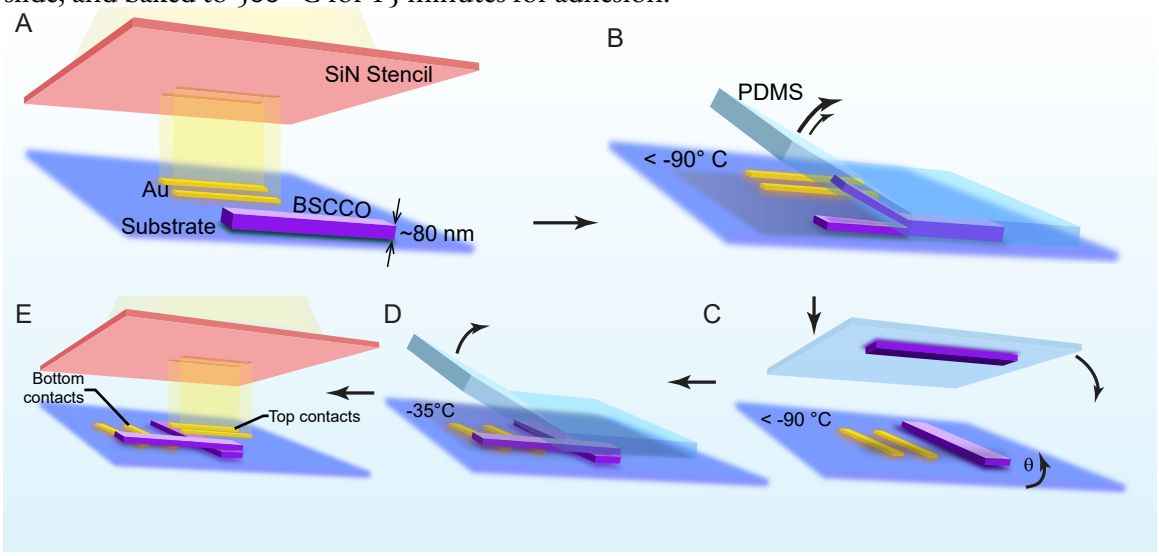

Figure B.1: Fabrication Process.

We first identify a flat, near optimally-doped BSCCO crystal roughly 80 nm thick, exfoliated onto a pre-baked and oxygen plasma cleaned substrate (Figure B.1). Next, we evaporate gold contacts next to (but in contact with) the BSCCO using a stencil mask technique[26], with a Peltier-cooled evaporator sample stage (-30 ° C). We then cool the substrate to -80 ° C, and touch a small corner of a PDMS stamp to the BSCCO. After the stamp cools down, we quickly[141] pull it off. The competition of adhesion forces between BSCCO, the substrate and cold PDMS often cleaves the crystal along a flat plane between BiO planes. We rapidly rotate the substrate by an angle θ, and place the upper BSCCO crystal on top of both the lower crystal and gold contacts. Next, the substrate is heated to -35 ° C and the PDMS slowly[141] removed. Finally, a second set of gold contacts is evaporated onto the *top* surface of the *bottom* BSCCO crystal using a stencil mask. This contact geometry minimizes resistance contribution from intrinsic Josephson junctions along the c-axis in each bulk crystal. We emphasize that the BSCCO crystals were kept at or below room temperature, and away from air throughout the fabrication process. Figure 8.1B shows a completed device. Time between fabrication and measurements are kept as short as possible, within 2 days.

B.2 Measurement Method

All electrical measurements were performed using using 4 contacts to eliminate contact resistances. dV/dI measurements are performed by adding AC ($15 < f < 150$ Hz) and DC voltages generated by a Stanford Research Systems SR830 lock-in amplifier (with 1/1000 voltage divider) and Keithley 2400 SourceMeter, with a toroidal transformer. The voltage output passes through a large resistor to form a current source. The voltage across the junction is amplified with a SR570 low-noise preamp, and measured with a Agilent 34401A multimeter and SR830 lock-in amplifier. Cryogenic temperatures are reached using helium flow cryostats.

Shapiro step measurements are performed by generating a $f_{RF} < 50$ GHz microwave signal

(Keysight E8257D) and guiding it to the sample through a low-loss semi-rigid coaxial cable with 1.85 mm air dielectric connector (Pasternack PE3C6490). It is epoxy-set into a KF-25 adapter at the cryostat wall (Torr-Seal. Caution: Torr-Seal epoxy will crack if significantly cooled). The coax shield is cut about 3 mm shorter than the center wire, forming an improvised antenna a few mm above the sample substrate. Care was taken not minimize bends to the coax cable.

The AFM topography data is taken after the electrical measurement, in a Park AFM system in non-contact mode.

B.3 List of Devices for Angle-Dependent $I_C R_N$ Analysis

Here we list all devices used in the angle-dependent $I_C R_N$ analysis. We have excluded non-superconducting devices and those with less than 2 contacts on each side of the Josephson junction, which is necessary for a 4-point measurement. To keep doping levels consistent between devices, we have also eliminated junctions with superconducting transition temperature below 79 K. We take T_C to be the temperature where the junction resistance falls to within 1% of the value at $90K$, at zero current bias.

R_N is extracted just under T_C at high bias, in order to minimize contributions from in-plane resistance, whose critical current is expected to be high.

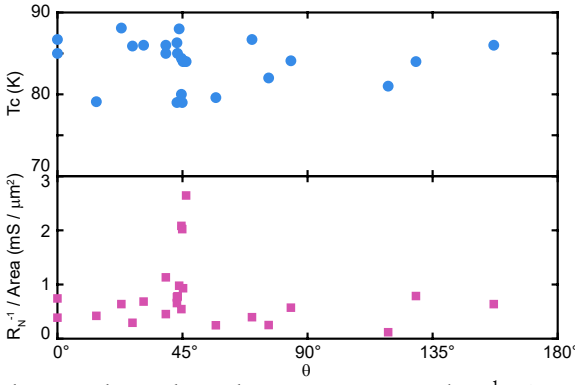

Figure B.2: Angular dependence and sample quality. Junction T_C and R_N^{-1} / Area vs angle respectively, showing no systematic angular dependence of junction transport quality.

Table B.1: Summary of device transport characteristics.

θ degrees	Area μ m^2	T_C K	R_N Ω	R_N^{-1} / Area mS/μ m^2	$I_C(30K)$ / Area A / cm^2
0	376	86.7	3.6	0.743	1220
0	1393	85	1.9	0.388	577
14	255	79.1	9.3	0.422	927
23	522	88.1	3.0	0.639	1050
27	497	85.9	6.9	0.294	326
119	736	81	11.4	0.119	55
31	417	86	3.5	0.685	106
39	446	85	2.0	1.132	250
39	737	86	3.0	0.454	200
129	144	84	8.8	0.787	140
43	111	86.3	13.7	0.658	90
43	170	79	7.7	0.764	14
43.2	77	85	16.6	0.782	222
43.8	568	88	1.8	0.978	119
44.6	151	80	3.2	2.083	116
44.6	294	84.4	6.2	0.546	45
44.9	123	79	4.0	2.022	38
45.2	182	84	5.9	0.931	32
46.3	130	84	2.9	2.643	412
57	374	79.6	10.8	0.248	170
157	148	86	10.6	0.638	1250
70	293	86.7	8.6	0.397	671
76	227	82	17.5	0.252	442
84	296	84.1	5.9	0.573	848

Figure B.2 shows that while each device is somewhat unique, there is no systematic angular dependence on the junction T_C or conductivity R_N^{-1}/A. The angular variation in $I_C R_N$ is due to intrinsic effects near 45° rather than extrinsic differences in junction transparency or quality.

B.4 dV/dI Data for All Samples

Figure B.3 shows the dV/dI color plots for all devices, in the same format as shown in Fig 8.2A in the main text.

Figure B.4 shows the $I_C R_N(T)$ for all devices, in the same format as shown in Fig 8.2C in the main text.

B.5 Voltage Jump at the Critical Current

The *I-V* characteristics features a jump at I_C, which provides an independent way to measure the symmetry of the superconducting order parameter. Figure B.5 shows the twist angle dependence of $V(I_C)$ for all devices, at four different temperatures. $V(I_C)$ closely matches the expected $|\cos(2\varphi)|$ dependence expected of SIS Josephson junctions between *d*-wave superconductors.

B.6 Anomalous temperature dependence of Critical Current

To better understand the temperature dependence of the critical current in twisted samples, including close to 45° twist, it is useful to derive an exact expression for $I(\phi)$ that does not rely on perturbative expansion in the interlayer coupling t. To this end we rewrite the Hamiltonian as $\mathcal{H} = \sum_{\boldsymbol{k}} \Psi^\dagger_{\boldsymbol{k}} H_{\boldsymbol{k}} \Psi_{\boldsymbol{k}} + E_0$ where $\Psi_{\boldsymbol{k}} = (c_{\boldsymbol{k}\uparrow 1}, c^\dagger_{-\boldsymbol{k}\downarrow 1}, c_{\boldsymbol{k}\uparrow 2}, c^\dagger_{-\boldsymbol{k}\downarrow 2})^T$ represents a four-component Nambu spinor, E_0 is a constant and the BdG Hamiltonian is a 4×4 matrix

$$H_{\boldsymbol{k}} = \begin{pmatrix} \xi_{\boldsymbol{k}1} & \Delta_{\boldsymbol{k}1} & t & 0 \\ \Delta^*_{\boldsymbol{k}1} & -\xi_{\boldsymbol{k}1} & 0 & -t \\ t & 0 & \xi_{\boldsymbol{k}2} & \Delta_{\boldsymbol{k}2} \\ 0 & -t & \Delta^*_{\boldsymbol{k}2} & -\xi_{\boldsymbol{k}2} \end{pmatrix}. \tag{B.1}$$

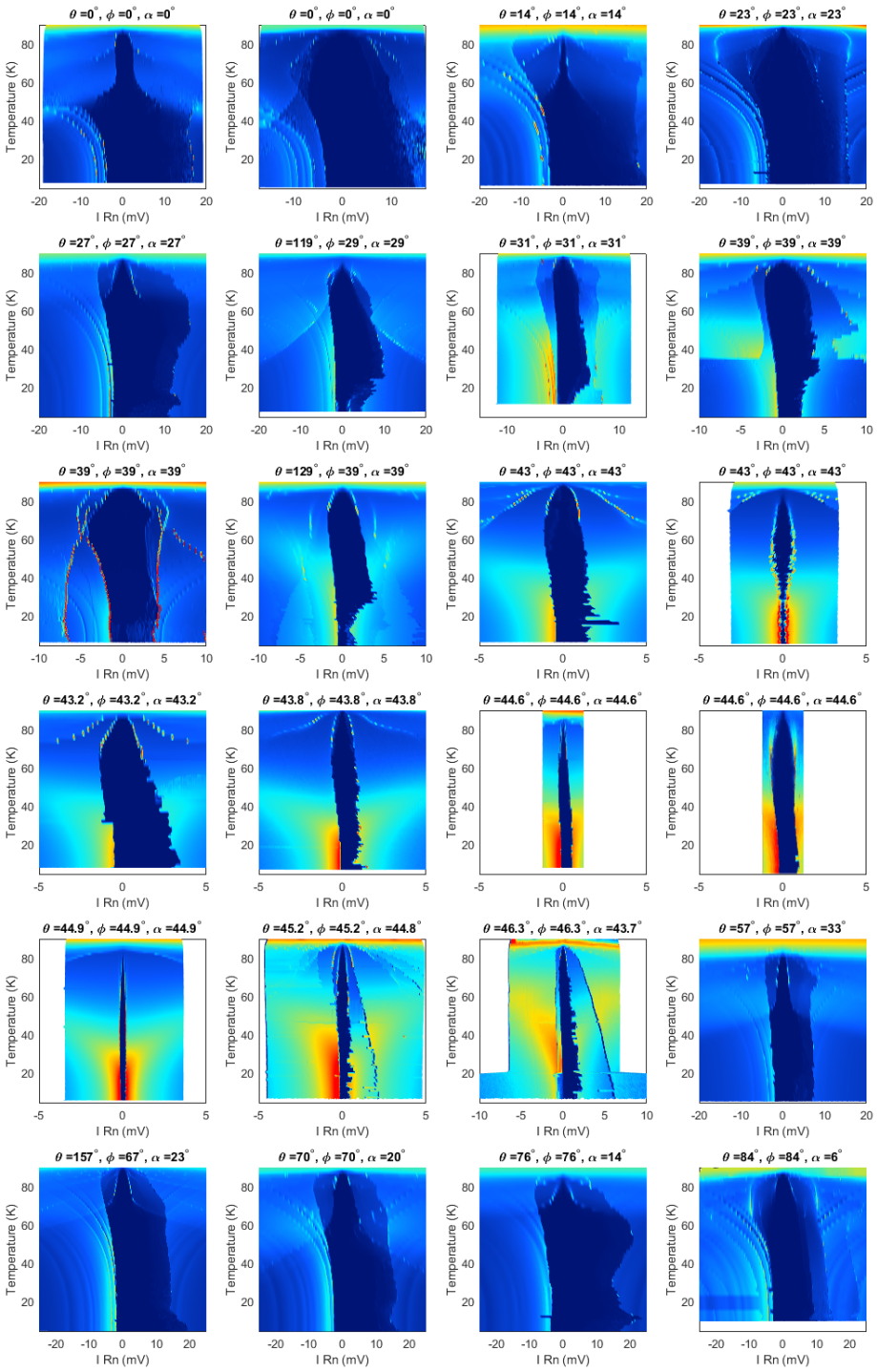

Figure B.3: Color Plot of dV/dI for All Junctions.

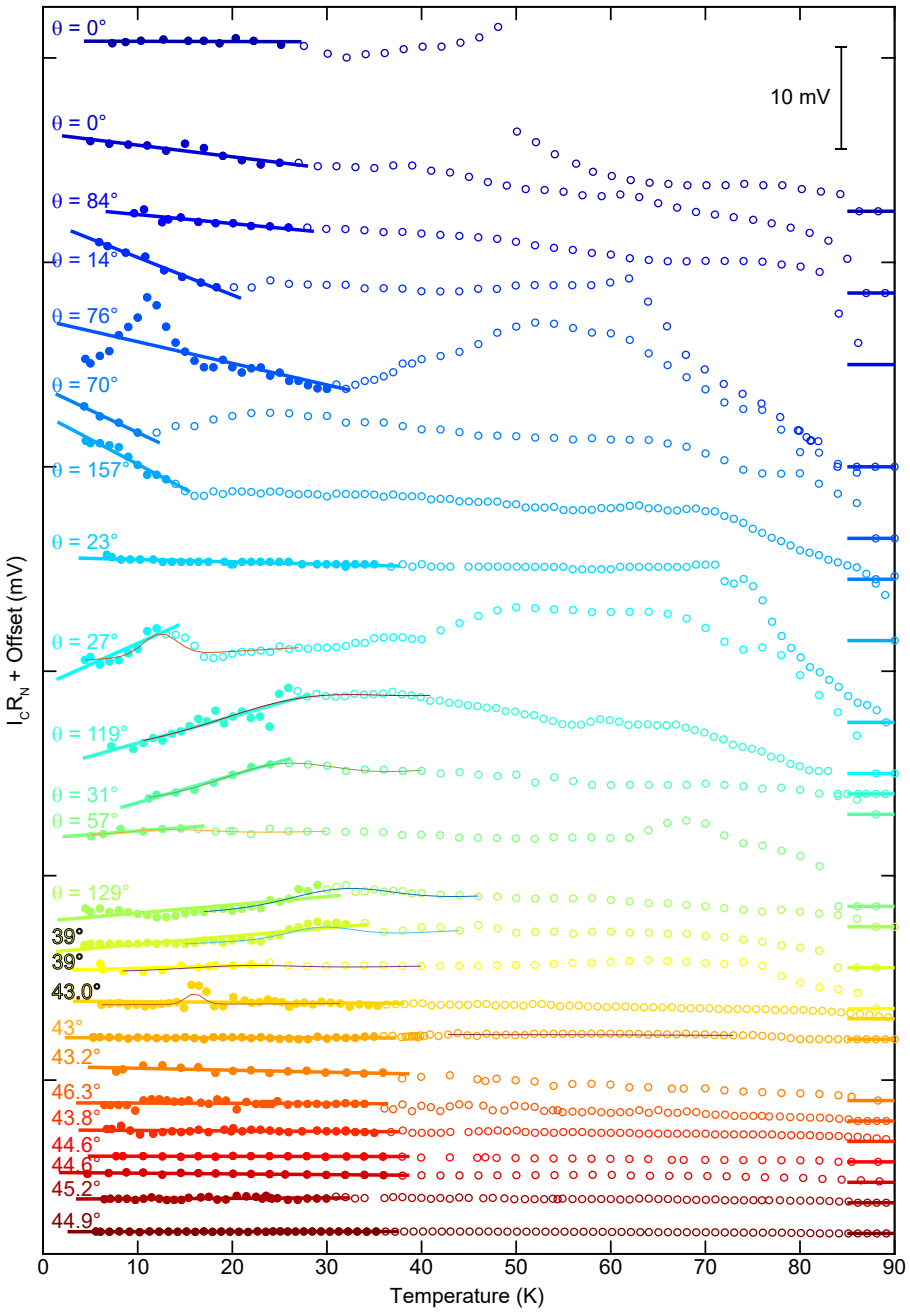

Figure B.4: $I_C R_N(T)$ **for all samples with** $T_C > 79$ **K.** Solid points are used to extract $d[I_C R_N]/dT$ by linear fit (lines). Red curves fits to the peak in $I_C R_N(T)$. Horizontal lines at right side of plot shows the offset for each curve, where $I_C R_N = 0$. Curves are ordered by $|\varphi - \pi/4|$ where $\varphi = \theta \bmod \pi/2$.

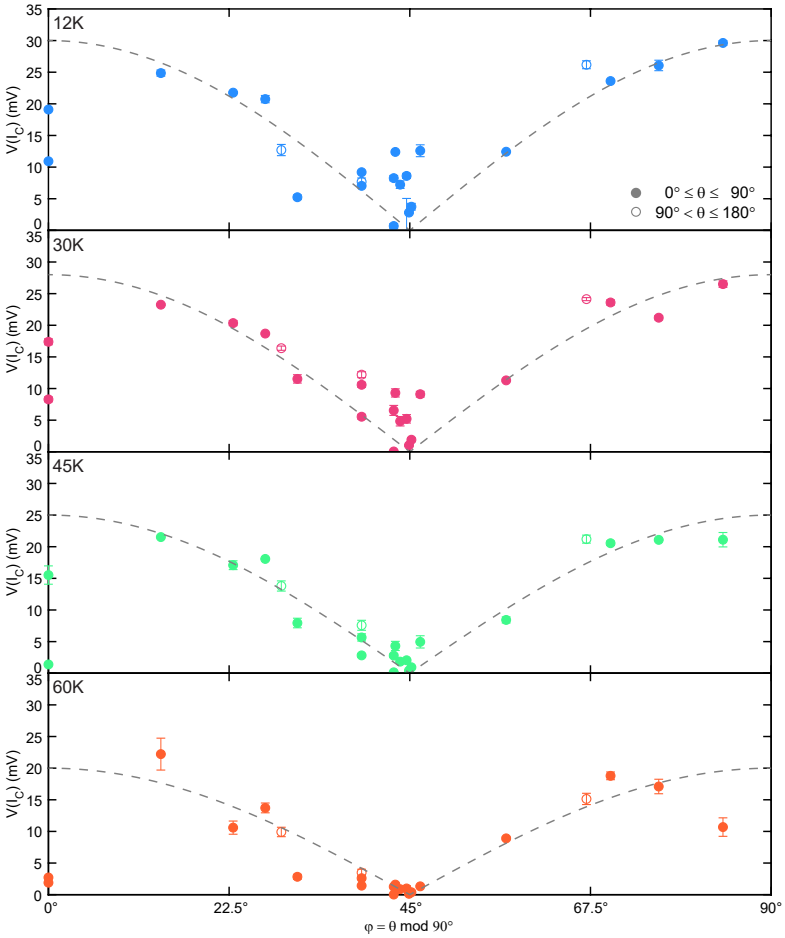

Figure B.5: $V(I_C)$ **vs** φ. Dashed line shows the $|\cos(2\varphi)|$ dependence expected for JJs between d-wave superconductors.

Here $\xi_{\boldsymbol{k}\alpha}$ and $\Delta_{\boldsymbol{k}\alpha}$ represent the single-particle dispersion and the gap function, respectively, in layer $\alpha = 1, 2$, related by rotation through twist angle θ. The free energy of the system is given by

$$\mathcal{F}_{\text{BdG}} = E_0 - 2k_B T \sum_{\boldsymbol{k}a} \ln\left[2\cosh\left(E_{\boldsymbol{k}a}/2k_B T\right)\right]. \tag{B.2}$$

where the sum extends over all positive energy eigenvalues $E_{\boldsymbol{k}a}$ of $H_{\boldsymbol{k}}$. The interlayer supercurrent can now be obtained from the Josephson relation

$$I(\phi) = (2e/\hbar) d\mathcal{F}_{\mathrm{BdG}}/d\phi, \tag{B.3}$$

where ϕ is the phase difference between the layers, assumed to be held constant.

To enable analytic progress we assume a simple rotation-invariant dispersion relation $\xi_{\boldsymbol{k}} = \hbar^2 k^2/2m - \mu$ common to both layers and we focus on the case when interlayer tunneling conserves the in-plane momentum. The twist is encoded in the gap functions $\Delta_{\boldsymbol{k}1,2} = \Delta \cos(2\alpha_{\boldsymbol{k}} \pm \theta)$ where $\alpha_{\boldsymbol{k}}$ denotes the polar angle of vector $\boldsymbol{k}$. The two positive eigenvalues of the BdG Hamiltonian (B.1) are then given by

$$E_{\boldsymbol{k}\pm} = \sqrt{(\Delta_{\boldsymbol{k}1}^2 + \Delta_{\boldsymbol{k}2}^2)/2 + \xi_{\boldsymbol{k}}^2 + t^2 \pm D_{\boldsymbol{k}}(\phi)} \tag{B.4}$$

where $D_{\boldsymbol{k}}^2(\phi) = (\Delta_{\boldsymbol{k}1}^2 - \Delta_{\boldsymbol{k}2}^2)^2/4 + t^2(\Delta_{\boldsymbol{k}1}^2 + \Delta_{\boldsymbol{k}2}^2 + 4\xi_{\boldsymbol{k}}^2 - 2\Delta_{\boldsymbol{k}1}\Delta_{\boldsymbol{k}2}\cos\phi)$. Noting that the phase ϕ only enters through the cosine term in $D_{\boldsymbol{k}}^2(\phi)$ it is possible, with use of Eq. (B.3), to express the supercurrent as

$$I(\phi) = -\sin\phi \frac{et^2}{2\hbar} \sum_{\boldsymbol{k}} \frac{\Delta_{\boldsymbol{k}1}\Delta_{\boldsymbol{k}2}}{D_{\boldsymbol{k}}(\phi)} \sum_{a=\pm} \frac{a}{E_{\boldsymbol{k}a}} \tanh \frac{1}{2}\beta E_{\boldsymbol{k}a}. \tag{B.5}$$

This relation is non-perturbative in t, which gives small but non-vanishing critical current even at $\theta = 45°$, in agreement with experimental observations.

To determine I_c it is necessary to find the maximum of $I(\phi)$ given by Eq. (B.5). Because the maximum is attained at a generic value of ϕ this can generally only be done numerically. We find, however, that for twist angles not too close to $45°$ the maximum occurs near $\phi = \pi/2$ and one can approximate $I_c \approx I(\pi/2)$ to a good accuracy. The temperature dependence of the critical

current can therefore be usefully analyzed from the expression

$$I_c(T) \simeq \frac{et^2}{2\hbar} \sum_{\boldsymbol{k}} \frac{\Delta_{\boldsymbol{k}1}\Delta_{\boldsymbol{k}2}}{D_{\boldsymbol{k}}(\pi/2)} \sum_{a=\pm} \left[\frac{-a}{E_{\boldsymbol{k}a}} \tanh \frac{1}{2}\beta E_{\boldsymbol{k}a} \right]_{\phi\to\pi/2}. \tag{B.6}$$

Noting that by definition $E_{\boldsymbol{k}+} > E_{\boldsymbol{k}-}$ it is easy to show that the last term $\sum_{a=\pm}[\dots]$ in the above equation is non-negative for all temperatures T, as is $D_{\boldsymbol{k}}(\pi/2)$. The sign of the contribution of each momentum $\boldsymbol{k}$ to the critical current is therefore solely determined by the product of the two d-wave gap functions $\Delta_{\boldsymbol{k}1}\Delta_{\boldsymbol{k}2} = \Delta^2 \cos(2\alpha_{\boldsymbol{k}} + \theta)\cos(2\alpha_{\boldsymbol{k}} - \theta)$. It is easy to see that for non-zero twist this product is *negative* in the vicinity of the Brillouin zone diagonals, i.e. the nodal region of the original untwisted d-wave superconductor, and is positive in the rest of the BZ. This structure provides for a simple intuitive understanding of the observed decrease in $I_c(0)$ with an increasing twist angle. When $\theta = 0$ there are only positive contributions to $I_c(0)$ from the $\boldsymbol{k}$ sum and all momenta contribute coherently. On the other hand for $\theta > 0$ nodal regions begin to contribute negatively, eventually driving the critical current to near zero when $\theta \simeq 45^\circ$.

The sign structure in Eq. (B.6) also helps explain the anomalous increase in $I_c(T)$ at low temperatures observed for non-zero twist angles. Nonzero temperature promotes existence of pair-breaking excitations which tend to suppress the supercurrent. In a d-wave superconductor low-energy excitations reside in the nodal region of the BZ meaning that at low temperatures Cooper pairs composed of electrons with momenta in the nodal region are broken with the highest probability. We argued above, however, that in a twisted configuration nodal regions give a *negative* contribution to $I_c(0)$. Reducing this negative contribution by thermal excitations will therefore produce a *net increase* in the total supercurrent. A detailed analysis of Eq. (B.6) given in Ref.[269] indeed shows an exponentially activated increase in $I_c(T)$ at the lowest temperatures that can be attributed to a spectral gap $\sim t^2/\Delta$ induced by the $\pi/2$ interlayer phase difference. At temperatures above this small energy scale one finds $I_c(T) \simeq I_c(0) + a_\theta T - b_\theta T^3$ with a_θ and b_θ non-negative, twist-angle dependent coefficients. The theoretical analysis thus predicts an ap-

proximately linear increase in $I_c(T)$ up to a maximum at $T_{\max} = \sqrt{a_\theta/3b_\theta}$, followed by a decrease at higher temperatures. Coefficient a_θ is found to grow with increasing θ, reflecting the increasing range of momenta where $\Delta_{\boldsymbol{k}1}\Delta_{\boldsymbol{k}2} < 0$. This causes the position of the maximum $T_{\max}$ to shift to higher temperatures for larger θ, giving rise to a behavior that is qualitatively consistent with $I_c(T)$ measured in our twisted junctions.

B.7 Shapiro Step Frequency Dependence

Shapiro steps are expected to appear at multiples n of $hf/2e$, where f is the illuminating microwave frequency. We explicitly check this dependence in Figure B.6, where the periodic dV/dI dips fan out linearly with f, at both integer and half-integer n, as expected. This is evidence that the observed dV/dI dips are indeed Shapiro steps.

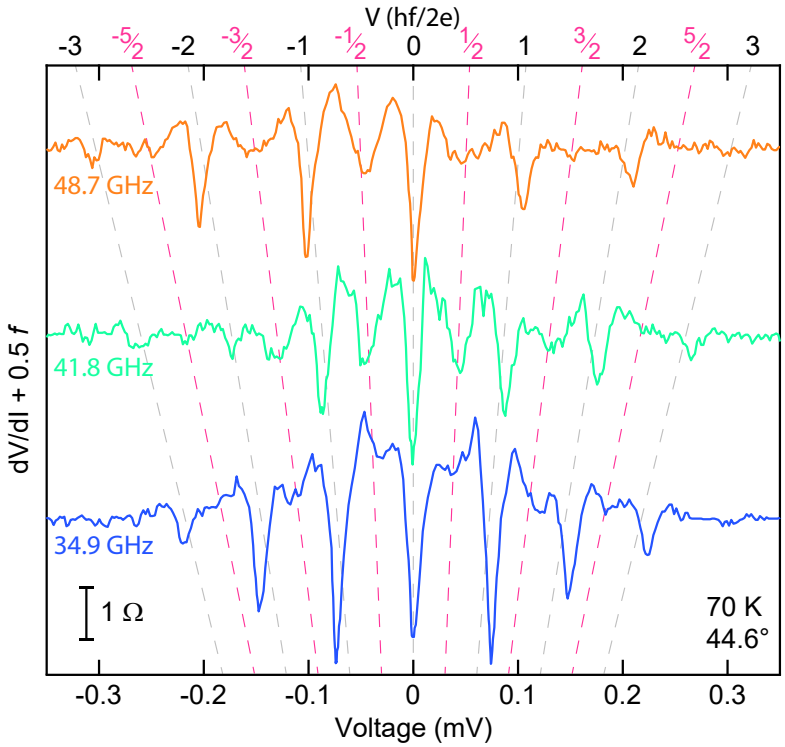

Figure B.6: Shapiro step frequency dependence, showing junction dV/dI vs. V under microwave illumination at frequency f. Each trace is offset by $0.5f$, so that the expected position of each Shapiro step follows the dashed lines. Half-integer steps are highlighted in red.

B.8 Josephson Length Estimate

The magnetic fields enclosed in Josephson junctions are expected to vary on scale of the Josephson length λ_J[81]. Junctions with lateral size exceeding λ_J may contain Josephson vortices, whose dynamics can also induce subharmonic Shapiro steps. Such steps usually appear at nonzero magnetic fields in large junctions.

We can estimate the Josephson length by the expression $\lambda_J = \sqrt{\hbar/2e\mu_0 J_C d}$, where J_C is the critical current density and d is the thickness of the bulk crystal surface layer where magnetic fields may penetrate[81]. From our Fraunhofer patterns, $d \approx 30$ nm and is bounded above by the total thickness of the device. In our 44.6° junction, the critical current density is 9.7 A / cm^2, which corresponds to $\lambda_J = 300\mu m$. This is 10 times larger than the actual lateral size of the device, which is about 25 μm on the longest axis. For such small devices, subharmonic Shapiro steps originating from flux dynamics is not expected to appear.

In addition, our Shapiro steps are detected at zero magnetic field, and only appear when the twist angle *theta* is within about a 1° range around 45°. This is precisely the angle where J_C is maximally suppressed and λ_J reaches a maximum. We therefore conclude that the half-integer Shapiro steps are unlikely to originate from flux motion.

References

[1] F. Arute, K. Arya, R. Babbush, D. Bacon, J. C. Bardin, R. Barends, R. Biswas, S. Boixo, F. G. S. L. Brandao, D. A. Buell, B. Burkett, Y. Chen, Z. Chen, B. Chiaro, R. Collins, W. Courtney, A. Dunsworth, E. Farhi, B. Foxen, A. Fowler, C. Gidney, M. Giustina, R. Graff, K. Guerin, S. Habegger, M. P. Harrigan, M. J. Hartmann, A. Ho, M. Hoffmann, T. Huang, T. S. Humble, S. V. Isakov, E. Jeffrey, Z. Jiang, D. Kafri, K. Kechedzhi, J. Kelly, P. V. Klimov, S. Knysh, A. Korotkov, F. Kostritsa, D. Landhuis, M. Lindmark, E. Lucero, D. Lyakh, S. Mandrà, J. R. McClean, M. McEwen, A. Megrant, X. Mi, K. Michielsen, M. Mohseni, J. Mutus, O. Naaman, M. Neeley, C. Neill, M. Y. Niu, E. Ostby, A. Petukhov, J. C. Platt, C. Quintana, E. G. Rieffel, P. Roushan, N. C. Rubin, D. Sank, K. J. Satzinger, V. Smelyanskiy, K. J. Sung, M. D. Trevithick, A. Vainsencher, B. Villalonga, T. White, Z. J. Yao, P. Yeh, A. Zalcman, H. Neven, and J. M. Martinis, "Quantum supremacy using a programmable superconducting processor," *Nature*, 574, 7779, 505–510, 2019.

[2] N. Ashcroft and N. Mermin, *Solid State Physics*. Philadelphia, P.A.: Saunders College Publishing, 1976.

[3] P. Ajayan, P. Kim, and K. Banerjee, "Two-dimensional van der Waals materials," *Physics Today*, 69, 9, 38–44, 2016.

[4] A. K. Geim and I. V. Grigorieva, "Van der Waals heterostructures," *Nature*, 499, 7459, 419–425, 2013.

[5] K. S. Novoselov, "Electric Field Effect in Atomically Thin Carbon Films," *Science*, 306, 5696, 666–669, 2004.

[6] K. S. Novoselov, D. Jiang, F. Schedin, T. J. Booth, V. V. Khotkevich, S. V. Morozov, and A. K. Geim, "Two-dimensional atomic crystals," *Proc. Natl. Acad. Sci. USA*, 102, 10451, 2005.

[7] T.-A. Chen, C.-P. Chuu, C.-C. Tseng, C.-K. Wen, H.-S. P. Wong, S. Pan, R. Li, T.-A. Chao, W.-C. Chueh, Y. Zhang, Q. Fu, B. I. Yakobson, W.-H. Chang, and L.-J. Li, "Wafer-scale single-crystal hexagonal boron nitride monolayers on Cu (111)," *Nature*, 579, 7798, 219–223, 2020.

[8] M. Blei, J. L. Lado, Q. Song, D. Dey, O. Erten, V. Pardo, R. Comin, S. Tongay, and A. S. Botana, "Synthesis, engineering, and theory of 2D van der Waals magnets," *Appl. Phys. Rev.*, 8, 2, 021301, 2021.

[9] M. Xu, T. Liang, M. Shi, and H. Chen, "Graphene-Like Two-Dimensional Materials," *Chemical Reviews*, 113, 5, 3766–3798, 2013.

[10] Y. Zhang, Y.-W. Tan, H. L. Stormer, and P. Kim, "Experimental observation of the quantum Hall effect and Berry's phase in graphene," *Nature*, 438, 7065, 201–204, 2005.

[11] K. I. Bolotin, F. Ghahari, M. D. Shulman, H. L. Stormer, and P. Kim, "Observation of the fractional quantum Hall effect in graphene," *Nature*, 462, 7270, 196–199, 2009.

[12] C. R. Dean, A. F. Young, I. Meric, C. Lee, L. Wang, S. Sorgenfrei, K. Watanabe, T. Taniguchi, P. Kim, K. L. Shepard, and J. Hone, "Boron nitride substrates for high-quality graphene electronics," *Nat. Nano.*, 5, 10, 722–726, 2010.

[13] K. F. Mak, C. Lee, J. Hone, J. Shan, and T. F. Heinz, "Atomically Thin MoS 2 : A New Direct-Gap Semiconductor," *Phys. Rev. Lett.*, 105, 13, 136805, 2010.

[14] A. Tsen, B. Hunt, Y. Kim, Z. Yuan, S. Jia, R. J. Cava, J. Hone, P. Kim, C. Dean, and A. Pasupathy, "Nature of the quantum metal in a two-dimensional crystalline superconductor," *Nat. Phys.*, 12, 3, 208–212, 2016.

[15] I. Tamir, A. Benyamini, E. J. Telford, F. Gorniaczyk, A. Doron, T. Levinson, D. Wang, F. Gay, B. Sacépé, J. Hone, K. Watanabe, T. Taniguchi, C. R. Dean, A. N. Pasupathy, and D. Shahar, "Sensitivity of the superconducting state in thin films," *Sci. Adv.*, 5, 3, 1–7, 2019.

[16] A. Benyamini, E. J. Telford, D. M. Kennes, D. Wang, A. Williams, K. Watanabe, T. Taniguchi, D. Shahar, J. Hone, C. R. Dean, A. J. Millis, and A. N. Pasupathy, "Fragility of the dissipationless state in clean two-dimensional superconductors," *Nat. Phys.*, 15, 9, 947–953, 2019.

[17] B. Huang, G. Clark, E. Navarro-Moratalla, D. R. Klein, R. Cheng, K. L. Seyler, D. Zhong, E. Schmidgall, M. A. McGuire, D. H. Cobden, W. Yao, D. Xiao, P. Jarillo-Herrero, and X. Xu, "Layer-dependent ferromagnetism in a van der Waals crystal down to the monolayer limit," *Nature*, 546, 7657, 270–273, 2017.

[18] D. R. Klein, D. MacNeill, J. L. Lado, D. Soriano, E. Navarro-Moratalla, K. Watanabe, T. Taniguchi, S. Manni, P. Canfield, J. Fernández-Rossier, and P. Jarillo-Herrero, "Probing magnetism in 2D van der Waals crystalline insulators via electron tunneling," *Science*, 360, 6394, 1218–1222, 2018.

[19] K. S. Burch, D. Mandrus, and J.-G. Park, "Magnetism in two-dimensional van der Waals materials," *Nature*, 563, 7729, 47–52, 2018.

[20] L. J. Sandilands, Y. Tian, K. W. Plumb, Y.-J. Kim, and K. S. Burch, "Scattering Continuum and Possible Fractionalized Excitations in α - RuCl 3," *Phys. Rev. Lett.*, 114, 14, 147201, 2015.

[21] A. Banerjee, J. Yan, J. Knolle, C. A. Bridges, M. B. Stone, M. D. Lumsden, D. G. Mandrus, D. A. Tennant, R. Moessner, and S. E. Nagler, "Neutron scattering in the proximate quantum spin liquid α-RuCl $_3$," *Science*, 356, 6342, 1055–1059, 2017.

[22] M. Hasan and C. Kane, "Colloquium: Topological insulators," *Rev. Mod. Phys.*, 82, 4, 3045–3067, 2010.

[23] J. G. Checkelsky, Y. S. Hor, R. J. Cava, and N. P. Ong, "Bulk Band Gap and Surface State Conduction Observed in Voltage-Tuned Crystals of the Topological Insulator Bi 2 Se 3," *Phys. Rev. Lett.*, 106, 19, 196801, 2011.

[24] Y. Deng, Y. Yu, M. Z. Shi, Z. Guo, Z. Xu, J. Wang, X. H. Chen, and Y. Zhang, "Quantum anomalous Hall effect in intrinsic magnetic topological insulator MnBi $_2$ Te $_4$," *Science*, 367, 6480, 895–900, 2020.

[25] Y. Yu, L. Ma, P. Cai, R. Zhong, C. Ye, J. Shen, G. D. Gu, X. H. Chen, and Y. Zhang, "High-temperature superconductivity in monolayer Bi2Sr2CaCu2O8+δ," *Nature*, 575, 7781, 156–163, 2019.

[26] S. Y. Zhao, N. Poccia, M. G. Panetta, C. Yu, J. W. Johnson, H. Yoo, R. Zhong, G. D. Gu, K. Watanabe, T. Taniguchi, S. V. Postolova, V. M. Vinokur, and P. Kim, "Sign-Reversing Hall Effect in Atomically Thin High-Temperature Bi2.1Sr1.9CaCu2.0 O8+δ Superconductors," *Phys. Rev. Lett.*, 122, 24, 1–6, 2019.

[27] M. Liao, Y. Zhu, J. Zhang, R. Zhong, J. Schneeloch, G. Gu, K. Jiang, D. Zhang, X. Ma, and Q.-K. Xue, "Superconductor–Insulator Transitions in Exfoliated Bi $_2$ Sr $_2$ CaCu $_2$ O $_{8+\delta}$ Flakes," *Nano Lett.*, 18, 9, 5660–5665, 2018.

[28] M. J. Gray, J. Freudenstein, S. Y. F. Zhao, R. O'Connor, S. Jenkins, N. Kumar, M. Hoek, A. Kopec, S. Huh, T. Taniguchi, K. Watanabe, R. Zhong, C. Kim, G. D. Gu, and K. S. Burch, "Evidence for Helical Hinge Zero Modes in an Fe-Based Superconductor," *Nano Lett.*, 19, 8, 4890–4896, 2019.

[29] B. Lei, J. H. Cui, Z. J. Xiang, C. Shang, N. Z. Wang, G. J. Ye, X. G. Luo, T. Wu, Z. Sun, and X. H. Chen, "Evolution of High-Temperature Superconductivity from a Low- T c Phase Tuned by Carrier Concentration in FeSe Thin Flakes," *Phys. Rev. Lett.*, 116, 7, 077002, 2016.

[30] Y. Li, H. Yan, B. Xu, L. Zhen, and C.-Y. Xu, "Electrochemical Intercalation in Atomically Thin van der Waals Materials for Structural Phase Transition and Device Applications," *Adv. Mat.*, 33, 6, 2000581, 2021.

[31] F. Miao, S.-J. Liang, and B. Cheng, "Straintronics with van der Waals materials," *npj Quantum Materials*, 6, 1, 59, 2021.

[32] S. J. Haigh, A. Gholinia, R. Jalil, S. Romani, L. Britnell, D. C. Elias, K. S. Novoselov, L. A. Ponomarenko, A. K. Geim, and R. Gorbachev, "Cross-sectional imaging of individual layers and buried interfaces of graphene-based heterostructures and superlattices," *Nat. Mater.*, 11, 9, 764–767, 2012.

[33] C. R. Dean, L. Wang, P. Maher, C. Forsythe, F. Ghahari, Y. Gao, J. Katoch, M. Ishigami, P. Moon, M. Koshino, T. Taniguchi, K. Watanabe, K. L. Shepard, J. Hone, and P. Kim, "Hofstadter's butterfly and the fractal quantum Hall effect in moiré superlattices," *Nature*, 497, 7451, 598–602, 2013.

[34] X. Liu, K. Watanabe, T. Taniguchi, B. I. Halperin, and P. Kim, "Quantum Hall drag of exciton condensate in graphene," *Nat. Phys.*, 13, 8, 746–750, 2017.

[35] H. Yoo, R. Engelke, S. Carr, S. Fang, K. Zhang, P. Cazeaux, S. H. Sung, R. Hovden, A. W. Tsen, T. Taniguchi, K. Watanabe, G.-C. Yi, M. Kim, M. Luskin, E. B. Tadmor, E. Kaxiras, and P. Kim, "Atomic and electronic reconstruction at the van der Waals interface in twisted bilayer graphene," *Nat. Mater.*, 18, 5, 448–453, 2019.

[36] Y. Cao, V. Fatemi, S. Fang, K. Watanabe, T. Taniguchi, E. Kaxiras, and P. Jarillo-Herrero, "Unconventional superconductivity in magic-angle graphene superlattices," *Nature*, 556, 7699, 43–50, 2018.

[37] S. Franssila, *Introduction Microfabrication*. West Sussex, U.K.: Wiley, 2nd ed., 2010.

[38] A. Cheng, T. Taniguchi, K. Watanabe, P. Kim, and J.-D. Pillet, "Guiding Dirac Fermions in Graphene with a Carbon Nanotube," *Phys. Rev. Lett.*, 123, 21, 216804, 2019.

[39] L. A. Jauregui, A. Y. Joe, K. Pistunova, D. S. Wild, A. A. High, Y. Zhou, G. Scuri, K. De Greve, A. Sushko, C.-H. Yu, T. Taniguchi, K. Watanabe, D. J. Needleman, M. D. Lukin, H. Park, and P. Kim, "Electrical control of interlayer exciton dynamics in atomically thin heterostructures," *Science*, 366, 6467, 870–875, 2019.

[40] X. Liu, Z. Hao, K. Watanabe, T. Taniguchi, B. I. Halperin, and P. Kim, "Interlayer fractional quantum Hall effect in a coupled graphene double layer," *Nat. Phys.*, 15, 9, 893–897, 2019.

[41] T. I. Andersen, B. L. Dwyer, J. D. Sanchez-Yamagishi, J. F. Rodriguez-Nieva, K. Agarwal, K. Watanabe, T. Taniguchi, E. A. Demler, P. Kim, H. Park, and M. D. Lukin, "Electron-phonon instability in graphene revealed by global and local noise probes," *Science*, 364, 154–157, 2019.

[42] B. Keimer, S. A. Kivelson, M. R. Norman, S. Uchida, and J. Zaanen, "From quantum matter to high-temperature superconductivity in copper oxides," *Nature*, 518, 7538, 179–186, 2015.

[43] Q. Si, R. Yu, and E. Abrahams, "High Temperature Superconductivity in Iron Pnictides and Chalcogenides," *Nat. Rev. Mater.*, 1, 1, 2016.

[44] X. Chen, P. Dai, D. Feng, T. Xiang, and F.-C. Zhang, "Iron-based high transition temperature superconductors," *National Science Review*, 1, 3, 371–395, 2014.

[45] A. Devarakonda, H. Inoue, S. Fang, C. Ozsoy-Keskinbora, T. Suzuki, M. Kriener, L. Fu, E. Kaxiras, D. C. Bell, and J. G. Checkelsky, "Clean 2D superconductivity in a bulk van der Waals superlattice," *Science*, 370, 231–236, 2020.

[46] I. M. Vishik, M. Hashimoto, R.-H. He, W.-S. Lee, F. Schmitt, D. Lu, R. G. Moore, C. Zhang, W. Meevasana, T. Sasagawa, S. Uchida, K. Fujita, S. Ishida, M. Ishikado, Y. Yoshida, H. Eisaki, Z. Hussain, T. P. Devereaux, and Z.-X. Shen, "Phase competition in trisected superconducting dome," *Proc. Natl. Acad. Sci. USA*, 109, 45, 18332–18337, 2012.

[47] I. Bozovic and J. N. Eckstein, "High Temperature Superconducting Multilayers and Heterostructures Grown By Atomic Layer-By-Layer Molecular Beam Epitaxy," *Annu. Rev. Mater. Sci..*, 25, 679–709, 1995.

[48] Y. J. Chung, K. A. Villegas Rosales, K. W. Baldwin, P. T. Madathil, K. W. West, M. Shayegan, and L. N. Pfeiffer, "Ultra-high-quality two-dimensional electron systems," *Nat. Mater.*, 20, 5, 632–637, 2021.

[49] J. Wu, A. T. Bollinger, X. He, and I. Božović, "Spontaneous breaking of rotational symmetry in copper oxide superconductors," *Nature*, 547, 7664, 432–435, 2017.

[50] I. Bozovic, G. Logvenov, M. A. J. Verhoeven, P. Caputo, E. Goldobin, and M. R. Beasley, "Giant Proximity Effect in Cuprate Superconductors," *Phys. Rev. Lett.*, 93, 15, 157002, 2004.

[51] C.-L. Song, X.-C. Ma, and Q.-K. Xue, "Emergent high-temperature superconductivity at interfaces," *MRS Bulletin*, 45, 5, 366–372, 2020.

[52] Q.-Y. Wang, Z. Li, W.-H. Zhang, Z.-C. Zhang, J.-S. Zhang, W. Li, H. Ding, Y.-B. Ou, P. Deng, K. Chang, J. Wen, C.-L. Song, K. He, J.-F. Jia, S.-H. Ji, Y.-Y. Wang, L.-L. Wang, X. Chen, X.-C. Ma, and Q.-K. Xue, "Interface-Induced High-Temperature Superconductivity in Single Unit-Cell FeSe Films on SrTiO $_3$," *Chinese Physics Letters*, 29, 3, 037402, 2012.

[53] D. Huang and J. E. Hoffman, "Monolayer FeSe on SrTiO $_3$," *Annu. Rev. Cond. Mat. Phys.*, 8, 1, 311–336, 2017.

[54] J. A. Mundy, C. M. Brooks, M. E. Holtz, J. A. Moyer, H. Das, A. F. Rébola, J. T. Heron, J. D. Clarkson, S. M. Disseler, Z. Liu, A. Farhan, R. Held, R. Hovden, E. Padgett, Q. Mao, H. Paik, R. Misra, L. F. Kourkoutis, E. Arenholz, A. Scholl, J. A. Borchers, W. D. Ratcliff, R. Ramesh, C. J. Fennie, P. Schiffer, D. A. Muller, and D. G. Schlom, "Atomically engineered ferroic layers yield a room-temperature magnetoelectric multiferroic," *Nature*, 537, 7621, 523–527, 2016.

[55] S. Fan, Q. A. Vu, M. D. Tran, S. Adhikari, and Y. H. Lee, "Transfer assembly for two-dimensional van der Waals heterostructures," *2D Materials*, 7, 2, 022005, 2020.

[56] L. Wang, I. Meric, P. Y. Huang, Q. Gao, Y. Gao, H. Tran, T. Taniguchi, K. Watanabe, L. M. Campos, D. A. Muller, J. Guo, P. Kim, J. Hone, K. L. Shepard, and C. R. Dean, "One-dimensional electrical contact to a two-dimensional material," *Science*, 342, 6158, 614–617, 2013.

[57] P. Zomer, M. Guimaraes, J. Brant, N. Tombros, and B. van Wees, "Fast pick up technique for high quality heterostructures of bilayer grapheneand hexagonal boron nitride," *Appl. Phys. Lett.*, 105, 013101, 2014.

[58] A. V. Kretinin, Y. Cao, J. S. Tu, G. L. Yu, R. Jalil, K. S. Novoselov, S. J. Haigh, A. Gholinia, A. Mishchenko, M. Lozada, T. Georgiou, C. R. Woods, F. Withers, P. Blake, G. Eda, A. Wirsig, C. Hucho, K. Watanabe, T. Taniguchi, A. K. Geim, and R. V. Gorbachev, "Electronic Properties of Graphene Encapsulated with Different Two-Dimensional Atomic Crystals," *Nano Lett.*, 14, 6, 3270–3276, 2014.

[59] G. Mirabelli, C. McGeough, M. Schmidt, E. K. McCarthy, S. Monaghan, I. M. Povey, M. McCarthy, F. Gity, R. Nagle, G. Hughes, A. Cafolla, P. K. Hurley, and R. Duffy, "Air sensitivity of MoS $_2$, MoSe $_2$, MoTe $_2$, HfS $_2$, and HfSe $_2$," *J. Appl. Phys.*, 120, 12, 125102, 2016.

[60] S. Y. F. Zhao, G. A. Elbaz, D. K. Bediako, C. Yu, D. K. Efetov, Y. Guo, J. Ravichandran, K.-A. Min, S. Hong, T. Taniguchi, K. Watanabe, L. E. Brus, X. Roy, and P. Kim, "Controlled Electrochemical Intercalation of Graphene/ *h*- BN van der Waals Heterostructures," *Nano Lett.*, 18, 1, 460–466, 2018.

[61] D. K. Bediako, M. Rezaee, H. Yoo, D. T. Larson, S. Y. F. Zhao, T. Taniguchi, K. Watanabe, T. L. Brower-Thomas, E. Kaxiras, and P. Kim, "Heterointerface effects in the electrointercalation of van der Waals heterostructures," *Nature*, 558, 7710, 425–429, 2018.

[62] O. Can, T. Tummuru, R. P. Day, I. Elfimov, A. Damascelli, and M. Franz, "High-temperature topological superconductivity in twisted double-layer copper oxides," *Nat. Phys.*, 17, 4, 519–524, 2021.

[63] J. G. Bednorz and K. Muller, "Possible High Tc Superconductivity in the Ba-La-Cu-O System," *Zeitschrift fur Physik B*, 64, 189–193, 1986.

[64] A. Schilling, M. Cantoni, J. D. Guo, and H. R. Ott, "Superconductivity above 130 K in the Hg–Ba–Ca–Cu–O system," *Nature*, 363, 6424, 56–58, 1993.

[65] G. Campi, A. Bianconi, N. Poccia, G. Bianconi, L. Barba, G. Arrighetti, D. Innocenti, J. Karpinski, N. D. Zhigadlo, S. M. Kazakov, M. Burghammer, M. v. Zimmermann, M. Sprung, and A. Ricci, "Inhomogeneity of charge-density-wave order and quenched disorder in a high-Tc superconductor," *Nature*, 525, 7569, 359–362, 2015.

[66] M. Tinkham, *Introduction to Superconductivity*. Mineola, N.Y.: Dover Publications, 2nd ed., 1996.

[67] J. Ketterson and Song, S.N., *Superconductivity*. Cambridge, U.K.: Cambridge University Press, 1999.

[68] L. N. Cooper, "Bound Electron Pairs in a Degenerate Fermi Gas," *Phys. Rev.*, 104, 4, 1189–1190, 1956.

[69] J. Bardeen, L. N. Cooper, and J. R. Schrieffer, "Theory of Superconductivity," *Phys. Rev.*, 108, 5, 1175–1204, 1957.

[70] W. N. Kang, "MgB2 Superconducting Thin Films with a Transition Temperature of 39 Kelvin," *Science*, 292, 5521, 1521–1523, 2001.

[71] E. Snider, N. Dasenbrock-Gammon, R. McBride, M. Debessai, H. Vindana, K. Vencatasamy, K. V. Lawler, A. Salamat, and R. P. Dias, "Room-temperature superconductivity in a carbonaceous sulfur hydride," *Nature*, 586, 7829, 373–377, 2020.

[72] D. Pines and P. Nozieres, *The theory of quantum liquids*. New York, N.Y.: W.A. Benjamin, Inc., 1966.

[73] C. Tsuei and J. Kirtley, "Pairing symmetry in cuprate superconductors," *Rev. Mod. Phys.*, 72, 4, 969–1016, 2000.

[74] D. J. Van Harlingen, "Phase-sensitive tests of the symmetry of the pairing state in the high-temperature superconductors - evidence for d symmetry," *Rev. Mod. Phys.*, 67, 2, 515–535, 1995.

[75] N. Bulut and D. J. Scalapino, "D x 2 - y 2 symmetry and the pairing mechanism," *Phys. Rev. B*, 54, 21, 14971–14973, 1996.

[76] M. Sato and Y. Ando, "Topological superconductors: A review," *Reports on Progress in Physics*, 80, 7, aa6ac7, 2017.

[77] S. R. Elliott and M. Franz, "*Colloquium* : Majorana fermions in nuclear, particle, and solid-state physics," *Rev. Mod. Phys.*, 87, 1, 137–163, 2015.

[78] M. Hashimoto, I. M. Vishik, R.-H. He, T. P. Devereaux, and Z.-X. Shen, "Energy gaps in high-transition-temperature cuprate superconductors," *Nat. Phys.*, 10, 7, 483–495, 2014.

[79] D. A. Wright, J. P. Emerson, B. F. Woodfield, J. E. Gordon, R. A. Fisher, and N. E. Phillips, "Low-Temperature Specific Heat of YBa2Cu3O72d, o l d l 0.2: Evidence for d-Wave Pairing," *Phys. Rev. Lett.*, 82, 7, 4, 1999.

[80] J. Y. T. Wei, "Directional Tunneling and Andreev Reflection on YBa2Cu3O72d Single Crystals: Predominance of d-Wave Pairing Symmetry Verified with the Generalized Blonder, Tinkham, and Klapwijk Theory," *Phys. Rev. Lett.*, 81, 12, 4, 1998.

[81] A. Barone and G. Paterno, *Physics and Applications of the Josephson Effect*. New York, N.Y.: Wiley, 1982.

[82] H. Hilgenkamp, "Pi-phase shift Josephson structures," *Superconductor Science and Technology*, 21, 3, 034011, 2008.

[83] F. Tafuri, ed., *Fundamentals and Frontiers of the Josephson Effect*. Cham, Switzerland: Springer Nature, 2019.

[84] H. B. Wang, P. H. Wu, and T. Yamashita, "Terahertz Responses of Intrinsic Josephson Junctions in High T C Superconductors," *Phys. Rev. Lett.*, 87, 10, 107002, 2001.

[85] R. L. Kautz and R. Monaco, "Survey of chaos in the rf-biased Josephson junction," *J. Appl. Phys.*, 57, 3, 875–889, 1985.

[86] H. B. Wang, Y. Aruga, J. Chen, K. Nakajima, T. Yamashita, and P. H. Wu, "Individual Shapiro steps observed in resistively shunted intrinsic Josephson junctions on Bi2Sr2CaCu2O8+x single crystals," *Appl. Phys. Lett.*, 77, 1017, 2000.

[87] Y.-J. Doh, J. Kim, K.-T. Kim, and H.-J. Lee, "Microwave-induced constant voltage steps in surface junctions of Bi2Sr2CaCu2O8¿? single crystals," *Phys. Rev. B*, 61, 6, R3834, 2000.

[88] A. A. Golubov, M. Y. Kupriyanov, and E. Il'ichev, "The current-phase relation in Josephson junctions," *Rev. Mod. Phys.*, 76, 2, 411–469, 2004.

[89] H. Sellier, C. Baraduc, F. Lefloch, and R. Calemczuk, "Half-integer shapiro steps at the $0 - \pi$ crossover of a ferromagnetic josephson junction," *Phys. Rev. Lett.*, 92, 257005, June 2004.

[90] L. P. Gor'kov, "Microscopic derivation of the Ginzburg-Landau equations in the theory of superconductivity," *Soviet Physics JETP*, 36, 6, 1918–1923, 1959.

[91] G. Blatter, M. V. Feigel'man, V. B. Geshkenbein, A. I. Larkin, and V. M. Vinokur, "Vortices in high-temperature superconductors," *Rev. Mod. Phys.*, 66, 4, 1125–1388, 1994.

[92] N. Poccia, A. Ricci, and A. Bianconi, "Misfit Strain in Superlattices Controlling the Electron-Lattice Interaction via Microstrain in Active Layers," *Advances in Condensed Matter Physics*, 2010, 1–7, 2010.

[93] I. M. Hayes, R. D. McDonald, N. P. Breznay, T. Helm, P. J. W. Moll, M. Wartenbe, A. Shekhter, and J. G. Analytis, "Scaling between magnetic field and temperature in the high-temperature superconductor BaFe2(As1-xPx)2," *Nat. Phys.*, 12, 10, 916–919, 2016.

[94] N. Doiron-Leyraud, P. Auban-Senzier, S. René de Cotret, C. Bourbonnais, D. Jérome, K. Bechgaard, and L. Taillefer, "Correlation between linear resistivity and T c in the Bechgaard salts and the pnictide superconductor Ba (Fe 1 - x Co x) 2 As 2," *Phys. Rev. B*, 80, 21, 214531, 2009.

[95] E. Dagotto, "Complexity in Strongly Correlated Electronic Systems," *Science*, 309, 5732, 257–262, 2005.

[96] D. J. Scalapino, "A common thread: The pairing interaction for unconventional superconductors," *Rev. Mod. Phys.*, 84, 4, 1383–1417, 2012.

[97] G. Ghiringhelli, M. Le Tacon, M. Minola, S. Blanco-Canosa, C. Mazzoli, N. B. Brookes, G. M. De Luca, A. Frano, D. G. Hawthorn, F. He, T. Loew, M. M. Sala, D. C. Peets, M. Salluzzo, E. Schierle, R. Sutarto, G. A. Sawatzky, E. Weschke, B. Keimer, and L. Braicovich, "Long-Range Incommensurate Charge Fluctuations in (Y,Nd)Ba2Cu3O6+x," *Science*, 337, 6096, 821–825, 2012.

[98] S. A. Kivelson, I. P. Bindloss, E. Fradkin, V. Oganesyan, J. M. Tranquada, A. Kapitulnik, and C. Howald, "How to detect fluctuating stripes in the high-temperature superconductors," *Rev. Mod. Phys.*, 75, 4, 1201–1241, 2003.

[99] M. Fratini, N. Poccia, A. Ricci, G. Campi, M. Burghammer, G. Aeppli, and A. Bianconi, "Scale-free structural organization of oxygen interstitials in La2CuO4+y," *Nature*, 466, 7308, 841–844, 2010.

[100] I. Zeljkovic, Z. Xu, J. Wen, G. Gu, R. S. Markiewicz, and J. E. Hoffman, "Imaging the Impact of Single Oxygen Atoms on Superconducting Bi2+ySr2-yCaCu2O8+x," *Science*, 337, 6092, 320–323, 2012.

[101] W. D. Wise, M. C. Boyer, K. Chatterjee, T. Kondo, T. Takeuchi, H. Ikuta, Y. Wang, and E. W. Hudson, "Charge-density-wave origin of cuprate checkerboard visualized by scanning tunnelling microscopy," *Nat. Phys.*, 4, 9, 696–699, 2008.

[102] N. Poccia, G. Campi, M. Fratini, A. Ricci, N. L. Saini, and A. Bianconi, "Spatial inhomogeneity and planar symmetry breaking of the lattice incommensurate supermodulation in the high-temperature superconductor Bi 2 Sr 2 CaCu 2 O 8 + y," *Phys. Rev. B*, 84, 10, 100504, 2011.

[103] N. Poccia, A. Ricci, G. Campi, M. Fratini, A. Puri, D. D. Gioacchino, A. Marcelli, M. Reynolds, M. Burghammer, N. L. Saini, G. Aeppli, and A. Bianconi, "Optimum inhomogeneity of local lattice distortions in La2CuO4+y," *Proc. Natl. Acad. Sci. USA*, 109, 39, 15685–15690, 2012.

[104] N. Poccia, M. Fratini, A. Ricci, G. Campi, L. Barba, A. Vittorini-Orgeas, G. Bianconi, G. Aeppli, and A. Bianconi, "Evolution and control of oxygen order in a cuprate superconductor," *Nat. Mater.*, 10, 733–736, 2011.

[105] D. D. Awschalom, M. E. Flatte, and N. Samarth, "Spintronics," *Scientific American*, 8, 2002.

[106] N. Plakida, *High-Temperature Cuprate Superconductors*. Berlin, Germany: Springer-Verlag, 2010.

[107] N. P. Armitage, P. Fournier, and R. L. Greene, "Progress and perspectives on electron-doped cuprates," *Rev. Mod. Phys.*, 82, 3, 2421–2487, 2010.

[108] J. M. Tranquada, B. J. Sternlieb, J. D. Axe, Y. Nakamura, and S. Uchida, "Evidence for stripe correlations of spins and holes in copper oxide superconductors," *Nature*, 375, 6532, 561–563, 1995.

[109] I. Bozovic and J. N. Eckstein, "High temperature superconducting multilayers and heterostructures grown by atomic layer-by-layer molecular beam epitaxy," *Annu. Rev. Mater. Sci.*., 25, 679–709, 1995.

[110] J. Wu, A. T. Bollinger, Y. Sun, and I. Božović, "Hall effect in quantum critical charge-cluster glass," *Proc. Natl. Acad. Sci. USA*, 113, 16, 4284–4289, 2016.

[111] S. E. Sebastian and C. Proust, "Quantum Oscillations in Hole-Doped Cuprates," *Annu. Rev. Cond. Mat. Phys.*, 6, 1, 411–430, 2015.

[112] N. Doiron-Leyraud, C. Proust, D. LeBoeuf, J. Levallois, J.-B. Bonnemaison, R. Liang, D. A. Bonn, W. N. Hardy, and L. Taillefer, "Quantum oscillations and the Fermi surface in an underdoped high-Tc superconductor," *Nature*, 447, 7144, 565–568, 2007.

[113] R. P. Vasquez, "Intrinsic photoemission signals , surface preparation , and surface stability of high temperature supercqnductors," *J. Electron Spectrosc.*, 66, 209–222, 1994.

[114] K. Schlenga, G. Hechtfischer, R. Kleiner, W. Walkenhorst, P. Muller, H. Johnson, M. Veith, W. Brodkorb, and E. Steinbeiss, "Subgap Structures in Intrinsic Josephson Junctions of Tl-2223 and Bi-2212," *Phys. Rev. Lett.*, 76, 26, 4943–4946, 1996.

[115] R. Kleiner, F. Steinmeyer, G. Kunkel, and P. Muller, "Intrinsic Josephson effects in Bi-2212 single crystals," *Phys. Rev. Lett.*, 68, 15, 2394–2397, 1992.

[116] J. Kirtley, *Pairing Symmetry Effects*, ch. 9. Cham, Switzerland: Springer, 2019.

[117] R. Khasanov, S. Strassle, D. Di Castro, T. Masui, S. Miyasaka, S. Tajima, A. Bussmann-Holder, and H. Keller, "Multiple gap symmetries for the order parameter of cuprate superconductors from penetration depth measurements," *Phys. Rev. Lett.*, 99, 23, 237601, 2007.

[118] Y. Zhu, M. Liao, Q. Zhang, F. Meng, R. Zhong, J. Schneeloch, G. Gu, L. Gu, X. Ma, D. Zhang, and Q.-K. Xue, "Presence of s-wave pairing in josephson junctions made of twisted ultrathin bi2sr2cacu208+x flakes," *Phys. Rev. X*, 11, 031011, 2021.

[119] A. T. Bollinger, G. Dubuis, J. Yoon, D. Pavuna, J. Misewich, and I. Božović, "Superconductor–insulator transition in La2 - xSr x CuO4 at the pair quantum resistance," *Nature*, 472, 7344, 458–460, 2011.

[120] A. M. Perez-Muñoz, P. Schio, R. Poloni, A. Fernandez-Martinez, A. Rivera-Calzada, J. C. Cezar, E. Salas-Colera, G. R. Castro, J. Kinney, C. Leon, J. Santamaria, J. Garcia-Barriocanal, and A. M. Goldman, "*In Operando* evidence of deoxygenation in ionic liquid gating of YBa $_2$ Cu $_3$ O $_{7-X}$," *Proc. Natl. Acad. Sci. USA*, 114, 2, 215–220, 2017.

[121] T. Timusk and B. Statt, "The pseudogap in high-temperature superconductors: An experimental survey," *Reports on Progress in Physics*, 62, 1, 61–122, 1999.

[122] P. Zhou, L. Chen, Y. Liu, I. Sochnikov, A. T. Bollinger, M.-G. Han, Y. Zhu, X. He, I. Božović, and D. Natelson, "Electron pairing in the pseudogap state revealed by shot noise in copper oxide junctions," *Nature*, 572, 7770, 493–496, 2019.

[123] Y. Wang, L. Li, and N. P. Ong, "Nernst effect in high- T c superconductors," *Phys. Rev. B*, 73, 2, 024510, 2006.

[124] B. Sacépé, C. Chapelier, T. I. Baturina, V. M. Vinokur, M. R. Baklanov, and M. Sanquer, "Pseudogap in a thin film of a conventional superconductor," *Nat. Commun.*, 1, 1, 140, 2010.

[125] S. Badoux, W. Tabis, F. Laliberté, G. Grissonnanche, B. Vignolle, D. Vignolles, J. Béard, D. A. Bonn, W. N. Hardy, R. Liang, N. Doiron-Leyraud, L. Taillefer, and C. Proust, "Change of carrier density at the pseudogap critical point of a cuprate superconductor," *Nature*, 531, 7593, 210–214, 2016.

[126] S.-D. Chen, M. Hashimoto, Y. He, D. Song, K.-J. Xu, J.-F. He, T. P. Devereaux, H. Eisaki, D.-H. Lu, J. Zaanen, and Z.-X. Shen, "Incoherent strange metal sharply bounded by a critical doping in Bi2212," *Science*, 366, 6469, 1099–1102, 2019.

[127] H. Y. Hwang, B. Batlogg, H. Takagi, H. L. Kao, J. Kwo, R. J. Cava, J. J. Krajewski, and W. F. Peck, "Scaling of the Temperature Dependent Hall Effect in La 2 -xSr," *Phys. Rev. Lett.*, 72, 16, 2636–2639, 1994.

[128] L. J. Sandilands, A. A. Reijnders, A. H. Su, V. Baydina, Z. Xu, A. Yang, G. Gu, T. Pedersen, F. Borondics, and K. S. Burch, "Origin of the insulating state in exfoliated high- T c two-dimensional atomic crystals," *Phys. Rev. B*, 90, 8, 081402, 2014.

[129] D. Jiang, T. Hu, L. You, Q. Li, A. Li, H. Wang, G. Mu, Z. Chen, H. Zhang, G. Yu, J. Zhu, Q. Sun, C. Lin, H. Xiao, X. Xie, and M. Jiang, "High-Tc superconductivity in ultrathin Bi2Sr2CaCu2O8+x down to half-unit-cell thickness by protection with graphene," *Nat. Commun.*, 5, 1, 5708, 2014.

[130] R. Frisenda, E. Navarro-Moratalla, P. Gant, D. Pérez De Lara, P. Jarillo-Herrero, R. Gorbachev, and A. Castellanos-Gomez, "Recent progress in the assembly of nanodevices and van der waals heterostructures by deterministic placement of 2d materials," *Chem. Soc. Rev.*, 47, 53–68, 2018.

[131] L. Wang, I. Meric, P. Y. Huang, Q. Gao, Y. Gao, H. Tran, T. Taniguchi, K. Watanabe, L. M. Campos, D. A. Muller, J. Guo, P. Kim, J. Hone, K. L. Shepard, and C. R. Dean, "One-Dimensional Electrical Contact to a Two-Dimensional Material," *Science*, 342, 6158, 614–617, 2013.

[132] A. Castellanos-Gomez, M. Buscema, R. Molenaar, V. Singh, L. Janssen, H. van der Zant, and G. Steele, "Deterministic transfer of two-dimensional materials by all-dry viscoelastic stamping," *2D Materials*, 1, 011002, 2014.

[133] A. Y. Joe, *Interlayer Excitons in Atomically Thin van der Waals Semiconductor Heterostructures*. PhD thesis, Harvard University, 2021.

[134] S. Clarson, K. Dodgson, and J. Semlyen, "Studies of cyclic and linear poly(dimethylsiloxanes): 19. glass transition temperatures and crystallization behaviour," *Polymer*, 26, 930–934, 1984.

[135] J. Eisenhaure, S. Rhee, A. Al-Okaily, A. Carlson, P. Ferreira, and S. Kim, "The use of shape memory polymers for microassembly by transfer printing," *J. Microelectromechanical Sys.*, 23, 2012, 2014.

[136] R. Razouk and A. Salem, "The adsorption of water vapor on glass surfaces," *J. Phys. Chem.*, 52, 7, 1208–1227, 1948.

[137] Grace Davison, "Adsorbents for Process Applications," 2010.

[138] J. L. Briesacher, M. Nakamura, and T. Ohmi, "Gas Purification and Measurement at the PPT Level Gas Purification and Measurement at the PPT Level," *J. Electrochem. Soc.*, 138, 3717, 1991.

[139] J. Goff and S. Gratch, "Low-pressure properties of water from -160 to 212 f," *Trans. Am. Soc. Heating Ventilating Eng.*, 52, 95–122, 1946.

[140] H. Vomel, D. E. David, and K. Smith, "Accuracy of tropospheric and stratospheric water vapor measurements by the cryogenic frost point hygrometer: Instrumental details and observations," *Journal of Geophysical Research Atmospheres*, 112, 8, 1–14, 2007.

[141] M. Meitl, Z.-T. Zhu, V. Kumar, K. Lee, X. Feng, Y. Huang, I. Adesida, R. Nuzzo, and J. Rogers, "Transfer printing by kinetic control of adhesion to an elastomeric stamp," *Nat. Mater.*, 5, 33–38, 2006.

[142] S. Nawaz, R. Arpaia, F. Lombardi, and T. Bauch, "Microwave response of superconducting $YBa_2Cu_3O_{7-\delta}$ nanowire bridges sustaining the critical depairing current: Evidence of josephson-like behavior," *Phys. Rev. Lett.*, 110, 167004–5, 2013.

[143] L. Li, I. Bayn, M. Lu, C.-Y. Nam, T. Schroder, A. Stein, N. Harris, and D. Englund, "Nanofabrication on unconventional substrates using transferred hard masks," *Sci. Rep.*, 5, 7802, 2015.

[144] U. Zondiner, A. Rozen, D. Rodan-Legrain, Y. Cao, R. Queiroz, T. Taniguchi, K. Watanabe, Y. Oreg, F. von Oppen, A. Stern, E. Berg, P. Jarillo-Herrero, and S. Ilani, "Cascade of Phase Transitions and Dirac Revivals in Magic Angle Graphene," *Nature*, 582, November 2019, 2019.

[145] W. Wen, G. Zhao, C. Hong, Z. Song, and R.-H. He, "3D Negative Electronic Compressibility as a New Emergent Phenomenon," *Journal of Superconductivity and Novel Magnetism*, 33, 1, 229–239, 2020.

[146] S. L. Tomarken, Y. Cao, A. Demir, K. Watanabe, T. Taniguchi, P. Jarillo-Herrero, and R. C. Ashoori, "Electronic Compressibility of Magic-Angle Graphene Superlattices," *Phys. Rev. Lett.*, 123, 4, 046601, 2019.

[147] A. Fujimori, A. Ino, J. Matsuno, T. Yoshida, K. Tanaka, and T. Mizokawa, "Core-level photoemission measurements of the chemical potential shift as a probe of correlated electron systems," *Journal of Electron Spectroscopy and Related Phenomena*, 124, 2-3, 127–138, 2002.

[148] J. P. Eisenstein, L. N. Pfeiffer, and K. W. West, "Negative compressibility of interacting two-dimensional electron and quasiparticle gases," *Phys. Rev. Lett.*, 68, 5, 674–677, 1992.

[149] S. C. Dultz and H. W. Jiang, "Thermodynamic Signature of a Two-Dimensional Metal-Insulator Transition," *Phys. Rev. Lett.*, 84, 20, 4689–4692, 2000.

[150] M. Dresselhaus and G. Dresselhaus, "Intercalation compounds of graphite," *Advances in Physics*, 30, 1, 1, 1981.

[151] T. E. Weller, M. Ellerby, S. S. Saxena, R. P. Smith, and N. T. Skipper, "Superconductivity in the intercalated graphite compounds C6Yb and C6Ca," *Nat. Phys.*, 1, 1, 39–41, 2005.

[152] S. Cahen, Lagrange, P., Mareche, J.-F., and Herold, C., "Analogies and differences between calcium-based and europium-based graphite intercalation compounds," *Comptes Rendus Chimie*, 16, 385–390, 2013.

[153] W. Bao, J. Wan, X. Han, X. Cai, H. Zhu, D. Kim, D. Ma, Y. Xu, J. N. Munday, H. D. Drew, M. S. Fuhrer, and L. Hu, "Approaching the limits of transparency and conductivity in graphitic materials through lithium intercalation," *Nat. Commun.*, 5, 1, 4224, 2014.

[154] J. Chapman, Y. Su, C. A. Howard, D. Kundys, A. N. Grigorenko, F. Guinea, A. K. Geim, I. V. Grigorieva, and R. R. Nair, "Superconductivity in Ca-doped graphene laminates," *Scientific Reports*, 6, 1, 23254, 2016.

[155] N. Kim, K. S. Kim, N. Jung, L. Brus, and P. Kim, "Synthesis and Electrical Characterization of Magnetic Bilayer Graphene Intercalate," *Nano Lett.*, 11, 2, 860–865, 2011.

[156] C. Weeks, J. Hu, J. Alicea, M. Franz, and R. Wu, "Engineering a Robust Quantum Spin Hall State in Graphene via Adatom Deposition," *Phys. Rev. X*, 1, 2, 021001, 2011.

[157] S. N. Shirodkar and E. Kaxiras, "Li intercalation at graphene/hexagonal boron nitride interfaces," *Phys. Rev. B*, 93, 24, 245438, 2016.

[158] M. Kuhne, F. Paolucci, J. Popovic, P. M. Ostrovsky, J. Maier, and J. H. Smet, "Ultrafast lithium diffusion in bilayer graphene," *Nat. Nano.*, 12, 9, 895–900, 2017.

[159] D. K. Efetov and P. Kim, "Controlling Electron-Phonon Interactions in Graphene at Ultrahigh Carrier Densities," *Phys. Rev. Lett.*, 105, 25, 256805, 2010.

[160] N. Jung, N. Kim, S. Jockusch, N. J. Turro, P. Kim, and L. Brus, "Charge Transfer Chemical Doping of Few Layer Graphenes: Charge Distribution and Band Gap Formation," *Nano Lett.*, 9, 12, 4133–4137, 2009.

[161] M. Inaba, H. Yoshida, Z. Ogumi, T. Abe, Y. Mizutani, and M. Asano, "In Situ Raman Study on Electrochemical Li Intercalation into Graphite," *Journal of The Electrochemical Society*, 142, 1, 20–26, 1995.

[162] C.-F. Chen, C.-H. Park, B. W. Boudouris, J. Horng, B. Geng, C. Girit, A. Zettl, M. F. Crommie, R. A. Segalman, S. G. Louie, and F. Wang, "Controlling inelastic light scattering quantum pathways in graphene," *Nature*, 471, 7340, 617–620, 2011.

[163] R. Geick, C. H. Perry, and G. Rupprecht, "Normal Modes in Hexagonal Boron Nitride," *Phys. Rev.*, 146, 2, 543–547, 1966.

[164] D. Yoon, H. Moon, Y.-W. Son, J. S. Choi, B. H. Park, Y. H. Cha, Y. D. Kim, and H. Cheong, "Interference effect on Raman spectrum of graphene on SiO 2 / Si," *Phys. Rev. B*, 80, 12, 125422, 2009.

[165] A. C. Ferrari, J. C. Meyer, V. Scardaci, C. Casiraghi, M. Lazzeri, F. Mauri, S. Piscanec, D. Jiang, K. S. Novoselov, S. Roth, and A. K. Geim, "Raman Spectrum of Graphene and Graphene Layers," *Phys. Rev. Lett.*, 97, 18, 187401, 2006.

[166] D. K. Efetov, P. Maher, S. Glinskis, and P. Kim, "Multiband transport in bilayer graphene at high carrier densities," *Phys. Rev. B*, 84, 16, 161412, 2011.

[167] V. Kresin, Y. Ovchinnikov, and S. Wolf, "Inhomogeneous superconductivity and the "pseudogap" state of novel superconductors," *Physics Reports*, 431, 5, 231–259, 2006.

[168] J.-H. She and J. Zaanen, "BCS superconductivity in quantum critical metals," *Phys. Rev. B*, 80, 18, 184518, 2009.

[169] W. B. Gao, Q. Q. Liu, L. X. Yang, Y. Yu, F. Y. Li, C. Q. Jin, and S. Uchida, "Out-of-plane effect on the superconductivity of Sr 2 - x Ba x CuO 3 + δ with T c up to 98 K," *Phys. Rev. B*, 80, 9, 094523, 2009.

[170] T. H. Geballe, R. H. Hammond, and P. M. Wu, "What T tells," *Physica C*, 514, 9–16, 2015.

[171] A. Bianconi, A. Valletta, A. Perali, and N. L. Saini, "Superconductivity of a striped phase at the atomic limit," *Physica C*, 296, 3-4, 269–280, 1998.

[172] A. Yamamoto, M. Onoda, E. Takayama-Muromachi, F. Izumi, T. Ishigaki, and H. Asano, "Rietveld analysis of the modulated structure in the superconducting oxide Bi 2 (Sr,Ca) 3 Cu 2 O 8 + x," *Phys. Rev. B*, 42, 7, 4228–4239, 1990.

[173] J. A. Slezak, J. Lee, M. Wang, K. McElroy, K. Fujita, B. M. Andersen, P. J. Hirschfeld, H. Eisaki, S. Uchida, and J. C. Davis, "Imaging the impact on cuprate superconductivity of varying the interatomic distances within individual crystal unit cells," *Proc. Natl. Acad. Sci. USA*, 105, 9, 3203–3208, 2008.

[174] A. Bianconi, M. Lusignoli, N. L. Saini, P. Bordet, Å. Kvick, and P. G. Radaelli, "Stripe structure of the CuO 2 plane in Bi 2 Sr 2 CaCu 2 O 8 + y by anomalous x-ray diffraction," *Phys. Rev. B*, 54, 6, 4310–4314, 1996.

[175] J. Zaanen, "The benefit of fractal dirt," *Nature*, 466, 7308, 825–826, 2010.

[176] P. G. Radaelli, J. D. Jorgensen, A. J. Schultz, B. A. Hunter, J. L. Wagner, F. C. Chou, and D. C. Johnston, "Structure of the superconducting La 2 CuO 4 + ∂ phases (Δ ≈0.08,0.12) prepared by electrochemical oxidation," *Phys. Rev. B*, 48, 1, 499–510, 1993.

[177] Y. Koyama, S.-I. Nakamura, Y. Inoue, and T. Ohno, "Direct observation of a structural-fluctuation enhancement in a superconducting state of Tl 2 Ba 2 Ca 2 Cu 3 O 10 by electron diffraction," *Phys. Rev. B*, 46, 9, 5757–5759, 1992.

[178] W. Dmowski, R. J. McQueeney, T. Egami, Y. P. Feng, S. K. Sinha, T. Hinatsu, and S. Uchida, "Temperature-dependent x-ray diffuse scattering from single crystals of La 2 - x Sr x CuO 4," *Phys. Rev. B*, 52, 9, 6829–6839, 1995.

[179] J. P. Castellan, B. D. Gaulin, H. A. Dabkowska, A. Nabialek, G. Gu, X. Liu, and Z. Islam, "Two- and three-dimensional incommensurate modulation in optimally-doped Bi 2 Sr 2 CaCu 2 O 8 + ∂," *Phys. Rev. B*, 73, 17, 174505, 2006.

[180] M. Izquierdo, S. Megtert, J. P. Albouy, J. Avila, M. A. Valbuena, G. Gu, J. S. Abell, G. Yang, M. C. Asensio, and R. Comes, "X-ray diffuse scattering experiments from bismuth-based high- T c superconductors," *Phys. Rev. B*, 74, 5, 054512, 2006.

[181] R. Comes, M. Izquierdo, S. Megtert, P. Albouy, J. Avila, M. Valbuena, G. Gu, J. Abell, and M. Asensio, "X-ray diffuse scattering experiments on bismuth based high Tc superconductors," *Physica C*, 460-462, 730–731, 2007.

[182] I. Zeljkovic, J. Nieminen, D. Huang, T.-R. Chang, Y. He, H.-T. Jeng, Z. Xu, J. Wen, G. Gu, H. Lin, R. S. Markiewicz, A. Bansil, and J. E. Hoffman, "Nanoscale Interplay of Strain and Doping in a High-Temperature Superconductor," *Nano Lett.*, 14, 12, 6749–6753, 2014.

[183] I. Zeljkovic, E. J. Main, T. L. Williams, M. C. Boyer, K. Chatterjee, W. D. Wise, Y. Yin, M. Zech, A. Pivonka, T. Kondo, T. Takeuchi, H. Ikuta, J. Wen, Z. Xu, G. D. Gu, E. W. Hudson, and J. E. Hoffman, "Scanning tunnelling microscopy imaging of symmetry-breaking structural distortion in the bismuth-based cuprate superconductors," *Nat. Mater.*, 11, 7, 585–589, 2012.

[184] T. Valla, I. Pletikosić, I. K. Drozdov, and G. D. Gu, "Reconstruction of the Bi 2 Sr 2 CaCu 2 O 8 + ∂ Fermi surface," *Phys. Rev. B*, 100, 24, 241112, 2019.

[185] C. Howald, H. Eisaki, N. Kaneko, and A. Kapitulnik, "Coexistence of periodic modulation of quasiparticle states and superconductivity in Bi2Sr2CaCu2O8+," *Proc. Natl. Acad. Sci. USA*, 100, 17, 9705–9709, 2003.

[186] E. Carlson and K. Dahmen, "Using disorder to detect locally ordered electron nematics via hysteresis," *Nat. Commun.*, 2, 1, 379, 2011.

[187] E. W. Carlson, S. Liu, B. Phillabaum, and K. A. Dahmen, "Decoding Spatial Complexity in Strongly Correlated Electronic Systems," *Journal of Superconductivity and Novel Magnetism*, 28, 4, 1237–1243, 2015.

[188] F. Massee, Y. K. Huang, M. S. Golden, and M. Aprili, "Noisy defects in the high-Tc superconductor Bi2Sr2CaCu2O8+x," *Nat. Commun.*, 10, 1, 544, 2019.

[189] D. Pelc, M. Vučković, M. S. Grbić, M. Požek, G. Yu, T. Sasagawa, M. Greven, and N. Barišić, "Emergence of superconductivity in the cuprates via a universal percolation process," *Nat. Commun.*, 9, 1, 4327, 2018.

[190] Y. Saito, T. Nojima, and Y. Iwasa, "Highly crystalline 2D superconductors," *Nature Reviews Materials*, 2, 1, 16094, 2017.

[191] E. Sterpetti, J. Biscaras, A. Erb, and A. Shukla, "Comprehensive phase diagram of two-dimensional space charge doped Bi2Sr2CaCu2O8+x," *Nat. Commun.*, 8, 1, 2060, 2017.

[192] S. K. Sahu, D. Jangade, A. Thamizhavel, M. M. Deshmukh, and V. Singh, "Elastic properties of few unit cell thick superconducting crystals of $Bi_2Sr_2CaCu_2O_{8+\delta}$," *Applied Physics Letters*, 115, 14, 143102, 2019.

[193] S. Agrestini, N. L. Saini, G. Bianconi, and A. Bianconi, "The strain of CuO_2 lattice: The second variable for the phase diagram of cuprate perovskites," *Journal of Physics A: Mathematical and General*, 36, 35, 9133–9142, 2003.

[194] S. Agrestini, C. Metallo, M. Filippi, L. Simonelli, G. Campi, C. Sanipoli, E. Liarokapis, S. De Negri, M. Giovannini, A. Saccone, A. Latini, and A. Bianconi, "Substitution of Sc for Mg in MgB 2 : Effects on transition temperature and Kohn anomaly," *Phys. Rev. B*, 70, 13, 134514, 2004.

[195] A. Ricci, N. Poccia, B. Joseph, L. Barba, G. Arrighetti, G. Ciasca, J.-Q. Yan, R. W. McCallum, T. A. Lograsso, N. D. Zhigadlo, J. Karpinski, and A. Bianconi, "Structural phase transition and superlattice misfit strain of R FeAsO (R = La , Pr , Nd , Sm)," *Phys. Rev. B*, 82, 14, 144507, 2010.

[196] S. Gao, F. Flicker, R. Sankar, H. Zhao, Z. Ren, B. Rachmilowitz, S. Balachandar, F. Chou, K. S. Burch, Z. Wang, J. van Wezel, and I. Zeljkovic, "Atomic-scale strain manipulation of a charge density wave," *Proc. Natl. Acad. Sci. USA*, 115, 27, 6986–6990, 2018.

[197] A. F. Isakovic, P. G. Evans, J. Kmetko, K. Cicak, Z. Cai, B. Lai, and R. E. Thorne, "Shear Modulus and Plasticity of a Driven Charge Density Wave," *Phys. Rev. Lett.*, 96, 4, 046401, 2006.

[198] H. Yan, N. Bouet, J. Zhou, X. Huang, E. Nazaretski, W. Xu, A. P. Cocco, W. K. S. Chiu, K. S. Brinkman, and Y. S. Chu, "Multimodal hard x-ray imaging with resolution approaching 10 nm for studies in material science," *Nano Futures*, 2, 1, 011001, 2018.

[199] E. Nazaretski, H. Yan, K. Lauer, N. Bouet, X. Huang, W. Xu, J. Zhou, D. Shu, Y. Hwu, and Y. S. Chu, "Design and performance of an X-ray scanning microscope at the Hard X-ray Nanoprobe beamline of NSLS-II," *Journal of Synchrotron Radiation*, 24, 6, 1113–1119, 2017.

[200] J. Zhang, Y. Ding, C.-C. Chen, Z. Cai, J. Chang, B. Chen, X. Hong, A. Fluerasu, Y. Zhang, C.-S. Ku, D. Brewe, S. Heald, H. Ishii, N. Hiraoka, K.-D. Tsuei, W. Liu, Z. Zhang, Y. Q. Cai, G. Gu, T. Irifune,

and H.-k. Mao, "Evolution of a Novel Ribbon Phase in Optimally Doped Bi $_2$ Sr $_2$ CaCu $_2$ O $_{8+\delta}$ at High Pressure and Its Implication to High- T_C Superconductivity," *The Journal of Physical Chemistry Letters*, 9, 15, 4182–4188, 2018.

[201] A. Ricci, N. Poccia, B. Joseph, D. Innocenti, G. Campi, A. Zozulya, F. Westermeier, A. Schavkan, F. Coneri, A. Bianconi, H. Takeya, Y. Mizuguchi, Y. Takano, T. Mizokawa, M. Sprung, and N. L. Saini, "Direct observation of nanoscale interface phase in the superconducting chalcogenide K x Fe 2 - y Se 2 with intrinsic phase separation," *Phys. Rev. B*, 91, 2, 020503, 2015.

[202] A. Singer, J. G. Ramirez, I. Valmianski, D. Cela, N. Hua, R. Kukreja, J. Wingert, O. Kovalchuk, J. M. Glownia, M. Sikorski, M. Chollet, M. Holt, I. K. Schuller, and O. G. Shpyrko, "Nonequilibrium Phase Precursors during a Photoexcited Insulator-to-Metal Transition in V 2 O 3," *Phys. Rev. Lett.*, 120, 20, 207601, 2018.

[203] P. G. Evans, "X-ray Microdiffraction Images of Antiferromagnetic Domain Evolution in Chromium," *Science*, 295, 5557, 1042–1045, 2002.

[204] A. A. Sinchenko, R. V. Chernikov, A. A. Ivanov, P. Monceau, T. Crozes, and S. A. Brazovskii, "Hall effect in the pinned and sliding charge density wave state of NbSe $_3$," *Journal of Physics: Condensed Matter*, 21, 43, 435601, 2009.

[205] A. Lupascu, R. Feng, L. Sandilands, Z. Nie, V. Baydina, G. Gu, S. Ono, Y. Ando, D. Kwok, N. Lee, S.-W. Cheong, K. Burch, and Y.-J. Kim, "Structural study of Bi2Sr2CaCu2O8+δ exfoliated nanocrystals," *Appl. Phys. Lett.*, 101, 223106–6, 2012.

[206] A. Augieri, F. Rizzo, V. Galluzzi, A. Mancini, F. Fabbri, A. A. Armenio, A. Vannozzi, V. Pinto, A. Rufoloni, L. Piperno, A. Masi, G. Celentano, L. Barba, G. Arrighetti, and G. Campi, "Correlated Disorder in YBCO and Composite YBCO Films Revealed by Means of Synchrotron X-Ray Diffraction," *IEEE Transactions on Applied Superconductivity*, 28, 4, 1–4, 2018.

[207] M. P. A. Fisher, "Hall effect at the magnetic-field-tuned superconductor-insulator transition," *Physica A*, 177, 1-3, 553–560, 1991.

[208] A. T. Dorsey and M. P. A. Fisher, "Hall effect near the vortex-glass transition in high-temperature superconductors," *Phys. Rev. Lett.*, 68, 5, 694–697, 1992.

[209] Z. D. Wang, J. Dong, and C. S. Ting, "Unified theory of mixed state Hall effect in type-II superconductors: Scaling behavior and sign reversal," *Phys. Rev. Lett.*, 72, 24, 3875–3878, 1994.

[210] N. B. Kopnin, "Hall effect in moderately clean superconductors and the transverse force on a moving vortex," *Phys. Rev. B*, 54, 13, 9475–9483, 1996.

[211] Y. Kato, "Charging Effect on the Hall Conductivity of Single Vortex in Type II Superconductors," *Journal of the Physical Society of Japan*, 68, 12, 3798–3801, 1999.

[212] J. Koláček and P. Vašek, "Hall voltage sign reversal in type II superconductors," *Physica C*, 336, 3-4, 199–204, 2000.

[213] S. Ullah and A. T. Dorsey, "Effect of fluctuations on the transport properties of type-II superconductors in a magnetic field," *Phys. Rev. B*, 44, 1, 262–273, 1991.

[214] T. Nishio and H. Ebisawa, "Hall resistivity of type-II superconductors in the renormalized regime," *Physica C*, 290, 1-2, 43–48, 1997.

[215] K. Michaeli, K. S. Tikhonov, and A. M. Finkel'stein, "Hall effect in superconducting films," *Phys. Rev. B*, 86, 1, 014515, 2012.

[216] P. Ao and D. J. Thouless, "Berry's phase and the Magnus force for a vortex line in a superconductor," *Phys. Rev. Lett.*, 70, 14, 2158–2161, 1993.

[217] D. I. Khomskii and A. Freimuth, "Charged Vortices in High Temperature Superconductors," *Phys. Rev. Lett.*, 75, 7, 1384–1386, 1995.

[218] M. V. Feigel'man, V. B. Geshkenbein, A. I. Larkin, and V. M. Vinokur, "Sign Change of the Flux-Flow Hall Effect in HTSC," *JETP Lett.*, 62, 10, 811–817, 1995.

[219] Z. A. Xu, N. P. Ong, Y. Wang, T. Kakeshita, and S. Uchida, "Vortex-like excitations and the onset of superconducting phase fluctuation in underdoped lasrcuo," *Nature*, 406, 3, 2000.

[220] Y. Wang, Z. A. Xu, T. Kakeshita, S. Uchida, S. Ono, Y. Ando, and N. P. Ong, "Onset of the vortexlike Nernst signal above T c in La 2 - x Sr x CuO 4 and Bi 2 Sr 2 - y La y CuO 6," *Phys. Rev. B*, 64, 22, 224519, 2001.

[221] X. Qiu, ed., *High-Temperature Superconductors*. Cambridge, UK: Woodhead Publishing, 2011.

[222] J. S. Wen, Z. J. Xu, G. Y. Xu, M. Hucker, J. M. Tranquada, and G. D. Gu, "Large Bi-2212 single crystal growth by the floating-zone technique," *Journal of Crystal Growth*, 310, 7, 1401–1404, 2008.

[223] A. Larkin and A. Varlamov, eds., *Theory of Fluctuations in Superconductors*. New York, NY: Oxford University Press, 2005.

[224] S. V. Postolova, A. Y. Mironov, M. R. Baklanov, V. M. Vinokur, and T. I. Baturina, "Reentrant Resistive Behavior and Dimensional Crossover in Disordered Superconducting TiN Films," *Scientific Reports*, 7, 1, 1718, 2017.

[225] M. Truccato, A. Agostino, G. Rinaudo, S. Cagliero, and M. Panetta, "Possible dominance of the Maki–Thompson process in the fluctuation conductivity of Bi-2212 superconducting whiskers," *Journal of Physics: Condensed Matter*, 18, 35, 8295–8312, 2006.

[226] S. V. Postolova, A. Y. Mironov, and T. I. Baturina, "Nonequilibrium transport near the superconducting transition in TiN films," *JETP Letters*, 100, 10, 635–641, 2015.

[227] B. Altshuler and A. Aronov, *Electron–Electron Interaction In Disordered Conductors*, ch. 9. Amsterdam, Netherlands: Elsevier Science, 1985.

[228] P. G. Baity, X. Shi, Z. Shi, L. Benfatto, and D. Popović, "Effective two-dimensional thickness for the Berezinskii-Kosterlitz-Thouless-like transition in a highly underdoped La 2 - x Sr x CuO 4," *Phys. Rev. B*, 93, 2, 024519, 2016.

[229] A. Pomar, M. V. Ramallo, J. Mosqueira, C. Torrón, and F. Vidal, "Fluctuation-induced in-plane conductivity, magnetoconductivity, and diamagnetism of Bi 2 Sr 2 CaCu 2 O 8 single crystals in weak magnetic fields," *Phys. Rev. B*, 54, 10, 7470–7480, 1996.

[230] C. Torrón, A. Díaz, A. Pomar, J. A. Veira, and F. Vidal, "Measurements of fluctuation-induced diamagnetism above the superconducting transition in YBa 2 Cu 3 O 7 - δ single crystals in low magnetic fields: Comparison with paraconductivity," *Phys. Rev. B*, 49, 18, 13143–13153, 1994.

[231] A. L. Solov'ev and V. M. Dmitriev, "Fluctuation conductivity and pseudogap in YBCO high-temperature superconductors (Review)," *Low Temperature Physics*, 35, 3, 169–197, 2009.

[232] D. Destraz, K. Ilin, M. Siegel, A. Schilling, and J. Chang, "Superconducting fluctuations in a thin NbN film probed by the Hall effect," *Phys. Rev. B*, 95, 22, 224501, 2017.

[233] N. P. Breznay, K. Michaeli, K. S. Tikhonov, A. M. Finkel'stein, M. Tendulkar, and A. Kapitulnik, "Hall conductivity dominated by fluctuations near the superconducting transition in disordered thin films," *Phys. Rev. B*, 86, 1, 014514, 2012.

[234] W. Liu, T. W. Clinton, A. W. Smith, and C. J. Lobb, "Hall-conductivity sign reversal and fluctuations in YBa2Cu3O7□? films," *Phys. Rev. B*, 55, 17, 11802, 1997.

[235] K. Nakao, K. Hayashi, T. Utagawa, Y. Enomoto, and N. Koshizuka, "Double sign reversal of the Hall effect in the mixed state of YBa 2 Cu 3 O x," *Phys. Rev. B*, 57, 14, 8662–8666, 1998.

[236] S. H. Pan, E. W. Hudson, A. K. Gupta, K.-W. Ng, H. Eisaki, S. Uchida, and J. C. Davis, "STM Studies of the Electronic Structure of Vortex Cores in Bi2Sr2CaCu2O81d," *Phys. Rev. Lett.*, 85, 1536, 2000.

[237] A. T. Bollinger and I. Božović, "Two-dimensional superconductivity in the cuprates revealed by atomic-layer-by-layer molecular beam epitaxy," *Superconductor Science and Technology*, 29, 10, 103001, 2016.

[238] A. Saxena, *High-Temperature Superconductors*. Heidelberg, Germany: Springer, 2nd ed., 2012.

[239] H. Won and K. Maki, "*D* -wave superconductor as a model of high- T c superconductors," *Phys. Rev. B*, 49, 2, 1397–1402, 1994.

[240] S. Misra, S. Oh, D. J. Hornbaker, T. DiLuccio, J. N. Eckstein, and A. Yazdani, "Atomic Scale Imaging and Spectroscopy of a C u O 2 Plane at the Surface of B i 2 S r 2 C a C u 2 O 8 + δ," *Phys. Rev. Lett.*, 89, 8, 087002, 2002.

[241] Y. Zhong, Y. Wang, S. Han, Y.-F. Lv, W.-L. Wang, D. Zhang, H. Ding, Y.-M. Zhang, L. Wang, K. He, R. Zhong, J. A. Schneeloch, G.-D. Gu, C.-L. Song, X.-C. Ma, and Q.-K. Xue, "Nodeless pairing in superconducting copper-oxide monolayer films on Bi2Sr2CaCu2O8+δ," *Science Bulletin*, 61, 16, 1239–1247, 2016.

[242] J. K. Ren, X. B. Zhu, H. F. Yu, Y. Tian, H. F. Yang, C. Z. Gu, N. L. Wang, Y. F. Ren, and S. P. Zhao, "Energy gaps in Bi2Sr2CaCu2O8+δ cuprate superconductors," *Scientific Reports*, 2, 1, 248, 2012.

[243] A. A. Varlamov, G. Balestrino, E. Milani, and D. V. Livanov, "The role of density of states fluctuations in the normal state properties of high Tc superconductors," *Advances in Physics*, 48, 6, 655–783, 1999.

[244] K. Makise, F. Ichikawa, T. Asano, and B. Shinozaki, "Field-tuned superconductor–insulator transitions and Hall resistance in thin polycrystalline MoN films," *Journal of Physics: Condensed Matter*, 30, 6, 065402, 2018.

[245] A. Glatz, A. A. Varlamov, and V. M. Vinokur, "Quantum fluctuations and dynamic clustering of fluctuating Cooper pairs," *EPL (Europhysics Letters)*, 94, 4, 47005, 2011.

[246] A. Y. Mironov, S. V. Postolova, and T. I. Baturina, "Quantum contributions to the magnetoconductivity of critically disordered superconducting TiN films," *Journal of Physics: Condensed Matter*, 30, 48, 485601, 2018.

[247] M. V. Burdastyh, S. V. Postolova, T. I. Baturina, T. Proslier, V. M. Vinokur, and A. Y. Mironov, "Superconductor–Insulator Transition in NbTiN Films," *JETP Letters*, 106, 11, 749–753, 2017.

[248] R. Ribeiro-Palau, C. Zhang, K. Watanabe, T. Taniguchi, J. Hone, and C. R. Dean, "Twistable electronics with dynamically rotatable heterostructures," *Science*, 361, 6403, 690–693, 2018.

[249] S. Carr, S. Fang, and E. Kaxiras, "Electronic-structure methods for twisted moiré layers," *Nature Reviews Materials*, 5, 10, 748–763, 2020.

[250] X. Lu, P. Stepanov, W. Yang, M. Xie, M. A. Aamir, I. Das, C. Urgell, K. Watanabe, T. Taniguchi, G. Zhang, A. Bachtold, A. H. MacDonald, and D. K. Efetov, "Superconductors, orbital magnets and correlated states in magic-angle bilayer graphene," *Nature*, 574, 7780, 653–657, 2019.

[251] Y. Saito, J. Ge, L. Rademaker, K. Watanabe, T. Taniguchi, D. A. Abanin, and A. F. Young, "Hofstadter subband ferromagnetism and symmetry-broken Chern insulators in twisted bilayer graphene," *Nat. Phys.*, 17, 4, 478–481, 2021.

[252] Y. Zhou, J. Sung, E. Brutschea, I. Esterlis, Y. Wang, G. Scuri, R. J. Gelly, H. Heo, T. Taniguchi, K. Watanabe, G. Zaránd, M. D. Lukin, P. Kim, E. Demler, and H. Park, "Bilayer Wigner crystals in a transition metal dichalcogenide heterostructure," *Nature*, 595, 7865, 48–52, 2021.

[253] X. Liu, Z. Hao, E. Khalaf, J. Y. Lee, Y. Ronen, H. Yoo, D. Haei Najafabadi, K. Watanabe, T. Taniguchi, A. Vishwanath, and P. Kim, "Tunable spin-polarized correlated states in twisted double bilayer graphene," *Nature*, 583, 7815, 221–225, 2020.

[254] D. M. Kennes, M. Claassen, L. Xian, A. Georges, A. J. Millis, J. Hone, C. R. Dean, D. N. Basov, A. N. Pasupathy, and A. Rubio, "Moiré heterostructures as a condensed-matter quantum simulator," *Nat. Phys.*, 17, 2, 155–163, 2021.

[255] L. Wang, E.-M. Shih, A. Ghiotto, L. Xian, D. A. Rhodes, C. Tan, M. Claassen, D. M. Kennes, Y. Bai, B. Kim, K. Watanabe, T. Taniguchi, X. Zhu, J. Hone, A. Rubio, A. N. Pasupathy, and C. R. Dean, "Correlated electronic phases in twisted bilayer transition metal dichalcogenides," *Nat. Mater.*, 19, 8, 861–866, 2020.

[256] K. Schlenga, R. Kleiner, G. Hechtfischer, M. Moble, S. Schmitt, P. Muller, C. Helm, C. Preis, F. Forsthofer, J. Keller, H. L. Johnson, M. Veith, and E. Steinbeiss, "Tunneling spectroscopy with intrinsic Josephson junctions in Bi-2212 and Tl-2223," *Phys. Rev. B*, 57, 22, 14518–14536, 1998.

[257] M. J. Naughton, R. C. Yu, P. K. Davies, J. E. Fischer, R. V. Chamberlin, Z. Z. Wang, T. W. Jing, N. P. Ong, and P. M. Chaikin, "Orientational anisotropy of the upper critical field in single-crystal YBa2Cu3O7 and Bi2.2CaSr1.9Cu2O8+x," *Phys. Rev. B*, 38, 13, 9280–9283, 1988.

[258] A. Bille, R. A. Klemm, and K. Scharnberg, "Models of c-axis twist Josephson tunneling," *Phys. Rev. B*, 64, 174507–23, 2001.

[259] K. Maki and S. Haas, "c-axis Josephson tunneling in d-wave superconductors," *Phys. Rev. B*, 67, 020510, 2003.

[260] Z. Yang, S. Qin, Q. Zhang, C. Fang, and J. Hu, "$\pi/2$-Josephson junction as a topological superconductor," *Phys. Rev. B*, 98, 104515, 2018.

[261] E. Goldobin, D. Koelle, R. Kleiner, and A. Buzdin, "Josephson junctions with second harmonic in the current-phase relation: properties of φ junctions," *Phys. Rev. B*, 76, 224523, 2007.

[262] P. Volkov, J. Wilson, and J. Pixley, "Magic angles and current-induced topology in twisted nodal superconductors," *ArXiv*, 2020.

[263] Q. Li, Y. N. Tsay, M. Suenaga, R. A. Klemm, G. D. Gu, and N. Koshizuka, "Bi 2 Sr 2 CaCu 2 O 8 1d Bicrystal c-Axis Twist Josephson Junctions : A New Phase-Sensitive Test of Order Parameter Symmetry," *Phys. Rev. Lett.*, 83, 20, 4160–4163, 1999.

[264] Y. Takano, T. Hatano, A. Fukuyo, A. Ishii, M. Ohmori, S. Arisawa, K. Togano, and M. Tachiki, "D-like symmetry of the order parameter and intrinsic Josephson effects in (formula presented) cross-whisker junctions," *Phys. Rev. B*, 65, 140513, 2002.

[265] Y. I. Latyshev, A. P. Orlov, A. M. Nikitina, P. Monceau, and R. A. Klemm, "c-axis transport in naturally grown Bi2Sr2CaCu 2O8+δ cross-whisker junctions," *Phys. Rev. B*, 70, 094517–7, 2004.

[266] Y. Zhu, Q. Li, Y. N. Tsay, M. Suenaga, G. Gu, and N. Koshizuka, "Structural origin of misorientation-independent superconducting behavior at [001] twist boundaries in Bi2Sr2CaCu2O8+x," *Phys. Rev. B*, 57, 14, 8601–8608, 1998.

[267] N. Poccia, S. Y. F. Zhao, H. Yoo, X. Huang, H. Yan, Y. S. Chu, R. Zhong, G. Gu, C. Mazzoli, K. Watanabe, T. Taniguchi, G. Campi, V. M. Vinokur, and P. Kim, "Spatially correlated incommensurate lattice modulations in an atomically thin high-temperature $bi_{2.1}sr_{1.9}Cacu_{2.0}o_{8+y}$ superconductor," *Phys. Rev. Materials*, 4, 114007, Nov 2020.

[268] A. Irie, S. Heim, S. Schromm, M. Moble, T. Nachtrab, M. Godo, R. Kleiner, P. Muller, and G. Oya, "Critical currents of small BSCCO intrinsic Josephson junction stacks in external magnetic fields," *Phys. Rev. B*, 62, 10, 6681–6686, 2000.

[269] S. Plugge, T. Tummuru, and M. Franz, "Josephson effects in twisted cuprate bilayers," *unpublished*, 2021.

[270] Y. I. Latyshev, J. E. Nevelskaya, and P. Monceau, "Dimensional Crossover for Intrinsic dc Josephson Effect in Bi2Sr2CaCu2O8 2212 Single Crystal Whiskers," *Phys. Rev. Lett.*, 77, 5, 932–935, 1996.

[271] L. Bulaevskii, J. Clem, and L. Glazman, "Fraunhofer oscillations in a multilayer system with Josephson coupling of layers," *Phys. Rev. B*, 46, 350, 1992.

[272] I. Nevirkovets, J. Evetts, and M. Blamire, "Transition from single junction to double junction behaviour in SISIS-type Nb-based devices," *Physics Letters A*, 187, 1, 119–126, 1994.

[273] M. J. A. Stoutimore, A. N. Rossolenko, V. V. Bolginov, V. A. Oboznov, A. Y. Rusanov, D. S. Baranov, N. Pugach, S. M. Frolov, V. V. Ryazanov, and D. J. Van Harlingen, "Second-harmonic current-phase relation in josephson junctions with ferromagnetic barriers," *Phys. Rev. Lett.*, 121, 17, 177702, 2018.

[274] G. Balestrino, E. Milani, C. Aruta, and A. A. Varlamov, "C -axis resistance peak above the critical temperature in layered superconductors," *Phys. Rev. B*, 54, 5, 3628–3632, 1996.

[275] J. M. B. Lopes dos Santos and E. Abrahams, "Superconducting fluctuation conductivity in a magnetic field in two dimensions," *Phys. Rev. B*, 31, 1, 172–176, 1985.

[276] T. I. Baturina, S. V. Postolova, A. Y. Mironov, A. Glatz, M. R. Baklanov, and V. M. Vinokur, "Superconducting phase transitions in ultrathin TiN films," *EPL (Europhysics Letters)*, 97, 1, 17012, 2012.

[277] P. Minnhagen, "Kosterlitz- Thouless transition for a two-dimensional superconductor: Magnetic-field dependence from a Coulomb-gas analogy," *Phys. Rev. B*, 23, 11, 5745–5761, 1981.

[278] P. Minnhagen, "The two-dimensional Coulomb gas, vortex unbinding, and superfluid-superconducting films," *Rev. Mod. Phys.*, 59, 4, 1001–1066, 1987.